ALMA MATER STUDIORUM - UNIVERSITÀ DI BOLOGNA

FACOLTÀ DI CHIMICA INDUSTRIALE

Master in Advanced Spectroscopy in Chemistry

Atmospheric corrosion of quaternary bronzes (Cu – Sn – Zn – Pb): Laboratory tests (accelerated ageing in wet & dry conditions) and field studies (the Bottego monument in Parma, Italy)

Presented by:	Tutor:
Jesús Héctor Morales Espejo	Dott.ssa Carla Martini
	Co-tutor:
	Dott.ssa Cristina Chiavari
	Dott.ssa Elena Bernardi
	Dott. Diego Cauzzi
	Dott.ssa Francesca Ospitali

Session I

Academic year 2010 - 2011

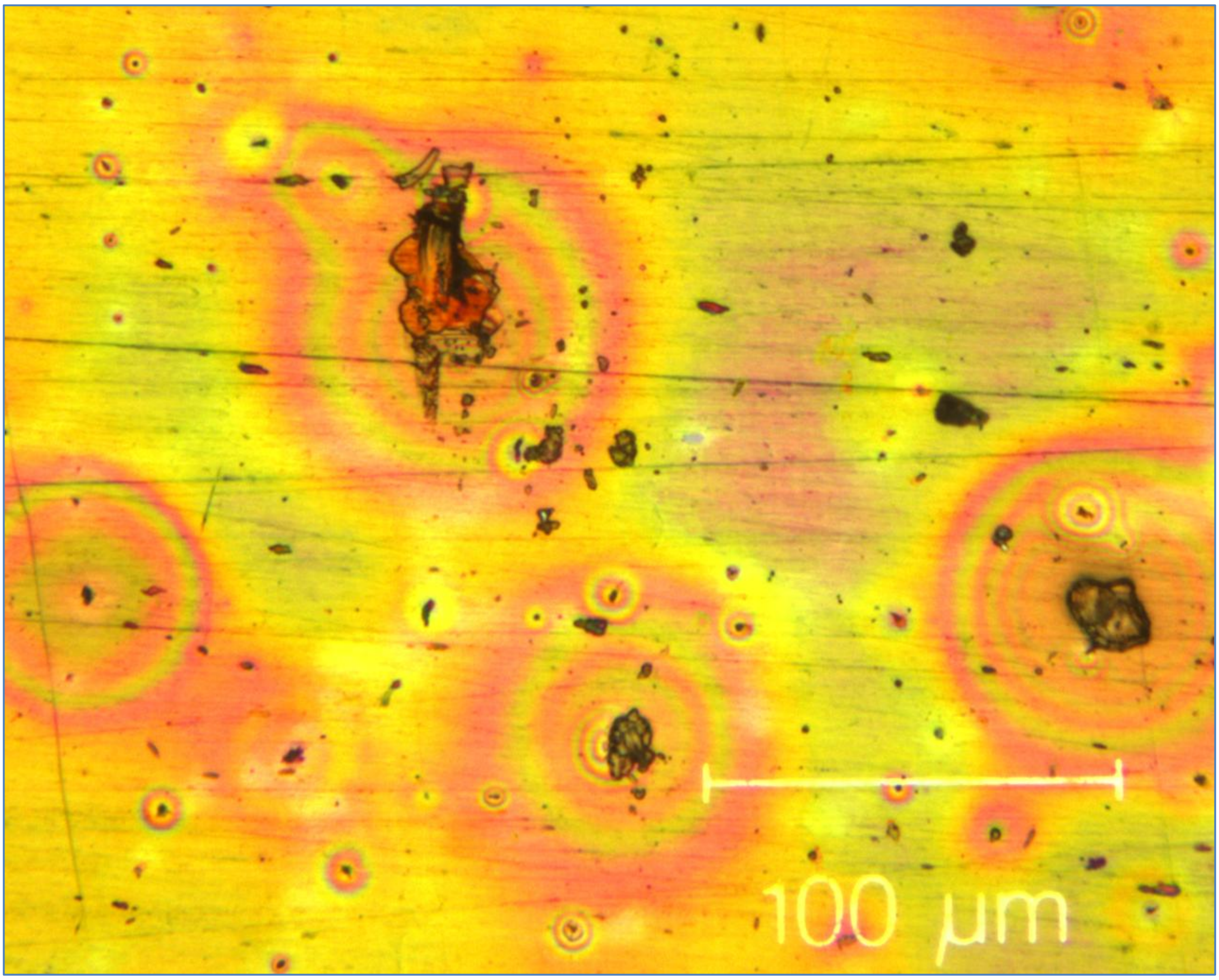

"Nature composes some of her loveliest poems

for the microscope and the telescope."

Theodore Roszak

To my beloved parents, Héctor and Clara,

because with their endless support and understanding

have made many of my dreams become true.

Contents

Aim and background

The interactions between outdoor bronzes and the environment, which lead to bronze corrosion, require a better understanding in order to design effective conservation strategies in the cultural heritage field.

The main points which require further investigations are:

1. Understanding the role of alloying elements: Even if copper is the main alloying element in bronze, the corrosion behaviours of copper and bronze are different because, in the case of bronze, each alloying element plays a different role. In particular, tin has been considered as a structural stabilizing agent in bronze patinas [1], and bronze corrosion has been described as a decuprification phenomenon involving complex migration processes [2, 3, 4, 5, 6].

2. Evaluating the influence of exposure geometry: In real outdoor bronze monuments, the corrosion behaviour is strongly influenced by the exposure geometry: Sheltered and unsheltered areas (with respect to the action of rainfall) may produce patinas with significantly different features [7, 8, 9, 10]. This must be taken into account when designing conservation procedures, since the patina is in most cases the support on which corrosion inhibitors are applied.

3. Selecting corrosion inhibitors which are both effective and non-toxic: Concerning this aim, particular attention should be devoted both to the inhibitor efficiency testing conditions and to the support on which the inhibitors are applied (e.g. bare metal or corroded metal). Reliable results can be obtained only by applying the inhibitors on a support which is representative of real application conditions and by testing the inhibitor efficiency under conditions which reproduce the complexity of outdoor exposure.

As far as points 1 and 2 are concerned, with the purpose to acquire a better understanding of the interactions between outdoor bronzes and the environment, different devices have been developed to simulate real outdoor conditions into the laboratory. In particular, owing to the collaboration between the Dept. SMETEC and the Dept. of Industrial Chemistry and Materials (Environmental and Cultural Heritage Chemistry Group), both from Università di Bologna, Facoltà di Chimica Industriale, accelerated ageing devices by wet & dry (simulating the action of stagnant rain in sheltered areas) and by dropping (simulating the leaching action of the rain in unsheltered areas) tests were designed and constructed [2, 3]. The comparison of the results of these tests with the investigations on real bronze monuments confirmed the effectiveness of accelerated ageing devices, and allowed the identification of the main features on bronze patinas formed under different exposure conditions [11].

About point 3, investigations on patina composition and chemical behaviour are important because, under the current conservation conditions for outdoor bronzes, most restorers work on patinated surfaces, and not on bare metal (which is only the case for contemporary art).

With the purpose to provide protection against atmospheric corrosion to the bare metal, different chemical agents have been tested and approved to be applied as corrosion inhibitors on outdoor bronzes. Nowadays, benzotriazole (BTA) and its derivatives are the most common compounds used with this aim. However, it has been demonstrated that BTA is efficient when applied on bare copper but not as efficient when applied on bare bronze [12]. Moreover, BTA and its derivatives are considered toxic and possibly carcinogenic [13]. Health issues during the application of inhibitors in conservation interventions are increasingly being taken into account [14]. Furthermore, outdoor bronzes are exposed to rain events and other phenomena which eventually are able to leach part of these compounds, releasing them into the environment. For these reasons, the identification of new corrosion inhibitors with high protective efficiency and non-toxic to the environment and the living organisms is essential.

Therefore, thanks to the collaboration with the Corrosion Studies Centre “Aldo Daccò” at the Università di Ferrara, silane-based inhibitors (already successfully tested on copper, magnesium, aluminum and iron [15]) were taken into consideration as a non-toxic, environmentally friendly alternative to BTA derivatives for bronze protection. Also, possible modifications of the inhibiting film deserve further research, such as the addition of nanoparticles, which, in the case of silane-based inhibitors applied on the AZ31 magnesium alloy [16] led to an increase of the protective efficiency.

In the present work, investigations on real patinas and application of corrosion inhibitors are performed with the intention to:

- Identify alloy and corrosion products on a real outdoor bronze monument, so as to compare the patina in sheltered/unsheltered areas, before and after the cleaning procedure carried out during the restoration intervention.

- Use accelerated ageing tests as a method to produce pre-patinated bronze surfaces for the application of candidate inhibitors.

- Evaluate and compare protective efficiency towards both bare and aged bronze of a silane-based inhibitor, 3-mercapto-propyl-trimethoxy-silane.

- Evaluate the influence of the addition of CeO_2 nanoparticles on the protective efficiency of 3-mercapto-propyl-trimethoxy-silane.

In order to achieve these aims, a wide range of spectroscopic techniques has been used, for characterising the core metal (SEM+EDS, XRF, AAS), the corroded surfaces (SEM+EDS, portable XRF, micro-Raman, ATR-IR, Py-GC-MS) and the ageing solutions (AAS).

Introduction

I.1 Bronze foundry alloys

I.1.1 Composition

Bronze is usually an alloy of copper (~90%) and tin (~10%), but its composition can vary widely. It is often used for applications where copper needs more strength and corrosion resistance or for ornamental purposes. Its colour is pink-salmon in pure state, but it is rarely seen like that because usually exhibits some oxidation or corrosion which changes its colour to lime-green or even dark-brown, depending on the composition of the bronze, weather, location, exposure, pollution, possible maintenance and if the alloy has received any protective treatment [17].

Nowadays different alloys are used as bronze in sculpture and construction [17]:

(a) Statuary bronze: Approximately 97 wt% copper, 2% tin and 1% zinc. Typically used in outdoor sculpture. It may be cast in any shape depending on the mold used.
(b) Architectural bronze: Approximately 57 wt% copper, 40% zinc and 3% lead. Used for door and window frames, mailboxes, rails, etc.
(c) Commercial “bronze”: Approximately 90 wt% copper and 10% zinc (mostly known as brass).

However, contemporary bronzes are alloys which can contain silicon, manganese, aluminium and other elements, with or without tin.

Bronzes include a number of different alloys containing also lead and zinc as alloying elements. Tin and zinc increase hardness and breaking strength, while lead improves machinability and castability.

Because bronze is not a native metal, its constituents tend to return to the most stable state and this is the reason of inherent problems in the bronze structure. The oxidation which takes place in bronze forms a layer of corrosion products, also called “patina”. Patinated surfaces may be more resistant to the effects of the exposure than bare bronze, maintaining the original appearance and changing more slowly [17].

I.1.2 Properties

The main component of bronze is copper. Copper is generally alloyed with other elements to improve its castability. Pure copper is extremely difficult to cast. However, in applications which require an excellent electrical conductivity of copper, alloying is avoided [17].

Some of the elements which give different properties to copper are [18]:

Tin: The oldest known alloying element in copper and the key alloying element in many bronzes. It is a solid-solution strengthener in copper, improves corrosion resistance, reduces the melting temperature of copper and increases the fluidity, making the alloy easier to melt and cast.

Zinc: Imparts strength and hardness. This is the major alloying element for brasses.

Lead: An element which is insoluble in copper. Because it solidifies last, is found at the grain boundaries or interdendritic areas. It is used to help to seal the shrinkage cavities formed toward the end of solidification of the alloy (i.e. it improves hot tearing resistance [19]). It also improves machinability.

Aluminium: Improves the strength and fluidity of copper alloys, but its solubility in copper is limited.

Silicon: Provides excellent fluidity to copper alloys, enabling them to be used for art and mold castings.

Nickel: Provides resistance to corrosion and improves the quality, strength and creep resistance of tin bronzes.

Beryllium: Increases strength by forming an interdendritic precipitate without compromising the electrical and thermal conductivity.

Chromium: Increases strength with a minor loss in electrical conductivity.

Iron: An element not soluble in copper. It increases the melting temperature of copper alloys. Excessive iron levels can cause segregation and hard spots. In tin bronzes, iron increases strength and hardness but reduces ductility.

However, alloying alters the oxidation rate of copper, generally slowing it in the case of tin addition, and speeding up oxidation in the case of nickel addition [20].

I.1.3 Microstructure

Metals can be formed by two main manufacturing methods: Casting and working. There are different ways to cast or work a metal.

Casting:

This is a technique that has been used for at least 6000 years [21]. There are two main growth mechanisms which can originate from the casting and cooling of a melt in a mold, regardless of the exact nature of the technology involved. It is important to emphasize that the kind of crystal growth that can occur depends on the composition of the metal [22], as well as on the cooling rate [23]. These two mechanisms are:

(1) Planar growth: This kind of growth takes place when any small protuberance on the solid/liquid interface is surrounded by liquid above the freezing temperature. Therefore, the growth stops until the rest of the interface catches up and the whole interface moves smoothly into the liquid.

(2) Dendritic growth: Dendrites (meaning “tree-like”) look as tiny fernlike growths scattered at random throughout the metal. They grow larger until meeting each other. The rate at which the metal is cooled influences their size. The slower the cooling rate the bigger the dendrites, and the easier to see them (sometimes even at naked eye). Dendrites exhibit arms which are usually referred as primary, secondary or tertiary [22]. Examples of this kind of growth can be seen in Fig. I.1.

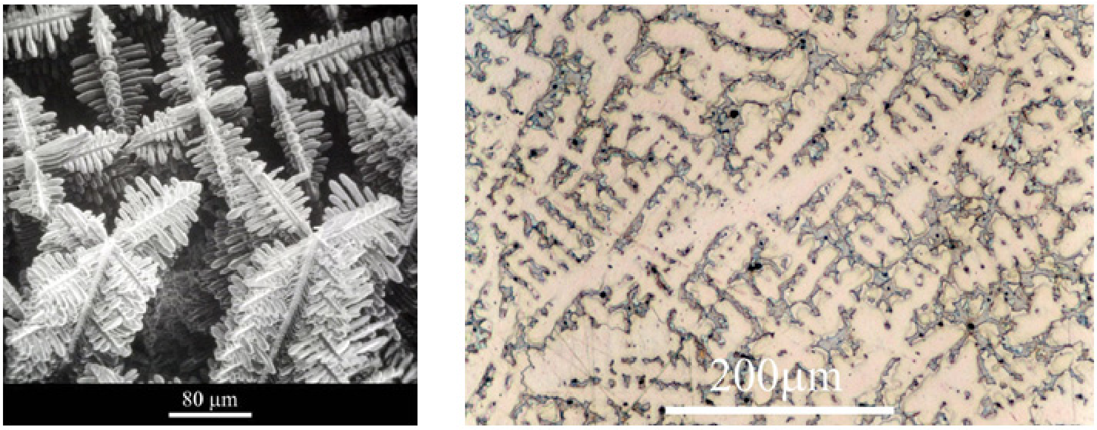

Fig. I.1 - Examples of dendrites [23]

Dendrites may be rather fuzzy or rounded in outline or quite sharp and well-defined, depending on the nature of the alloy and the cooling conditions of the melt.

The formation of dendrites is due to undercooling phenomena: The liquid ahead of the solidification front may be undercooled below its freezing temperature, even though it is hotter than liquid at the front. Therefore, if a small solid protuberance forms on the solid/liquid interface, it is encouraged to grow [24].

Dendritic growth occurs both in pure metals and in alloys; however, in alloys, the possible occurrence of constitutional undercooling makes the dendritic growth more likely.

Dendritic microstructures may also display solidification defects such as microsegregation (also known as “coring”), due to non-equilibrium solidification (Fig. I.2 a). In the case of copper-tin bronzes, copper melts at 1083°C and tin at 232°C and, therefore, when the alloy cools and begins to solidify, the first part of the dendrite’s arms to form are richer in copper since this constituent solidifies first, while the outer parts of the arms (branches) are richer in tin. Taking this into account, there is a “compositional gradient” from the inner region of a dendritic arm to the outer surface, and this kind of dendrites is usually referred as “cored” (Fig. I.2 b). Coring is a common feature in bronze castings [22].

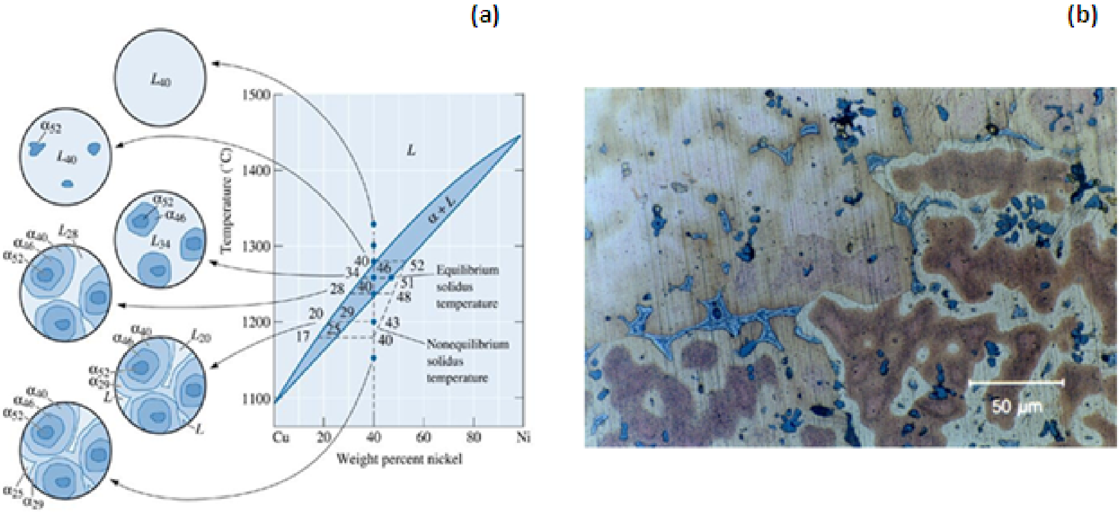

Fig. I.2 - Development of cored microstructure due to non-equilibrium solidification (a) [24], and an example of cored dendritic microstructure in bronze alloys (b): The Cu-rich core of dendrites is brown whilst the Sn-rich peripheral region is whitish.

Pure copper can occasionally be relatively free of impurities and, on slow cooling, no dendrites may be visible, producing an equi-axial, hexagonal grain structure (Fig. I.3 left). This kind of structure, in which all the grains are roughly the same size, randomly oriented and roughly hexagonal in section, corresponds to an ideal model of a metallic crystal. It is an equilibrium structure, with the least energy requirement, while the dendritic structure is a non-equilibrium one (Fig. I.3 right) [22].

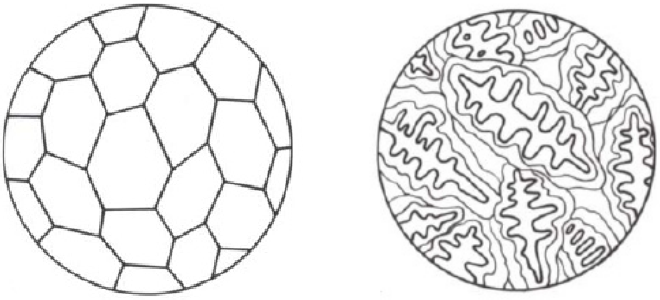

Fig. I.3 - Ideal model of a metallic crystal (left), usual dendritic structure in an alloy (right) [22]

Cast metals often display characteristic spherical holes or porosity (Fig. I.4 a), which can be due to dissolved gases in the melt, or shrinkage cavities (Fig. I.4 b), due to inadequate metal feeding after contraction of the metal during solidification [22].

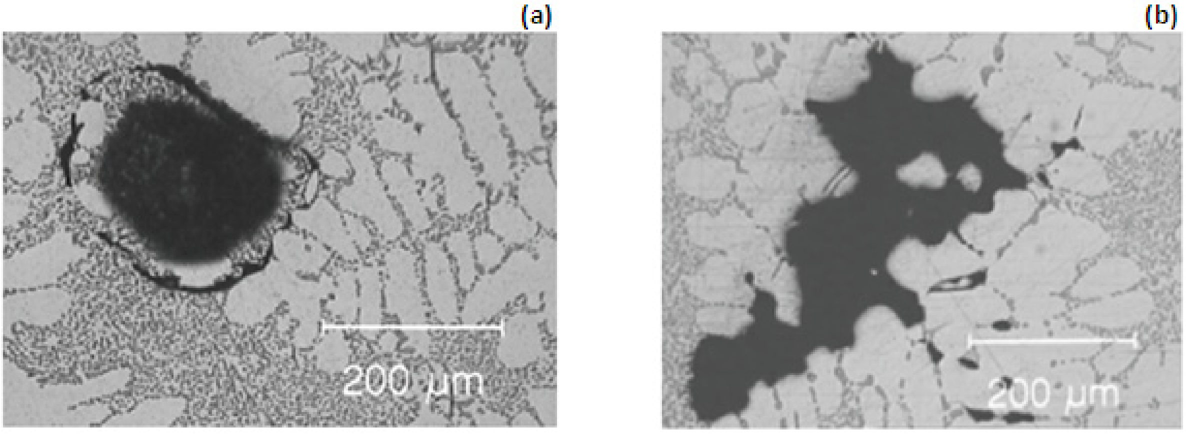

Fig. I.4 - Examples of gas porosity (a) and shrinkage cavities (b) in Al-Si alloys [25]

Working:

It is a method or combination of methods with the purpose to change the shape of a metal or alloy by mechanical techniques such as hammering, rolling, drawing, etc.

The grain structure of a metal can be deformed by hammering until grains are too brittle to continue working. If further hammering of the metal is required, then the metal must be annealed (around 500-800°C for copper alloys) in order to restore ductility and malleability [22]. This alternation between hammering and annealing can be repeated several times until achieving sufficient deformation of the starting material.

All the thermal and mechanical treatments modify the microstructure of the bronze. A scheme with the main modifications can be seen in Fig. I.5.

When working with alloys, it is important to specify the type of annealing required (stress-relief, solid-solution, etc.) and the time. A long-time annealing may lead to grain growth and a weakening of the structure of the final object. At short-time annealing, heterogeneity and residual stresses may not be eliminated sufficiently [22].

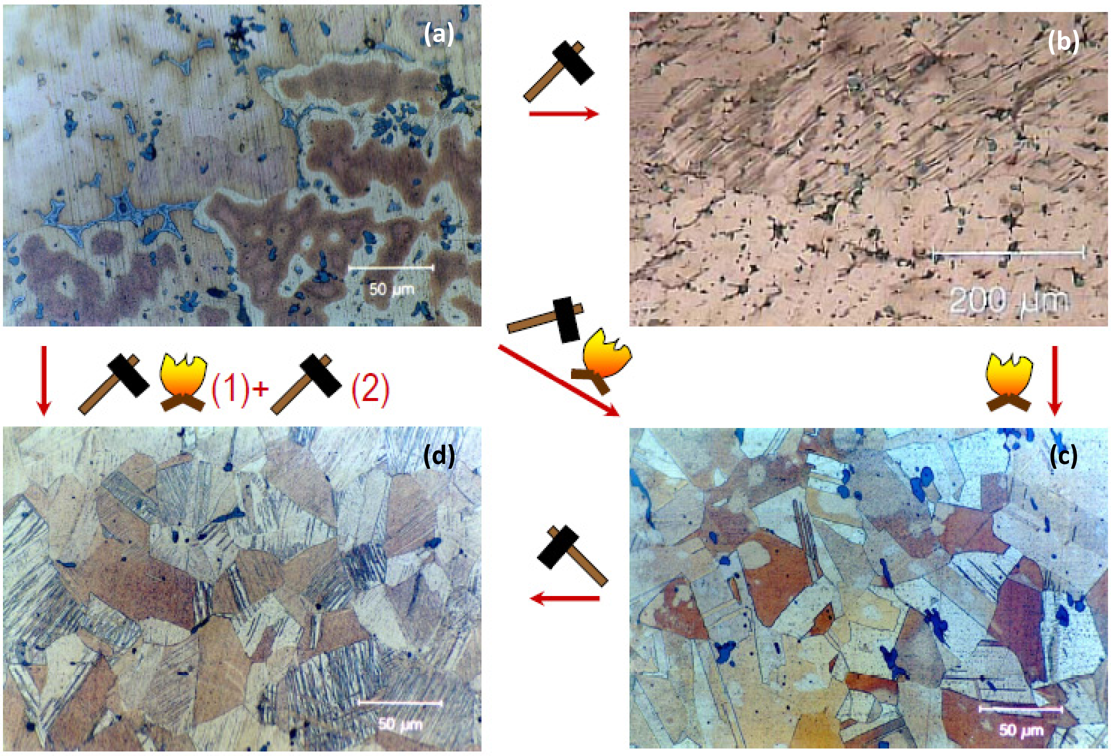

Fig. I.5 - Micro-structural modifications induced by thermal/mechanical treatments in the bronze microstructure: As-cast dendritic structure (a), deformed dendrites with slip bands (after cold working) (b), recrystallised microstructure (after annealing) (c), recrystallised microstructure with slip bands (after annealing followed by cold working) (d).

However, it is often difficult to completely remove by annealing the segregation that occurs during the casting operation [22].

Segregation is not the only phenomenon which affects the microstructure of a metal or alloy. The presence of two or more phases has an influence on mechanical and chemical properties.

A phase is any homogeneous state of a substance which has a definite composition. When two (or more) metals are mixed together to form an alloy there are different possibilities regarding their mutual solubility:

(a) Solid alloy showing complete solid solubility of the metals. In this case, as temperature rises, the solid alloy passes through a pasty, semisolid region in which some liquid is present in equilibrium with some solid and, finally, all the alloy becomes a liquid melt. If no segregation is present, then the microstructure will be a group of equi-axial, hexagonal grains of uniform composition.
(b) Solid can show only partial solubility of the metals in each other.
(c) Metals are completely immiscible in each other.

Depending on the solubility, different solid phases may be present for a same two-metal system. These phases are usually represented in phase diagrams, which show different regions where one phase or a mix of phases is present depending on the composition and the temperature [22].

For the case of partial solubility, three main types of phase diagrams may be generated:

(a) Eutectic diagrams: The solubility of two metals falls as the temperature falls (which is common for most alloys) and there is one temperature at which the liquid melt can pass directly to solid (meaning there is no pasty, semisolid region). That temperature is known as the eutectic point, which varies according to the nature of the alloying constituents. Some common examples of eutectic systems are silver-copper and lead-tin alloys [22].

(b) Eutectoid diagrams: A solid solution that already exists transforms into two distinct phases, making the diagrams more complex. Carbon steels and tin bronzes fall into this type.

(c) Peritectic diagrams: When a liquid reacts with an existing solid phase to form a new solid phase. A system which presents a series of peritectic reactions is the copper-zinc alloy.

In the case of complete immiscibility, alloys of copper-lead or zinc-lead are good examples. As temperature falls from the melt of these insoluble metals, one of them starts to precipitate, usually as globules of the low-concentration phase at grain boundaries of the metal matrix. In the case of leaded copper, practically all the copper solidifies before the lead-copper eutectic forms, which is 99.9% lead and 0.1% copper, practically pure lead. This means lead is segregated while the process of solidification takes place. Lead usually is present as dispersed spherical globules scattered at the grain boundaries and within the grains. The size of lead globules mainly depends on the total amount of lead in the alloy as well as from the cooling rate.

Tin bronzes may be divided into two regions: Low-tin bronzes and high-tin bronzes. Low-tin bronzes are those in which the tin content is less than 15.8 wt% (the maximum theoretical limit of the solubility of tin in the copper-rich solid solution, as shown in Fig. I.6 (in practice, the actual limit of solid solution is closer to 14 wt%).

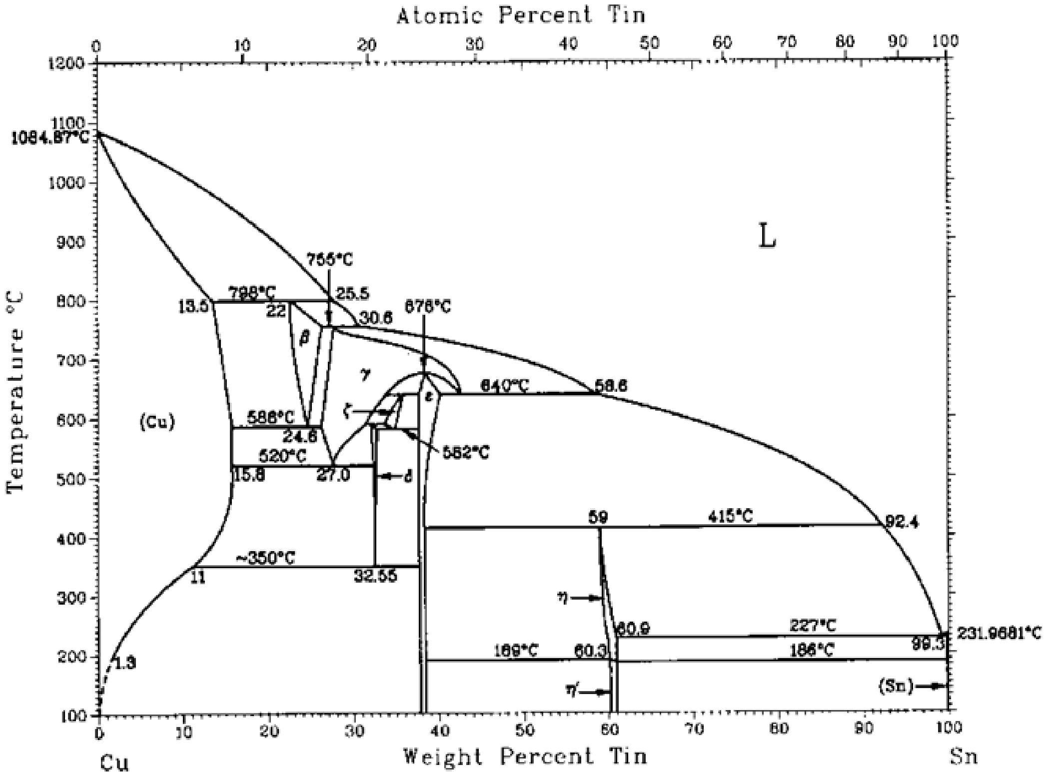

Fig. I.6 - Cu-Sn phase diagram [26]

When a tin bronze is cast, the alloy is extensively microsegregated, usually with cored dendritic growth, and an infill of the alpha + delta eutectoid surrounds the dendritic arms. The center of the dendrite arms are copper rich, since copper has the higher melting point, and the successive growth of the arms results in the deposition of more tin. At low-tin contents (between 2-5 wt%), it may be possible for all the tin to be absorbed into the dendritic growth; however, this varies considerably depending on the cooling rate of the bronze and the kind of casting involved. As the tin content increases the proportion of interdendritic eutectoid also increases.

Structural features seen in most low-tin bronzes are the following:

(a) Homogeneous bronzes in which all the tin has dissolved within the copper and which do not display coring or residual cast features.
(b) Cored bronzes in which there is an unequal distribution of copper and tin, but no eutectoid constituent is present.
(c) Bronzes in which both the Cu-rich alpha phase and the eutectoid constituent are present.
(d) Bronzes in which the alpha phase is extensively cored and where the eutectoid constituent is also present.

Most artistic casting display (b) or (d) microstructures, due to the unavoidable microsegregation which takes place in conventional casting conditions. The distinction between (b) and (d) is mainly based on the amount of tin in the alloy (if tin is below the solubility limit, then you get (b)-type microstructure; (d)-type microstructure instead is generated by tin % beyond the solubility limit).

I.2 Atmospheric corrosion of bronze

Bronze objects in outdoor environments are common and often not well maintained. Outdoor bronzes, if unprotected, undergo visible changes caused by the formation of corrosion products, the so-called “patina”. Sometimes these changes are desirable from an aesthetic point of view, but sometimes not [21]. Mattson, a researcher who started studying copper corrosion around 1958 in Sweden, said that “the atmosphere exposure of copper has generally no detrimental effect, but rather a beneficial one; it develops an interesting and pleasing play of colours on the metal surface, excellent for architectural purposes” [27].

The discolouration of a bronze surface may vary considerably with time, type of environment and exposure conditions. In general, there is a change in visual appearance from the characteristic lustrous to a more brownish, blackish or greenish surface, which increases with time of exposure [21]. This visual appearance is influenced by the microstructure of the cast bronze and, therefore, by the alloy composition; however, this composition is not the determinant factor in bronze deterioration.

The presence of sulphur and chlorine in the atmosphere, combined with moisture, is the most significant cause of bronze deterioration [17]. Already around 1930’s, W.H.J. Vernon conducted some experiments and discovered that the main components of several patina samples were naturally occurring minerals of sulfur and chlorine [28].

Other important factors influencing the corrosion process are surface inclination and environmental characteristics. A skyward facing surface in general forms a green patina layer more easily than a vertical or downward surface, because skyward surfaces are subjected to larger variations of surface temperature and also are more accessible to corrodants from precipitation and from coarse particles, therefore the humidity is easily trapped and retained in the patina (stagnation), promoting the conditions for green patina formation [21].

On the other hand, vertical or downward facing surfaces exhibit lower surface temperature variations and lower deposition rates, which seem to favor cuprite formation and the resulting colour is brownish.

Although in the past it was believed that patinas consisted of copper carbonate or copper sulphate, nowadays it is known that bronze patina consists of at least three different layers [21]:

- An inner layer composed of cuprite (Cu_2O)
- A middle layer of green copper salts, the most common of which is brochantite. White residues of tin oxide, SnO_2, are embedded in the green copper salts on tin-bronze

- An outer black and dull layer composed of deposited coarse particles such as fine quartz, aluminium oxide, iron oxide and soot

Concerning the chemical composition, some commonly phases found on bronze weathered in the atmosphere are [27]:

Cuprite [Cu_2O]: Insoluble in water and slightly soluble in acid.

Brochantite [$Cu_4(SO_4)(OH)_6$]: Nearly always the most common component of the green patina formed after long atmospheric exposure, even in situations like the Statue of Liberty located in New York Harbour and surrounded by salt sea water.

Antlerite [$Cu_3(SO_4)(OH)_4$]: Not uncommon as a patina constituent. It is stable in more acidic conditions than brochantite (Fig. I.8). This phase was found on the copper skin of the Statue of Liberty, and it is suggested that acid rain converts brochantite to less protective antlerite, which is more susceptible to erosion.

Posnjakite [$Cu_4(SO_4)(OH)_6{\cdot}H_2O$]: Just an hydrated form of brochantite. It may co-exist or undergo transformation to brochantite (Fig. I.7).

Atacamite [$Cu_2Cl(OH)_3$]: Soluble in weak acid. It has been found to be as abundant or more abundant than brochantite in patinas formed near the sea. Not found on specimens exposed for short times.

Paratacamite [$Cu_2Cl(OH)_3$]: Its presence is transitory and it eventually converts to atacamite. Not found on specimens exposed for long times.

Atmospheric particles: Alumina, iron oxide, silica and other components typical of wind-blown dust are frequently noted, as is soot.

Malachite [$Cu_2(CO_3)(OH)_2$]: Atmosphere does not favour the formation of this carbonate, but it is sometimes unexpectedly found in practice.

Gerhardtite [$Cu_2NO_3(OH)_3$]: Found just in some locations.

As it can be noticed, some phases are very similar and, in fact, they can be interconnected given that some phases are precursors of others. Krätschmer et al. [29] proposed a scheme about the evolution of sheltered copper patina as a function of exposure time, showing the different phases which have been experimentally observed and their connections. Many of the phases on copper patina are also present in bronze patina. This scheme can be seen in Fig. I.7.

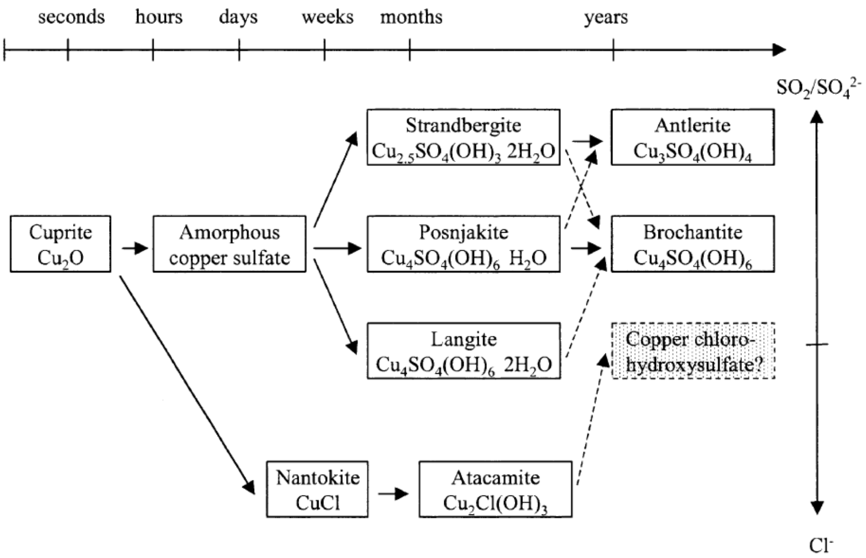

Fig. I.7 - A general patina evolution scheme of sheltered copper, displaying the formation of different compounds as a function of exposure time in either sulphate- or chloride-dominated environments. Experimentally observed phases are shown in white boxes, whereas one postulated phase is shown in a shaded box. Similarly, experimentally observed transitions from one phase to another are shown by solid arrows, and postulated transitions by dashed arrows [29].

The scheme in Fig. I.7 shows that cuprite is almost immediately formed once copper is exposed to the atmosphere. The transition from cuprite (crystalline cubic structure, high symmetry) to one of the copper hydroxysulphates (laminar structure) passes through an amorphous copper sulphate phase [30]. If the environment has acid conditions (high SO_2/SO_4^{2-} concentration), this amorphous phase transforms to strandbergite, while posnjakite and langite are favored in less acidic conditions. The eventual transformation to brochantite or antlerite is a slow process which takes years.

On the other hand, if the environment is rich in chlorides, cuprite goes directly to nantokite and later to atacamite in a process which may take a few months.

The process of formation of a patina can be described in five stages [17]:

(1) **Induction**: Oxidation takes place and produces the dark brown copper oxide film which serves as protective barrier against future pollutants. The composition of this film depends on the type and concentration of pollutants in the atmosphere, duration of exposure and the relative degree and duration of wetness on the surface. High concentrations of sulfides in the atmosphere can dramatically alter the chemistry at this stage.

Metallic copper oxidizes according to the following reaction [27]:

$$2\ Cu + ½\ O_2 \rightarrow Cu_2O$$

Pb exposed to the atmosphere has been reported to primarily form litharge (PbO), while Sn forms cassiterite (SnO_2) or, more probably, an amorphous hydrated oxide ($SnO_2 \cdot xH_2O$) [31].

(2) **Conversion to copper sulphate (sulphurization)**: Normally starts in horizontal surfaces because these are the ones with more exposure to moisture (rain, water run-off) and deposition of particles (especially SO_2 and H_2S), creating a situation where electrolytic reactions occur.

Copper ions from the cuprite are oxidized from Cu^+ to Cu^{2+} in the presence of a layer of surface water via the two partial reactions:

$$Cu^+ \rightarrow Cu^{2+} + e$$

$$½\ O_2 + H_2O + 2e \rightarrow 2OH^-$$

Atmospheric SO_2 is oxidised to sulphate by the reaction:

$$SO_2 + H_2O + ½\ O_2 \rightarrow H_2SO_4$$

And then Cu^{2+} reacts slowly to form basic salts according to:

$$Cu_2O + SO_4^{2-} + H_2O \rightarrow Cu_x(SO_4)(OH)_y \cdot nH_2O \quad \text{(posnjakite, brochantite or antlerite)}$$

$$Cu_2O + Cl^- + H_2O \rightarrow Cu_2Cl(OH)_3 \quad \text{(paratacamite or atacamite)}$$

Some thin and light green patches can be observed on the more exposed areas, due to the formation of brochantite (if SO_2 is present) or atacamite/paratacamite (if Cl^- is present) [32].

PbO is known to react rapidly with SO_2 and HSO_4^-(aq) forming insoluble sulphite ($PbSO_3$) and sulphate ($PbSO_4$), respectively. Anglesite ($PbSO_4$) tends to form a protective layer. Other lead species like lanarkite (Pb_2SO_4O), PbO and minium (Pb_3O_4) have been detected [31].

SnO_2 and $SnO_2 \cdot xH_2O$ have acidic character and react slowly or not at all with SO_2 and HSO_4^-(aq). An amorphous gel of the hydrated oxide has been suggested to form on bronzes exposed in outdoor environments [31].

As for Zn, it has been reported that it reacts with SO_2 to form $ZnSO_3$, which is subsequently oxidised to soluble $ZnSO_4$ [31].

(3) **Run-off streaking and scab formation**: The degree of solubility of the copper sulphates and sulphides formed in previous stages may vary widely.

Not all the brochantite is retained on the surface. Some is lost in runoff and this leads to commonly observed staining of the base of bronze statues [27].

Streaking and uneven discolouration occur due to differential weathering of the corrosion products. Patterns of green streaking on a dark blackish surface may appear. If this happens, conservation techniques are likely to be required.

(4) **Pitting**: Generally caused by microscopic particles of chlorides deposited from the air and coming from saline soils or salt spray near to bodies of salt water. The chlorine reacts with the copper in bronze to form copper chloride. This phenomenon can even spread below protective coating, patina or what appears to be a stable surface. It is commonly known as “bronze disease”.

Likewise, it has been reported that brochantite can react with chloride ions if the chloride concentration is very high [27].

Copper chloride is relatively unstable and it is important to remove it by conservation techniques which employ electrochemical methods to avoid the continuing corrosion of the bronze.

(5) **Conversion to blue-green copper sulphate**: All exposed surfaces form a lime-green colour and matte texture, which is the familiar solid green bronze. It is actually a phase of active corrosion. The time scale for this patina formation varies with local environmental conditions and is reported to be between 20 and 70 years in Europe [27].

As it can be seen, patinas are chemically and structurally complex [33], and the process of formation includes repeated dissolution and precipitation, processes which are triggered by strongly varying humidity conditions resulting in a gradual accumulation of less-soluble corrosion products in the patina, whereas more easily dissolved compounds (like those of zinc) are washed away [14]. As a result, the patina will be more and more corrosion resistant and the corrosion rate is expected to gradually decrease with exposure time. Patinas are also not spatially or chemically uniform [28]. Chiavari et al. [11] reported that for outdoor bronzes which are exposed to rain events, if the surface is under stagnant rain conditions, the patina acts as a multilayer system where a Sn-enriched layer is covered by Cu and Pb compounds, and Zn dissolves completely; while in the case of runoff conditions, the patina is a thin porous layer strongly enriched in insoluble Sn oxides across which Cu, Zn and Pb cations migrate and most of them are leached into the environment.

Moreover, some non-reactive substances, like Al_2O_3 or SiO_2, may be present in the patina, coming from soil dusts and various particulate materials [32, 34].

Rain events and humidity play a key role in the patina formation because they are the main sources of electrolyte feeding electrochemical reactions and also leach pollutants from the atmosphere, increasing the aggressiveness of the electrolyte. On the other hand, rain events provide a mechanism to clean the surface from heavily deposited materials occurring during drying periods. After rain events, the corrosion product layer remains wet feeding the corrosion reaction, evaporation leads to increasing ionic concentration and electrochemical activity, under such condition saturation, can easily occur leading to salt precipitation and patina thickening

[35]. Electrolytes may change the pH of rainwater, and it has been demonstrated that reduced-pH events accelerate bronze corrosion and, hence, deterioration [36].

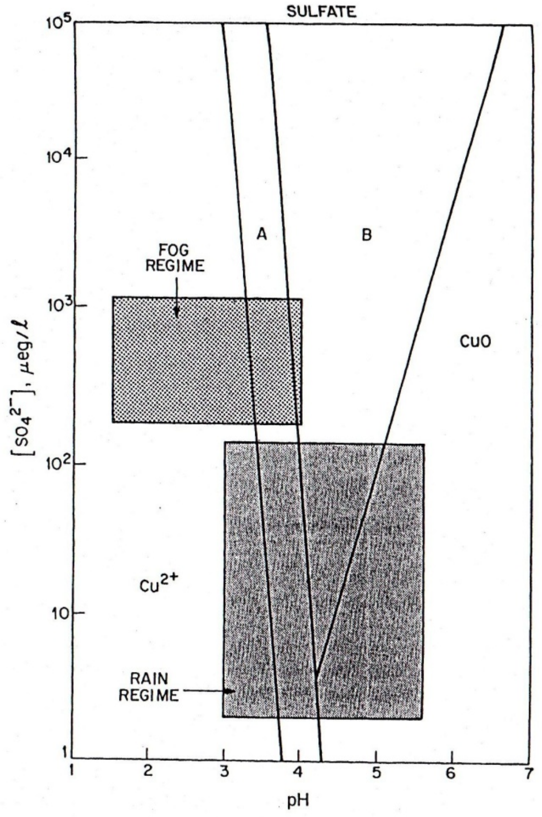

Fig. I.8 - Stability diagram for the system Cu-SO_3-H_2O. Typical ranges of SO_4^{2-} and pH in rain and fog are indicated. “A” and “B” display the regions in which antlerite and brochantite are stable, respectively [21].

An example of how electrolyte concentration and pH impact on the corrosion process is illustrated in Fig. I.8. This diagram shows the stability for the system Cu-SO_3-H_2O. Brochantite stability region (marked as “B”) is centered within the rain regime. Furthermore, as precipitation on a metal surface begins to evaporate, the ionic concentration will increase, the pH will decrease and the system will move upward into a region of much wider brochantite stability and toward antlerite stability. In the case of fog, antlerite is clearly the preferred crystalline form, being more susceptible to corrosion [21].

However, diagram in Fig. I.8 is designed to represent chemical equilibrium conditions, which may not be met in the exposure of material to the atmosphere and, in addition, it only applies to pure systems, when the reality is that many other ions and molecules are present, often at fairly high concentrations. As a result, this stability diagram should be regarded as only a crude guide to the chemical products expected as a consequence of patina formation [21].

One of the studies carried out in the CULT-STRAT project showed that the bronze corrosion rate in the main European cities especially depends on SO_2 concentration, relative humidity, temperature and pollutant particulates under 10 microns (PM_{10}). According to this project, the estimated bronze corrosion rate in 2008 was around 0.3 to 0.9 $\mu m\ yr^{-1}$ for different European cities, being Madrid one of the cities with the minimum corrosion rate and London the one with the maximum [37].

One of the most extensive exposure programs was the one developed by the United Nations Economic Commission for Europe (UN/ECE), where corrosion rates of a cast bronze were investigated. It was found that for a bronze with 6-8 wt% of tin, 3-5% zinc and 5-7% lead, the average corrosion rate measured as mass loss during an eight-year period ranged from 1.7 to 14.7 g/m^2-yr for unsheltered samples, while it ranged from 0.9 to 9.0 g/m^2-yr for sheltered samples and, in the last case, the corrosion rate showed no decrease with exposure time [21].

However, another important observation of this program was that wettability of exposed bronze surfaces decreased with increased SO_2 concentration. Wettability is a measure of the water repellent effect. Low values of wettability indicate a surface is hydrophobic and water molecules are then not easily adsorbed or absorbed. The lower wettability in more polluted sites is most likely caused by absorption of organic compounds from industrial and transportation activities. Organic species frequently are found in patina constituents and have been suggested to promote the cementation and adhesion of copper patina [21].

Monuments have an uneven surface and develop more complex patinas than any artificial patina formed by accelerated laboratory test. In addition, the real atmosphere is much more complex than any well-defined test design or simulated rain composition [32].

Picciochi et al. [38] exposed bronze samples to different environments, finding interesting differences in the patinas, summarized in Table I.1.

Table I.1 - Differences between patinas formed in urban and marine environments [38]

	Urban environment	**Marine environment**
Colour	Brownish-green	Green-bluish
Morphology	Compact and uniform	Non-uniform, loose and less adherent films to the substrate surface. However the degree of adhesion increases with time.
Elemental species	More concentration of oxides and sulfates Presence of tin More copper and oxygen	More concentration of chlorides Tin is not present
Main compounds	Cuprite is the main compound Basic sulfates, brochantite and posnjakite Some atacamite and paratacamite	Cuprite is the main compound Atacamite and paratacamite Crystals of sodium chloride, silica and gypsum after twelve months

I.3 Conservation procedures for outdoor bronzes

The question of whether patinas are protective is complex. As described in the previous section, the corrodibility of the metal surface in any environment depends upon multiple factors, including alloy composition, manufacture, exposure history and geometry. In particular, the quality of the bronze casting is of crucial importance, since inhomogeneous and porous casting greatly increases susceptibility to corrosion [20].

In the art field, the most common approach to reduce the metallic corrosion is to make a treatment on the surface of an art object, even if the surface is already corroded (which is mostly the case). Conservation practice considers the application of a double protection layer composed by an inner layer of corrosion inhibitor combined with an outer barrier layer of a traditional coating (wax, lacquer, resin) [39].

On already corroded bronze statuary, loose corrosion products may need to be removed before any surface treatment can be applied. Methods to remove corrosion products include various forms of abrasion (scalpels, abrasives applied through slurry or pad, even abrasion with bronze wool), blasting (ground walnut shells, high pressure water, ground maize and wheat starch), chemical stripping (chelating or complexing agents, washing with detergent) and there are also reports about laser cleaning of corroded bronze [20, 21]. It is important to attempt to remove hygroscopic residues in surface pits, because the bronze surface may otherwise continue to corrode [21].

In order to achieve sufficient wetting during application of the coating, the surface tension of the coating must be lower than that of the metal surface. Cleaning of the metal raises the surface tension so that good wetting can occur.

Artificial patination offers an alternative in which the bronze surface is chemically treated so that corrosion products are formed more uniformly to a desired appearance. However, the patina composition may be quite different from that formed naturally and many artificial patinas are not very protective [21].

Several properties of the inhibitor-coating system that are desirable for good outdoor durability include [20]:

(a) Good ultraviolet light resistance
(b) Sufficient flexibility to withstand thermal stresses
(c) Chemical compatibility with the metal surface in order to achieve good adhesion and good chemical resistance to the environment
(d) Relatively low oxygen and water permeability

However, it is not easy or even possible to match all desirable qualities into one single material. Furthermore, the treatment should avoid changes in appearance of the statues such as color changes, darkening from saturating coatings and shininess from some synthetic polymer coatings, as well as having a safe method for removal in case it starts to fail [20].

Corrosion inhibitor is defined as a substance which, when added in a small concentration to a corrosive medium, effectively reduces the corrosion rate of a metal [40].

Benzotriazole (BTA) and its derivatives are the most world-widely used inhibitors in the area of conservation of cultural heritage because of their efficiency in the corrosion protection of copper. However, BTA has proved to be much less efficient in the case of bronze due to the scarce reactivity of BTA to lead and tin contained in the alloy [39]. Brunoro studied the effect of different BTA derivatives with alkyl chains on bronzes and on copper, and in simulated urban rain the best protection was provided by an inhibitor with eight carbon atoms in an alkyl chain; however, the presence of other alloying elements reduced the effectiveness of this inhibitor [40].

Another important drawback of using BTA as inhibitor is that it is toxic and potentially carcinogenic, reason why the coating industry is currently focused in the development of new environmentally-friendly inhibitors such as acrylic resins, acrylic urethanes and silanes.

Concerning acrylics, Keserović et al. [41] studied three different environmentally-friendly corrosion inhibitors applied on bronze: An imidazole derivative, a vapor phase compound which creates a soft lubricating film on metal surface, and a water-based acrylic primer with a mixture of non-toxic inhibitors. They found that, as expected, corrosion rate decreases with time due to the formation of corrosion products on the metal surface and that the imidazole derivative showed much less protection than the other two inhibitors when staying in a humidity chamber for 336 h at 25°C. Proving at 35°C, the trend was the same for the imidazole derivative with a maximum inhibiting efficiency around 68%, while the vapor phase and the water-based acrylic showed efficiencies of 98% and almost 100%, respectively.

In recent years, silanes have been extensively studied as treatments to protect metals and alloys such as copper, aluminium, magnesium and iron, because they gather attractive characteristics as protectors and are ecologically friendly, constituting a valid substitute for harmful chromate treatments used in some industries. Another important characteristic of silanes is that they form a film able to induce strong chemical bonds with the substrate and with organic layers; these bonds are very resistant to hydrolysis and therefore the adhesion is very stable also in humid environment [42].

Deflorian et al. [42] proved the efficiency of 3-glycidyloxypropyltrimethoxysilane (GPS, 1.5 wt% in ethanol solution) on aluminium and copper substrates. Dipping in a silane bath at pH = 7.8 for a few minutes and curing 24 h at room temperature worked well for aluminium but poor results were obtained for copper. Therefore, copper needed surface passivation in acid and alkaline solutions, as well as mechanical polishing using abrasive paper; the silane bath was used at different pH (4, 5 and 6), different curing methods were applied (room temperature, 100°C or 200°C in an oven for 30 or 60 min). They concluded that it is possible to deposit silane layer on copper and aluminium substrates and hence to pre-treat multi-metal systems. To obtain a better deposition it is necessary to cure at high temperature (200°C) the silane layer producing a very protective layer (which is not feasible in the cultural heritage field). The silane pretreatment guarantees an increase of adhesion properties and delamination resistance of the organic coating due to the resistance of the silane-metal interface to hydrolysis phenomena.

In a more recent publication, Deflorian, Fedel et al. [43] proved GPS again, but now in two different forms: As neat and as a mixture of GPS with tetraethoxysilane (TEOS) in an unknown concentration due to patent copyright. Pure copper panels were dipped for 2 min in different silane solutions: 2 panels in a 5 wt% solution of neat GPS, 2 in a 5 wt% solution of GPS+TEOS and the last 2 in a 50 wt% solution of GPS+TEOS. After dipping, a thermal treatment was applied at 200°C and using two different times, 10 and 30 min. Results showed that neat GPS is not able to interact correctly with copper oxide to form an homogeneous network on it, and that longer curing times (30 min in this case) and less concentrated solutions give more benefic effects. In addition, they performed a test of a system including painting (copper/silane + epoxy coating), confirming that the best behaviour was for the substrate dipped in a 5 wt% GPS+TEOS solution for 30 min.

Ying-Sing Li et al. [44] tested the efficiency of bis(trimethoxysilyl)ethane and (3-mercaptopropyl)trimethoxysilane as sol-gels on pure copper and aluminium wires. The pre-treated substrates were immersed in the sol-gel for 2 min and then withdrawn at 2.6 cm min^{-1}, dried in ambient conditions and placed in an oven for high temperature curing for 3 hours; finally they were exposed in NaCl solutions. Electrochemical methods indicated that the sol-gel coatings improved the corrosion protection of both metals.

Zucchi et al. [45] tested the efficiency of 4 silane compounds (3-mercapto-propyl-trimethoxy-silane (PropS-SH), n-octadecyl-trimethoxy-silane (OctadecS), bis-trimethoxy-silyl-ethane (BTSE) and phenyl-trimethoxy-silane (PhS)) on oxygen free high conductivity (OFHC) copper cylindrical electrodes. They immersed the electrodes in silane hydroalcoholic solutions (90/6/4 v/v alcohol/water/silane) at room temperature for different times between 2 and 60 min and adjusted pH to 4, 7 and 10. The silane solutions were maintained under stirring conditions for 1 h to allow the hydrolysis of the Si–OCH_3 groups. After the pretreatment, the copper electrodes were dried with hot air and cured for 1 h in an air oven at 100°C. The test solution was 0.6M NaCl solution. Electrochemical tests indicated that BTSE had poor inhibiting efficiency at all pH's and pretreatment times, while PhS was good only in acid conditions (pH = 4). OctadecS showed excellent efficiencies in almost all cases, but its efficiency diminishes when short pretreatment times are used in neutral and basic conditions, while PropS-SH showed excellent results (above 99% in all cases) independently of the pH or the pretreatment time. They concluded that thiolate bond allows a better anchorage of the silane layer to the copper surface than the oxane bond, and that the presence of an aromatic moiety or, better, of a long aliphatic chain, favours the formation of a protective layer, although the inhibiting performances are not very persistent. Balbo et al. [39] reported that, in the case of bronze, PropS-SH has exhibited interesting protective properties, strongly dependent on the application conditions, because its silanol groups (SiOH) react with each other by crosslinking and contribute to the formation of a SiOSi network.

Zucchi et al. [15] also studied the formation of the PropS-SH film on copper and the influence of some parameters on the properties of the silanic film. Experimental conditions were the same used in [10], but the pretreatment time was fixed to 60 min and pH to 4; however, tests were performed on fresh specimens, 24 h room temperature aged ones (aged specimens) and on 1 h, 100°C air oven cured ones (cured specimens). Results showed that even with very short dipping treatments, PropS-SH molecules can bond to copper through the thiol group, weakly at the beginning (probably by H-bonds) and successively by a stronger thiolate (Cu-S-C) bond for the condensation between this group and the -OH group of the hydroxilated copper surface. In curing, further condensation takes place mainly in the outermost part of the film, leading to a denser, less permeable and, therefore, more corrosion resistant coating. Curing promotes the transformation of PropS-SH molecules in a three-dimensional layer by the siloxane (-Si-O-Si-) bond formation through the condensation of the silanol groups of different molecules. Thompson et al. [46] schematized the bonding between the PropS-SH molecules and the metal surface as well as the formation of siloxane bonds as shown in Fig. I.9.

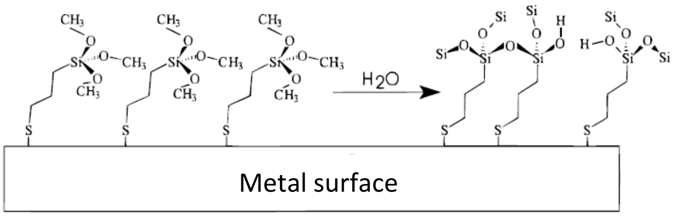

Fig. I.9 – Scheme of PropS-SH monolayer surface chemistry [46]

Zucchi, Monticelli et al. [47] subsequently investigated the formation of the OctadecS film on copper. Experimental conditions were the same as in [15]. They concluded that after sole dipping treatment, OctadecS film is very thin, highly porous and hence scarcely protective. In the case of aged specimens, a certain condensation between the loosely adsorbed OctadecS molecules is allowed but inhibiting effects are not persistent. On the other hand, the curing process, which markedly favours siloxane bond formation, gives rise to a much thicker, less defective layer, where the inhibiting action is noticeable and persistent.

Traditional coatings used as overlay coatings in outdoor bronzes include oils (such as lemon, paraffin, linseed and castor oils) and natural waxes (such as Carnauba and beeswax mixtures). However, these coating treatments easily saturate existing patinas, causing darkening. Drying oils are reported to last up to one year and are increasingly insoluble with age, while waxes require frequent maintenance, ideally every six months. Moreover, natural waxes, particularly animal waxes, may contain some free acids which can potentially attack the metal surface and are also subject to hydrolysis at the ester group [20]. For these reasons, professional conservators currently prefer the use of microcrystalline waxes, which are straight, cyclic or branched organic products refined from petroleum. They are derived from the same raw material as paraffin wax but they have a microcrystalline structure, which confers on them plasticity in marked contrast with brittle paraffin wax [48].

The protective ability of waxes has usually been attributed to their ability to create a hydrophobic surface. The result of waxing is a significant reduction in thickness of corrosion products of both untreated and patinated bronzes, in particular at highly polluted sites. Likewise, waxing results in a slowing down of colour changes. It has been experimentally proved that, after three years of outdoor exposure, the colours of waxed bronze samples in different sites were closer to the colours of the pristine bronze than the colours of the exposed untreated bronze samples [21]. A common problem involves the melting of the wax from statues that are exposed to sunshine [49].

In the range of lacquers and resins, different polymeric coatings have been proposed for the protection of corroded objects: Nitrocellulose lacquers, polysiloxanes, polyurethane, polyesther resins and acrylic resins such as Paraloid® B72, an ethyl methyl acrylate co-polymer which is widely used in conservation treatments [50, 51].

Brostoff [20] proved the efficiency of five of the most effective coating systems used in the art field (Incralac® plus wax; BTA plus wax; Nikolas® 11565 acrylic undercoat with Nikolas® 9778 acrylic urethane as middle coat and wax topcoat; BTA plus a BASF® acrylic urethane with wax topcoat; and two-layer Nikolas® 11650 acrylic emulsion/urethane dispersion with wax topcoat) on four different substrates (polished cast bronze, artificially patinated cast bronze, 50-year old copper roof, walnut shell blasted copper) . Results indicated that after 120 days of accelerated simulated weathering, the BTA plus wax system was the one who showed the worst coating performance on all the tested substrates. However, the behavior of the coating performance varies with increasing time. The Nikolas® 11565/Nikolas® 9778/wax system seems to offer the best corrosion protection but, in general terms, all the tested systems showed poor efficiency on the artificially patinated bronze. Another important conclusion of this study is that the wax coating is a poor barrier to acid rain-type exposure at different thickness, and does not provide significant protection in outdoor exposures except as a patina reinforcement for a limited period of time.

Kosec et al. [49] investigated the protective action of three coating systems (3 wt% BTA ethanol solution, Paraloid® B44 with 3 wt% BTA, and Carnauba wax melted around 82°C mixed with white spirit (a hydrocarbon mixture rich in aliphatics)) on bronze coupons (88/6/6 w/w Cu/Sn/Zn). Some bronze coupons were tested as bare metal while others were artificially patinated with a solution of potassium sulphide to obtain a brown patina, and a solution of ammonium carbonate and ammonium chloride to obtain a green patina (this green patina was grown on the brown one). The artificial rain solution was prepared with distilled water, 0.2 g L^{-1} Na_2SO_4, 0.2 g L^{-1} $NaHCO_3$, 0.2 g L^{-1} $NaNO_3$ at pH = 5. Results indicated that BTA in ethanol solution showed better behaviour for bare bronze and on brown patinated surface, but no positive effect was observed for the green patina. On the other hand, Carnauba wax and to a greater extent Paraloid® B44 doped with 3% BTA showed improved protection against corrosion and dissolution in simulated urban rain for bare bronze and both types of patina; however, their inhibitory properties tend to weaken over time.

On another publication, Kosec et al. [40] proved the efficiency of 6 coating systems (3 wt% BTA in ethanol solution, 3 wt% 1-(p-tolyl) 4-methyl imidazole (TMI) in ethanol solution, BTA in Paraloid B44, TMI in Paraloid® B44, Paraloid® B44 itself, and Carnauba wax) on bronze coupons and using an artificial rain solution with the same composition as used in [49]. They proved these coatings on three different kinds of patina: A chemical green chloride patina, a chemical green nitrate patina and an electrochemical patina. Results showed that the protection of the patina depends more on the structure/composition than on the thickness of the patina [32, 49]. Protective efficiency of BTA and TMI applied as ethanol solutions was not confirmed, although it is common in practice. Both inhibitors applied with Paraloid® B44 achieved significant corrosion protection (more notorious in green chloride and electrochemical patinas than in the green nitrate one, where BTA fails) but this effect decreases over time. Carnauba wax provided good corrosion protection (its melting point of 85°C is much better than beeswax at 62°C) and can be considered a suitable choice for conservation purposes, although Paraloid® B44 shows to be more effective.

Because patina is the support for protective treatments and because the characteristics and chemistry of patina are different according to the exposed areas, the development of new environmentally-friendly and non-toxic inhibitors is an important matter in the cultural heritage field. One of the most recent findings is the use of ceria nanoparticles for the improvement of wear and corrosion resistance in acidic media. The beneficial effects of cerium oxides/hydroxides have been attributed to improved barrier properties, cathodic and anodic polarization effects and enhancement of the passive behaviour among others.

Montemor et al. [52] proved the coating efficiency of a silane solution modified with CeO_2 nanoparticles on galvanized steel substrates, obtaining positive impact both in the barrier properties and corrosion inhibition. Zanotto et al. [16], after applying a silane coating enriched with CeO_2 nanoparticles on a magnesium alloy concluded that cerium addition enhances silane film barrier properties (less porous and defective, and thus more protective, probably leading to a more closed and interconnected sol-gel silane network), that cerium ions (in the Ce^{+4} oxidised form) can substitute some Si atoms during polymerization/condensation sol-gel process (leading to the formation of a Si-O-Ce network) or they can be entrapped within the silane coating in the form of soluble species (as cerium oxides/hydroxides), and that the higher Ce^{3+} modified silane efficiency may be linked to the precipitation of very insoluble cerium hydroxide corrosion products at the damaged areas (providing a “self-healing effect”). Up to now, literature does not report any prove of silane modified with CeO_2 nanoparticles on bronze substrates.

Based on this trend about silane coating research and due to the fact that literature about the application of this kind of coatings on bronze is scarce, the second part of this work is focused on the performance of a silane coating on quaternary bronze substrates, testing these in an artificial acid rain solution. Taking into account what is reported for copper in [45] and for bronze in [39], PropS-SH was selected as the silane coating under analysis. This coating is analysed in two forms: In its conventional form and with addition of ceria nanoparticles, with the purpose to determine if ceria provides any beneficial effect on the silane coating performance.

Experimental

Section 1

Field tests: Characterization of the bronze and the corrosion products from the outdoor bronze monument to Vittorio Bottego

(Parma Railway Station, Italy)

1.1 Description of monument and samples

Samples were obtained from the statue of Vittorio Bottego, Italian explorer in the 1890’s, and from two other statues in the surroundings, both with the form of African natives, and each one representing one of the two rivers explored by Bottego during his expeditions to Africa: The Omo and the Giuba rivers. Bottego monument was located at Piazza Carlo Alberto dalla Chiesa, in Parma (Fig. 1.1), and had to be temporarily removed and taken to a restoration workshop due to the renovation of Parma Railway Station. Images of the three statues in the restoration workshop can be seen in Fig. 1.2.

Fig. 1.1 - Bottego statue (left) [53] and detail of the whole monument including Omo and Giuba statues, including a fountain below the bronze statues (right) [54] in Parma, Italy

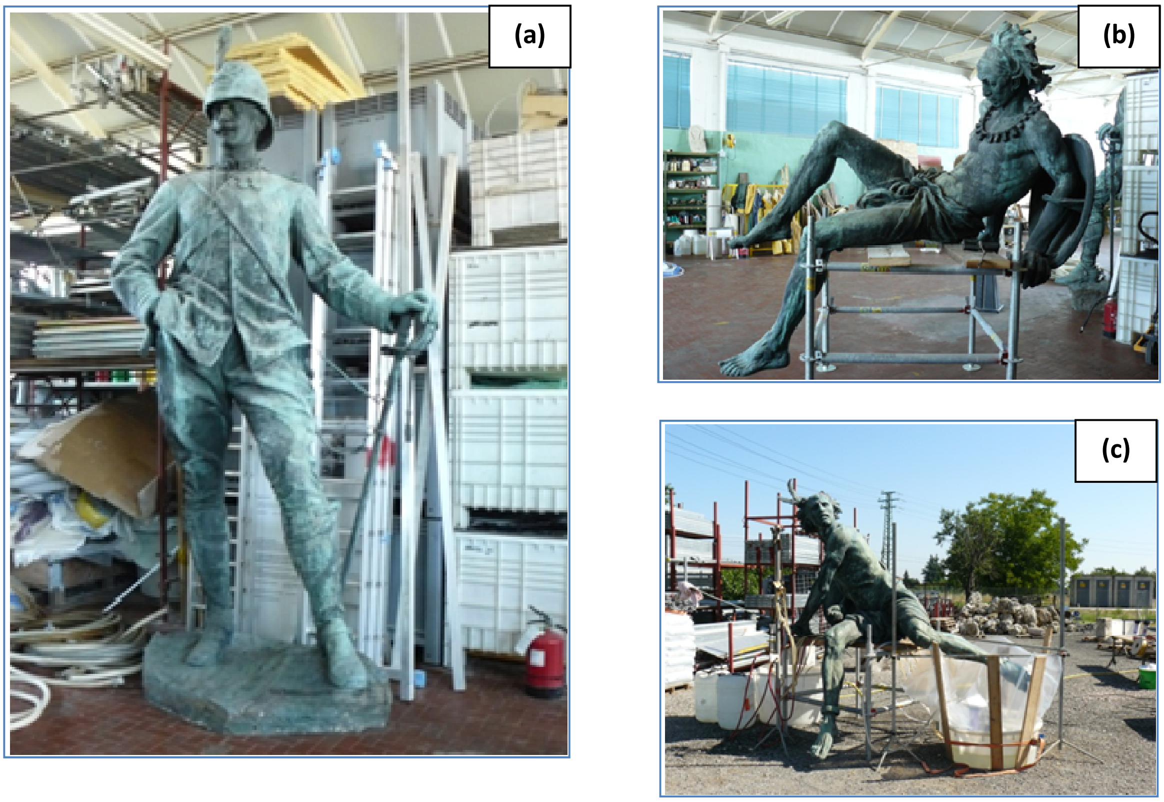

Fig. 1.2 - Statues of monument to Bottego in the restoration workshop: Bottego (a), Giuba (b), Omo (c)

During the restoration of the statues in the workshop of the Arche’s Restauri s.n.c., small samples were taken from both the metal and the corrosion products on the three statues. Table 1.1 describes the different samples (sheltered/unsheltered denomination refers to the exposure conditions of the sampling area):

Table 1.1 - Samples obtained from the three statues

Sample	Sampling point	Description	Geom. exposure
B1	Bottego statue, right leg, inner part	Metallic sample	
B2	Bottego statue, right cheek, external layer	Corrosion product	Sheltered
B3	Bottego statue, right cheek, intermediate layer	Corrosion product	Sheltered
B4	Bottego statue, right cheek, internal layer	Corrosion product	Sheltered
B5	Bottego statue, right side of helmet, external layer	Corrosion product	Unsheltered
B6	Bottego statue, right side of helmet, intermediate layer	Corrosion product	Unsheltered
B7	Bottego statue, right side of helmet, internal layer	Corrosion product	Unsheltered
O1	Omo statue, support zone	Metallic sample	
O2	Omo statue, shield handle	Metallic sample	
O3	Omo statue, back, external layer	Corrosion product	Unsheltered
O4	Omo statue, back, internal layer	Corrosion product	Unsheltered
O5	Omo statue, foot	Corrosion product	Unsheltered
O6	Omo statue, neck, external layer	Corrosion product	Sheltered
O7	Omo statue, neck, internal layer	Corrosion product	Sheltered
G1	Giuba statue, support zone	Metallic sample	

As it can be seen in Table 1.1, some samples were solid metal and others, designated as corrosion products, were just scraped powders. When a sample is “sheltered”, it means that it has little or no contact with weathering factors as rain, sunlight, etc. due to its position in the statue (for example, a sample obtained from the armpit of the statue). “Unsheltered” is when the sample was taken from a position totally exposed to weathering factors.

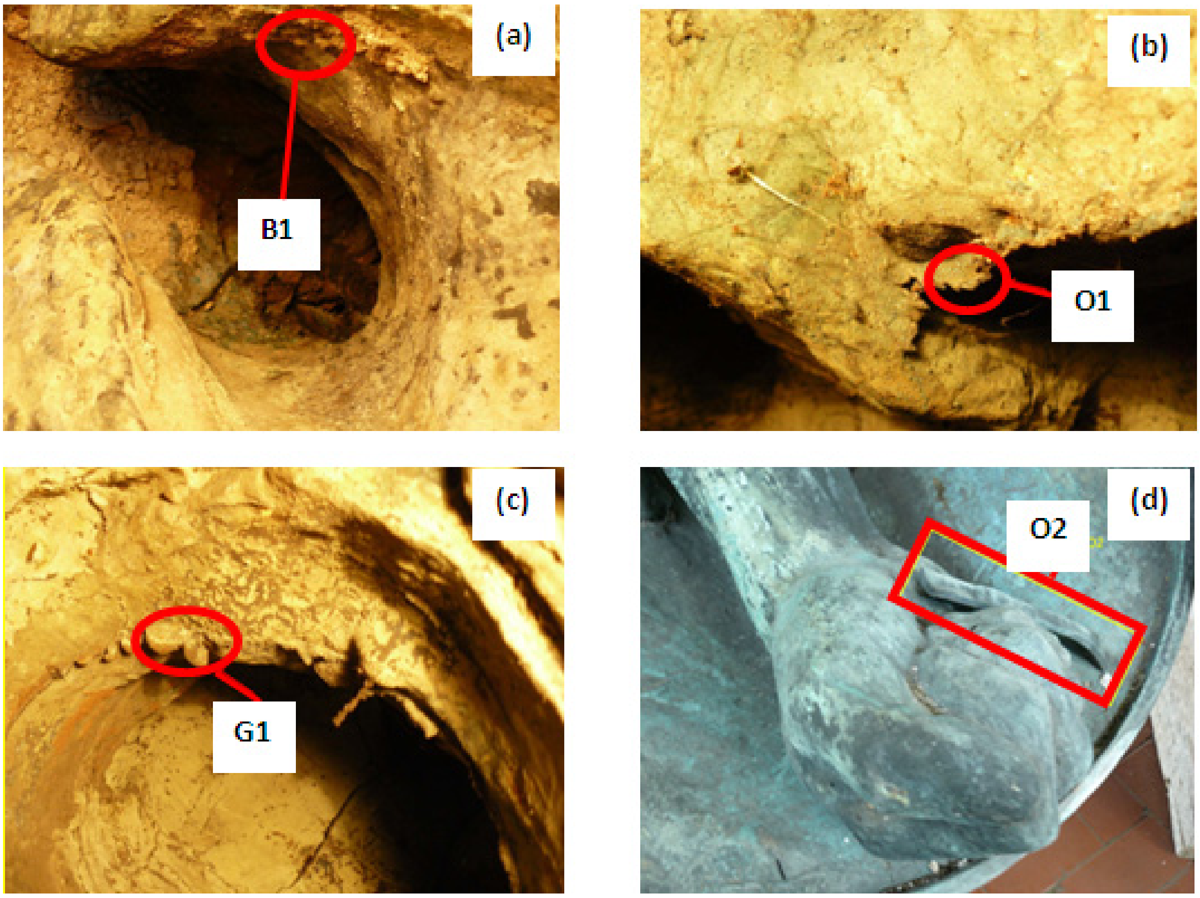

Fig. 1.3 - Metallic samples taken from the statues: B1 (a), O1 (b), G1 (c) and O2 (d).

Sample O2 consisted (Fig. 1.3 d) consisted of a detachable section of the shield handle: It was taken, analysed by non-invasive techniques and then put back in its original position.

The metallic samples from the alloy of the three statues (B1, O1 and G1) were investigated by different techniques (as shown in Fig. 1.5) with the purpose to obtain the maximum information about their chemical composition and morphology.

These three samples were cut into 2 pieces of different size, one suitable for metallographic analysis, and the other for chemical analysis. It is important to mention that the instrument used to cut the metal may alter the morphology during cutting; so, the most damaged piece was used for chemical analysis because of the complete dissolution that this type of analysis requires.

Fig. 1.4 - Corrosion products samples taken from the statues: Most samples were obtained by scraping different layers (according to appearance) in a single place (a,b,c,d). Only O5 was sampled as a single layer (e).

1.2 Experimental procedure

Figure 1.5 shows the process followed and the applied techniques for each kind of sample. It is important to remark that not all the samples were submitted to all the techniques. Each technique is explained in detail in Appendix A of this thesis.

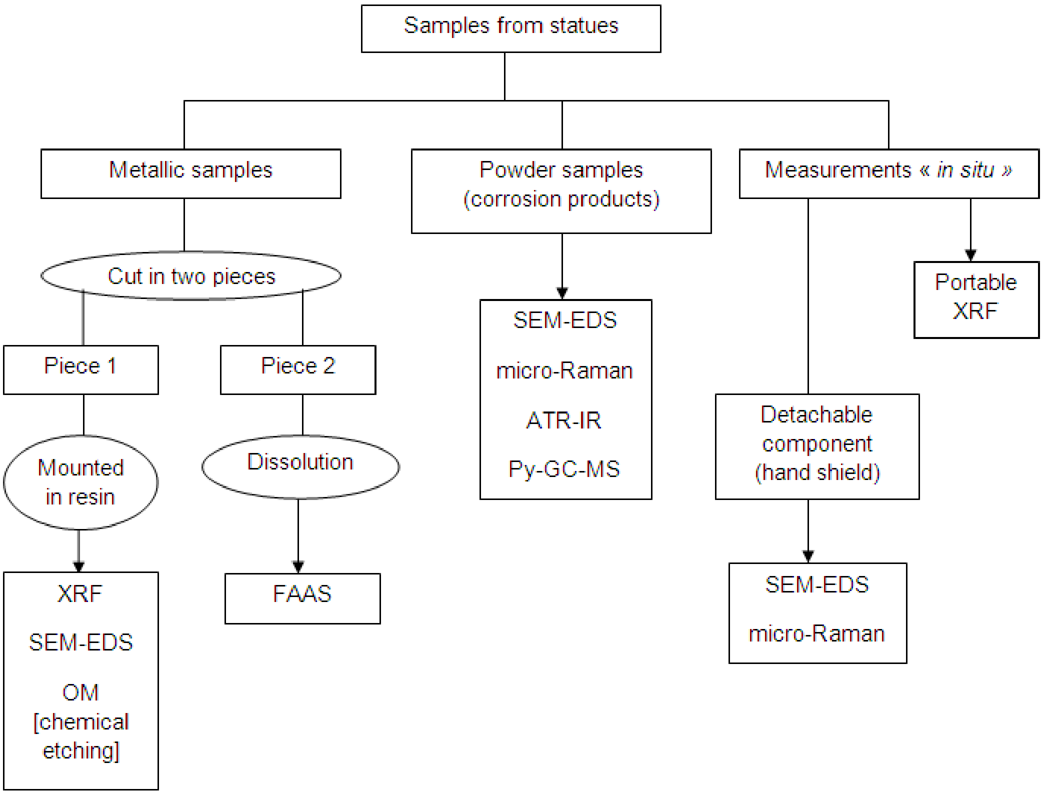

Fig. 1.5 - Diagram showing the techniques applied to the different kinds of samples

1.2.1 Metal composition

The general composition of the alloy was determined in samples taken from the metal flashes inside the statues (see Table 1.1 and Fig. 1.3) by using pincers. The composition was checked both in solid samples (by large-area EDS, on surface areas of 0.5 to 1 mm^2, as well as by XRF at the Dipartimento di Chimica Industriale e dei Materiali (Axios-Advanced spectrometer, Rh source, 4 kW, 6 mm diameter mask, LiF 220 crystal, Hiper Scintillator and Duplex detectors) and in samples dissolved in acid solution (by FAAS)).

Each one of the samples B1, O1 and G1 was cut into 2 pieces and one piece of each sample was used for the chemical analysis by flame atomic absorption spectroscopy (FAAS). These pieces were polished (with the purpose to analyze only the alloy and not the corrosion products) using sandpaper and weighted in an electronic balance (with a repeatability of ±1 mg). Later, they were dissolved in separated flasks with 8% volume of aqua regia ($HCl:HNO_3$ 3:1 v/v), according to the flask volume.

Samples were completely dissolved to avoid technical and quantitative problems when analyzing by FAAS. When dissolving in aqua regia, the rate of dissolution may be improved by heating below 60°C because, otherwise, tin in solution precipitates as metastannic acid (H_2SnO_3) [55].

Standards with concentration of 10, 5, 2.5 and 1 ppm were prepared by dilution of appropriate volumes according to the flask volume. In all cases a small volume of the Cu solution was added according to [55], because it has been demonstrated that the presence of copper enhances the readings of the other elements by approximately 8-10% by atomic absorption.

Finally, a Varian SpectrAA 100 spectrometer was used to build the calibration curves and determine the concentration of each metal in the B1, O1 and G1 samples.

Sample O2 (detachable handle of the shield, see Table 1.1 and Fig. 1.3) was also analysed, but only by non-invasive techniques (Extended Pressure Scanning Electron Microscopy (EP-SEM) in variable-pressure (VP) mode) after minimal polishing of one of the edges, so as to be able to place it again in its original position in the restored statue after analysis.

1.2.2 Metal microstructure

Metallic samples taken from the statues of the Bottego monument (samples B1, G1, O1, described in Table 1.1 and Fig. 1.3) were mounted in acrylic resin, grounded with SiC abrasive papers and polished by diamond paste. Firstly, the polished samples were analysed by EP-SEM in VP mode, with X-ray energy-dispersive spectroscopy (EDS) for localised microanalyses aiming at phase identification. Then, samples were chemically etched by $FeCl_3$/HCl (diluted with ethanol) and observed in plane by optical microscopy (OM), in bright field and in reflected polarised light.

1.2.3 Corrosion products

Corrosion products were analysed by large-area EDS (for elemental composition) as well as by micro-Raman spectroscopy (Invia-Renishaw, wavelength 514.5 nm), ATR-IR spectroscopy (at the Laboratory of the Soprintendenza B.S.A.E. in Bologna with an Avatar 360 FT-IR Smart Miracle spectrophotometer from Thermo Scientific; diamond ATR crystal; wavelength 4000-650 cm^{-1}; resolution 4 cm^{-1}) and Py-GC-MS (at the Dipartimento di Chimica “G. Ciamician”, Università di Bologna; CDS 1000 pyroprobe heated filament pyrolyser, directly connected to the injection port of a Varian 3400 gas-chromatograph coupled to a Saturn II ion-trap mass spectrometer, He as gas carrier at 1 ml min^{-1}, pyrolysis was carried out at 600°C for 10 s, using tetramethylammonium hydroxide (TMAH) as derivatizant) for phase composition.

The corrosion products of sample O2 were only analysed by micro-Raman spectroscopy.

1.2.4 Field measurements by portable XRF

Sheltered (neck and armpit) and unsheltered (calf and shoulder) areas on Omo statue were qualitatively analysed by portable XRF (Bruker Tracer III SD, Rh source, 40 keV, 9 µA and 20 s of time scan), before and after cleaning the surface of the statue.

Each cleaning cycle consisted of:

(1) 40 minutes with nebulized 5 wt% sodium bicarbonate solution, followed by
(2) 30 minutes with nebulized deionised water.

Two washing cycles were applied on calf area of the statue, while only one was applied for the shoulder and for the neck. Images during the cleaning of Omo statue can be seen in Fig. 1.6.

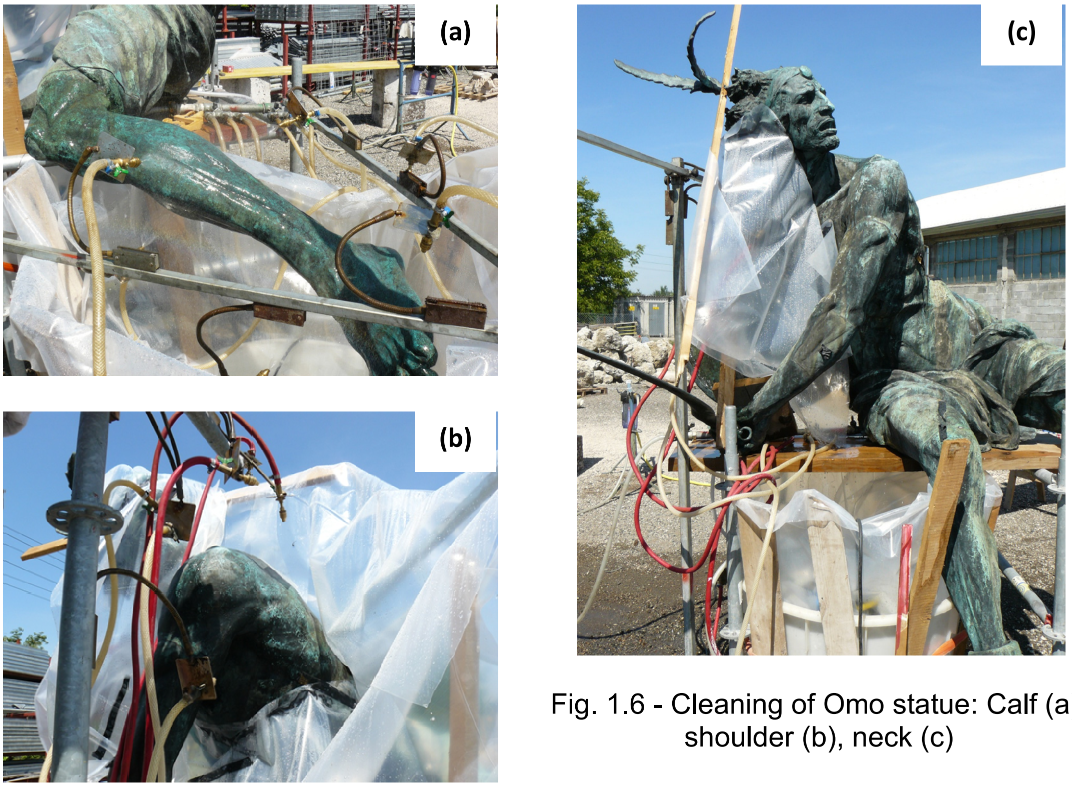

Fig. 1.6 - Cleaning of Omo statue: Calf (a), shoulder (b), neck (c)

1.3 Results

1.3.1 Metal composition

The results of the analysis performed on metallic samples are summarized and compared in Table 1.2.

Table 1.2 - Comparison of chemical composition of metallic samples (weight %) using three different techniques (FAAS, XRF, EDS)

	B1			O1			G1		
	AA	**XRF**	**EDS**	**AA**	**XRF**	**EDS**	**AA**	**XRF**	**EDS**
Cu	*	87.8	89.0 ± 0.1	*	90.2	91.5 ± 0.2	*	88.3	90.0 ± 0.5
Sn	7.14	7.2	7.1 ± 0.1	5.09	6.8	6.5 ± 0.4	5.18	7.6	6.7 ± 0.2
Pb	0.77	1.1	0.4 ± 0.2	0.37	0.8	0.7 ± 0.5	0.50	1.6	0.8 ± 0.1
Zn	3.97	3.1	3.6 ± 0.2	1.42	1.5	1.3 ± 0.3	2.91	1.9	2.6 ± 0.3
As	0.13	---	---	0.13	---	---	0.22	---	---
Fe	0.10	0.1	---	0.06	---	---	0.16	0.2	---
Bi	0.03	---	---	0.02	---	---	0.06	---	---
Sb	0.12	0.3	---	0.13	---	---	0.13	---	---
Ni	0.02	---	---	0.13	0.1	---	0.10	0.2	---
Co	0	---	---	0	---	---	0	---	---
Ag	0.05	---	---	0.09	---	---	0.07	---	---
Al	---	0.2	---	---	0.2	---	---	0.1	---
P	---	0.1	---	---	0.1	---	---	0.1	---
S	---	0.1	---	---	0.1	---	---	0.1	---
Si	---	0.1	---	---	---	---	---	---	---
Mg	---	---	---	---	0.3	---	---	---	---

(*) Cu to balance

First of all, before comparing the results in Table 1.2, differences in both the precision (or repeatability, estimated as relative standard deviation (RSD%) of multiple measurements on the same sample) of each investigation technique and in the standard deviation of data, averaged on different sampling points/areas, should be discussed:

- FAAS: RSD%, estimated on results measured in the present work, is always lower than 0.5-1.0% for most elements. As for the standard deviation due to the sampling point, in the present work it was possible to take only one sample per statue, therefore it was not possible to estimate it.

- XRF: In general, RSD% is about 0.5-1.0 % for most metallic elements. With respect to the standard deviation due to the sampling point, in the present work the dimensions of the mounted and polished samples, used for both XRF and EDS analyses allowed to make only one XRF measurement per sample, therefore it was not possible to estimate it.

- EDS: RSD% varies from about 1% (for metallic elements, if the measured amount is higher than the detection limit) to significantly higher values for light elements or when the concentration approaches the detection limit (which, for most metals in this system is about 0.1-0.2 wt%). As for the standard deviation due to the sampling point, in the present work the dimensions of the mounted and polished samples allowed to repeat the EDS measurement at 2 or 3 times in different areas of the polished surface, thus allowing to estimate the standard deviations reported in Table 1.2.

On the basis of results in Table 1.2, it is possible to observe differences:

(a) Between analytical techniques: These differences mainly concern Sn and Pb wt% and may be due to the analysed area as well as to the different preparation method. As for the size of analysed area, EDS scanned between 0.5 and 1 mm^2 while XRF did it in approximately 28 mm^2 (6 mm diameter). Both techniques have limited penetration into the metallic sample, while in FAAS, the sample was completely dissolved and this makes possible the bulk analysis.

    Another possible source of variation is that the sample used for FAAS was just sanded with abrasive paper until reaching an acceptable removal of the corrosion products, while the sample for XRF was mounted in resin and partially polished, and the sample for EDS was polished until mirror finish to be able to work with microscopy.

    Therefore, the general overestimation of Sn by EDS and XRF (in O1 and G1) may be due to the involvement of more superficial layers, which are more Sn rich due to decuprification [56]. In the case of Pb, the different size of analysed area is probably responsible for the observed differences in concentration because Pb is usually present in the alloy as scattered globules in the Cu-rich matrix (see 1.3.2), therefore the amount of Pb detected significantly depends on the size of analysed area [57].

(b) Between samples: Omo statue is the alloy with the highest Cu content, while Bottego statue is the one with the lowest. Zn and Sn are higher in the case of Bottego statue. These differences may be due to small variations in casting conditions and low control of casting parameters. Concerning Pb, it is difficult to establish which sample has the highest content because of the differences among analytical techniques, but Pb content is apparently a bit higher in the case of G1. Variations in composition from place to place are common, i.e. a Sn content variation of ±10% is not uncommon even for an integrally cast object [58].

Therefore, based on the metal composition in Table 1.2, the bronze on the three statues is identified as a quaternary bronze (presence of Cu, Sn, Zn, Pb).

1.3.2 Metal microstructure

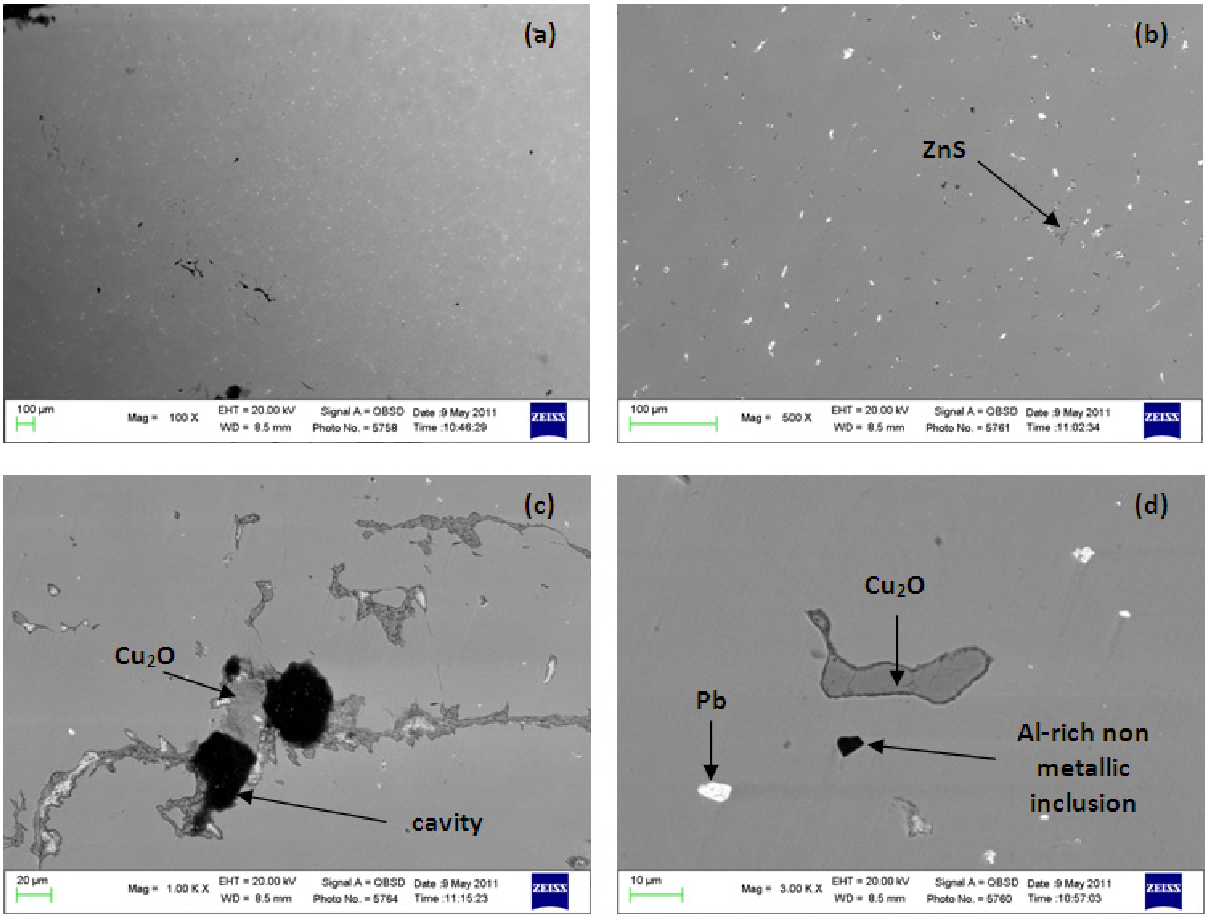

Figure 1.7 - Sample B1: Microstructure of the alloy: (a) Low magnification image; (b) Overview at medium magnification; (c, d) High magnification images of the inclusions and casting defects identified on the basis of EDS data

According to Fig. 1.7a, B1 shows an evident microsegregation (i.e. non-homogeneous distribution, see I.1.3 in the introduction) of Sn in the Cu-rich matrix, more evident than in other samples of Bottego monument. This is probably due to the higher Sn content (as shown in Table 1.2) rather than to a higher cooling rate.

Some inclusions may be observed as ZnS (in Fig. 1.7b, with elongated shape due to its ductility) and cuprite (Cu_2O, Fig. 1.7 c, d).

Pb globules are also present, as expected, and Al-rich inclusions were also detected (Fig. 1.7d), which is probably due to some contamination while casting the alloy.

Black areas (Fig. 1.7c) are just shrinkage cavities where the mounting resin (high in carbon content) partly filled up the voids.

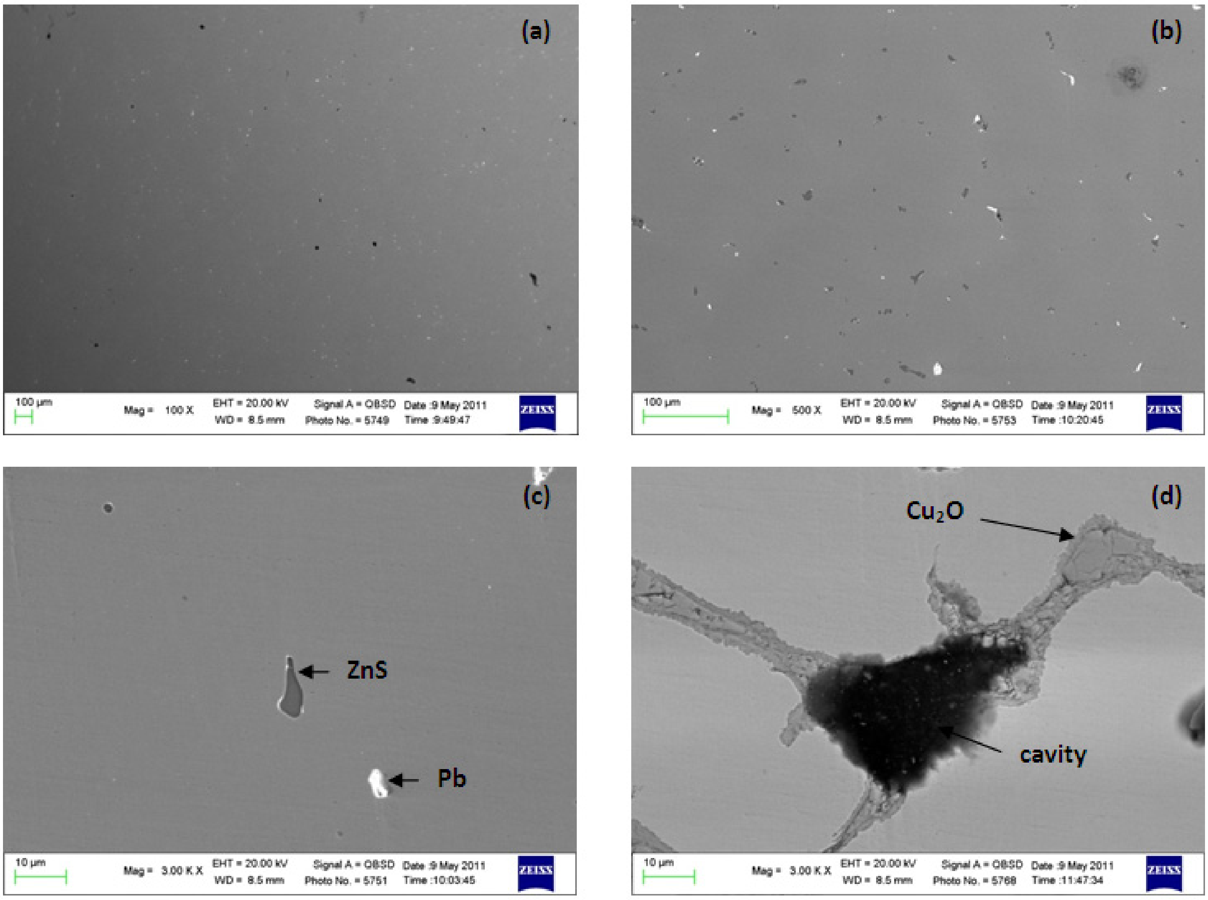

Figure 1.8 - Sample O1: Microstructure of the alloy: (a) Low magnification image; (b) Overview at medium magnification; (c, d) High magnification image of the inclusions and casting defects identified on the basis of EDS data

The microstructure of O1 looks homogeneous (Fig. 1.8 a, b). Microsegregation of Sn from the core of the dendrites to the peripheral area is not as evident as in the case of B1.

As in B1, some ZnS (Fig. 1.8c) and Cu_2O (Fig. 1.8d) inclusions were detected. The white zone in the borders of the ZnS inclusion in Fig 1.8(c) is due to the presence of Pb, which is also detected as globules in interdendritic spaces due to low Pb solubility in Cu [18].

Some pores (round shape) and shrinkage cavities (irregular shape) are detected, but the alloy has an overall good cast quality.

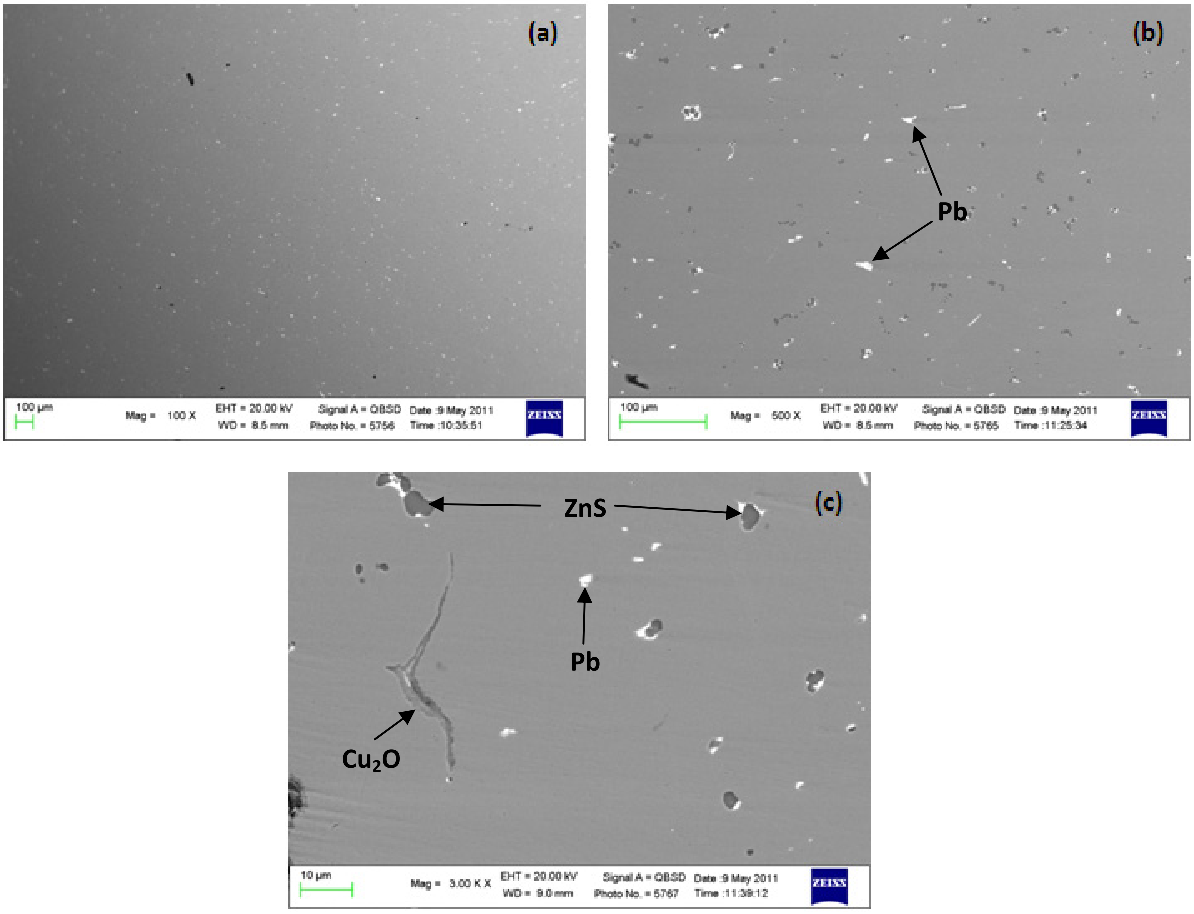

Figure 1.9 - Sample G1: Microstructure of the alloy: (a) Low magnification image; (b) Overview at medium magnification; (c) High magnification image of the inclusions identified on the basis of EDS data

Also in G1, microsegregation of Sn is not as evident as in B1. Pb globules (Fig. 1.9b) are larger and more frequent than those observed in B1 and O1; probably this confirms the higher Pb content showed in Table 1.2.

Again, some ZnS and Cu_2O inclusions in the Cu-rich matrix may be observed.

After observing the polished surfaces in the SEM, the samples were chemically etched in order to reveal the microstructure. The metallographic observation of etched samples from the Bottego monument showed evidences of extensive cold working, which is not common for bronze statues (usually displaying an as-cast, undeformed dendritic microstructure). Samples B1 and G1 (Fig. 1.10) display smaller grains than in the case of O1, probably due to a higher cooling rate.

Dendrites are still visible in some places underneath slip lines. Plastic deformation carried out for connecting and fitting the pieces of the statues before joining the different sections might be the reason for the formation of slip lines. Examples of assembly between different sections of the left leg in the Omo statue are shown in Fig. 1.11.

Also, the damaging and the subsequent repair work after World War II, when the statues were slightly affected by bombing the railway station (Fig. 1.11 a), might have contributed to plastic deformation.

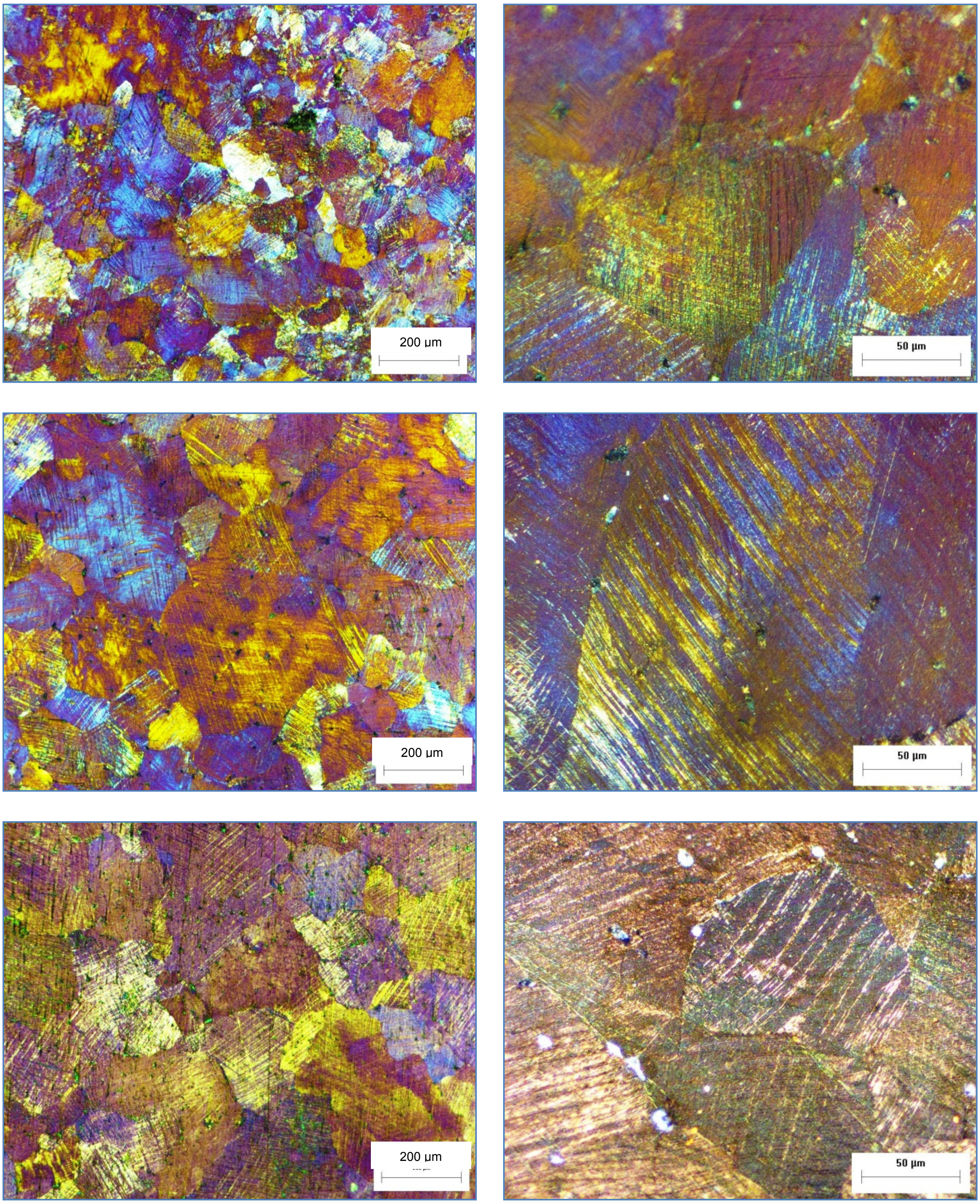

Fig. 1.10 - Alloy samples after chemical etching. B1, O1 and G1 (from top to bottom); magnifications 10x0.5 (left) and 50x0.5 (right).

Fig. 1.11 - Metal patch for fixing the damage due to bombing during World War II (a) and assembly between different sections in Omo statue (b, c)

1.3.3 Corrosion products

1.3.3.1 *In situ* investigations of shield handle (sample O2)

In relation to sample O2 (see Fig. 1.3d), it is possible to see at naked eye differences in colour of the bronze patina (mainly black, green and light blue areas were observed). Raman analyses were made with the purpose to identify which corrosion products are present in areas with different colouration (Figs. 1.12, 1.13, 1.14).

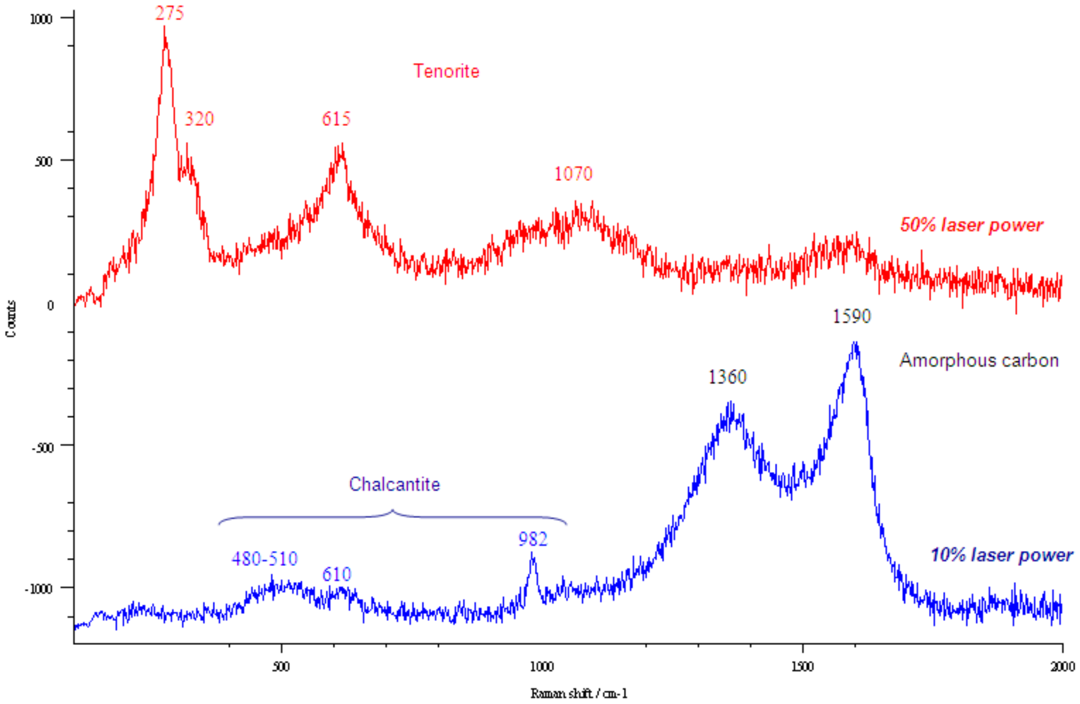

Figure 1.12 - Black areas in the patina on sample O2 (mostly unsheltered, shield handle in Omo statue) analysed by micro-Raman spectroscopy with different laser power (100% = 50 mW).

In Fig. 1.12, the red spectrum, obtained at higher laser power, indicates the presence of tenorite (CuO) due to overheating and transformation of chalcantite ($CuSO_4 \cdot 5H_2O$), which is detected at lower laser power (blue spectrum) together with amorphous carbon from atmospheric contamination. The red shift of tenorite (about 15-20 cm^{-1}) is also due to overheating.

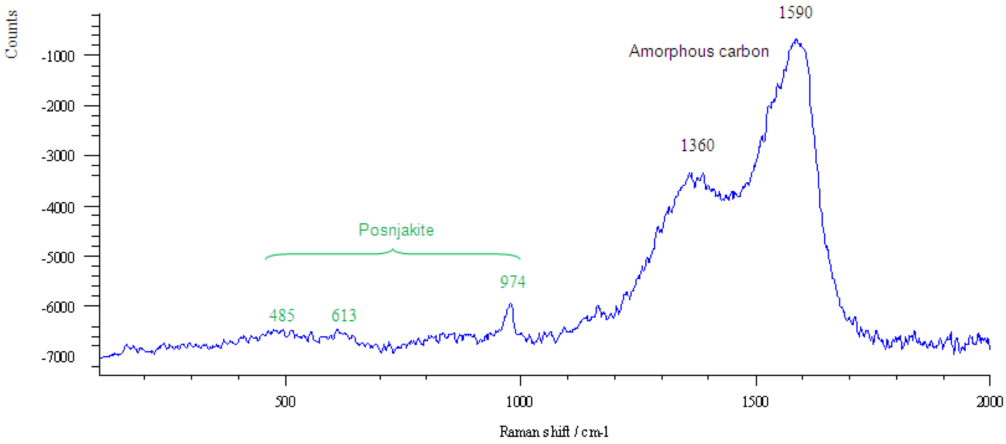

Fig. 1.13 - Green areas in the patina on sample O2 (mostly unsheltered, shield handle in Omo statue) analysed by micro-Raman spectroscopy: Presence of amorphous carbon and posnjakite.

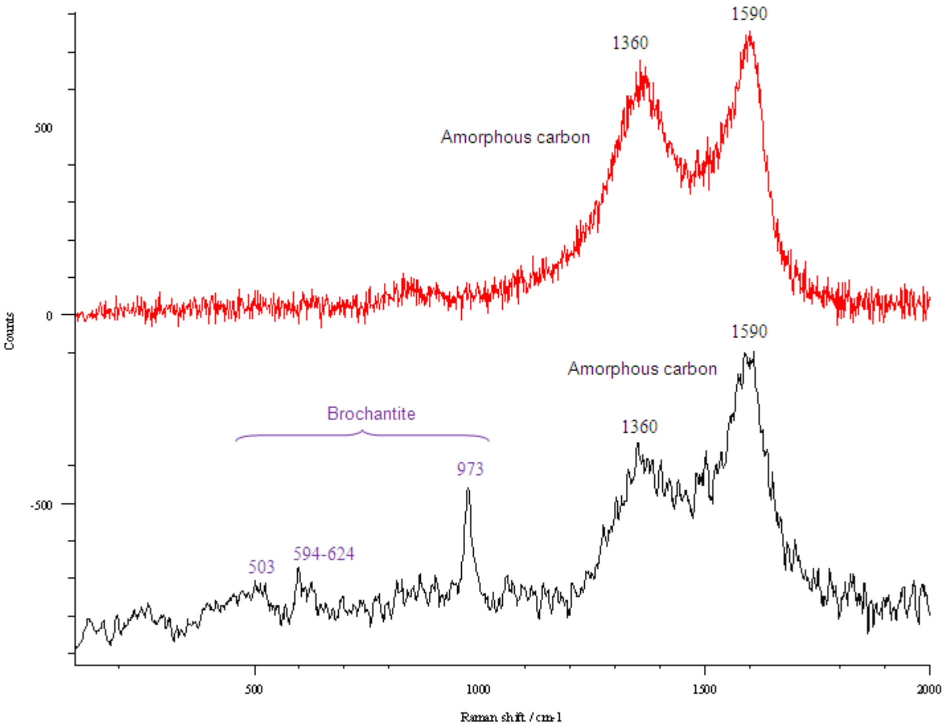

Figure 1.14 - Light blue areas in the patina on sample O2 (mostly unsheltered, shield handle in Omo statue) analysed by micro-Raman spectroscopy: Presence of amorphous carbon and brochantite.

Black patina is basically composed by amorphous carbon, probably originated by atmospheric deposition. Also some chalcantite was detected, which proved to be a thermally sensitive compound (as shown in Fig. 1.12).

Green and light blue patina is formed by white-green and blue crystals, identified as basic or hydrated Cu sulphates. A prevailing presence of posnjakite was detected, but also of brochantite (Figs. 1.13 and 1.14). Amorphous carbon, however, was present in all the analysed areas.

1.3.3.2 EDS profiles on scraped powders

Corrosion products for Bottego and Omo statues are shown in Figs. 1.15 and 1.16, respectively.

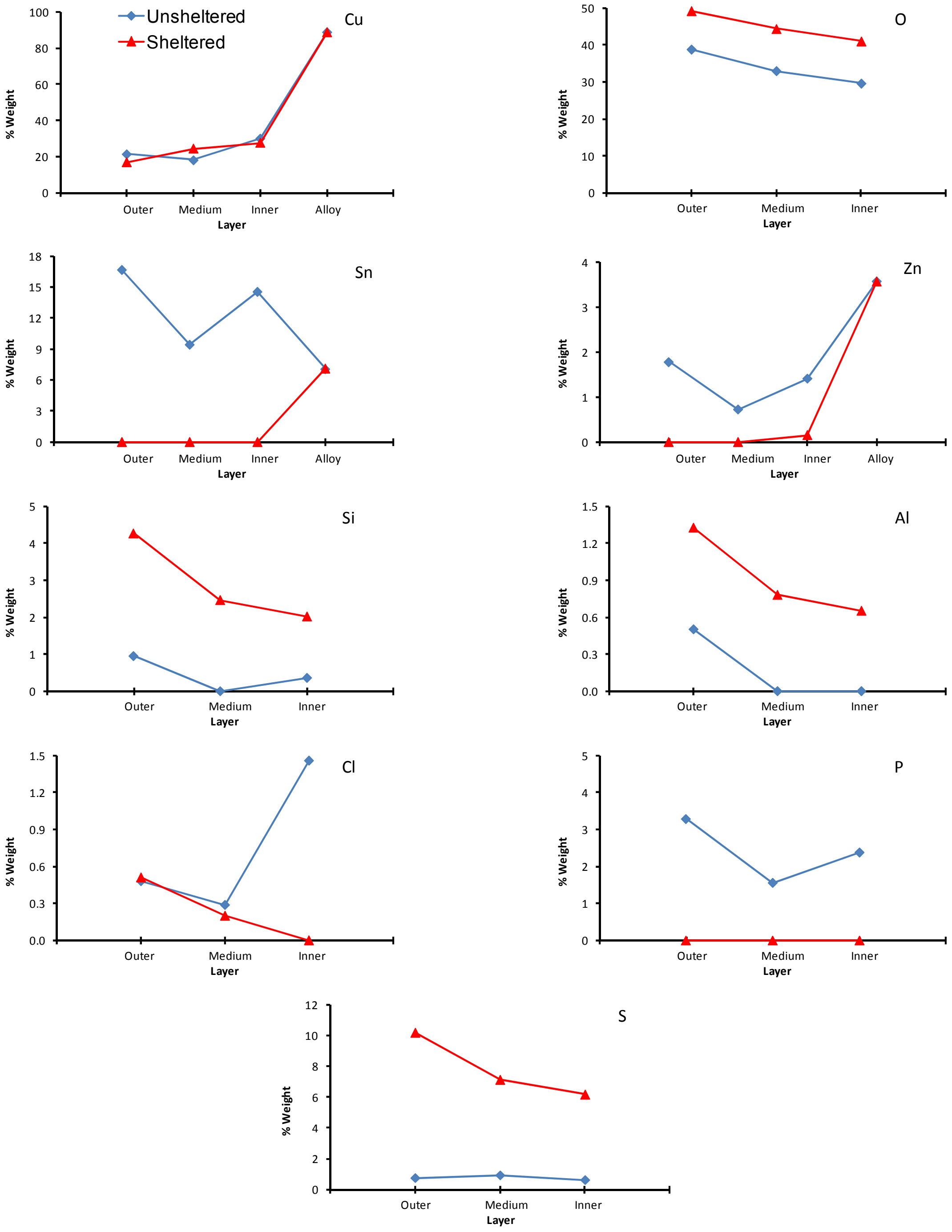

Fig. 1.15 - EDS results for corrosion products on Bottego statue. Elemental concentration changes from the outer to the inner layer for sheltered (red triangles) and unsheltered (blue diamonds) positions.

EDS results of the analysis of scraped corrosion products from the Bottego statue are reported in Fig. 1.15. Values for the alloy reported in these graphs are the averaged ones measured in the core metal by large area EDS (Table 1.2), because it was not possible to analyze the metal exactly in the spot from which corrosion products were scraped.

Cu, O, S: All of these elements are present in sheltered and unsheltered areas. Cu concentration generally increases on going from the outer, corroded layer towards the uncorroded core of the alloy, as a consequence of the conversion of the metal to corrosion products. Consequently, O decreases on going from the outer layer towards the core metal because it is involved in the formation of corrosion products. A similar trend is observed also for S, which participates to the formation of copper sulphates (detected in these samples by micro-Raman and ATR-IR analyses, Tables 1.3 and 1.4). It is worth noting that higher amounts of S are detected in sheltered areas (i.e. not exposed to the leaching action of the rainfall).

Zn: The concentration of this alloying element generally decreases on going towards the external layer, indicating dissolution into the environment.

Sn: Higher amounts of this element were detected in unsheltered areas (due to the leaching action of the rain which generates a corroded surface characterised by a relative enrichment of Sn-containing species [3]) (see also 1.3.4). In this case, the Sn-rich layer was not detected in sheltered areas, probably due to the scraping procedure which was not selective enough.

Si, Al: These elements are due to atmospheric contamination. They increase on going towards the outer layer (more noticeably in sheltered areas, where leaching due to rainfall does not occur).

Cl: The concentration of this aggressive pollutant increases on going towards the metal core in the case of unsheltered areas. The accumulation of chlorides at the interface between the corrosion products and the metal is typically observed also on other outdoor bronzes [59].

P: This element was only detected in unsheltered areas (see also 1.3.3.4).

Results for Omo statue are summarized in Fig 1.16.

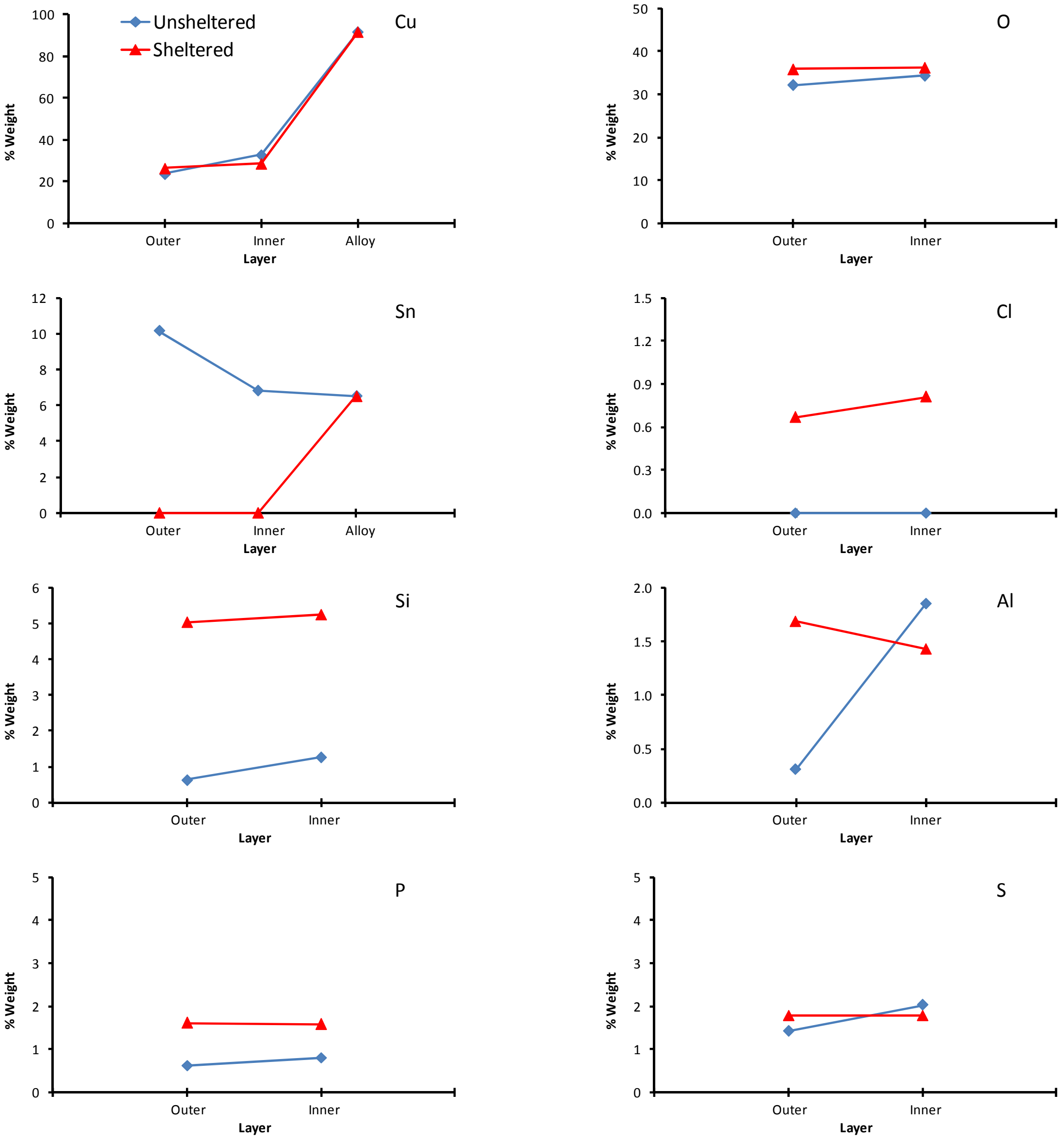

Fig. 1.16 - EDS results for corrosion products on Omo statue. Elemental concentration changes from the outer to the inner layer for sheltered (red triangles) and unsheltered (blue diamonds) positions.

In the Omo statue the trends for elements such as Cu, O and Sn are similar to those already discussed for Bottego.

Zn: Not detected, probably due to the high water solubility of its products [21].

Cl: Only detected in sheltered areas, with slightly higher values towards the interface with the metal.

S: Also for the Omo statue, sulphur was detected in scraped corrosion products (and copper sulphates were identified by micro-Raman and ATR-IR analyses, Tables 1.3 and 1.4), even if at lower concentration than in the Bottego statue. The concentration does not change significantly on going from the outer towards the inner layer and is comparable both in sheltered and in unsheltered areas.

This might be due to a “dilution” effect typical of EDS analysis, where the elements detected are summed up to 100% and the presence of high amounts of elements such as C (coming also from the adhesive for the preparation of the sample), might lead to a relative decrease of other elements (such as S) in samples where the total amount of powder is not enough to fully cover the sample holder.

P: Detected in sheltered and in unsheltered areas (even if in lower amounts than in sheltered ones) (see 1.3.3.4). Its presence might be due to environmental pollutants and/or to previous restoration procedures such as chemical cleaning [60, 61, 62] with phosphoric acid or phosphate-based cleaners (i.e. sodium hexametaphosphate, tetrasodium pyrophosphate) for removing calcareous encrustations (statues were located in a fountain, but not in direct contact with water).

Both in Bottego and in Omo statues it was not possible to detect Pb: This is probably due to the localised nature of Pb-rich corrosion products, which are dispersed into the volume of the scraped powders. Also, the uncertainty in the determination of Pb (due to overlapping of Pb and S peaks (Pb Mα = 2.343 keV vs S Kα = 2.307 keV [63])) when the primary beam’s accelerating voltage is lower than 25 kV, might be responsible for this effect.

1.3.3.3 Micro-Raman and ATR-IR analyses on scraped powders

Micro-Raman and ATR-IR spectra for corrosion products are collected in Appendices C and D, respectively. The main results are summarized in Tables 1.3 and 1.4, for sheltered and unsheltered areas respectively.

Table 1.3 - Identification of corrosion products in sheltered areas of the Bottego and Omo statues (**micro-Raman** and **ATR-IR** spectroscopy).

Location		Corrosion products							
		Brochantite	*Antlerite*	*Langite*	*Posnjakite*	*Atacamite*	*Gypsum*	*Calcite*	*Silicate*
Bottego *environment* ↓ *metal*	**B2**	**+**	**+/-**	**+**	**+**	**+/-**			
	B3	**+**	**+/-**	**+**	**+**		**+**		
	B4	**+**		**+**	**+**				
Omo *environment* ↓ *metal*	**O6**				**+**			**+**	**+**
	O7								**+**

+/- (traces) ; +(well detectable) ; ++ (abundant)

On the Bottego statue, the presence of sulphates (brochantite, antlerite and posnjakite, precursor of brochantite) was clearly observed. These compounds are typical outdoor bronze corrosion products [29].

Traces of basic chlorides (atacamite) were also observed, together with well-detectable inert compounds from environmental contamination (calcite, gypsum, silicates). Also amorphous carbon was detected in most micro-Raman spectra.

Table 1.4 - Identification of corrosion products in unsheltered areas of the Bottego and Omo statues (**micro-Raman** and **ATR-IR** spectroscopy)

Location		Corrosion products										
		Bro	*Ant*	*Langite*	*Posn*	*Chalc*	*Cuprite*	*Cass*	*Ata*	*Gypsum*	*Sili*	*Pho*
Bottego *environment* ↓ *metal*	**B5**				**+/-** **+/-**							**+**
	B6				**+/-** **+/-**					**+/-**		**+**
	B7				**+/-**							**+**
Omo *environment* ↓ *metal*	**O3**	**+**	**+/-**	**+**					**+/-**			
	O4	**+** **+**					**+**	**+**				
	O2	**+**			**++**	**+**						
	O5			**+**							**+**	

Ata=Atacamite; Bro=Brochantite; Ant=Antlerite; Posn=Posnjakite; Chalc=Chalcantite; Cass=Cassiterite; Pho=Phosphate; Sili=Silicate
+/- (traces) ; +(well detectable) ; ++ (abundant)

In general, for unsheltered areas, lower crystallinity (nearly amorphous compounds) was observed. Cu sulphates are less evident and atmospheric contaminants are present to a lower extent than in sheltered areas.

In the case of Omo statue, compounds such as oxides typically developed at the interface with metal (cuprite and cassiterite) were detected in inner layers.

The presence of phosphates in Bottego, as already observed by EDS (see comments to Fig. 1.15), may be due to both, interaction with the environment and cleaning procedures.

1.3.3.4 Py-GC-MS analyses on scraped powders

After identification of inorganic compounds in the corrosion products (through micro-Raman and ATR-IR), the remaining scraped powders were analysed by Py-GC-MS with the purpose to detect the possible presence of organic compounds on their surfaces.

All detected organic compounds are listed in Table 1.5. They were identified using reference spectra from the National Institute of Standards and Technology (NIST) digital library. The methylating agent used was tetramethylammonium hydroxide (TMAH), with the purpose to improve resolution, reason why all compounds reported appear as methylated. Pyrograms for Bottego samples are shown in Fig. 1.17 and for Omo samples in Fig. 1.18.

Table 1.5 - Organic compounds detected on corrosion products of statues (products arising from pyrolysis-methylation), molecular weight and their mass spectra

Peak	Compound name	M_w	*m/z* [a]
1	phosphoric acid, trimethyl ester	140	79(100), 80(57), 95(61), 110(53), 141(3)
2	dodecanoic acid, methyl ester	214	74 (100), 87 (60), 143 (16), 171 (13), **214** (13)
3	tetradecanoic acid, methyl ester	242	74 (100), 87 (66), 143 (28), 199 (18), **242** (18)
4	pentadecanoic acid, methyl ester	256	74 (100), 87 (71), 143 (24), 213 (13), **256** (20)
5	9-hexadecenoic acid, methyl ester	268	55 (100), 83 (45), 96 (52), 236 (28), **268** (7)
6	hexadecanoic acid, methyl ester	270	74 (100), 87 (67), 143 (25), 227 (15), **270** (27)
7	9-octadecenoic acid, methyl ester	296	55 (100), 69 (63), 83 (55), 264 (17), **296** (5)
8	octadecanoic acid, methyl ester	298	74 (100), 87 (71), 143 (30), 155 (18), **298** (40)

[a] *m/z* values of characteristic fragment ions (relative abundance); molecular ions are printed in bold.

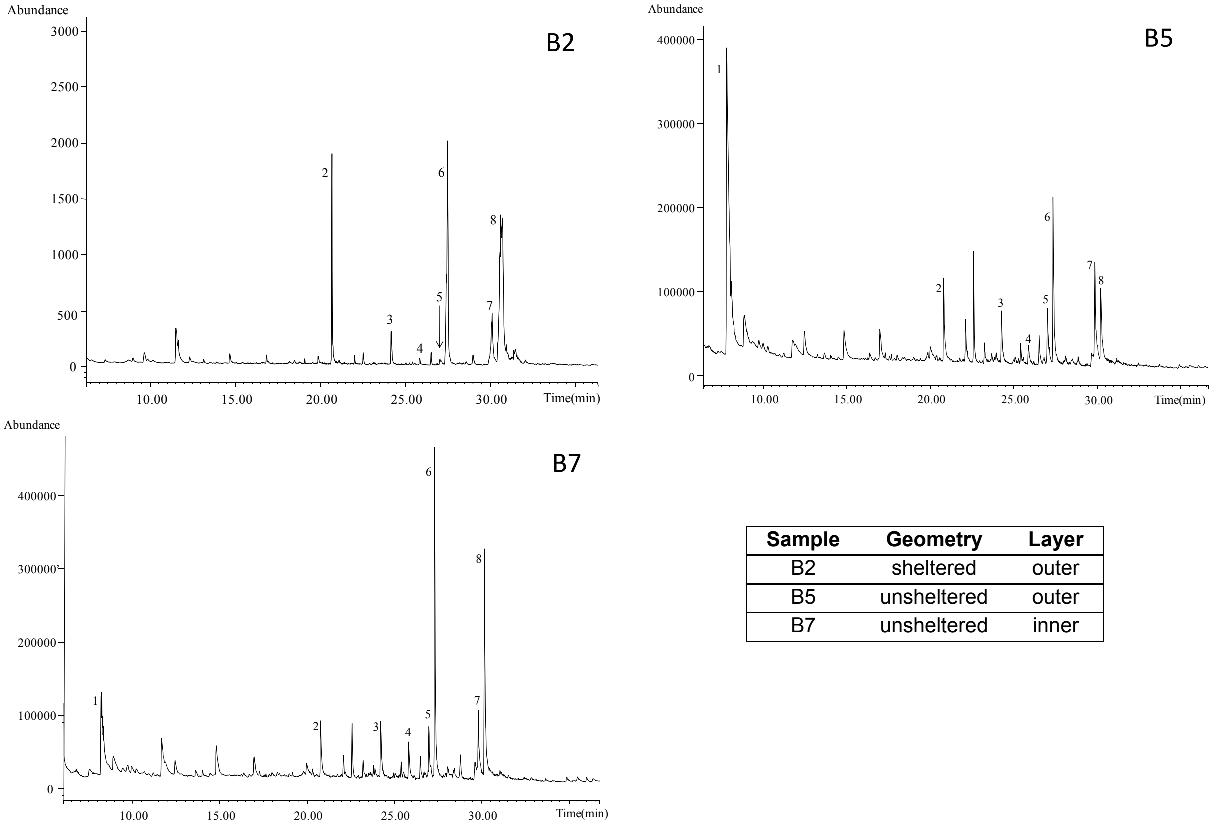

Sample	Geometry	Layer
B2	sheltered	outer
B5	unsheltered	outer
B7	unsheltered	inner

Fig. 1.17 – TIC pyrograms for Bottego samples, arising from pyrolysis-methylation. Peak assignation can be seen in Table 1.5.

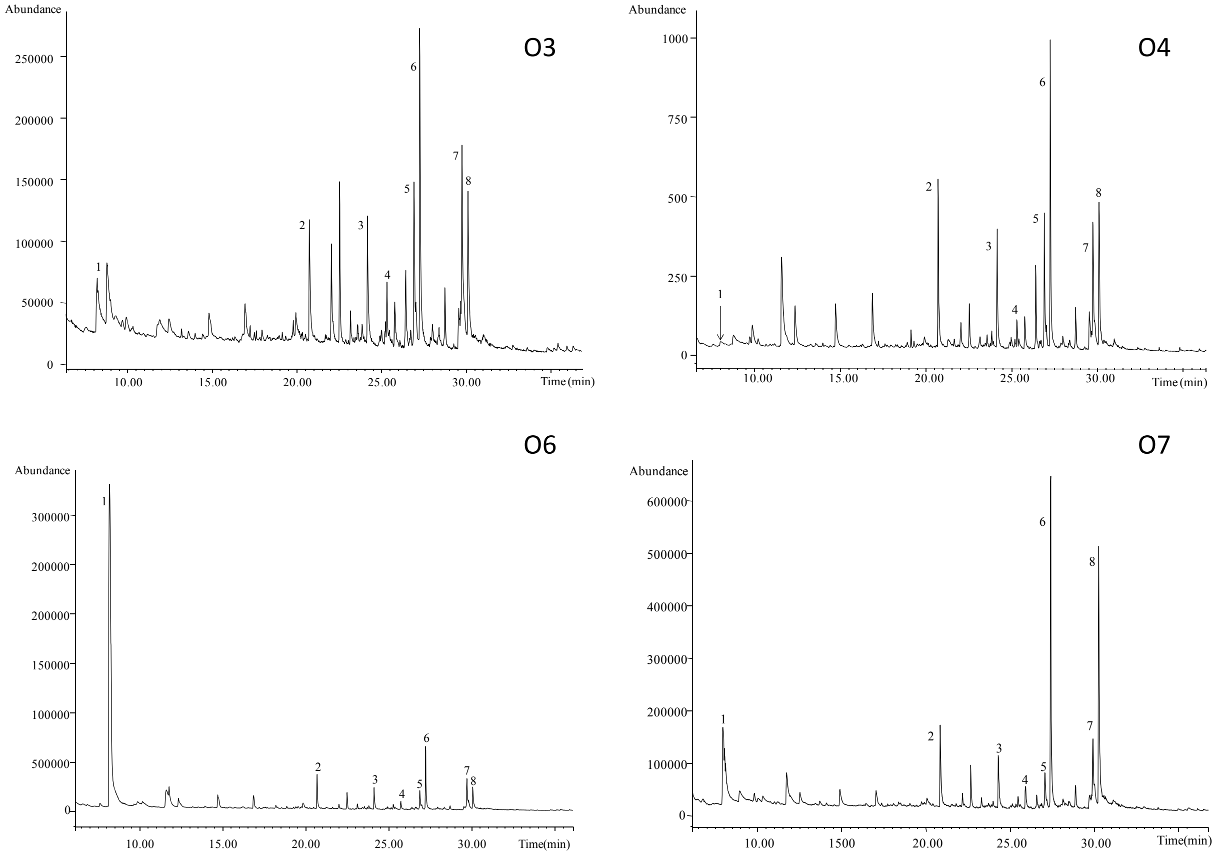

Sample	Geometry	Layer
O3	unsheltered	outer
O4	unsheltered	inner
O6	sheltered	outer
O7	sheltered	inner

Fig. 1.18 - TIC pyrograms for Omo samples arising from pyrolysis-methylation. Peak assignation can be seen in Table 1.5.

Concerning Bottego samples, B3 and B4 were also analysed, showing very similar results than B2. Significative compounds revealed are fatty acids. The main difference is that in B5 and B7 (both unsheltered) phosphoric acid-related compounds are present, while in B2, B3 and B4 (all sheltered) they are absent. In addition, the abundance of fatty acids in sheltered samples decreases on going from the outer (B2) to the inner layer (B4).

As for Omo samples, also fatty acids are the significative compounds present. Phosphoric acid-related compounds are present in all Omo samples although in different proportions, being especially high in the case of O6.

Phosphoric acid-related compounds were detected in the same samples were also EDS analysis highlighted the presence of P (Fig. 1.15).

The markers of siccative oil, suberic and azelaic acid, are absent in all samples from both statues.

In general, hexadecanoic (palmitic) and octadecanoic (stearic) acids are the two more abundant fatty acids in the samples. The presence of these compounds might be due to the application of a stearin wax-based protective treatment, whilst the application of other waxes which produce fatty acid residues such as beeswax [64] can be excluded [65].

1.3.4 Field measurements by portable XRF

XRF measurements were made *in situ* by a portable system so as to evaluate how conventional cleaning procedures, actually used by restorers in field work, affect the surface composition of corrosion products, depending on the exposure geometry (sheltered/unsheltered).

The portable system used for the measurement does not provide quantitative values, therefore only a very preliminary direct comparison of spectra is shown here. However, a more detailed comparison has been performed on the basis of relative intensity values of selected peaks (Table 1.6). All XRF spectra measured on the Omo statue are reported in Appendix E.

In Figs. 1.19 and 1.20 are reported the comparisons between XRF spectra measured *in situ* on sheltered and unsheltered areas of the Omo statue by the portable system before cleaning the corroded surface.

The comparison of spectra measured before cleaning on areas with the same exposure geometry (sheltered: neck and armpit, Fig. 1.19; unsheltered: shoulder/calf, Fig. 1.20) shows similar results for each typology.

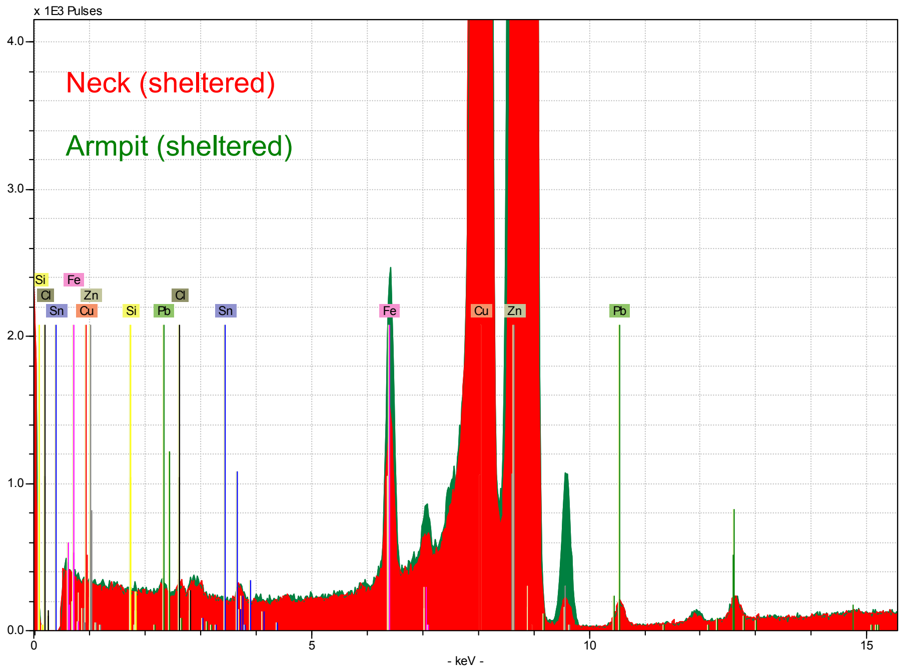

Fig. 1.19 - Comparison between portable XRF spectra measured on sheltered areas of the Omo (red corresponds to neck, and green to armpit of the statue).

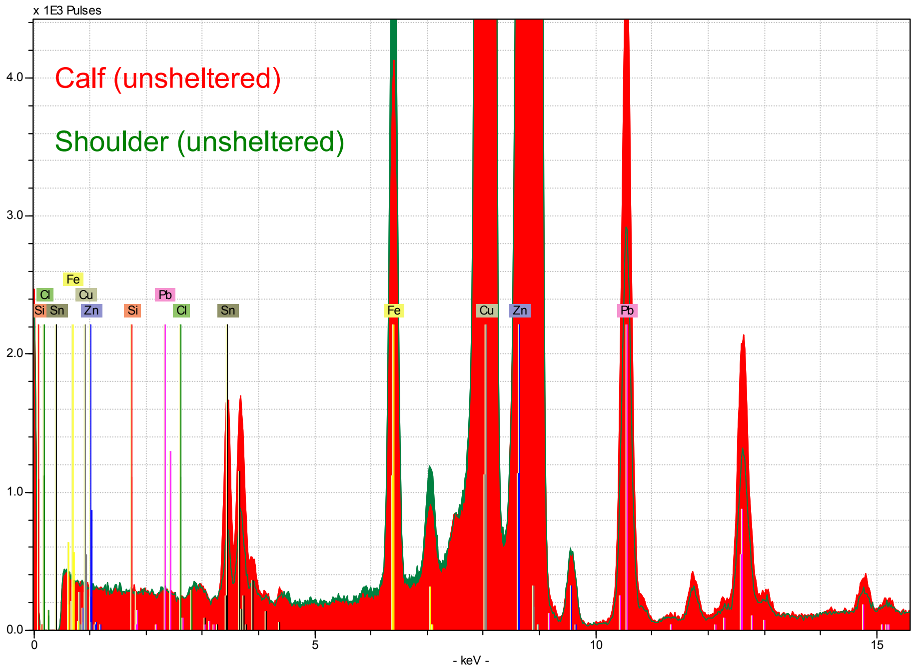

Fig. 1.20 - Comparison between portable XRF spectra measured on unsheltered areas of the Omo (red corresponds to calf and green to shoulder of the statue).

On the contrary, the comparison between XRF spectra measured on areas with different exposure geometry (Fig. 1.21) before cleaning, shows that unsheltered areas are richer in Sn and Pb than sheltered ones, whilst Cl gives a slightly more intense signal on sheltered areas (see EDS profiles in 1.3.3.2). These findings are in agreement with previous results obtained by analysing samples taken from different outdoor bronze statues [11, 59].

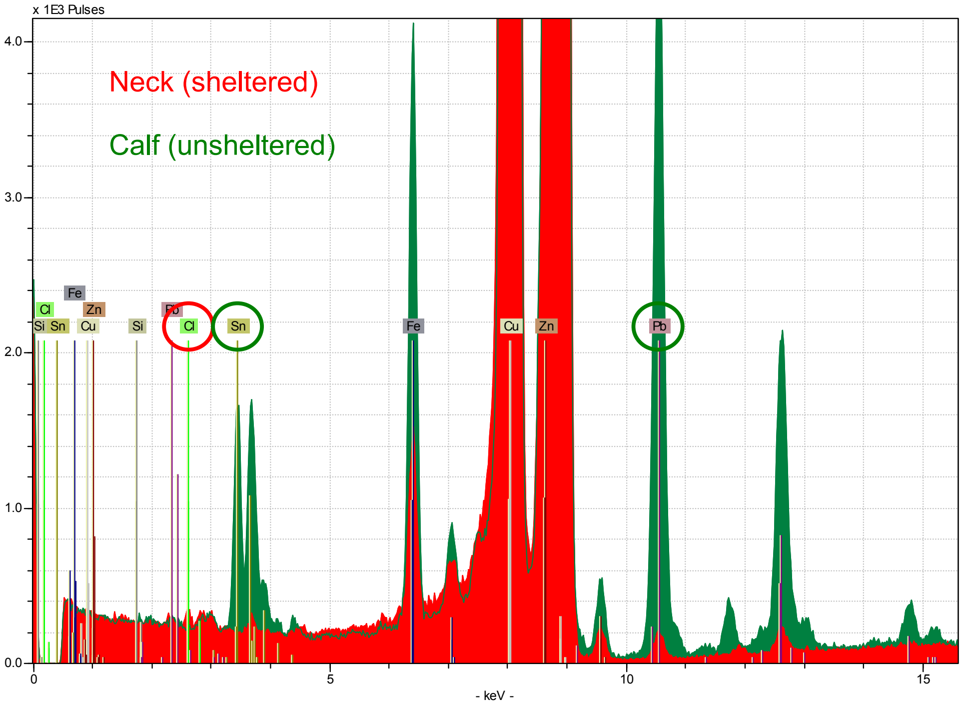

Fig. 1.21 - Comparison between portable XRF spectra measured on sheltered (red) and unsheltered (green) areas of the Omo statue. The main differences are highlighted by the circles around the element symbol.

The comparison of spectra obtained before and after cleaning the calf area (unsheltered), where at least two cleaning cycles were needed so as to decrease the conductibility of the rinsing solution, is shown in Fig. 1.22.

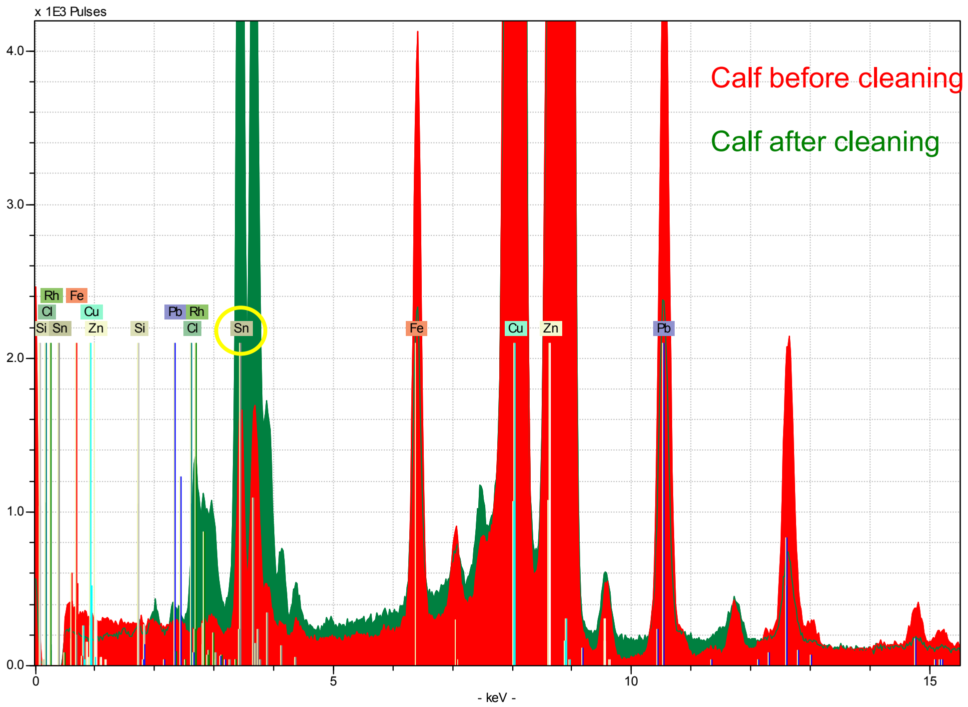

Fig. 1.22 - Comparison between portable XRF spectra measured on unsheltered area (calf) before cleaning (red) and after cleaning (green) of the Omo statue. The main differences are highlighted by the circles around the element symbol.

Even these extremely qualitative results show that after cleaning, the amount of Sn on the surface significantly increases, probably due to the removal of most of the compounds which are more soluble than Sn compounds [11], typically formed at the interface between metal and corrosion products on unsheltered areas of outdoor bronzes [56].

A more detailed comparison was also performed taking into account peak areas and peak heights and normalising with respect to the highest peak (the one from Cu Kα in this case); however, only the comparison using heights is reported here (Table 1.6), because it is less affected by errors in area calculations due to overlapping peaks.

Table 1.6 - Relative heights for Sn and Pb, before and after cleaning of Omo statue (Cu Kα peak's (8.04 keV) is taken as reference).

			Sn (%)	**Pb (%)**
Before cleaning	Unsheltered	Calf	0.8	2.3
		Shoulder	0.4	1.2
	Sheltered	Neck	0.0	0.1
		Armpit	0.0	0.1
After cleaning	Unsheltered	Calf	4.9	1.5
		Shoulder	1.2	2.1
	Sheltered	Neck	0.0	0.1

Table 1.6 confirms that:

(1) Before cleaning, unsheltered areas are characterized by higher concentrations of Sn and Pb than unsheltered ones

(2) The cleaning procedure leads to a further increase of Sn concentration in the two unsheltered areas under examination (shoulder and calf). The variations in Pb concentration, however, do not show a similar increasing trend after cleaning, probably due to the localised distribution of this element.

1.4 The Bottego monument: Concluding remarks

The following conclusions can be drawn from the investigations on both the metal and the corrosion products from the Bottego monument:

1. The alloy used for the monument consists of a quaternary (Cu-Zn-Sn-Pb) bronze. No significant differences were observed among the three statues both in terms of composition and microstructure. Micro-structural analysis indicated that the metal underwent cold deformation after casting (probably due to fitting and joining the different sections of each statue, and/or as a consequence of the damage due to bombing in World War II).

2. The exposure to the outdoor urban environment led to the formation of corrosion products with different features as a function of the exposure geometry (sheltered/unsheltered areas).

3. The main compounds identified on the corroded surfaces in sheltered areas (i.e. where rain stagnates) are Cu sulphates, with traces of Cu chlorides, and compounds due to atmospheric deposition (such as silicates, calcite, gypsum and amorphous carbon).

4. In unsheltered areas (i.e. exposed to the leaching action of rain) instead, a relative Sn enrichment was observed (both by analysing the scraped corrosion products in the laboratory and by *in situ* measurements, carried out during a real conservation intervention).

5. Also phosphates were detected, both in sheltered and unsheltered areas (probably due to a previous cleaning treatment) together with residues of fatty acids (without markers of siccative oils and corresponding to palmitic-stearic mixtures) probably used for a protective treatment.

Section 2

Laboratory tests: Study of the efficiency of protective treatments for outdoor bronzes by accelerated corrosion tests

In this section of the thesis, the results of two different accelerated corrosion tests are presented and discussed: Wet & dry test, simulating the alternated cycles of atmospheric exposure, and total immersion test. In the latter type of test, the sample is simply immersed in an aggressive solution and the testing conditions are not representative of real exposure in outdoor environment; however, this test was conducted for comparison with previous results (not contained in this thesis) and with a view to subsequent electrochemical measurements (such as galvanic coupling measurements for the study of gilded bronzes).

2.1 Wet & dry test

2.1.1 Tested material

Coupons of OPD quaternary bronze (manufactured by Opificio delle Pietre Dure, in Florence) were sanded with 600, 800 and 1000 grit sandpaper and rinsed with water, with the purpose to remove all the scratches (which are preferential sites for the corrosion process to occur), and obtain a shining surface. After sanding, they were washed with distilled water, dried with a hairdryer and put into a desiccator. Later, they were weighted and their lengths, widths and thicknesses were measured with the purpose to calculate the total surface area of each coupon. The chemical composition of the OPD bronze, measured in a previous work [39], is shown in Table 2.1.

Table 2.1 - OPD quaternary bronze composition

	Cu	Zn	Sn	Pb	Sb	Other
Weight %	91.9	2.9	2.4	1.0	0.8	1.0

All coupons for wet & dry test were submitted to indentation using a micro-Vickers device, with the purpose to characterize the surface in the same area of the sample, before and after the exposure test. This is shown in Fig. 2.1(a,b).

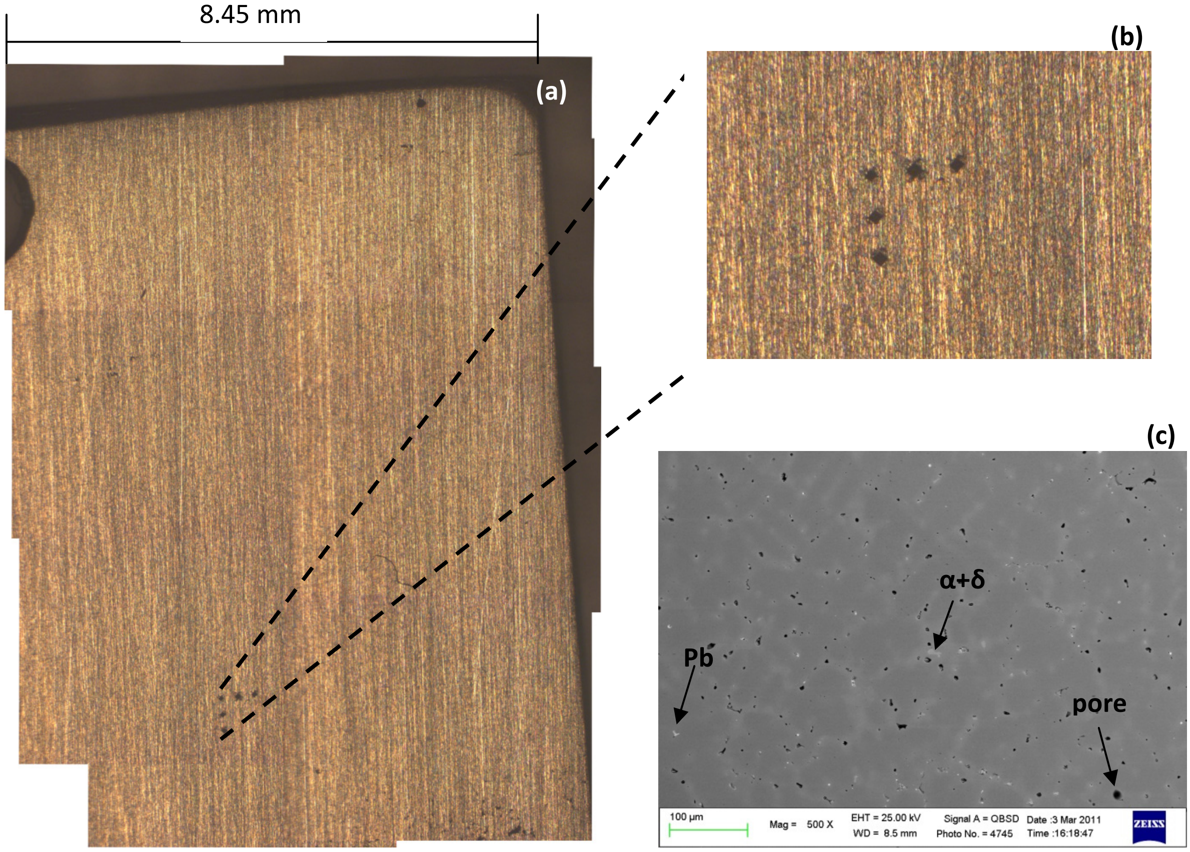

Fig. 2.1 - Detail of indentation marks done using micro-Vickers device (load 100 g), on every coupon for wet & dry test (a,b) and SEM image of that site (c)

The BSE-SEM image of the polished alloy, reported in Fig. 2.1, shows a dendritic microstructure with microsegregation of Sn, which took place during solidification (thus leading to an inhomogeneous distribution of Cu and Sn, with Sn enrichment in the peripheral regions of the dendrites). Some areas with Sn-rich eutectoid micro-constituent were also detected at the periphery of dendrites. Scattered Pb globules (white dots in Fig. 2.1 c), immiscible with the Cu-rich matrix, were observed in the same areas, together with some porosity (black dots).

More details on the microstructure can be seen in the X-ray maps of Fig. 2.2, showing the distribution of alloying elements at low magnification. Furthermore, a higher magnification detail with Pb globules is shown in X-ray maps of Fig. 2.3. These maps point out the presence of O and C in the area corresponding to the Pb globules, probably as a consequence of localised corrosion (already before starting any test).

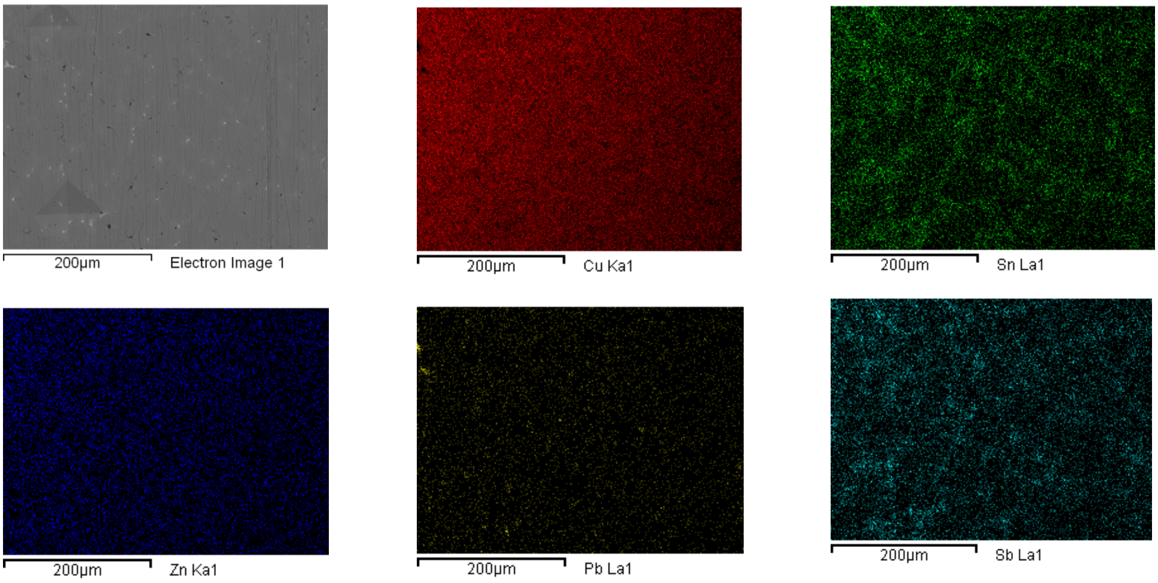

Fig. 2.2 - X-ray maps of the distribution of alloying elements at low magnification (10x)

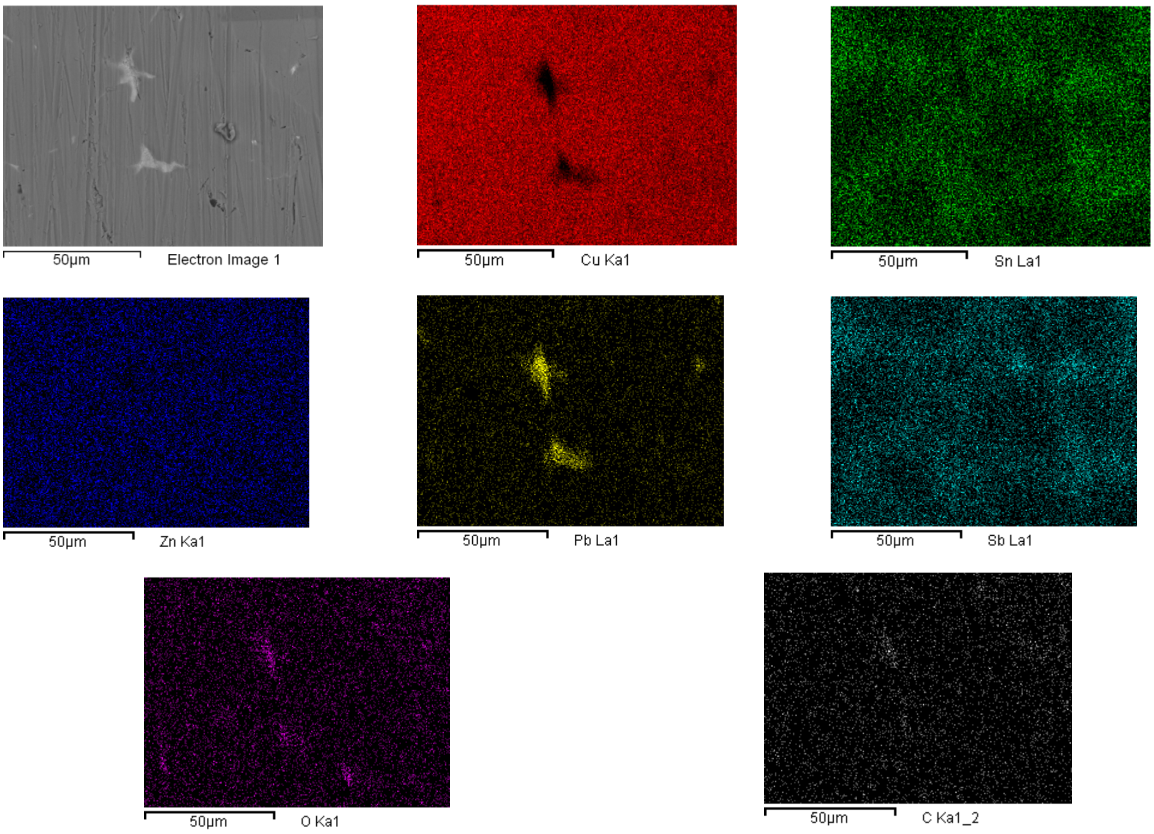

Fig. 2.3 - X-ray maps of the distribution of alloying elements at high magnification (50x)

2.1.2 Weathering method

The atmospheric exposure is simulated through an alternating immersion test during which the bronze coupons are periodically dipped into a synthetic rain solution (described below). A device designed so as to apply the wetting and drying cycles was used (Fig. 2.4). It conforms to the main conditions required by the standards UNI 4008-66, UNI EN ISO 11130 and ASTM 44. It consists of six glass jacketed cells interconnected and covered by a Teflon cap. In each cell, only one sample is suspended and connected to a mobile bar by a nylon thread passing through the cap. The vertical movement of each sample is related to the vertical displacement of the bar (max. 4 cm s^{-1}). The volume of the synthetic rain solution was 0.3 L per cell and the temperature of the cell solution was maintained constant at 298 K by a propylene glycol based water solution circulating through the jacket and connected to a refrigerated/heating circulator [2].

Specific software was used to run the bar automatically and to record the parameters of each test. The duration of one wet & dry corrosion cycle was 1 h, corresponding to 20 min of immersion (wet condition) and 40 min of emersion (dry condition). This wet/dry time ratio (1/2) is close to the ratio between rainy and dry days during the week in winter months in Bologna, Italy. Considering a time of about 20 min for the samples to get dry, a reasonable time of wetness (TOW) of 40 min is assumed to correspond to an hourly cycle [2].

This wet & dry test was used, at first, as a method for ageing the samples (i.e. for generating a corrosion layer on their surfaces) before applying corrosion inhibitors, so as to simulate the situation of actual conservation interventions, in which the restorers do not apply the protective films on bare metal but on the (more or less) cleaned “patina”. Subsequently, the wet & dry test was also used as an exposure test for proving the efficiency of protected surfaces after the application of inhibitor films.

The “ageing” (or “pre-patination”) cycle before inhibitor application took 15 days, in which the coupons were tested for 7 days, and then the synthetic rain solution was sampled and renewed for the remaining 8 days and sampled again. Renewal of the solution was made with the purpose to simulate more closely the real rain situation in which stagnant rainwater in contact with the metal surface is naturally renewed by rainfall cycles.

The solutions sampled during the 15 days of exposure were subsequently analysed by graphite furnace atomic absorption (GFAAS, Perkin-Elmer AAnalyst 400), whilst the corroded coupons’ surfaces were characterised by VP-SEM and micro-Raman spectroscopy (Invia-Renishaw, wavelength 514.5 nm, 50 mW).

Fig. 2.4 - Wet & dry device

2.1.3 Artificial acid rain solution

In order to reproduce the composition of the acid rain as closely as possible, synthetic rain was prepared according to the composition of a mixture of weekly natural rain samples (pH < 4.5), collected during the winter months in a monitoring atmospheric station in Bologna and influenced by the relatively close proximity to the Adriatic Sea. The synthetic rain was prepared with analytical grade reagents and ultra-pure deionised water (electrical resistance: 18 MΩ). The composition of the synthetic rain is shown in Table 2.2 [2].

Table 2.2 - Artificial acid rain water composition [2]

	Concentration (mg/L)		**Concentration (mg/L)**
SO_4^{2-}	1.90	NH_4^+	1.06
Cl^-	1.27	Ca^{2+}	0.34
NO_3^-	4.64	Na^+	0.53
CH_3COO^-	0.23	H^+	0.06
$HCOO^-$	0.05		

*pH 4.25

2.1.4 Application of corrosion inhibitors

Aged coupons were sent to the Centro di Corrosione “A. Daccò” at the Università di Ferrara for the application of a silane-based inhibitor selected on the basis of previous works [15, 39], as described in I.3 in the Introduction of this thesis.

The process followed to apply the inhibitor on the bronze coupons can be described in 4 steps:

1. Preparation of a solution with 90% ethanol, 5% water and 5% of the inhibitor, 3-mercapto-propyl-trimethoxy-silane (PropS-SH, pH 4), whose structure is shown in Fig. 2.5.
2. The solution needs 1 month for the process of hydrolysis of the Si–OCH_3 groups.
3. Coupons are completely immersed into the hydrolysed solution for 1 hour.
4. Coupons are taken out of the solution and dried for 10 days at room temperature (no heating is applied at any moment).

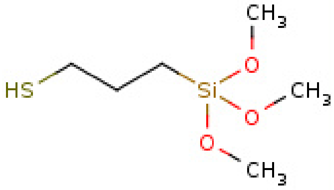

Fig. 2.5 - Chemical structure of the PropS-SH inhibitor

The curing time at room temperature was found to significantly affect the inhibiting efficiency and a period of 10 days was selected on the basis of previous work [39].

FT-IR analyses carried out at the Università di Ferrara for the characterisation of the inhibited bare metal surface (before ageing [39]) showed that:

(1) Hydrolysis of PropS-SH is demonstrated by the appearance of a peak (3400 cm^{-1}) related to the SiO-H bond stretching, which is absent both in the as-received PropS-SH (where siloxane SiO-CH_3 groups are still present) and in the silanic layer formed on the bronze samples after curing (where condensation of silanol groups leads to the formation of O-Si-O bridges).

(2) Crosslinking of the polymer network due to condensation of silanol groups is evident by the decrease after curing of bands (910 cm^{-1}) attributed to the stretching of Si-OH bonds,

accompanied by an increase of the peaks at 1120 and 1050 cm^{-1}, related to the asymmetric stretching of Si-O-Si bonds.

(3) The formation of thiolate bonds (Alloy-S-C) during immersion in the inhibiting solution (hydrolysed PropS-SH) is demonstrated by the disappearance, after curing, of the band (2570 cm^{-1}) due to S-H stretching.

Both neat PropS-SH and PropS-SH+CeO_2 nanoparticles were tested, so as to evaluate the influence of the nanoparticles on the protective efficiency of the inhibitor. The size of nanoparticles ranges from 20 to 40 nm and the concentration used was 250 ppm in the ethanol solution.

Together with a reference sample (which was aged but not inhibited), the inhibited coupons were submitted to the wet & dry test. The “exposure” cycle lasted for 15 days. Also in this case, the ageing solution was sampled after the first 7 days and renewed for the remaining 8 days, and sampled again.

A summary of the development of this test is shown in Table 2.3.

Table 2.3 - Development of the wet & dry test

Code	Bronze sample	Pre-patinated 15 days ?	Inhibited ?	Inhibitor
A-NI	WD-1	Yes	No	None
NA-P	WD-2	No	Yes	PropS-SH
A-P	WD-3	Yes	Yes	PropS-SH
A-PC	WD-4	Yes	Yes	PropS-SH + CeO_2 nanoparticles

The solutions sampled during this second wet & dry cycle were subsequently analysed by GFAAS.

SEM-EDS (VP mode), micro-Raman (Invia-Renishaw, wavelength 514.5 nm, power 50 mW), optical microscopy and color analysis by reflectance spectrophotometry (D65-Solar, 10°, specular component included) and by glossmeter (BYK-Gardner Micro-TRI-gloss at 20°, 60° and 85°) were performed on each one of the exposed coupons at the end of the wet & dry test.

2.2 Total immersion test

Coupons of OPD bronze (composition shown in Table 2.1) were polished until mirror finish (using rotating discs covered with soft cloths impregnated with diamond pastes of 3 and 1 μm size and an oily lubricant), washed and put into a desiccator. Subsequently they were inhibited with PropS-SH (with and without ceria nanoparticles) in the same conditions as for the wet & dry test (see 2.1.4).

After 10 days of room temperature curing time, the inhibited coupons were weighted, measured and, finally, submitted to the total immersion test, which lasted for 5 days.

Sample NI-NaCl, made of the same OPD bronze and with no inhibitor, was previously tested in NaCl 3.5 wt% solution. Therefore, this test was not repeated, and the sample P-NaCl is used to compare the efficiency of the inhibitor in a typical corrosive solution such as NaCl 3.5 wt%. Artificial acid rain used in this test has the same composition as described in 2.1.3.

Table 2.4 summarizes the development of this test.

Table 2.4 - Development of the total immersion test

Code	Sample	Applied inhibitor	Solution used for total immersion	Volume of solution used for total immersion (mL)
NI-NaCl	TI-0	Not inhibited	NaCl 3.5 %wt	600 ± 3.5
P-NaCl	TI-1	PropS-SH	NaCl 3.5 %wt	235 ± 2
P-AR	TI-2	PropS-SH	Acid rain 10x [a]	235 ± 5
PC-AR	TI-3	PropS-SH + CeO_2 nanoparticles	Acid rain 10x [a]	230 ± 5
NI-AR	TI-4	Not inhibited	Acid rain 10x [a]	230 ± 5

[a] Acid rain 10x means that the solution was 10 times more concentrated with the purpose to accelerate the corrosion process

For the total immersion test, coupons were attached with a piece of nylon to a glass bar and each one was suspended into a 250 mL flask with the corresponding solution, as shown in Figure 2.6.

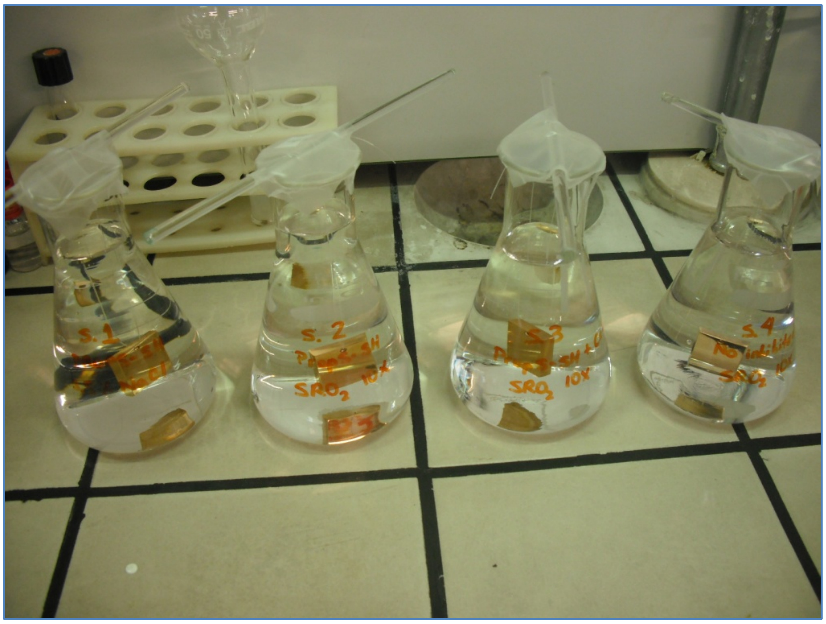

Fig. 2.6 - Coupons totally immersed in the solution (beginning of the test)

A pH 5.7 was measured for NaCl 3.5 %wt solution, and pH 3.3 for the acid rain 10x solution.

The amount of each alloying element released into the solution at the beginning (1 or 2 days) and at the end of the test (5 days) were measured by atomic absorption spectroscopy (FAAS for high-concentrated species and GFAAS for low-concentrated ones).

In addition, SEM-EDS (VP mode), micro-Raman (Invia-Renishaw, wavelength 514.5 nm, power 50 mW) and optical microscopy analysis were performed on each coupon at the end of the total immersion test. Reflectance spectrophotometry was not performed due to the small dimensions of the coupons.

2.3 Wet & dry test: Results

2.3.1 Gravimetric measurements

These measurements were done with the aim to investigate how the inhibitor performance changes with: (a) The substrate for application (bare or aged (pre-patinated) bronze) and (b) The addition of ceria nanoparticles.

Coupons were weighted several times during the whole test with the purpose to observe the mass variations during the ageing and exposure cycles. Results are shown in Table 2.5.

Table 2.5: Mass change in the development of wet & dry test

Code	Sample	Area (cm^2)	Initial mass (g)[a]	Mass after ageing (g)[b]	Mass after inhibition (g)[b]	Mass after exposure (g)[b]
A-NI	WD-1	22.35 ± 0.74	32.9985	32.9975	32.9975	32.9964
NA-P	WD-2	21.0 ± 0.20	30.9658	30.9658	30.9703	30.9702
A-P	WD-3	19.03 ± 0.13	32.6767	32.6760	32.6806	32.6804
A-PC	WD-4	20.53 ± 0.10	35.2107	35.2104	35.2153	35.2151

[a] With an error ± 0.0002

[b] With an error ± 0.0001

Figure 2.7 shows graphs for the mass variation on the ageing and exposure cycles.

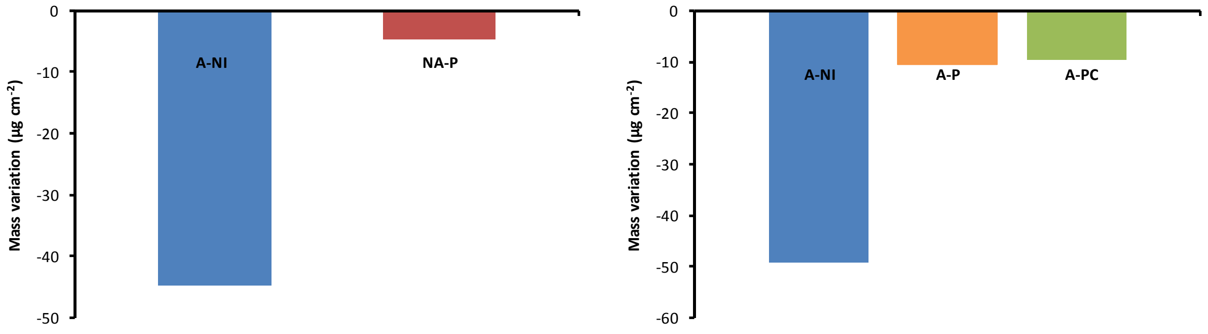

Fig. 2.7 - Mass variation: On bare bronzes during ageing cycle (left) and on aged (pre-patinated) bronzes during the exposure cycle (right).

In both cases, on bare and on pre-patinated bronze, the application of inhibitor reduces the mass decrease.

2.3.2 Ageing solutions

Elemental concentrations (in ppb) were measured for each one of the sampled solutions and normalised by the area of the respective coupon. Results are shown in Table 2.6.

Table 2.6 - Amount of metals released in artificial acid rain solutions after wet & dry test

	Code	**Applied inhibitor**	**Time of W&D (d)**	**Cu (µg cm^{-2})**	**Zn (µg cm^{-2})**	**Pb (µg cm^{-2})**
Pre-patination cycle	A-NI	---	7	20.2	2.7	8.8
			15	27.3	1.4	2.6
	A-P	---	7	23.4	4.0	9.0
			15	32.0	1.6	1.8
	A-PC	---	7	19	5.2	11.3
			15	32.7	1.9	2.8
Exposure cycle (inhibitor testing)	A-NI	Non inhibited	7	25.6	1.4	2.3
			15	29.4	1.6	1.3
	NA-P	PropS-SH	7	3.4	0.4 [a]	1.2
			15	3.2	0.9	1.2
	A-P	PropS-SH	7	3.2	0.5 [a]	0.2
			15	3.8	0.5 [a]	0.4
	A-PC	PropS-SH + CeO_2 nanoparticles	7	1.5	0.4 [a]	0.2
			15	3.2	0.4 [a]	0.2

[a] Zn was above the detection limit but below the quantification limit (QL = 60 ppb). For this reason, a value half the QL was considered.

Measurements for Sb were also performed, but the metal release was under the detection limit in all cases.

On the basis of the results in Table 2.6, graphs in Figs. 2.8 and 2.9 were obtained. Results for Zn are not shown because the release of this metal was under the quantification limit.

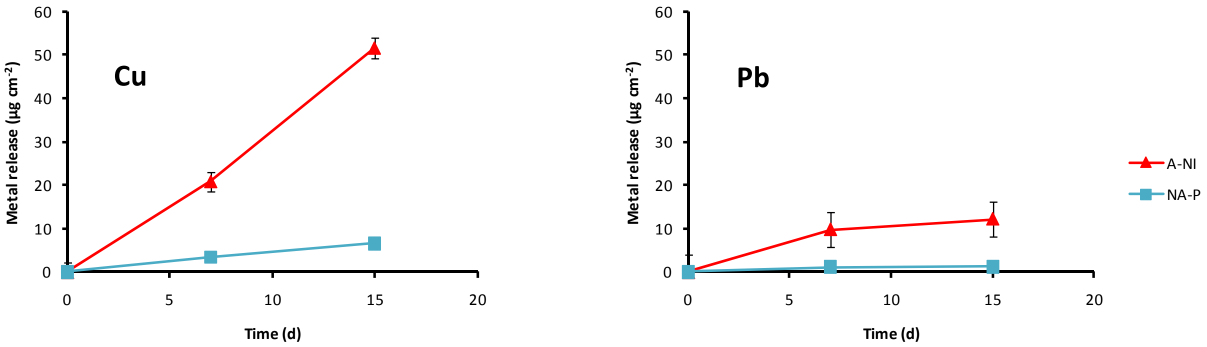

Fig. 2.8 - Metal release (Cu, Pb) in artificial acid rain solution in the wet & dry test for non-inhibited (A-NI) and inhibited (NA-P) bronze coupons during ageing cycle

According to Fig. 2.8, for both elements the inhibitor is effective in reducing the amount of metal released into the acid rain solution.

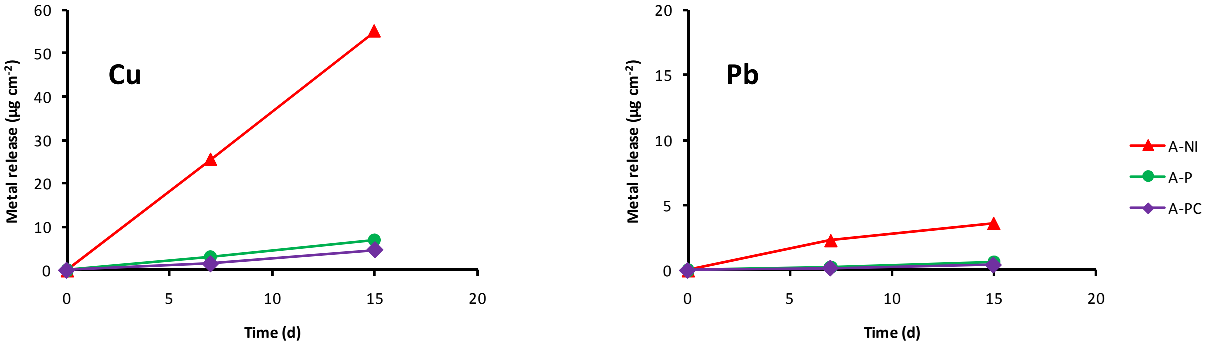

Fig. 2.9 - Metal release (Cu, Pb) in artificial acid rain solution in the wet & dry test for non-inhibited (A-NI) and inhibited (A-P, A-PC) bronze coupons during exposure cycle

Also in the case of aged (pre-patinated) bronze surfaces, the inhibitor shows to be efficient in reducing the release of both metals.

Bronze inhibited with PropS-SH with ceria nanoparticles (A-PC) shows a slightly better efficiency to reduce the metal release compared to pure PropS-SH (A-P).

2.3.3 Inhibitor efficiency

Inhibitor efficiency is calculated with the purpose to express how much the corrosion protection improves in the inhibited bronze coupons compared to the non-inhibited one. Inhibitor efficiency is calculated using:

$$IE = \frac{M_{sol,NI} - M_{sol,I}}{M_{sol,NI}} \ x \ 100 \qquad (2.1)$$

Where:

IE = inhibitor efficiency (percentage)

IE is 100% if no metal is released from the inhibited coupon, and 0% if the inhibited coupon releases as much metal as the non-inhibited one).

M_{sol} = amount of metal in the acid rain solution (Cu or Pb, in µg cm^{-2})

NI = non-inhibited coupon

I = inhibited coupon

Eq. 2.1 was used both for calculating the inhibition efficiencies for each alloying element and for the total inhibition efficiency which is the sum of the values for the alloying elements.

Table 2.7 - Inhibitor efficiencies (%) calculated for bare and aged (pre-patinated) bronzes in the wet & dry test (A-NI coupon is taken as reference)

	Cu		**Zn**		**Pb**		**Total**	
	7 d	**15 d**	**7 d**	**15 d**	**7 d**	**15 d**	**7 d**	**15 d**
NA-P	83.2	86.1	85.2	68.3	86.8	79.8	84.2	83.8
A-P	87.5	87.4	64.3	70.0	90.0	83.3	86.7	86.4
A-PC	94.1	91.5	71.4	70.0	92.1	88.8	92.8	90.3

Table 2.7 shows that PropS-SH exhibits higher inhibitor efficiency when applied on pre-patinated surfaces than on bare bronze. This result is very interesting, because one of the weakest points in the use of the most widely used bronze inhibitor, BTA (see I.3 in the Introduction), is actually the lower inhibition efficiency towards patinated surfaces than towards bare metal [49].

Furthermore, PropS-SH with ceria nanoparticles is more efficient than in its pure form. This is evident in the case of Pb at late stages (15 d), but also for copper and for the total inhibition efficiency.

In general, inhibitor efficiency for the alloying elements after 15 days increases as follows: Zn < Pb < Cu.

In addition, with the purpose to observe the corrosion behaviour of Cu and Pb in ageing and exposure cycles, metal ratios in the ageing solutions were calculated and compared to metal ratios in the alloy, so as to evaluate preferential corrosion effects. Results are shown in the graphs in Fig. 2.10 and 2.11.

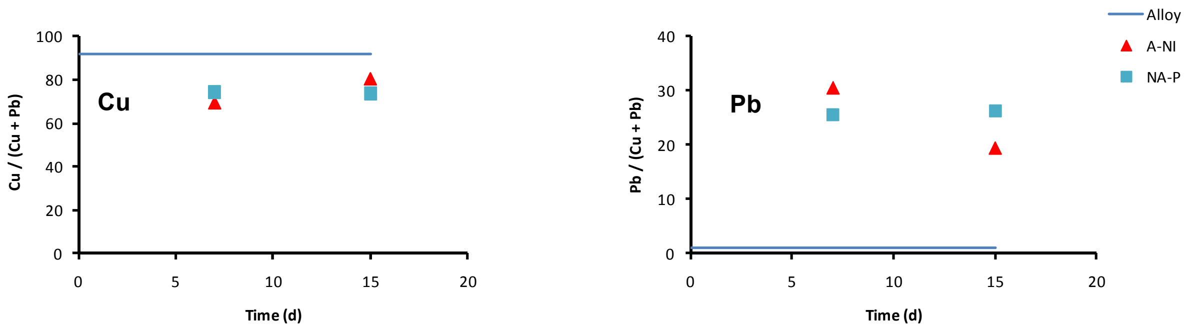

Fig. 2.10 - Comparison of corrosion behaviour for each metal respect to the alloy content, for the non-inhibited (A-NI) and the inhibited (NA-P) bronzes in the ageing (pre-patination) cycle.

In the case of bare bronze and on the basis of Fig. 2.10, Cu is more protected against corrosion than Pb. The latter undergoes preferential corrosion (i.e. higher amounts of Pb were measured in solution than in the alloy).

No significant differences are observed between the behaviour of inhibited and non-inhibited bare bronze.

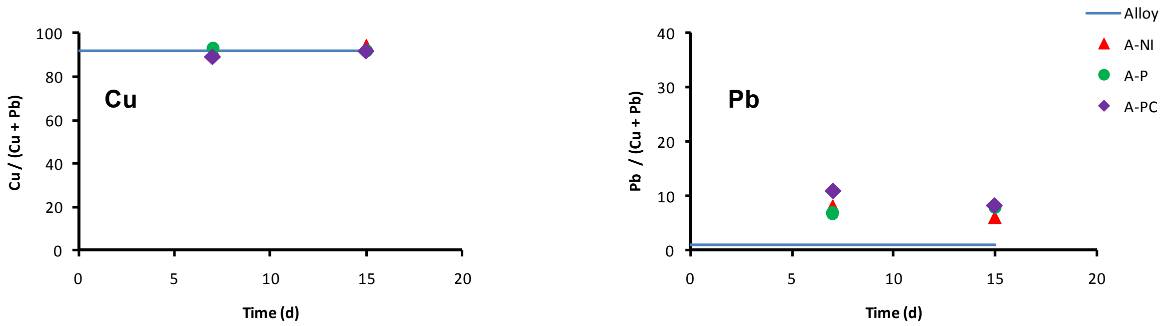

Fig. 2.11 – Comparison of corrosion behaviour for each metal respect to the alloy content, for the non-inhibited (A-NI) and the inhibited (A-P, A-PC) bronzes in the exposure cycle.

Also in aged (pre-patinated) bronze, Pb undergoes preferential corrosion (whilst Cu displays ratio values in solution comparable to those in the alloy), even if to a lesser extent than in bare bronze. Again, there are not significant differences between the inhibited and non-inhibited samples.

2.3.4 Characterisation of corroded surfaces

Low magnification optical images of corroded surfaces after the exposure cycle are compared in Fig. 2.12. Higher magnification details in bright field as well as in reflected polarised light are compared in Figs. 2.13 to 2.16.

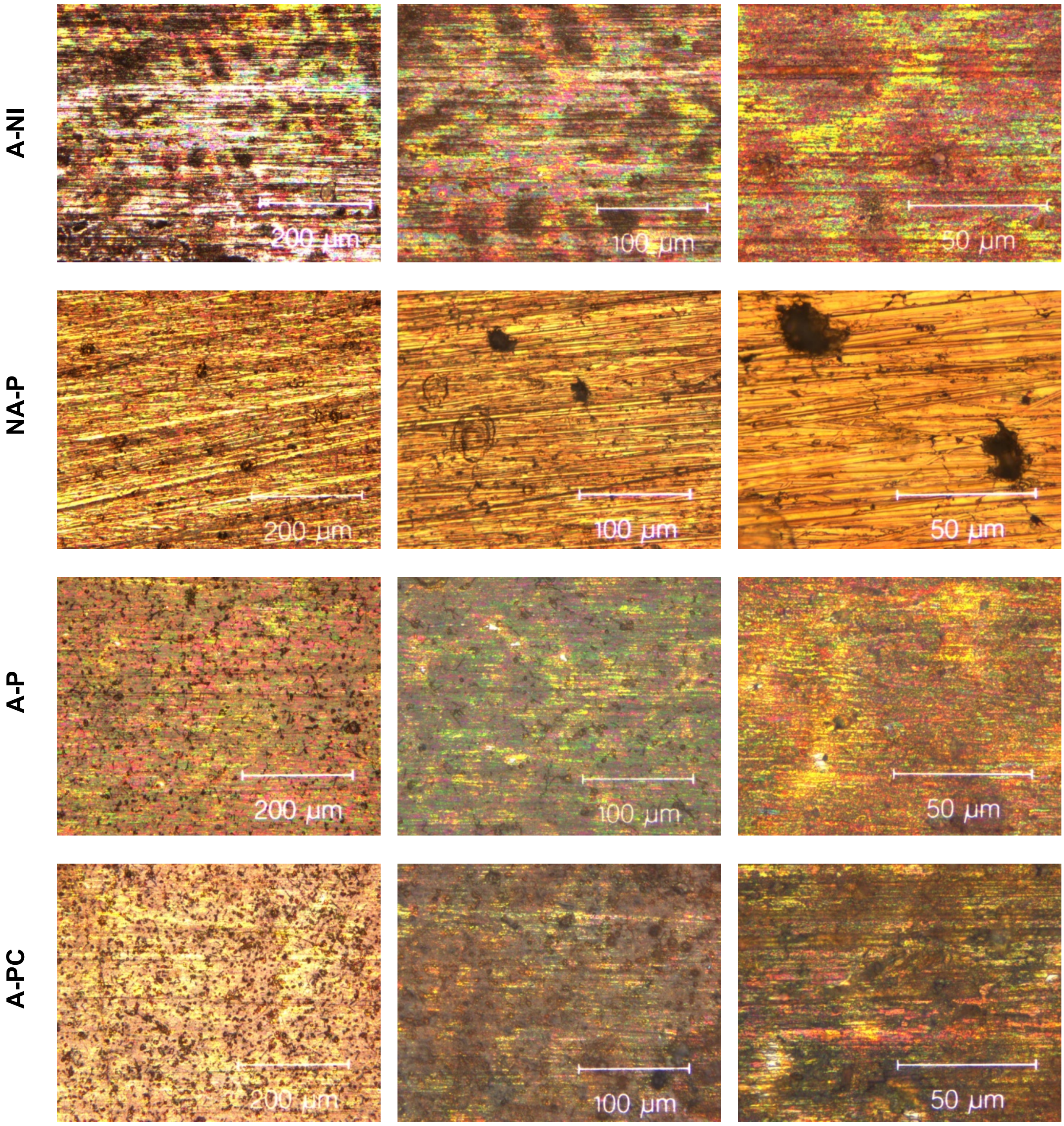

Fig. 2.12 - Bright field images of corroded surfaces after exposure cycle of wet & dry test. Coupons A-NI, NA-P, A-P, A-PC (top to bottom), with increasing magnification from left to right.

Corrosion products are more evident in the non-inhibited coupon (A-NI) than in the others and do not hide micro-structural features such as coring. The pre-patination is visible under the inhibitor layer in the case of A-P and A-PC.

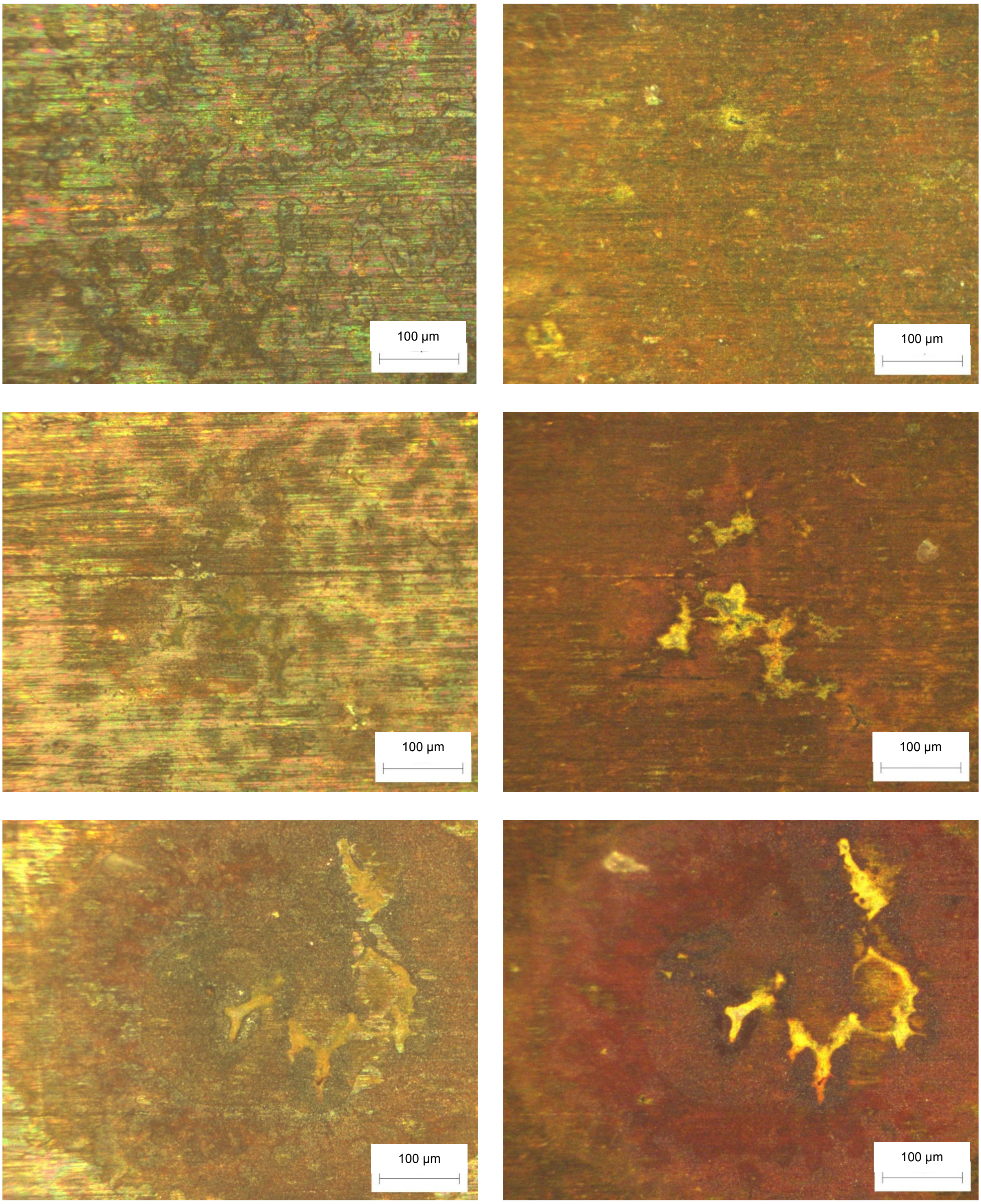

Fig. 2.13 - Optical microscopy images for A-NI coupon. Three different sites (top to bottom) were observed as bright field (left) and reflected polarised light (right).

The details in polarised light show some non-homogeneous areas in the corrosion products' layer, probably corresponding to interdendritic spaces.

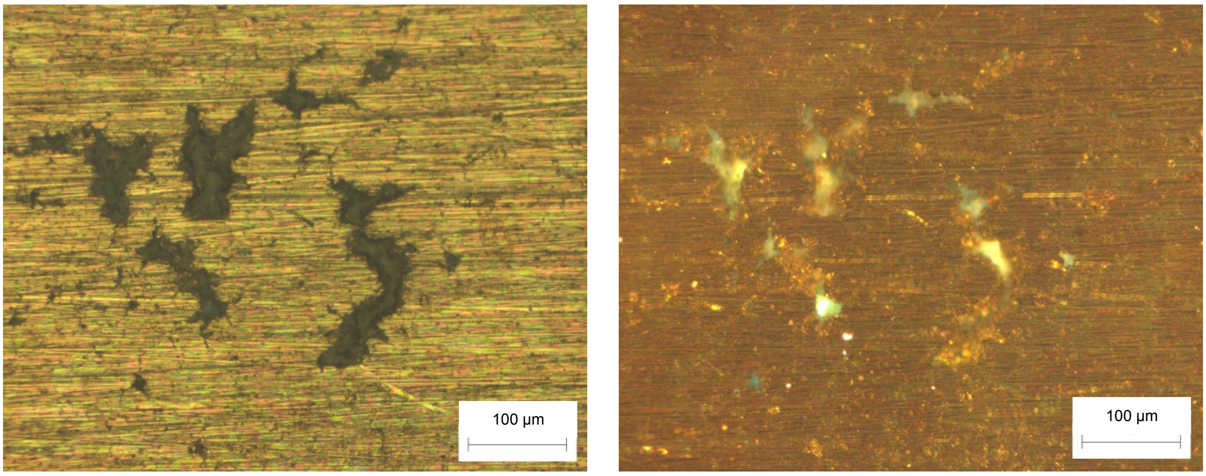

Fig. 2.14 - Optical microscopy images for NA-P coupon, observed as bright field (left) and reflected polarised light (right).

In Fig. 2.14 some non-homogeneities (whitish in the polarised light image) may be observed on the corroded surfaces.

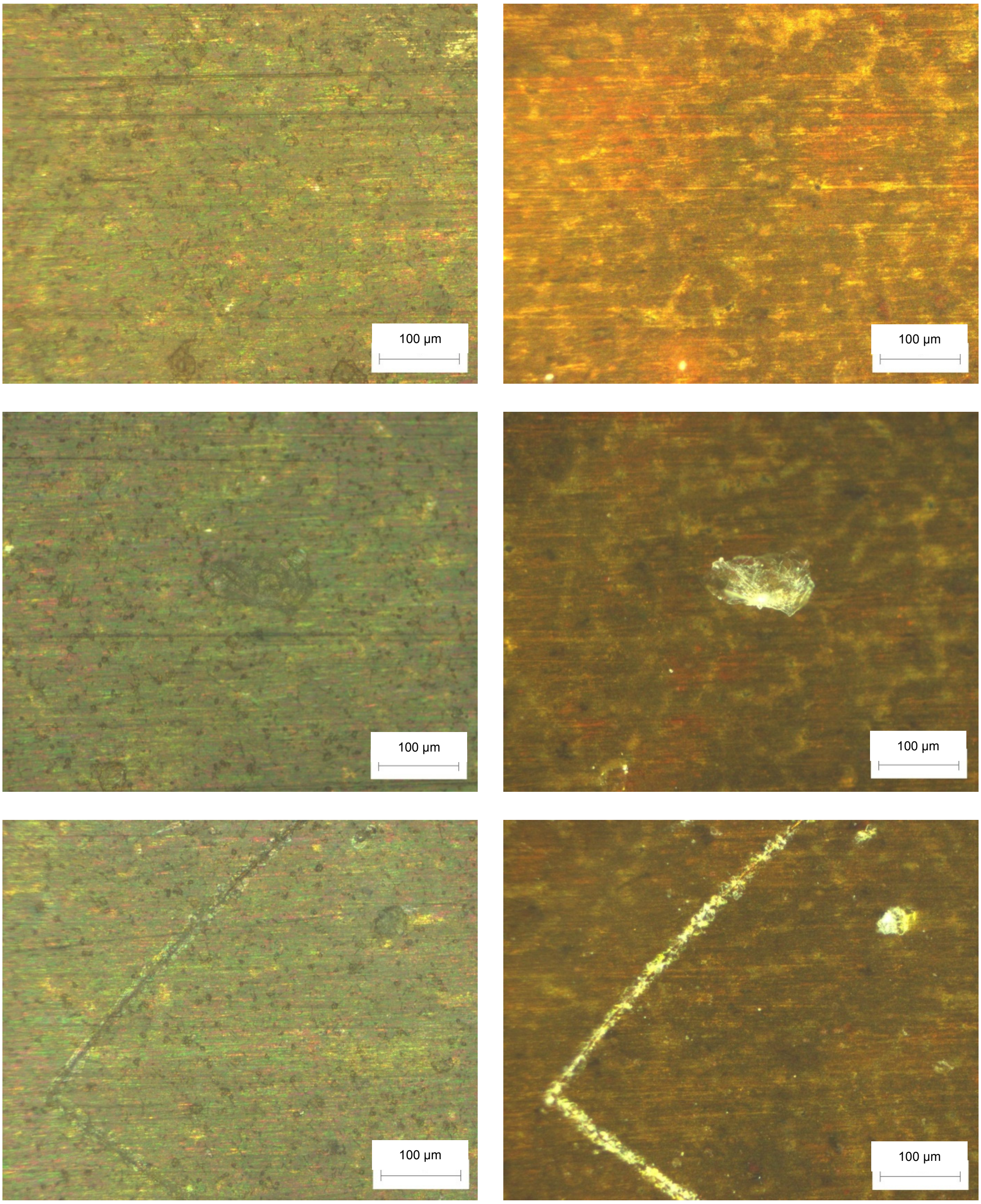

Fig. 2.15 - Optical microscopy images for A-P coupon. Three different sites (top to bottom) were observed as bright field (left) and reflected polarised light (right).

The details in Fig. 2.15 show probably some damaged areas (detachment or scratches) in the inhibited samples which appear as whitish areas in the polarised light images.

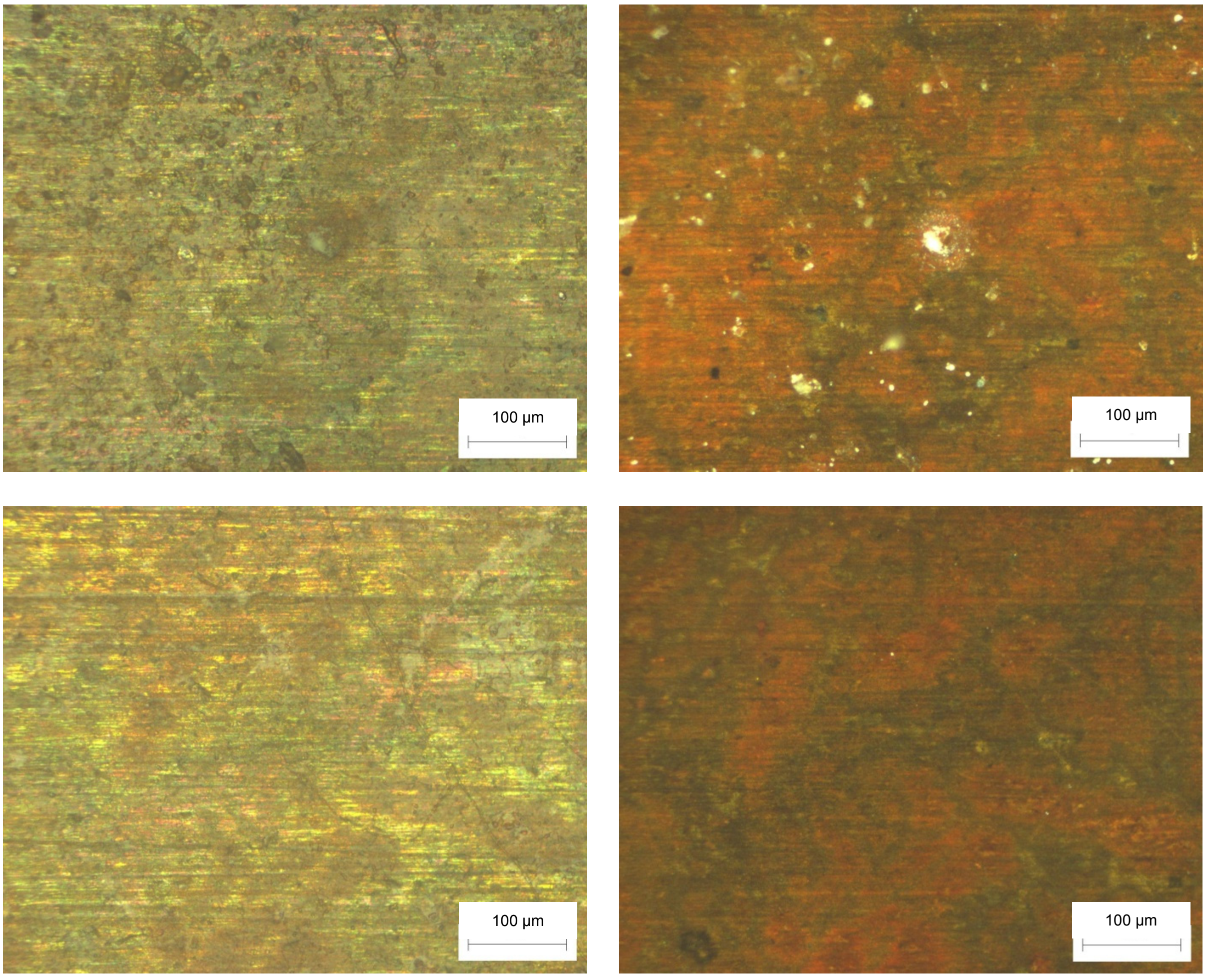

Fig. 2.16 - Optical microscopy images for A-PC coupon. Two different sites (top to bottom) were observed as bright field (left) and reflected polarised light (right).

Fig. 2.16 shows some spots (white ones in the polarised light image) which are not clearly attributable to the inhibitor film or to corrosion products, but it also shows a homogeneous area for the PropS-SH+CeO_2 nanoparticles inhibited coupon (A-PC).

More detailed investigation was carried out on corroded surfaces by SEM-EDS and micro-Raman spectroscopy, with the purpose to observe differences in the chemical composition and morphology of the surfaces of the coupons when inhibitor is applied and exposed to artificial acid rain. The main results are shown below as comparisons.

Firstly, it is interesting to analyse how the microstructure of bare bronze changes after 15 days of ageing, which is shown in Fig. 2.17.

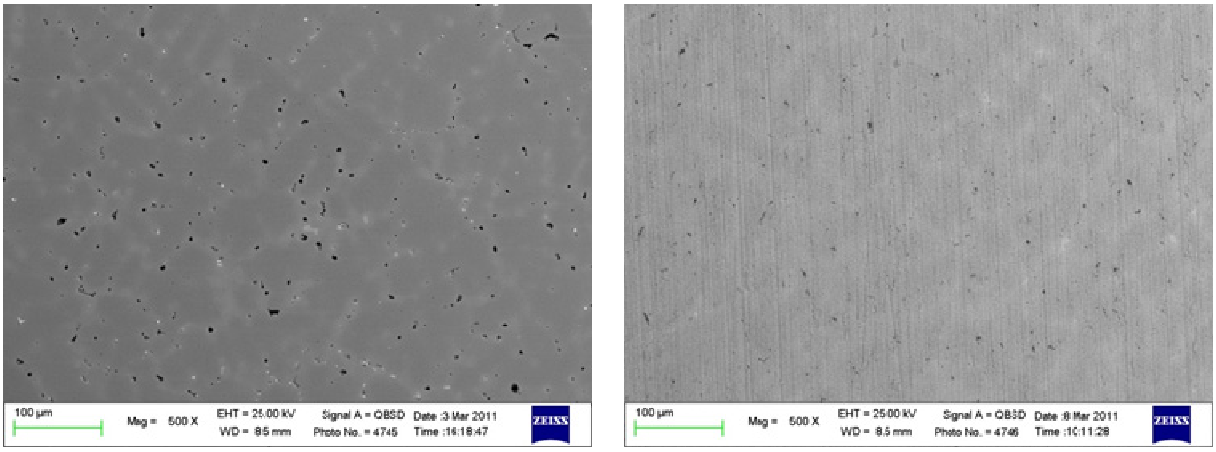

Fig. 2.17 - Comparison of bare bronze microstructure before (left) and after (right) ageing cycle

After ageing, the surface is widely covered by a thin layer of corrosion products, being the polishing marks and micro-structural features (coring) still visible. Concerning the chemical composition, results are shown in Table 2.8.

Table 2.8 - EDS results for bare bronze before and after ageing (pre-patination) cycle

Sample	C	O	Al	Cl	Cu	Zn	Sn	Sb	Pb
Bare bronze					91.9	2.9	2.4	0.8	1.0
Aged bronze	3.3	8.3	0.3	0.1	82.7	1.6	2.7	0.7	0.4

EDS results for aged bronze show the presence of elements due to the formation of corrosion products such as C, O and Cl (not present in the bare bronze) and a relative enrichment in Sn content (due to the decrease of all the other alloying elements). This result is very interesting, because it demonstrates that the ageing (pre-patination) cycle is able to reproduce a specific feature which identifies real patinated surfaces, i.e. the relative Sn enrichment (already observed also both when analysing scraped corrosion products (see 1.3.3.2) and on the basis of portable XRF measurements on the Omo statue (see 1.3.4, Fig. 1.22)). Therefore, the pre-patination carried out by wet & dry test in acid rain produced aged bronze specimens which are representative of the real support for bronze inhibitors.

As for corrosion products, Raman spectra shown in Fig. 2.18 reveal mainly the presence of cuprite and nantokite.

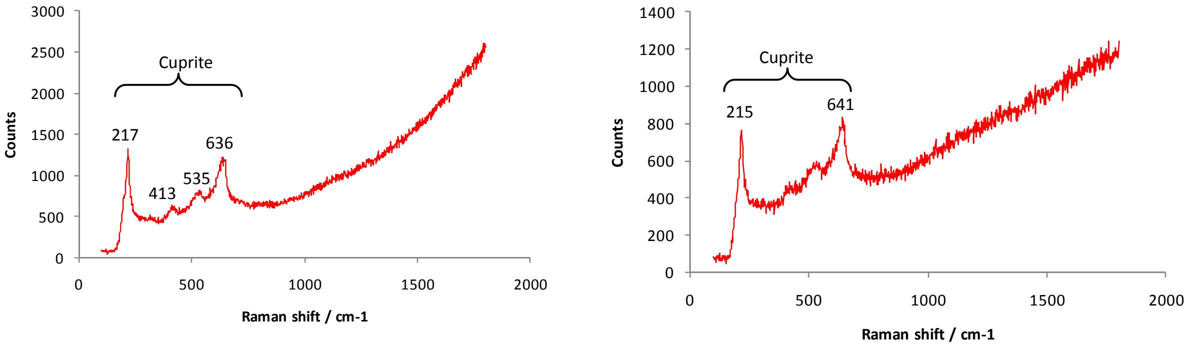

Fig. 2.18 - Raman spectra for two sites on the aged bronze surface

Subsequently, when PropS-SH was applied on NA-P coupon, it was possible to analyse how this silane-based inhibitor attaches to the bare bronze surface. This can be observed in Fig. 2.19.

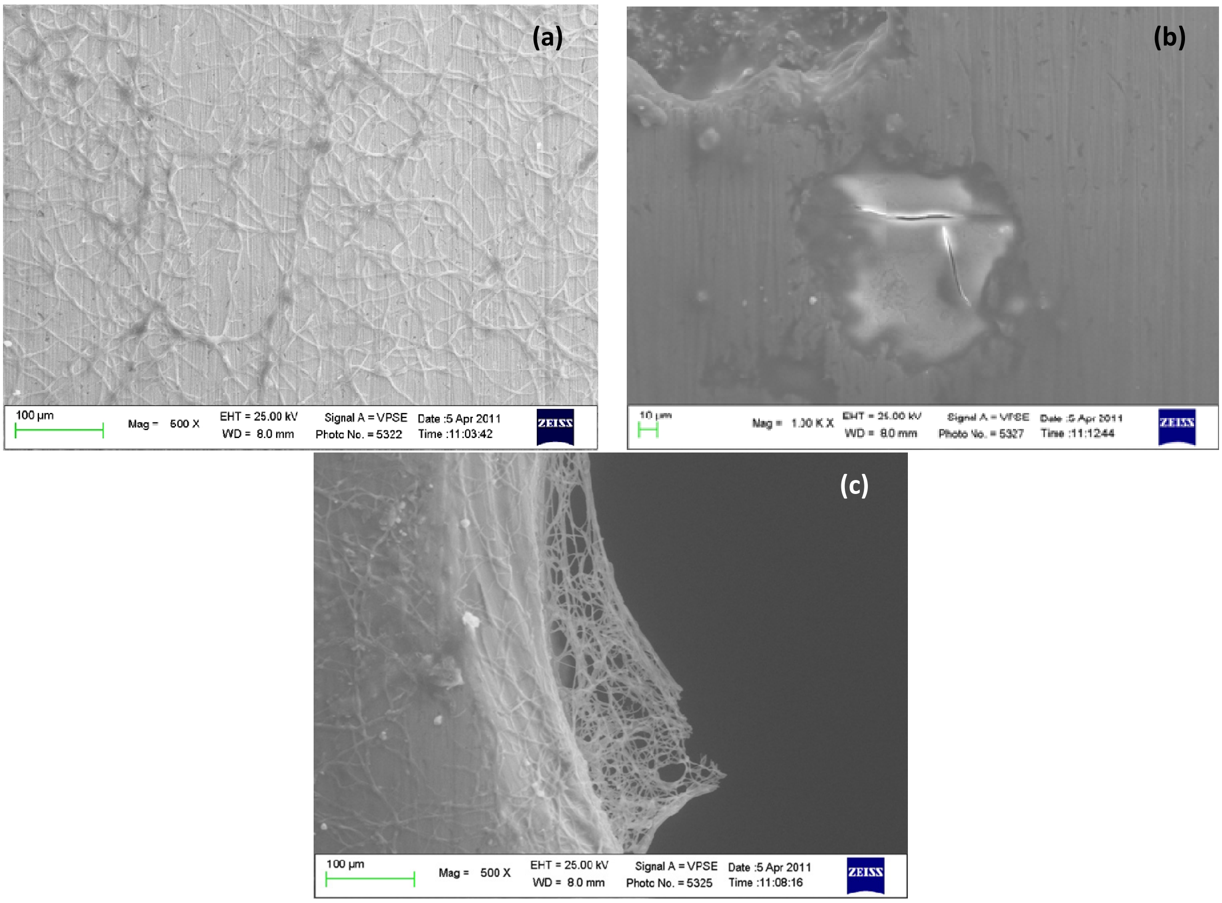

Fig. 2.19 - Application of inhibitor on bare bronze: Network on the inhibited surface (a), bubble in the inhibiting film (b), morphology of the inhibiting film in the area of the suspension hole on the metal coupon (c).

Based on Fig. 2.19 (a,c), the inhibitor film can be described as forming a cross-linked network, like a spider web, on the bare bronze surface. The network morphology is particularly evident in correspondence with suspension hole where it develops out of the metal surface (Fig. 2.19 c). However, observing at higher magnification, it may be observed that the film is not free of defects such as bubbles (Fig. 2.19 b).

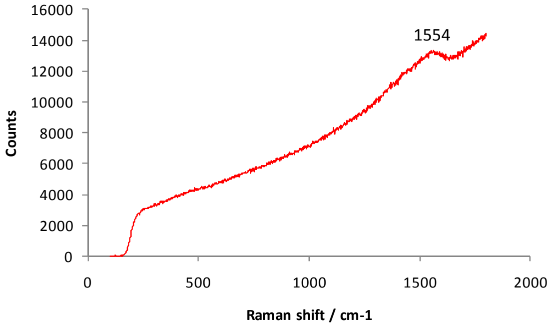

Fig. 2.20: Raman spectrum of inhibited bare bronze

Regarding corrosion products, Raman spectrum in Fig. 2.20 shows strong fluorescence due to the presence of organic compounds with bands related to the presence of hydrolysed silane (1400 – 1600 cm^{-1}) [46, 66].

The area of the indentation marks (shown in Fig. 2.1) was analysed for NA-P coupon at different times: Before applying inhibitor, after applying inhibitor and after 15 days of ageing cycle. SEM images can be seen in Fig. 2.21.

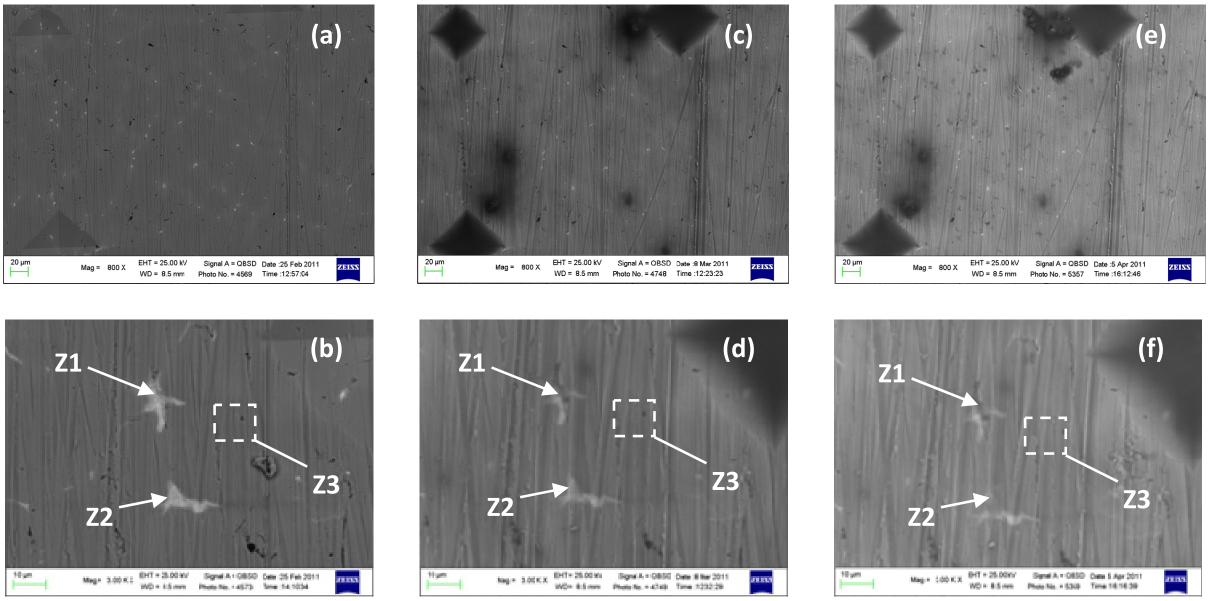

Fig. 2.21 - Comparison of bare bronze (NA-P coupon) at different times: Before applying inhibitor (a,b), after applying inhibitor (c,d) and after 15 days of ageing cycle (e,f)

Low magnification images (Fig. 2.21 a, c, e) show that polishing lines are more evident when PropS-SH is applied. Likewise, indentation marks become darker as a consequence of inhibitor deposition into them. In relation to chemical composition, results are summarized in Table 2.9.

Table 2.9 - Comparison of EDS results for bare bronze, just after inhibition, and after ageing (pre-patination) cycle. Points Z1, Z2 and area Z3 are identified in Fig. 2.21 (b, d, f).

	Sample	**C**	**O**	**Si**	**S**	**Cl**	**Cu**	**Zn**	**Sn**	**Pb**
Z1	Bare bronze	15.0	14.8	0.5	1.1	0.2	22.0		3.4	43.2
	Inhibited bare bronze	16.9	15.4	7.7	6.8		34.1		1.2	18.1
	Inhibited and aged bronze	19.5	18.5	6.9	6.7		26.8		0.6	21.0
Z2	Bare bronze	11.1	8.9	0.2	0.3	0.9	34.6		1.6	42.8
	Inhibited bare bronze	16.8	14.4	6.6	5.9	0.5	31.0	1.1		23.7
	Inhibited and aged bronze	19.4	16.8	5.8	5.5	1.2	26.8	0.2	0.9	23.4
Z3	Bare bronze	3.6	0.9		0.1	0.1	91.4	2.6	1.1	0.2
	Inhibited bare bronze	17.6	11.8	7.1	4.9		55.8	1.5	1.3	
	Inhibited and aged bronze	15.9	13.6	7.4	5.4		55.8	1.1	0.9	

On the basis of Table 2.9, Z1 and Z2 can be considered as Pb-rich globules, while Z3 corresponds to the Cu-rich matrix.

As expected, Si increases after inhibition because of the application of a silane-based inhibitor and it does not change significantly after the ageing cycle (it decreases slightly in Pb globules). Concerning C, it also increases because of the PropS-SH application, however, after ageing, it increases only in the Pb-rich globules but not in the Cu-rich matrix. This is probably related to the formation of Pb carbonates.

Concerning O, it increases after ageing in all cases, but its amount is higher on Pb-rich globules than in the Cu-rich matrix due to localised corrosion of Pb, as already observed for C.

A slightly higher amount of S seems to be present in correspondence with Pb globules than in the Cu-rich matrix.

In Z3 (Cu-rich matrix), Zn and Sn generally decrease after ageing.

About Pb (globules in Z1 and Z2), it can be seen that its concentration approximately decreases by half when PropS-SH is applied. No significant variations are observed after ageing.

Another interesting comparison is that for the non-inhibited and the inhibited bronzes, both after ageing. This is shown in Fig. 2.22.

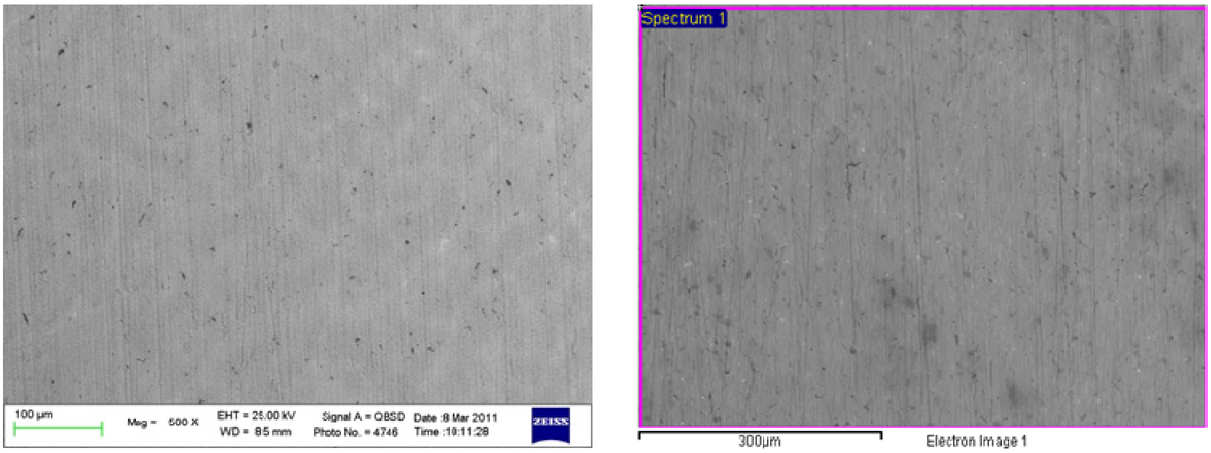

Fig. 2.22 - Comparison between non-inhibited (left) and inhibited (right) bronzes, both after ageing.

In the case of the inhibited coupon, the dendritic microstructure is less evident because the surface is less corroded.

Table 2.10 - EDS results for non-inhibited and inhibited bronzes, both after ageing cycle

Sample	C	O	Al	Si	S	Cl	Cu	Zn	Sn	Sb	Pb
Bare bronze							91.9	2.9	2.4	0.8	1.0
NI aged bronze	3.3	8.3	0.3			0.1	82.7	1.6	2.7	0.7	0.4
Inhib. aged bronze	19.6	11.0		4.3	3.1		58.5	1.2	1.6	0.8	

*NI = non-inhibited

On the basis of EDS results shown in Table 2.10, after ageing (pre-patination) cycle, elements due to the formation of corrosion products such as Cl appear in the non-inhibited aged bronze but Cl is not detected in the inhibited aged surface.

Pb is also not detectable in the inhibited aged bronze. This might be due to either a different reactivity of Pb towards PropS-SH or to the preferential dissolution of this element.

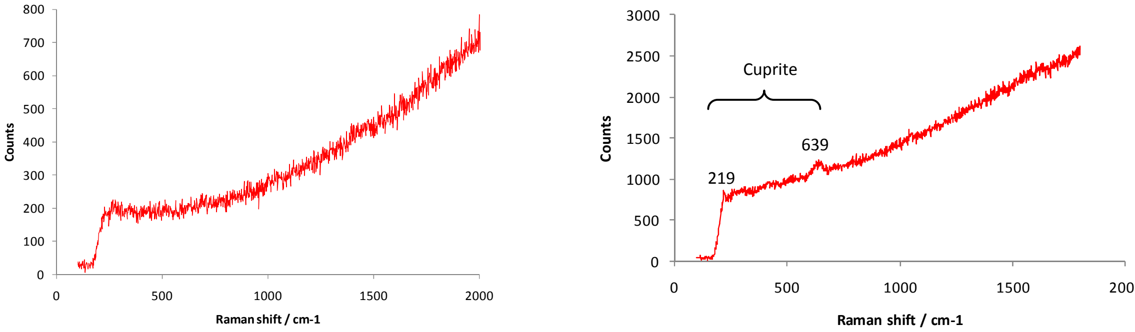

Fig. 2.23 - Raman spectra after ageing (pre-patination) cycle in two different sites on inhibited aged bronze.

Concerning corrosion products, Raman spectra for inhibited bronze in Fig. 2.23 show fluorescence due to the presence of organic compounds on the surface, however with lower intensities compared to the spectra before ageing the inhibited surface (Fig. 2.20). Moreover, traces of cuprite, formed as a consequence of ageing, were detected.

Hitherto, only changes due to the ageing cycle have been compared. In relation to the exposure cycle, firstly, a SEM image of the non-inhibited aged (pre-patinated) bronze after exposure cycle is shown in Fig. 2.24.

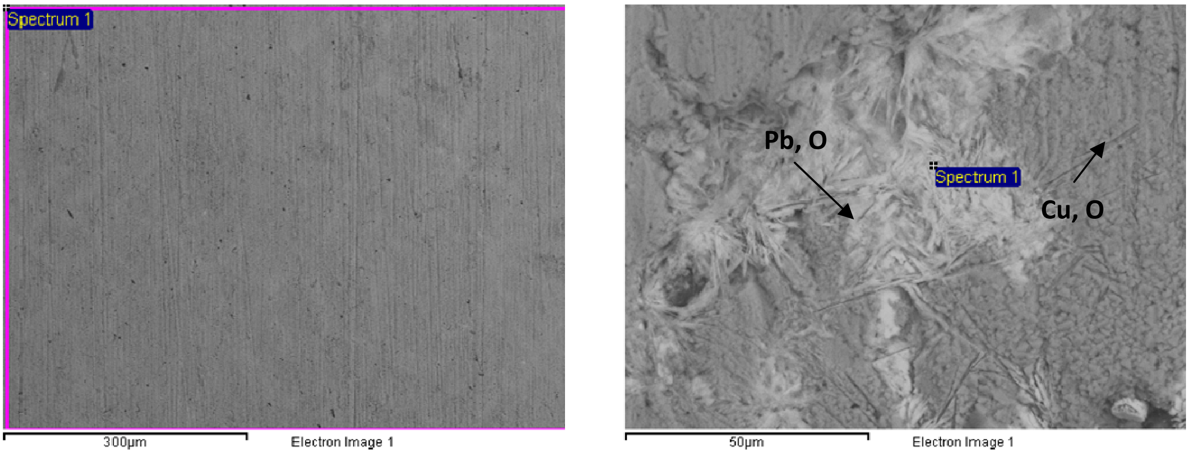

Fig. 2.24: Non-inhibited aged bronze (A-NI coupon): Surface after exposure cycle (left), detail at high magnification (right).

The surface after exposure cycle appears covered by a thin layer of corrosion products (Fig. 2.24 left). However, the polishing marks and micro-structural features (coring) are still visible but less distinguishable than after the ageing cycle (Fig. 2.17 right). The higher magnification detail in Fig. 2.24 right shows some Pb-rich localised corrosion products in the oxidised Cu-rich matrix.

Table 2.11 - EDS results for bare bronze, after ageing cycle and after exposure cycle (no inhibitor in any case)

Sample	C	O	Al	Cl	Cu	Zn	Sn	Sb	Pb
Bare bronze					91.9	2.9	2.4	0.8	1.0
Aged bronze	3.3	8.3	0.3	0.1	82.7	1.6	2.7	0.7	0.4
Exposed bronze		9.6			87.6		2.1		0.7

According to EDS results in Table 2.11, elements like C and Cl are not detected after the exposure cycle. Zn, which decreased after ageing cycle, is no more detectable after the exposure cycle. On the other hand, O shows a slight increase.

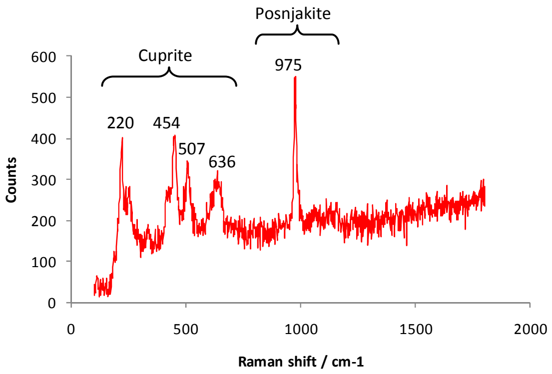

Fig. 2.25 - Raman spectrum of aged bronze after 15 days of exposure

Regarding corrosion products, these mainly consist of cuprite and posnjakite (Fig. 2.25).

Now, results about the comparison between inhibitors, with and without ceria nanoparticles, on the coupons after exposure are reported. This is shown in SEM images of Fig. 2.26.

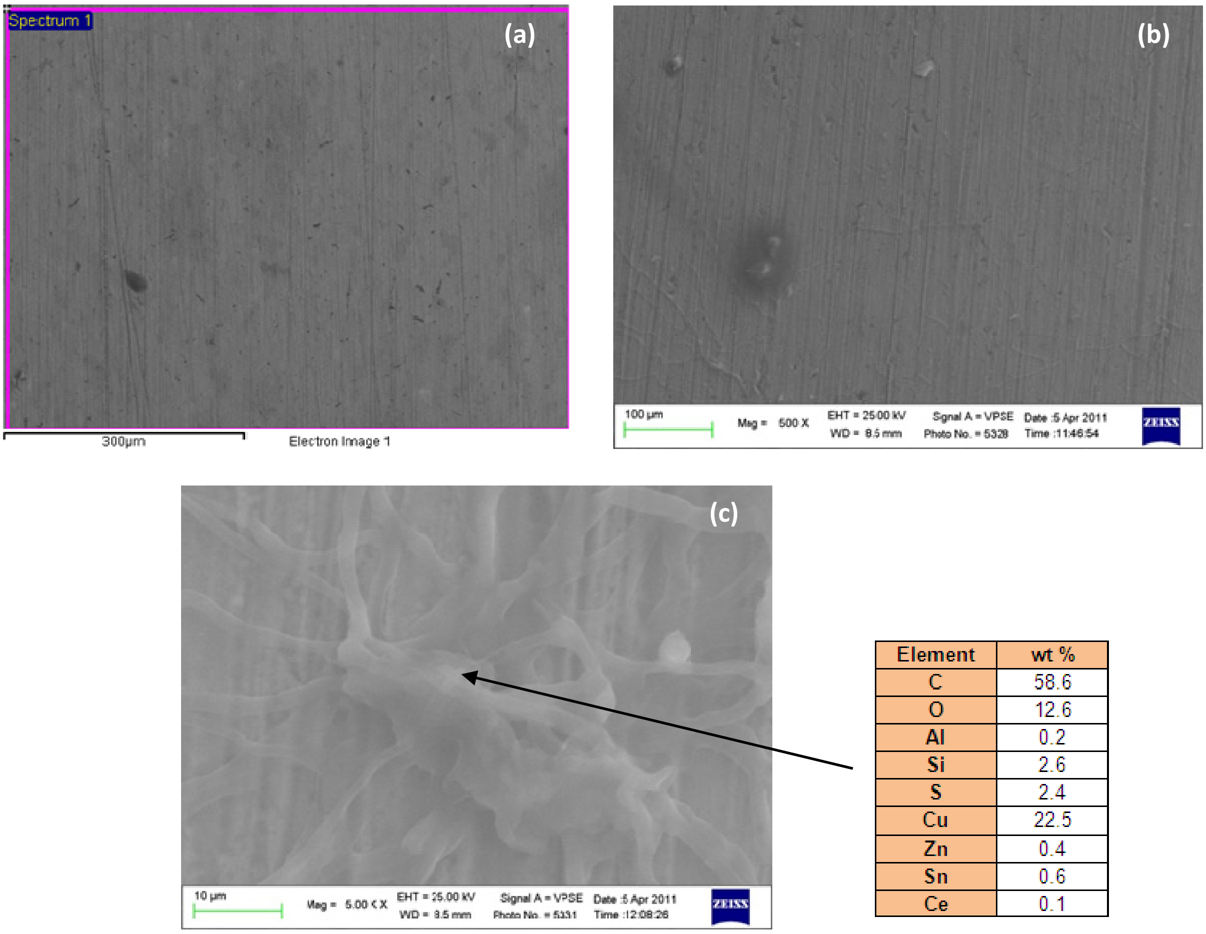

Element	wt %
C	58.6
O	12.6
Al	0.2
Si	2.6
S	2.4
Cu	22.5
Zn	0.4
Sn	0.6
Ce	0.1

Fig. 2.26 - Comparison of aged (pre-patinated) bronze surfaces after exposure: Inhibited with PropS-SH (a); inhibited with PropS-SH+CeO_2 nanoparticles at low magnification (b) and at high magnification showing the EDS results for a specific site where Ce is detected (c).

For the coupon inhibited with neat PropS-SH, the dendritic microstructure of the surface is still slightly visible while for the case of PropS-SH+CeO_2 nanoparticles it is not visible anymore, probably because of the formation of a thicker layer due to the nanoparticles. Chemical composition of these surfaces is shown in Table 2.12.

Table 2.12 - Aged and inhibited bronzes after exposure cycle

Sample	C	O	Al	Si	S	Cu	Zn	Sn	Sb	Pb	Ce
PropS-SH	17.5	14.0		4.5	3.4	59.0		1.6			
PropS-SH+CeO_2	20.1	14.5	0.3	5.7	4.6	51.6	0.9	1.4	0.8		0.2

C, Si and S, three elements present in the inhibitor formulation, are higher in the surface inhibited with ceria nanoparticles than in the one inhibited with neat PropS-SH. Also this could suggest that the inhibitor with ceria attaches to a larger extent to the pre-patinated bronze surface than neat PropS-SH does.

Again, Pb is not detectable on both inhibited surfaces as already observed when the inhibitor is applied on bare bronze and aged (Table 2.10). Ce is, as expected, found on the surface with ceria nanoparticles (see Fig. 2.28).

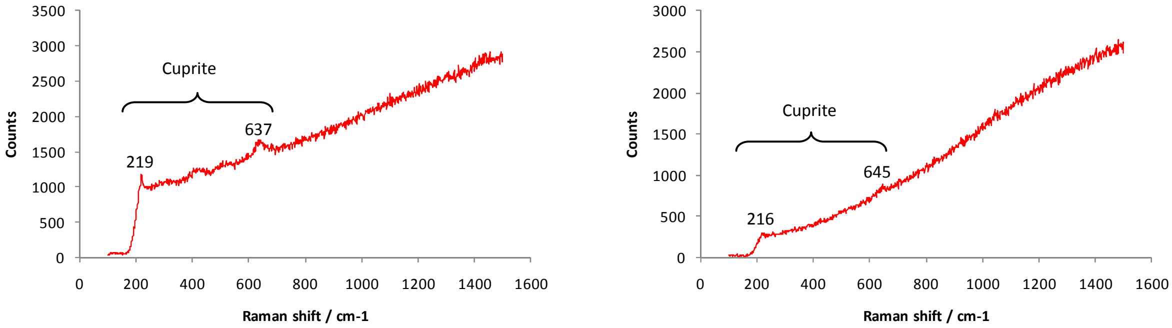

Fig. 2.27: Raman spectra of aged and inhibited bronzes after exposure cycle: With PropS-SH (left) and PropS-SH+CeO_2 nanoparticles (right)

Raman spectra shown in Fig. 2.27 reveal the presence of cuprite as corrosion product. Intensities show that cuprite is more abundant on the surface with neat PropS-SH than on the one with PropS-SH+CeO_2 nanoparticles.

2.3.5 Color measurement

This test was performed with the purpose to identify any variation in the appearance of the bronze coupons due to the application of the inhibitor, as well as any variation before and after the exposure cycle.

CIELAB color scale was used to make the measurements. At least 5 values (± standard deviation) on only one side of each coupon were measured and their L*, a* and b* parameters were averaged to obtain ΔE*. More information about these parameters can be seen in Appendix A.

During the measurements, yellow, green and dark spots on the coupons after the test were not considered to avoid statistical bias that could increase ΔE*. Results about differences in colour and gloss due to the application of the inhibitor are shown in Table 2.13.

Table 2.13 - Comparison of aesthetical parameters in the wet & dry test, differences due to the application of inhibitor on pre-patinated bronzes. The non-inhibited, pre-patinated bronze (A-NI) is taken as reference for comparison.

	ΔE*	**ΔGloss**
A-P	11 ± 1	4 ± 9
A-PC	10 ± 2	14 ± 9

According to Table 2.13, and taking into account that ΔE* ≥ 3 is considered a significant color difference in the field of cultural heritage [67], PropS-SH and PropS-SH+CeO_2 nanoparticles significantly change the color.

Likewise, the inhibitor increases the gloss of the bronze coupons but, in this case, PropS-SH+CeO_2 nanoparticles produces a considerably glossier surface than pure PropS-SH.

The high standard deviations for ΔGloss are due to the non-uniformity of the coupons' surface.

Results about differences in colour and gloss due to the exposure test are shown in Table 2.14.

Table 2.14 - Comparison of aesthetical parameters in the wet & dry test, differences between the values measured after and before the exposure cycle.

	ΔE*	**ΔGloss**
A-NI	3 ± 2	13 ± 10
NA-P	5 ± 2	-28 ± 7
A-P	2 ± 1	-13 ± 8
A-PC	3 ± 3	-50 ± 5

According to Table 2.14, as expected, the highest difference in color is for the non-aged coupon (NA-P) because of the lack of corrosion products at the beginning of the exposure test. Concerning the rest of the coupons, their color differences are similar and not remarkably significant.

Probably because the inhibited coupons showed a decrease in gloss (negative values) their surfaces are rougher after the exposure test and, as a consequence, exhibit less specular reflection, which is desirable in the case of bronze statues. PropS-SH+CeO_2 nanoparticles applied on pre-patinated surface shows a better performance in keeping a rougher surface than neat PropS-SH.

A-NI coupon shows a positive ΔGloss, which means that this coupon is glossier (probably smoother) after the exposure to the artificial acid rain solution.

2.4 Total immersion test: Results

2.4.1 Gravimetric measurements

In this case inhibitors were applied on bare bronze and the investigations evaluated the performance in different environments.

Coupons were weighted before and after the test. Results are shown in Table 2.15.

Table 2.15 - Mass variation in the development of total immersion test

Code	Sample	Original area (cm^2)	Mass after inhibition (g)[a]	Mass after 5 days (g)[a]
NI-NaCl	TI-0	45.51	76.6369	76.3663
P-NaCl	TI-1	12.30	17.7797	17.7796
P-AR	TI-2	13.46	19.6567	19.6566
PC-AR	TI-3	11.71	16.3132	16.3131
NI-AR	TI-4	11.50	16.2306	16.2290

[a] With an error ± 0.0001

Calculating the mass decrease for coupons immersed in NaCl and in artificial acid rain, graphs shown in Fig. 2.28 were obtained.

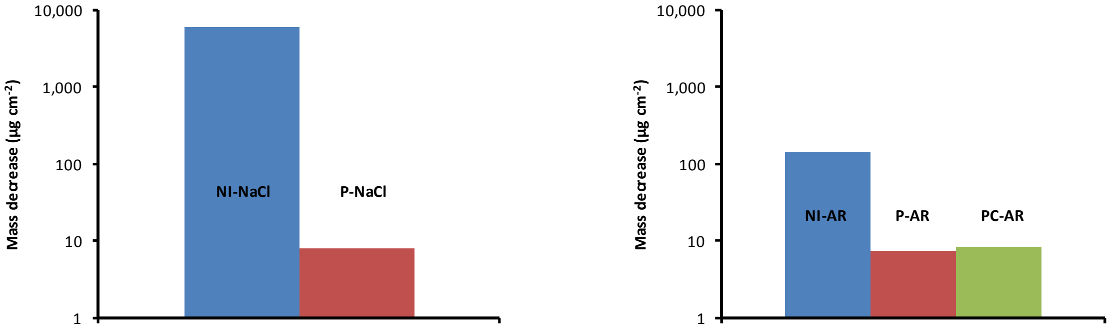

Fig. 2.28 - Mass decrease for bronze coupons immersed in NaCl solution (left) and in artificial acid rain (right). (logarithmic scale)

The mass decrease in NaCl solution is much higher than in acid rain in the case of bare bronze. As for inhibited bronzes, these show similar mass decrease in both solutions.

Furthermore, the mass decrease is three (in NaCl) and one (in acid rain) order of magnitude lower on the inhibited surface than on the non-inhibited one.

2.4.2 Ageing solutions

Elemental concentrations (in ppb) were measured for each one of the sampled solutions and normalised by the area of the respective coupon. Results are shown in Table 2.16.

Table 2.16 – Amount of metals released in ageing solutions after total immersion test

Code	**Applied inhibitor**	**Solution used for total immersion**	**Volume used for total immersion (mL)**	**Time of total immersion (d)**	**Cu (µg cm^{-2})**	**Zn (µg cm^{-2})**	**Pb (µg cm^{-2})**
NI-NaCl	Not inhibited	NaCl 3.5 wt%	600 ± 3.5	2	19.0	0.8	1.8
				5	50.5	1.6	4.6
P-NaCl	PropS-SH	NaCl 3.5 wt%	235 ± 2	1	1.9	0.6 [a]	---[b]
				5	6.9	0.6 [a]	---[b]
P-AR	PropS-SH	Acid rain 10x	235 ± 5	1	1.0	0.5 [a]	2.2
				5	7.4	0.5 [a]	2.8
PC-AR	PropS-SH + CeO_2 nanoparticles	Acid rain 10x	230 ± 5	1	0.7	0.6 [a]	0.2
				5	1.9	0.6 [a]	0.3
NI-AR	Not inhibited	Acid rain 10x	230 ± 5	1	165.9	9.8	30.4
				5	212.6	22.3	34.9

[a] Zinc was above the detection limit but below the quantification limit (QL = 60 ppb). For this reason, a value half the QL was considered.

[b] In this case, Pb was not detectable.

On the basis of the results in Table 2.16, graphs in Figs. 2.29, 2.30 and 2.31 were obtained.

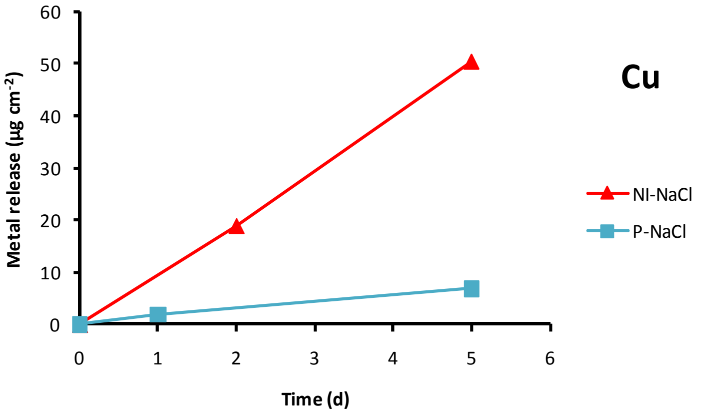

Fig. 2.29 - Cu release in NaCl solution in total immersion test, comparison between inhibited and non-inhibited coupons

It is observed in Fig. 2.29 that when immersing in NaCl 3.5 wt% solution, inhibitor is effective in reducing the release of Cu into the solution.

As for immersion in acid rain, Fig. 2.30 shows a clear difference between the non-inhibited coupon (NI-AR) compared to the two inhibited ones. The amount released for both metals (Cu, Pb) is significantly reduced when applying PropS-SH as neat and, even more, with ceria nanoparticles. This is shown in more detail in Fig. 2.31.

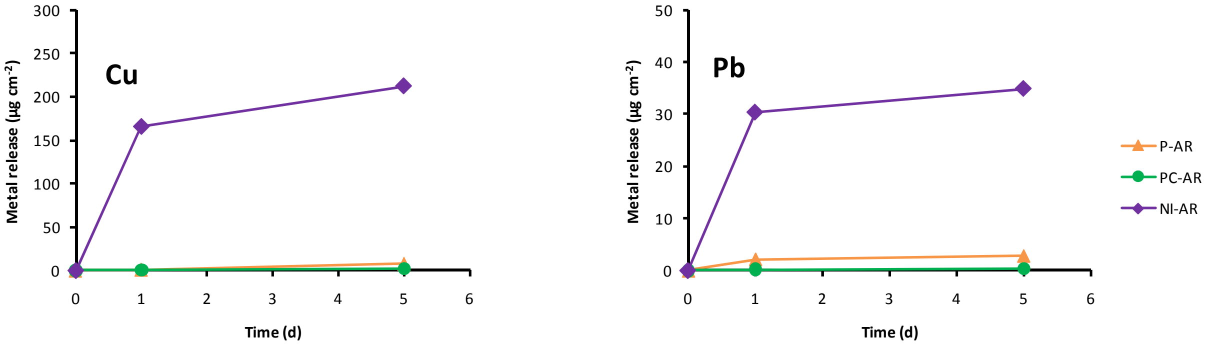

Fig. 2.30 - Metal release (Cu, Pb) in artificial acid rain solutions in total immersion test

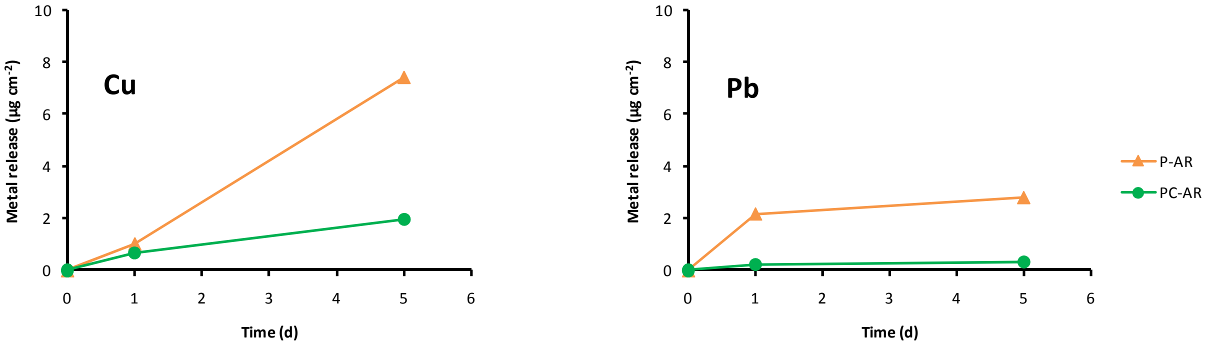

Fig. 2.31 - Metal release (Cu, Pb) in artificial acid rain solutions after total immersion test (detail from Fig. 2.30).

In Fig. 2.31, it is possible to observe that PropS-SH+CeO_2 nanoparticles offers more corrosion protection in acid rain because it reduces more the release of both metals, Cu and Pb, in solution comparing with PropS-SH.

2.4.3 Inhibitor efficiency

It is calculated in the same way that for wet & dry test (see 2.3.3, Eq. 2.1), just taking into account that in this test there are two kinds of ageing solutions: NaCl 3.5 wt% and acid rain.

Table 2.17 - Inhibitor efficiencies (%) calculated in total immersion test (non-inhibited coupons, NI-NaCl and NI-AR, are taken as reference for the corresponding environment)

	Cu		Zn		Pb		Total	
	1d	**5d**	**1d**	**5d**	**1d**	**5d**	**1d**	**5d**
P-NaCl	90.0 [a]	86.3	25.0 [a]	62.5	---	---	---	---
P-AR	99.4	96.5	94.9	97.8	92.8	92.0	98.2	96.0
PC-AR	99.6	99.1	93.9	97.3	99.3	99.1	99.3	99.0

[a] This value was obtained taking the metal release into the solution after 1 day for P-NaCl and after 2 days for NI-NaCl

No values were calculated for Pb in NaCl because this element was not detected in the ageing solutions (Table 2.16). It is worth noticing that AR solution is more aggressive than NaCl towards Pb because of the presence of acetate and formate (Table 2.2).

On the basis of results in Table 2.17, PropS-SH proves to be efficient in both environments (NaCl solution and artificial acid rain solution). However, efficiency is lower in NaCl solution, especially for Zn.

In general, Cu and Pb show higher efficiencies compared to Zn.

In the case of acid rain, PropS-SH+CeO_2 nanoparticles has a higher efficiency compared to pure PropS-SH, especially in the case of Pb.

Inhibitor efficiencies are higher compared to wet & dry test, because alternate immersion is a more severe test than continuous immersion.

Moreover, with the purpose to evaluate the tendency towards preferential corrosion of Cu and Pb during the total immersion test in artificial acid rain, metal ratios were obtained and results are shown in the graphs in Fig. 2.32.

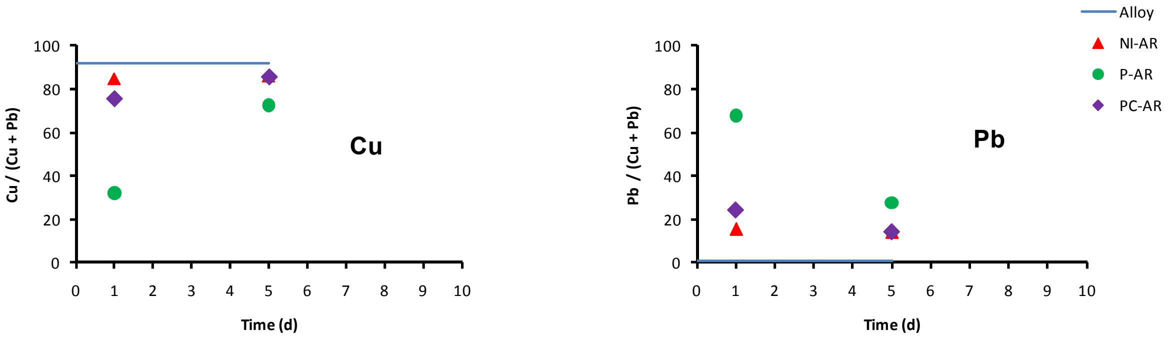

Fig. 2.32 - Comparison of corrosion behaviour for each metal respect to the alloy content, for the non-inhibited (NI-AR) and the inhibited (P-AR, PC-AR) bronzes in total immersion test (artificial acid rain).

On the basis of Fig. 2.32, contrarily to Cu, Pb shows preferential corrosion, remarkably in the case of PropS-SH inhibited sample (P-AR). Preferential corrosion of Pb is less evident in the case of non-inhibited sample (NI-AR) and for the one inhibited with PropS-SH+CeO_2 nanoparticles (PC-AR).

2.4.4 Characterisation of corroded surfaces

Low magnification optical images of corroded surfaces at the end of the total immersion test are compared in Fig. 2.33. Higher magnification details in bright field as well as in reflected polarised light are compared in Figs. 2.34 to 2.37.

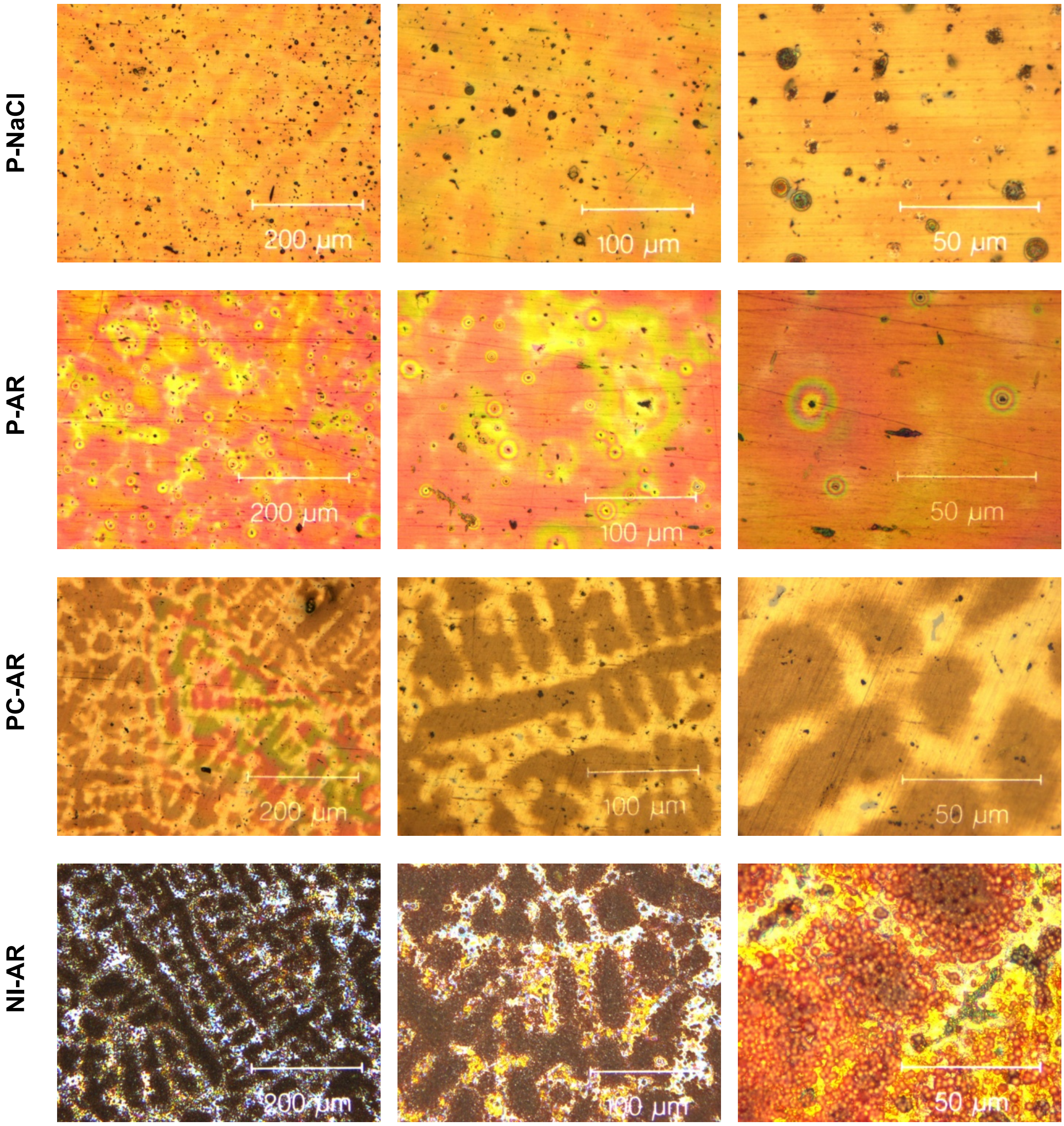

Fig. 2.33 - Bright filed images of corroded surfaces after total immersion test (5 days). Coupons P-NaCl, P-AR, PC-AR and NI-AR (top to bottom), with increasing magnification from left to right.

Fig. 2.33 shows that for P-NaCl and P-AR coupons (both inhibited with neat PropS-SH) it is possible to observe the dendritic microstructure and both exhibit a localised corrosion, probably involving the preferential dissolution of Pb (as already discussed for P-AR in commenting Fig. 2.32). As for NI-AR, the corrosion is really extensive, dendritic microstructure clearly defined and polishing lines are not visible anymore, while for PC-AR, the corrosion is generalized but, compared to NI-AR less extensive (dendritic microstructure defined but polishing lines still visible).

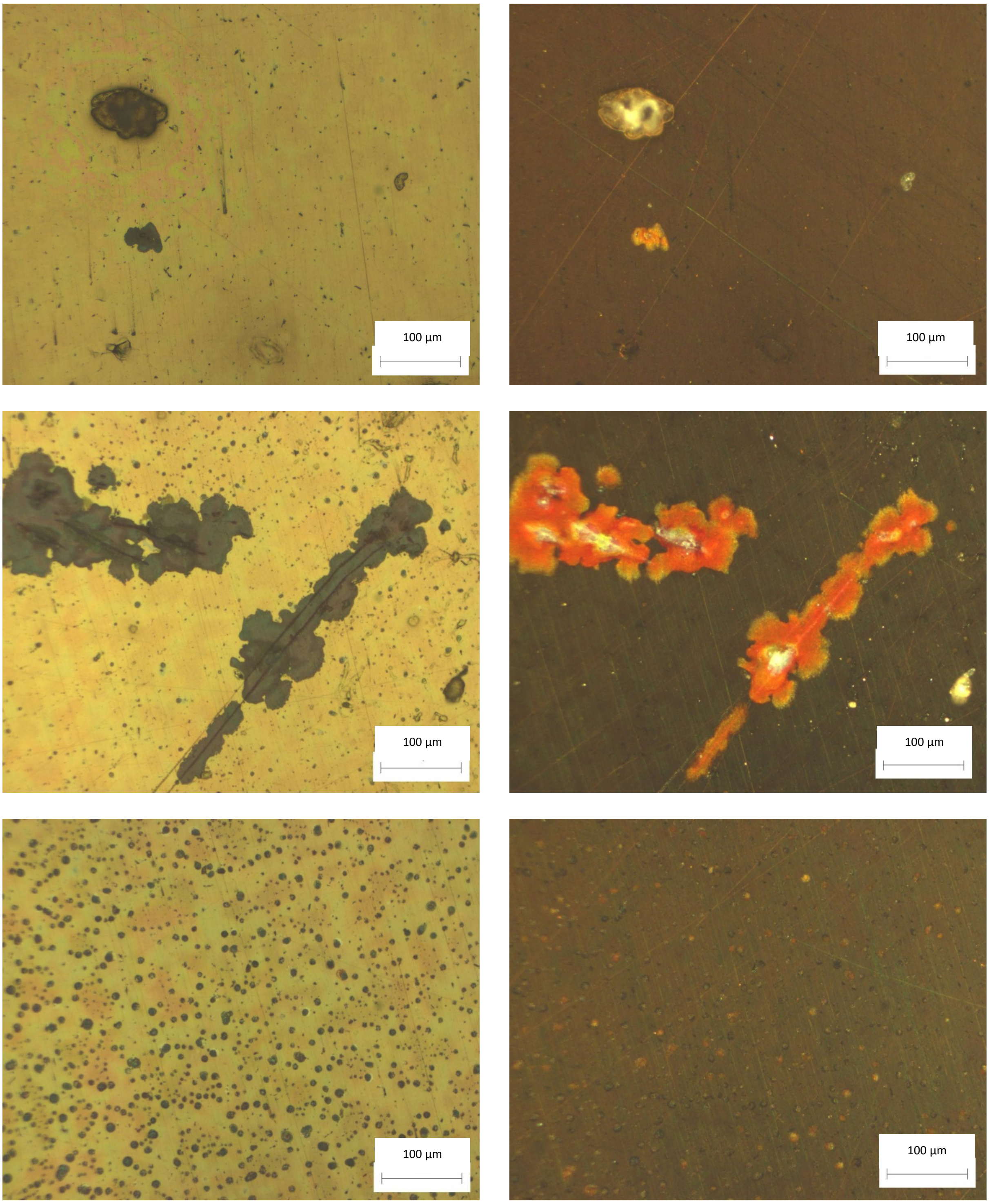

Fig. 2.34 - Optical microscopy images for P-NaCl coupon. Three different sites (top to bottom) were observed as bright field (left) and reflected polarised light (right).

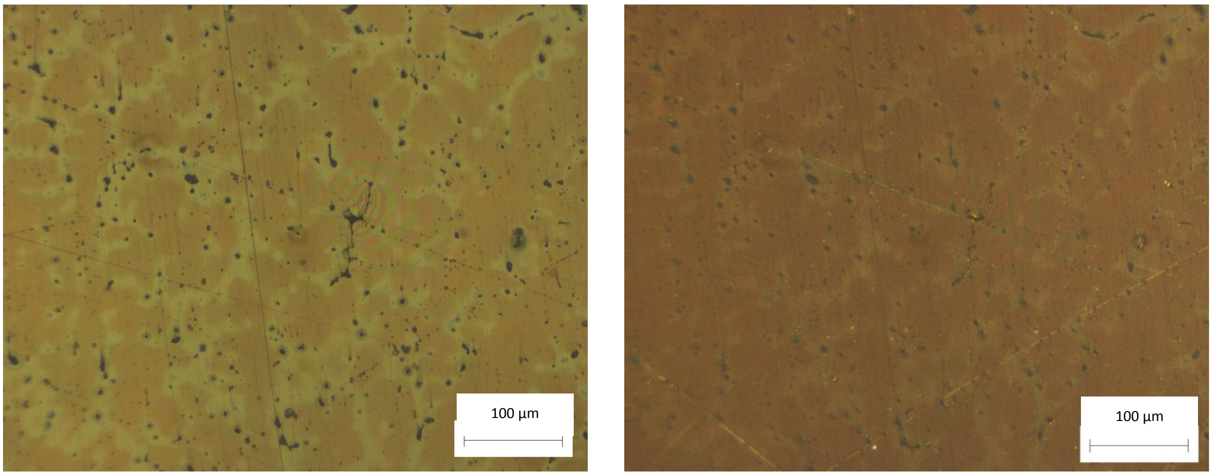

Fig. 2.35 - Optical microscopy images for P-AR coupon, observed as bright field (left) and reflected polarised light (right).

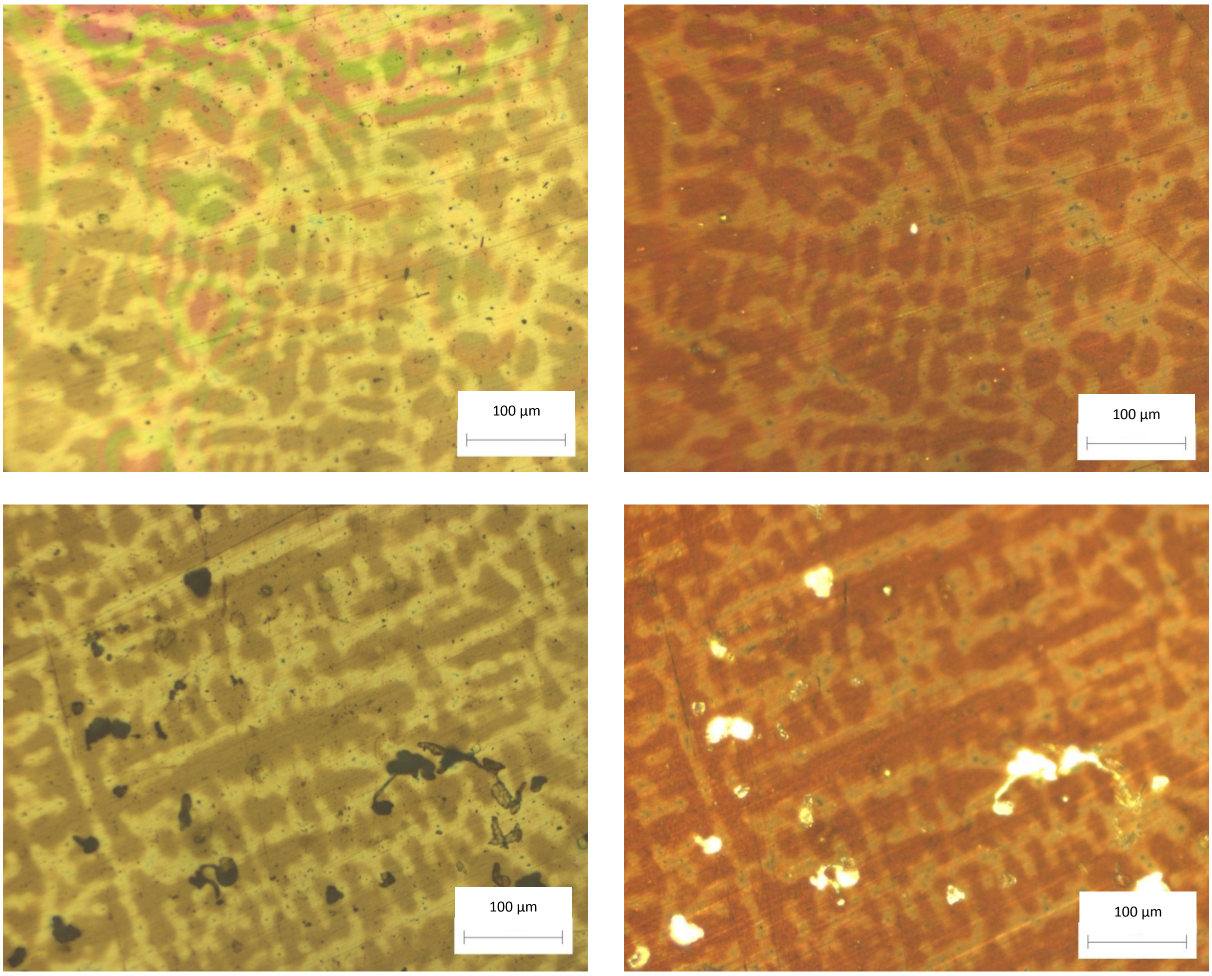

Fig. 2.36 - Optical microscopy images for PC-AR coupon. Two different sites (top to bottom) were observed as bright field (left) and reflected polarised light (right).

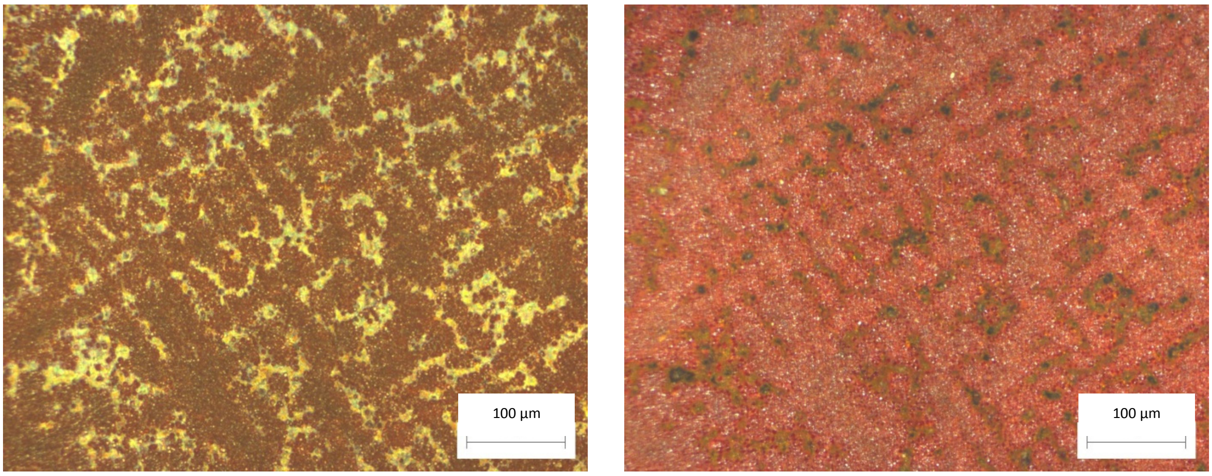

Fig. 2.37 - Optical microscopy images for NI-AR coupon, observed as bright field (left) and reflected polarised light (right).

Reflected polarised light images highlight the presence of corrosion products (reddish areas) in P-NaCl (Fig. 2.34, upper right) with a localised distribution, and in NI-AR (Fig. 2.37, right) with generalized diffusion on the exposed surface.

Deeper investigation was carried out on corroded surfaces by SEM-EDS and micro-Raman spectroscopy, with the purpose to observe differences in the chemical composition and morphology of the surfaces of the coupons when exposed to NaCl solution and artificial acid rain. The main results are shown below as comparisons.

2.4.4.1 Total immersion in NaCl

As a beginning, it is important to analyse how the microstructure of bare and inhibited bronzes change when exposed to NaCl solution, which is shown in Fig. 2.38.

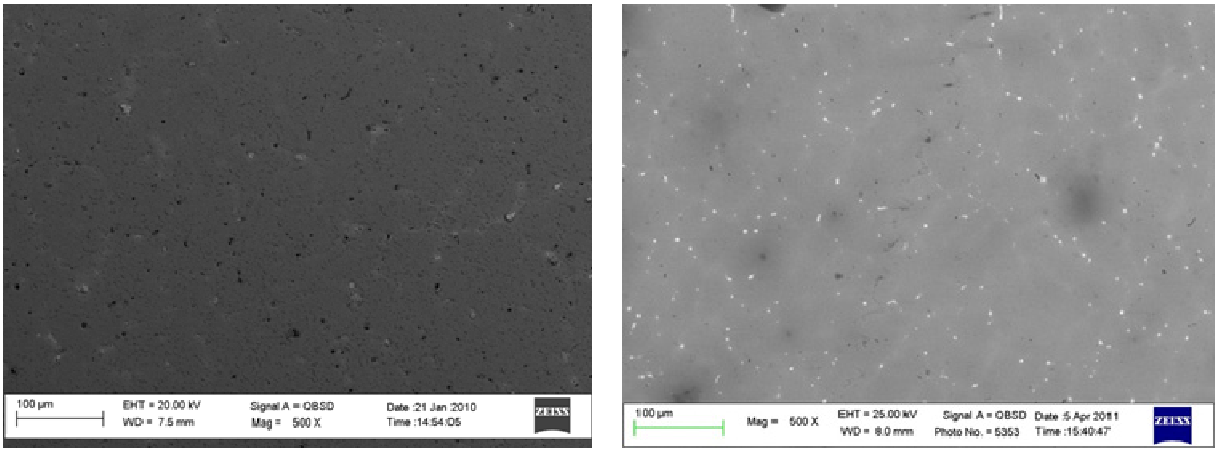

Fig. 2.38 - Comparison of bronze after 5 days of immersion in NaCl 3.5 wt% solution: Bare (NI-NaCl, left) and inhibited with PropS-SH (P-NaCl, right).

Bare bronze immersed in NaCl solution shows extensive corrosion: It is completely covered with corrosion products (hence the darker shade of grey), while for the inhibited coupon, it shows a clean surface with some clusters of inhibitor (darker areas in Fig. 2.38, right).

Table 2.18 – EDS results for bare bronze and just after inhibition, as well as non-inhibited (NI-NaCl) and inhibited (P-NaCl) bronzes immersed in NaCl solution during total immersion test

Sample	C	O	Si	S	Cl	Cu	Zn	Sn	Sb	Pb	Other
BI bare bronze						91.9	2.9	2.4	0.8	1.0	
BI inhib. bronze	17.8	12.3	5.8	4.0		57.1	1.4	1.6	0.8		
AI bare bronze		12.3			0.7	80.3	1.4	2.6	0.7	1.7	0.2
AI inhib. bronze	17.3	11.7	6.9	5.6		55.1	1.5	1.4	0.6		

AI = after immersion; BI = before immersion

Observing EDS results (shown in Table 2.18), bare bronze after immersion exhibits the presence of O, for the formation of cuprite, and Cl, as a consequence of the interaction with NaCl solution in which was immersed. A decrease in Zn is also evident.

Regarding the inhibited bronze, C, Si and S appear as a consequence of the application of the inhibitor. Once again, Pb cannot be detected when inhibitor is applied. After immersion, there is not a remarkable difference in chemical composition but, in contrast to the bare bronze, Cl is not present on the inhibited surface.

Raman analyses of the non-inhibited surface showed the presence of cuprite and localised corrosion products consisting of atacamite. The presence of chlorides is also demonstrated by SEM-EDS analysis (Fig. 2.39).

Only traces of cuprite and cassiterite were detected on the inhibited surface (Fig. 2.40).

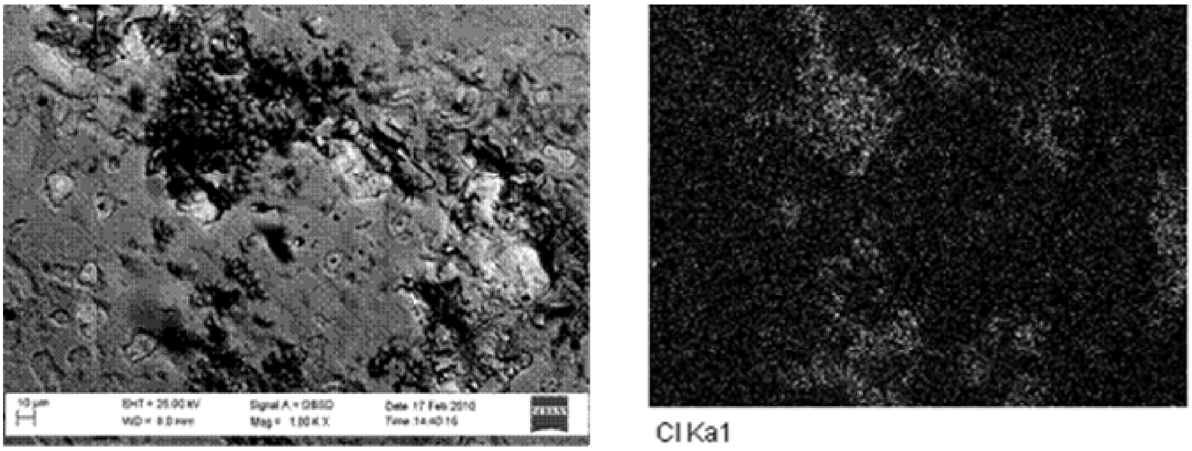

Fig. 2.39 - Localised corrosion products detected on bare bronze surface after total immersion test in NaCl solution (left) and X-ray map of Cl distribution (right).

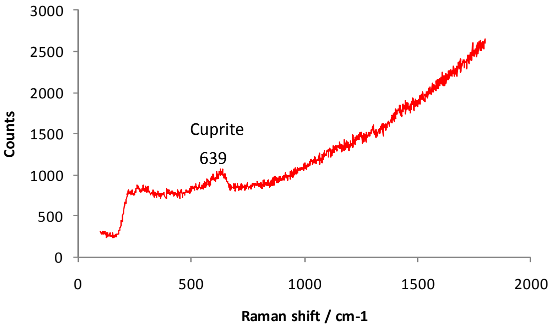

Fig. 2.40 - Raman spectrum of inhibited coupon (P-NaCl) after total immersion test

2.4.4.2 Total immersion in artificial acid rain

While characterizing the PC-AR coupon, it was possible to observe a cluster of ceria nanoparticles, which appears as a considerably large white spot in Fig. 2.41, left. EDS spectrum of this particular cluster is shown in Fig. 2.41, right. Signals for Ce can be seen between 4.7 and 5.5 keV.

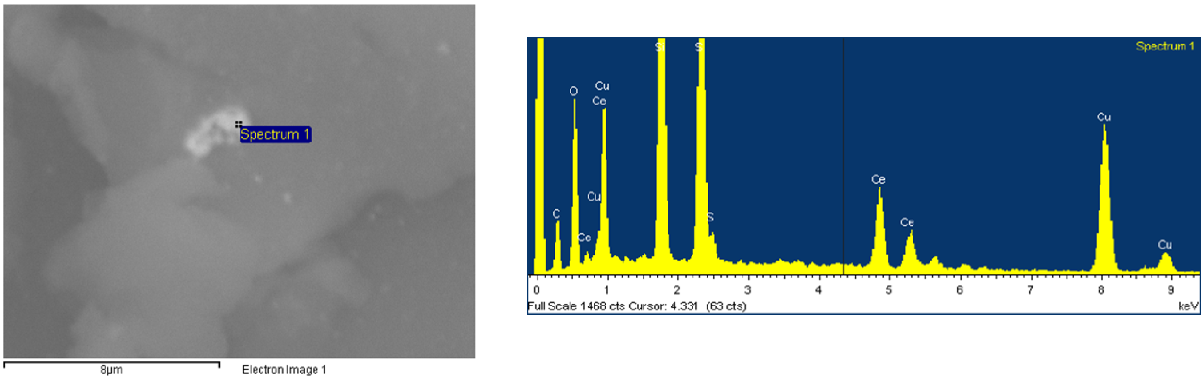

Fig. 2.41 - SEM image (left) and EDS spectrum (right) of a cluster of CeO_2 nanoparticles found on PC-AR coupon

In relation to coupons immersed in artificial acid rain solution, SEM images showing the morphology of corroded surfaces can be seen in Fig. 2.42.

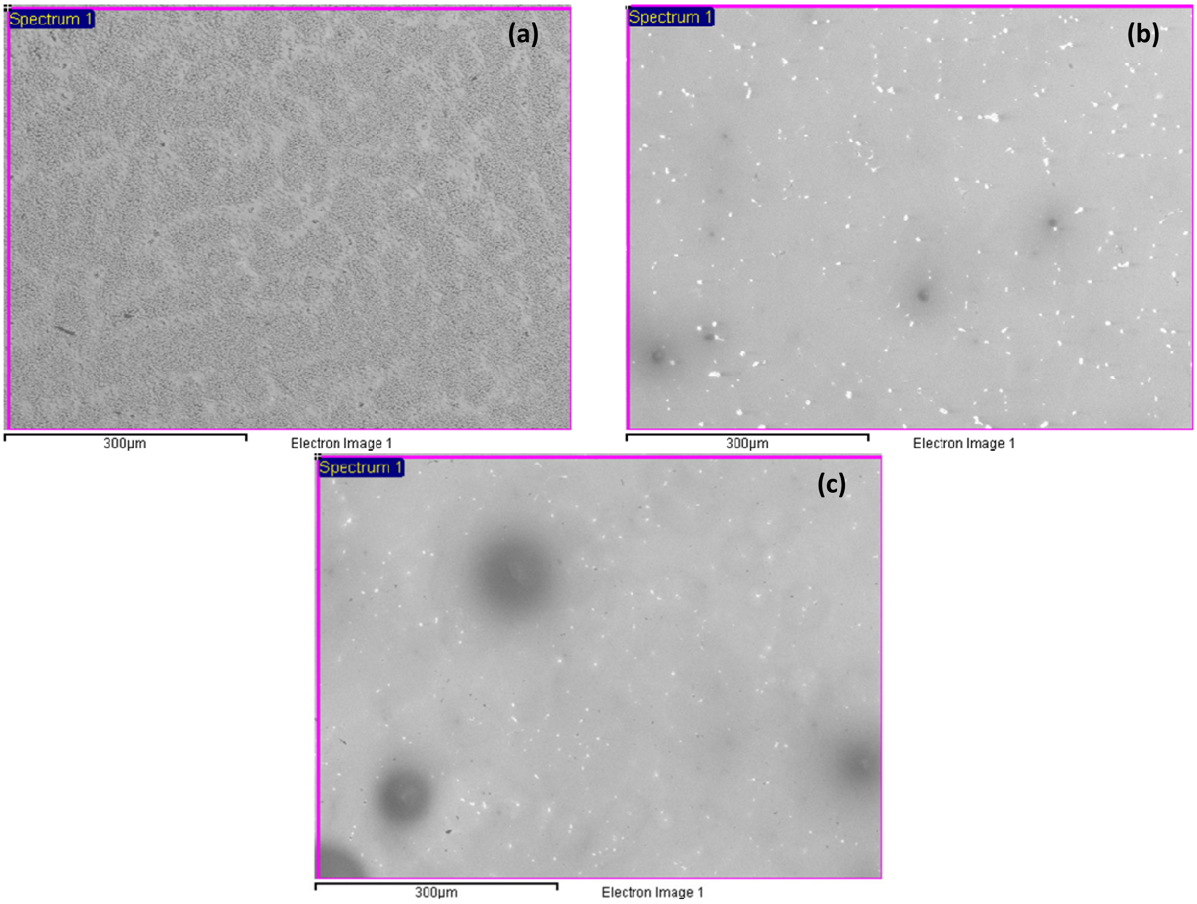

Fig. 2.42 - Comparison of bronzes after total immersion test in acid rain: Bare (a), inhibited with PropS-SH (b) and inhibited with PropS-SH+CeO_2 nanoparticles (c).

Bare bronze after total immersion is extensively corroded (Fig. 2.42 a). Raman analysis identified the presence of cuprite (Fig. 2.43, left).

The formation of corrosion products on the bronze surface, however, is delayed by the presence of inhibitor (Fig. 2.42, b and c). Inhibited coupons with and without ceria nanoparticles show a clean surface with some clusters of inhibitor; however, these clusters are larger in the case of PropS-SH+CeO_2 nanoparticles (Fig. 2.42 c) than for pure PropS-SH, probably due to increased thickness of the inhibiting film with CeO_2. As for corrosion products, cuprite with less intense signals than for the non-inhibited sample was identified on P-AR surface (Fig. 2.43, right). Just strong fluorescence was observed in the case of PC-AR, which again suggests that probably the inhibitor film is thicker for this coupon and, therefore, more protective.

Table 2.19 - EDS results for bare bronze (NI-AR) before and after total immersion in artificial acid rain, as well as for inhibited bronzes (P-AR, PC-AR) after immersion.

Sample	C	O	Si	S	Cl	Cu	Zn	Sn	Sb	Pb
BI bare bronze						91.9	2.9	2.4	0.8	1.0
AI bare bronze	2.0	16.8		1.7	0.3	76.7		2.5	0.8	1.0
PropS-SH AI bronze	16.8	11.9	7.0	5.4		55.9	1.4	1.5	0.5	
PropS-SH+CeO_2 AI bronze	18.5	11.3	6.7	5.0		55.9	1.4	1.2		

AI = after immersion; BI = before immersion

On the basis of EDS results in Table 2.19, concerning bare bronze, C, O, S and Cl appear on the coupon’s surface after immersion due to the formation of corrosion products, while Zn is not present anymore. Pb is again not detectable for inhibited coupons.

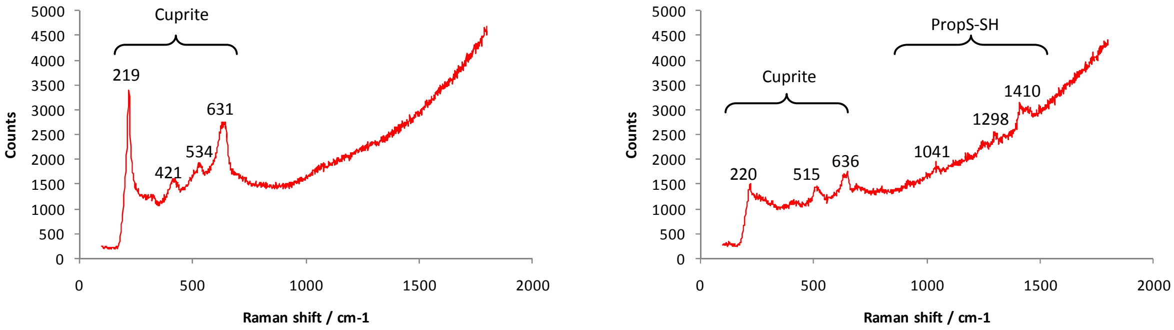

Fig. 2.43 - Raman spectra of non-inhibited bronze (NI-AR, left) and inhibited with PropS-SH (P-AR, right) after total immersion in artificial acid rain.

2.4.4.3 Total immersion NaCl vs acid rain

Finally, a comparison between PropS-SH inhibited coupons tested in different environments (NaCl and acid rain) was performed, as it can be seen in Fig. 2.44.

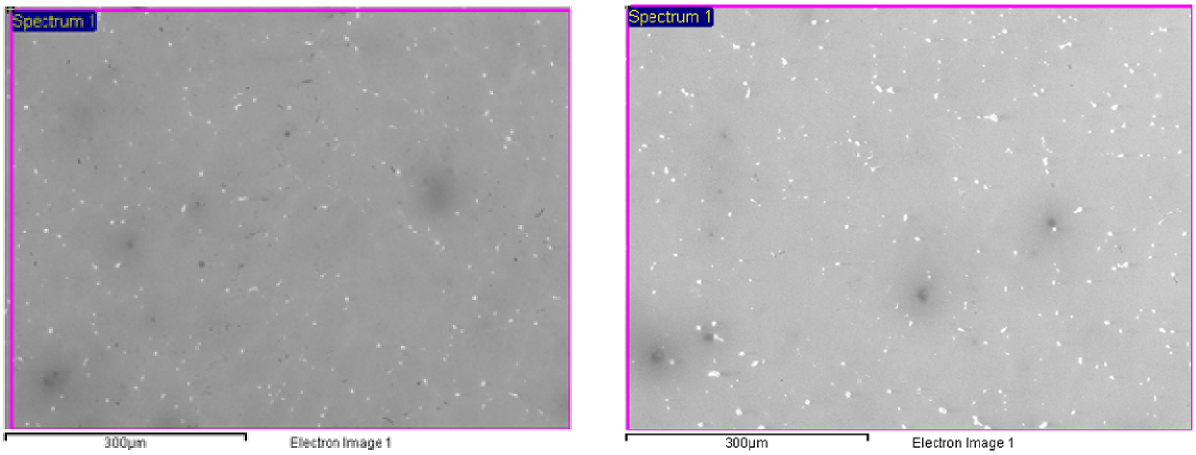

Fig. 2.44 - Comparison between PropS-SH inhibited bronzes after immersion in NaCl 3.5 wt% solution (left) and in artificial acid rain (right)

SEM images reveal that there is not a remarkable difference between bronze surfaces in both environments, as already observed when comparing gravimetric measurements (see 2.4.1), and confirmed by the EDS results in Table 2.20.

Table 2.20 - EDS results for inhibited bronzes with PropS-SH after total immersion test in different environments: NaCl and artificial acid rain.

Sample	C	O	Si	S	Cu	Zn	Sn	Sb
PropS-SH in NaCl	17.3	11.7	6.9	5.6	55.1	1.5	1.4	0.6
PropS-SH in AR	16.8	11.9	7.0	5.4	55.9	1.4	1.5	0.5

2.5 Accelerated corrosion tests: Concluding remarks

The following conclusions can be drawn from the results of both wet & dry (alternated) and total immersion (continuous) tests, carried out on a quaternary bronze alloy (Cu-Zn-Sn-Pb) in order to compare the performance of silane-based inhibitors. It is worth noting that, in this work, the inhibitor performance was evaluated not only on bare bronze (which is not representative of actual application conditions in the field of conservation) but also on pre-patinated bronze (as routinely done in conservation interventions).

1. The comparison of the corrosion behaviour between inhibited and non-inhibited bare bronze by wet & dry test shows that the 3-mercapto-propyl-trimethoxy-silane (PropS-SH) is effective in protecting the bronze, because it decreased both the mass variation and the metal release, and limited the formation of corrosion products on the exposed surface with respect to the non-inhibited surface.

2. The pre-patination procedure, carried out by the wet & dry ageing device, produced a layer of corrosion products consisting of cuprite and traces of chloride-based Cu compounds. This ageing (pre-patination) cycle was able to reproduce the relative Sn enrichment that actually happens in real patinated surfaces, making the bronze specimens representative of the real support for bronze inhibitors.

3. Also in the case of pre-patinated bronze, the application of the inhibitors (both PropS-SH and ProS-SH additivated with CeO_2 nanoparticles) led to a decrease of the mass variation and the metal release, and limited the formation of corrosion products on the exposed surface with respect to the non-inhibited surface.

4. The comparison of results obtained after the application of inhibitors on bare bronze and on pre-patinated bronze showed a higher inhibition efficiency for the silane-based inhibitors applied on pre-patinated bronzes.

5. In general, PropS-SH additivated with CeO_2 nanoparticles performed better (namely in terms of inhibition efficiency) than PropS-SH as neat both in wet & dry and total immersion tests.

6. As for the different environments taken into account for total immersion test, higher inhibition efficiencies were generally observed in artificial acid rain than in NaCl.

Further work is needed so as to understand how CeO_2 nanoparticles influence the protective efficiency of PropS-SH. In addition, the interactions between PropS-SH and the alloying elements (particularly Pb, which undergoes preferential corrosion) need to be thoroughly investigated.

Conclusions

The following conclusions can be drawn from both field studies on the Bottego monument and laboratory testing (accelerated ageing by wet & dry and total immersion):

1. The investigations on the Bottego monument confirmed the differentiation of the corrosion products as a function of the exposure geometry, already observed in previous works, further highlighting the need to take into account the different surface features when selecting conservation procedures such as the application of inhibitors (i.e. the relative Sn enrichment in unsheltered areas requires inhibitors which effectively interact not only with Cu but also with Sn).

2. The ageing (pre-patination) cycle on coupons was able to reproduce the relative Sn enrichment that actually happens in real patinated surfaces, making the bronze specimens representative of the real support for bronze inhibitors.

3. The non-toxic silane-based inhibitors display a good protective efficiency towards pre-patinated surfaces, differently from other widely used inhibitors such as benzotriazole (BTA) and its derivatives (which are also toxic).

4. The 3-mercapto-propyl-trimethoxy-silane (PropS-SH) additivated with CeO_2 nanoparticles generally offered a better corrosion protection than PropS-SH as neat, probably due to the higher thickness and polymeric network cross-linking in the inhibiting film.

Acknowledgments

Dott. Davide Gasparotto (Soprintendenza per i Beni Storici e Artistici di Parma e Piacenza), Mr. Stefano Volta and Ms. Silvia Simeti (Archè Restauri) for the collaboration in the work on the Bottego monument.

Dott.ssa Simona Montalbani and Prof. Giuseppe Chiavari (Dip. Chimica “G. Ciamician”, Università di Bologna) for PyGC-MS analysis.

Dott. Iuri Boromei (for SEM-EDS, micro-Raman and metallographic analysis), Dott. Alberto Mucchi (for atomic absorption spectrophotometry) and Dott. Simone Bugani (for laboratory XRF measurements) at Facoltà di Chimica Industriale, Università di Bologna.

Dott. Francesco Ardizzone (Bruker Corporation) for XRF measurements before cleaning Omo statue, and Bruker Corporation for providing the handheld XRF spectrometer.

References

[1] P. Piccardo, B. Mille, L. Robbiola (2007). Tin and copper oxides in corroded archaeological bronzes. Corrosion of metallic heritage artefacts: Investigation, conservation and prediction for long-term behaviour, European Federation of Corrosion Publications, edited by P. Dillmann, G. Béranger, P. Piccardo and H. Matthiesen, CRC Press, No. 48, pp. 239 – 262.

[2] C. Chiavari, E. Bernardi, C. Martini, F. Passarini, F. Ospitali, L. Robbiola (2010). The atmospheric corrosion of quaternary bronzes: The action of stagnant rain water. Corrosion Science, Vol. 52, pp. 3002 – 3010.

[3] E. Bernardi, C. Chiavari, B. Lenza, C. Martini, L. Morselli, F. Ospitali, L. Robbiola (2009). The atmospheric corrosion of quaternary bronzes: The leaching action of acid rain. Corrosion Science, Vol. 51, pp. 159 – 170.

[4] F. Ammeloot, C. Fiaud, E.M.M. Sutter (1999). Characterization of the oxide layers on a Cu-13Sn alloy in a NaCl acqueous solution without and with 0.1M benzotriazole: Electrochemical and photoelectrochemical contributions. Electrochimica Acta, Vol. 44, p. 2549 – 2558.

[5] I. Mabille, A. Bertrand, E.M.M. Sutter, C. Fiaud (2003). Mechanism of dissolution of a Cu13-Sn alloy in low-aggressive conditions. Corrosion Science, Vol. 45, pp. 855 – 866.

[6] C. Debiemme-Chouvy, F. Ammeloot, E.M.M. Sutter (2001). X-ray photoemission investigation of the corrosion film formed on a polished Cu-13Sn alloy in aerated NaCl solution. Applied Surface Science, Vol. 174, p. 55 – 61.

[7] I. Odnevall Wallinder, P. Verbiest, W. He, C. Leygraf (2000). Effects of exposure direction and inclination on the runoff rates of zinc and copper roofs. Corrosion Science, Vol. 42, pp. 1471 – 1487.

[8] L. Robbiola, C. Fiaud, S. Pennec (1993). Preprints of ICOM-Committee for Conservation. James & James Science Pub., Vol. 2, p. 796.

[9] L. Robbiola, J.M. Blengino, C. Fiaud (1998). Morphology and mechanisms of formation of natural patinas on archaeological Cu-Sn alloys. Corrosion Science, Vol. 40, pp. 2083 – 2111.

[10] R. Baboian, E.B. Cliver (1986). Corrosion on the Statue of Liberty: Part I. Materials Performance, Vol. 25, p. 80.

[11] C. Chiavari, E. Bernardi, C. Martini, L. Morselli, F. Ospitali, L. Robbiola, A. Texier (2010). Predicting the corrosion behaviour of outdoor bronzes: Assesment of artificially exposed and real outdoor samples. Metal 2010: International Conference on Metal Conservation (Charleston, South Carolina, USA). Edited by P. Mardikian, C. Chemello, C. Watters, P. Hull. (pp. 160 – 166).

[12] G. Brunoro, A. Frignani, A. Colledan, C. Chiavari (2003). Organic films for protection of copper and bronze against acid rain corrosion. Corrosion Science, Vol. 54, pp. 2219 – 2231.

[13] D.A. Pillard, J.S. Cornell, D.L. Dufresne, M.T. Hernández (2001). Toxicity of benzotriazole and benzotriazole derivatives to three aquatic species.Water Research, Vol. 35, pp. 557 – 560.

[14] Health Council of the Netherlands. (http://www.gezondheidsraad.nl/en/publications/123-benzotriazole-health-based-recommended-occupational-exposure-limit). June 28th 2011.

[15] F. Zucchi, A. Frignani, V. Grassi, G. Trabanelli, M. DalColle (2007). The formation of a protective layer of 3-mercapto-propyl-trimethoxy-silane on copper. Corrosion Science, Vol. 49, pp. 1570 – 1583.

[16] F. Zanotto, V. Grassi, A. Frignani, F. Zucchi (2011). Protection of the AZ31 magnesium alloy with cerium modified silane coatings. Materials Chemistry and Physics, Vol. 129, pp. 1 – 8.

[17] U.S. General Services Administration, Historic Preservation Technical Procedures. Bronze: Characteristics, uses and problems. (http://w3.gsa.gov/web/p/hptp.nsf/0/6c8c800d5618e023852565c50054b2c6?OpenDocument)

[18] K. Sadayapan, M. Sahoo, H.T. Michels (2008). Copper and copper alloy castings. Casting, Vol. 15, ASM Handbook, ASM International, pp. 1085 – 1094. (http://products.asminternational.org/hbk/do/highlight/content/)

[19] P. Piccardo, et al. (May 2004). European Microscopy & Analysis, pp. 5 – 7.

[20] L.B. Brostoff (2003). Coating strategies for the protection of outdoor bronze art and ornamentation. Doctoral thesis, University of Amsterdam.

[21] C. Leygfraf, T.E. Graedel (2000). Atmospheric corrosion. Edit. John Wiley & Sons. Electrochemical Society Series.

[22] D.A. Scott (1991). Metallography and microstructure of ancient and historic metals. Tien Wah Press Ltd. Singapore, pp. 5 – 29.

[23] [Cambridge] (http://www.doitpoms.ac.uk/tlplib/solidification_alloys/dendritic.php). June 25th 2011.

[24] D.R. Askeland, P.P. Phulé (2003). The Science and Engineering of Materials. 4th edition, Brooks-Cole.

[25] L. Ceschini, A. Morri, G. Sambogna (2008). The effect of hot isostatic pressing on the fatigue behaviour of sand-cast A356-T6 and A204-T6 aluminum alloys. Journal of Materials Processing Technology, Vol. 204, pp. 231 – 238.

[26] H. Baker (2002). Binary Phase Diagrams, Vol. 3 ASM Handbook, ASM International, Metals Park, online edition.

[27] D. De la Fuente, J. Simancas, M. Morcillo (2008). Morphological study of 16-year patinas formed on copper in a wide range of atmospheric exposures. Corrosion Science, Vol. 50, pp. 268 – 285.

[28] K. Nassau, P.K. Gallagher, A.E. Miller, T.E. Graedel (1987). The characterization of patina components by X-ray diffraction and evolved gas analysis. Corrosion Science, Vol. 27, No. 7, pp. 669 – 684.

[29] A. Krätschmer, I. Odnevall Wallinder, C. Leygraf (2002). The evolution of outdoor copper patina. Corrosion Science, Vol. 44, pp. 425 – 450.

[30] D. Ciccarella (2009). Corrosione atmosferica del bronzo quaternario G85: Prove di invecchiamento artificiale. Alma Mater Studiorum – Università di Bologna, Facoltà di Chimica Industriale, pp. 132 – 139.

[31] H. Strandberg, L.G. Johansson, O. Lindqvist (1997). The atmospheric corrosion of statue bronzes exposed to SO_2 and NO_2. Materials and Corrosion, Vol. 48, pp. 1 – 19.

[32] B.M. Rosales, R.M. Vera, J. P. Hidalgo (2010). Characterisation and properties of synthetic patina on copper base sculptural alloys. Corrosion Science, Vol. 52, pp. 3212 – 3224.

[33] G. Chiavari, A. Colucci, R. Mazzeo, M. Ravanelli (1999). Organic content evaluation of corrosion patinas in outdoor bronze monuments. Chromatographia, Vol. 49, pp. 35 – 41.

[34] V. Ariola, A. D'Alessandro, F. Lucarelli, G. Marcazzan, F. Mazzei, S. Nava, I. Garcia-Orellana, P. Prati, G. Valli, R. Vecchi, A. Zucchiatti (2006). Elemental characterization of PM10, PM2.5 and PM1 in the town of Genoa (Italy). Chemosphere, Vol. 62, pp. 226 – 232.

[35] R. del P.B. Hernández, I.V. Aoki, B. Tribollet, H.G. de Melo (2011). Electrochemical impedance spectroscopy investigation of the electrochemical behavior of copper coated with artificial patina layers and submitted to wet and dry cycles. Electrochimica Acta, Vol. 56, pp. 2801 – 2814.

[36] D. Dolske, J. Meakin (1991). Acid deposition impacts on historic bronze and marble statuary and monuments. Materials Performance, Vol. 30, pp. 53 – 57.

[37] D. de la Fuente, J.M. Cega, F. Viejo, I. Díaz, M. Morcillo (2011). City scale assessment model for air pollution effects on the cultural heritage. Atmospheric Environment, Vol. 45, pp. 1242 – 1250.

[38] R. Picciochi, A.C. Ramos, M.H. Mendonça, I.T.E. Fonseca (2004). Influence of the environment on the atmospheric corrosion of bronze. Journal of Applied Electrochemistry, Vol. 34, pp. 989 – 995.

[39] A. Balbo, C. Chiavari, C. Martini, C. Monticelli (2011). Non-toxic corrosion inhibitors for the conservation of Renaissance bronzes and gilded bronzes. Submitted to Corrosion Science.

[40] T. Kosec, H. Otmačić Ćurković, A. Legat (2010). Investigation of the corrosion protection of chemically and electrochemically formed patinas on recent bronze. Electrchimica Acta, Vol. 56, pp. 722 – 731.

[41] A. Keserović, H. Otmačić Ćurković, E. Stupnišel-Lisac, K. Marušić, A. Furman, M. Kharsham (2010). Corrosion inhibitors for bronze protection in polluted atmosphere. Proceedings Eurocorr 2010: From Earth's depths to space heights.

[42] F. Deflorian, S. Rossi, L. Fedrizzi (2006). Silane pre-treatments on copper and aluminum. Electrochimica Acta, Vol. 51, pp. 6097 – 6103.

[43] F. Deflorian, S. Rossi, L. Fedrizzi, M. Fedel (2008). Integrated electrochemical approach for the investigation of silane pre-treatments for painting copper. Progress in Organic Coatings, Vol. 63, pp. 338 – 344.

[44] Y.S. Li, W. Lu, Y. Wang, T. Tran (2009). Studies of (3-mercaptopropyl)trimethoxylsilane and bis(trimethoxysilyl)ethane sol-gel coating on copper and aluminum. Spectrochimica Acta Part A: Molecular and Biomolecular Spectroscopy, Vol. 73, pp. 922 – 928.

[45] F. Zucchi, V. Grassi, A. Frignani, G. Trabanelli (2004). Inhibition of copper corrosion by silane coatings. Corrosion Science, Vol. 46, pp. 2853 – 2865.

[46] W.R. Thompson, M. Cai, M. Ho, J.E. Pemberton (1997). Hydrolysis and condensation of self-assembled monolayers of (3-mercaptopropyl)trimethoxysilane on Ag and Au surfaces. Langmuir, Vol. 13, pp. 2291 – 2302.

[47] F. Zucchi, V. Grassi, A. Frignani, G. Trabanelli, C. Monticelli (2007). Octadeyl-trimethoxy-silane film formed on copper in different conditions. Materials Chemistry and Physics, Vol. 103, pp. 340 – 344.

[48] A.E. Wener (1971). Museums Journal, Vol. 57, p. 3.

[49] T. Kosec, A. Legat, I. Milošev (2010). The comparison of organic protective layers on bronze and copper. Progress in Organic Coatings, Vol. 69, pp. 199 – 206.

[50] H. Lane (1979). The conservation and restoration of metals. SSCR, Edinburgh, UK, p. 50.

[51] L. Green (1989). Conservation of metals. Ed. M. Jaro, Veszprem, Hungary, pp. 121 – 130.

[52] M. F. Montemor, R. Pinto, M.G.S. Ferreira (2009). Chemical composition and corrosion protection of silane films modified with CeO_2 nanoparticles. Electrochimica Acta, Vol. 54, pp. 5179 – 5189.

[53] (http://it.wikipedia.org/wiki/Vittorio_Bottego) May 29th 2011.

[54] (http://www.collezioni-f.it/ascari/bottego.html) May 29th 2011.

[55] M.J. Hughes, M.R. Cowell, P.T. Craddock (1976). Atomic absorption techniques in archaeology. Archaeomtry, Vol. 18, pp. 19 – 37.

[56] L. Robbiola, K. Rahmouni, C. Chiavari, C. Martini, D. Prandstraller, A. Texier, H. Takenouti, P. Vermaut (2008). New insight into the nature and properties of pale green surfaces of outdoor bronze monuments. Applied Physics A: Materials Science & Processing, Vol. 92, pp. 161 – 169.

[57] C. Chiavari, M. Degli Esposti, C. Martini, F. Ospitali (2011). Ancient metallurgy at Sumhuram (Sultanate of Oman): Technical aspects of raised inscriptions on south Arabian bronzes. Archaeometry, Vol. 53, pp. 528 – 546.

[58] (http://books.google.com) J. Paul Getty Museum (1990). Small bronze sculpture from the ancient world: papers delivered at a symposium. Dept. of Antiquities Conservation, pp. 41 – 42. June 3rd. 2011.

[59] C. Chiavari, K. Rahmouni, H. Takenouti, S. Joiret, P. Vermaut, L. Robbiola (2007). Composition and electrochemical properties of natural patinas of outdoor bronze monuments. Electrochimica Acta, Vol. 52, pp. 7760 – 7769.

[60] D.L. Hamilton (1997). Basic methos of conserving underwater archaeological material culture. Nautical Archaeology Program, Department of Anthropology, Texas A&M University. (http://www.antiquerestorers.com/Articles2008/preservation_of_artifacts.htm). June 13th. 2011.

[61] G. Morigi (1979). Il restauro dei materiali in bronzo e ferro. Grafo Edizioni, Brescia romana, Materiali per un museo, Catalogo della mostra, Vol. 1. (http://www.bcin.ca/Interface/openbcin.cgi?submit=submit&Chinkey=7193) June 13th. 2011.

[62] T. Stambolov (1985). The corrosion and conservation of metallic antiquities and works of arts. CL Publication, p. 105.

[63] Oxford Instruments. (http://oxford-instruments.com/products/xrf-analysers/Pages/xray-fluorescence.aspx). June 28th 2011.

[64] A. Burmester, J. Koller (1987). Known and new corrosion products on bronzes: Their identification, an assessment particularly in relation to organic coatings. Recent Advances in the Conservation and Analysis of Artifacts (compiled by J. Black), London, pp. 97 – 103.

[65] Applied pyrolysis handbook (2007). Edited by T. Wampler, 2nd. edition, Taylor & Francis Group, pp. 1 – 64.

[66] Sigma-Aldrich. (http://www.sigmaaldrich.com/spectra/rair/RAIR002519.PDF) June 19th 2011.

[67] C.M. Grossi, P. Brimblecombe, R. Esbert, F.J. Alonso (2007). Color changes in architectural limestones from pollution and cleaning. Color research and application, Vol. 32, pp. 320 – 331.

[68] M. Pollard, C. Heron (1996). Archaeological Chemistry. pp. 26 – 31.

[69] E. Metcalfe (1991). Atomic Absorption and Emission Spectroscopy: Analytical Chemistry by Open Learning. Edit. John Wiley & Sons, pp. 51 – 55.

[70] G. Tricot (2010). Material from the course Analysis of solids. Université Lille 1.

[71] J. Goldstein (2003). Scanning electron microscopy and X-ray microanalysis. Science, Vol. 1, pp. 1 – 2.

[72] Elsevier (2004). Non-destructive microanalysis of cultural heritage materials. Edited by K. Janssens and R. Van Grieken, Vol. XLII, pp. 73 – 83.

[73] (http://www.sdm.buffalo.edu/scic/sem-eds.html) May 5th 2011.

[74] H.H. Willard, L.L. Merritt Jr., J.A. Dean, F.A. Settle Jr. (1988). Instrumental methods of analysis. 7th edition, pp. 108 – 109, 224 – 255, 287 – 288, 311 – 313, 321 – 323, 465 – 466, 513 – 514, 540 – 541.

[75] L. Nasdala, D.C. Smith, R. Kaindl, M.A. Ziemann (2004). EMU notes in mineralogy, Vol. 6, Chapter 7, p. 286.

[76] J.M. Hollas (2004). Modern spectroscopy. 4th. Edition, Edit. Wiley.

[77] J.M. Challinor (2001). The development and applications of thermally assisted hydrolysis and methylation reactions. Analytical Applied Pyrolysis, Vol. 61, pp. 3 – 34.

[78] G. Chiavari, D. Fabbri, S. Prati (2001). In sity pyrolysis and silylation for analysis of lipid materials used in paint layers. Chromatographia, Vol. 53, pp. 311 – 314.

[79] (http://www.hunterlab.com/appnotes/an07_96a.pdf) June 5th 2011.

[80] (http://en.wikipedia.org/wiki/Color_difference) June 6th 2011.

[81] (http://en.wikipedia.org/wiki/Gloss_(material_appearance)) June 1st. 2011.

[82] RSC analytical spectroscopy monographs (2005). Raman spectroscopy in archaeology and art history. Edited by H.G.M. Edwards and J.M. Chalmers, Cambridge, pp. 436 – 461.

[83] OMNIC Library 5.1a. Nicolet Instrument Corp.

Appendix A

Analytical techniques

Atomic absorption spectroscopy (AAS)

This technique requires sample to be in a liquid form (normally dissolved in water), thus making the sample preparation stage somewhat complicated and it can only measure one element at a time (so-called sequential operation).

Because this is an absorption technique, a characteristic radiation comprising the absorption wavelength of the element to be analysed has to be generated. This is produced in a special lamp called hollow-cathode lamp, which consists of a glass (or quartz) envelope filled with a noble gas at low pressure. Within the envelope are two electrodes, one a wire and the other a hollow cup made from the element of interest. On application of a few hundred volts between the electrodes, the cathodic cup begins to glow with the characteristic radiation of the element, since the voltage is enough to cause electrons to travel from the wire to the cup; on impact, the atoms of the cup are excited and emit their characteristic radiation [68].

In the spectrometer, the light from this lamp is then guided towards the photomultiplier detector through the long axis of a long thin gas flame produced at a specially-shaped burner (Fig. A.1). The liquid sample is aspirated into the flame along with the combustible gases. The fuel and oxidant gases are pre-mixed in a chamber designed to ensure complete homogenization of the gases, and the flow of these gases causes the liquid sample to be sucked into the chamber via a capillary tube. The design of the mixing chamber also ensures that the sample liquid is effectively atomized into a fine aerosol before it enters the flame.

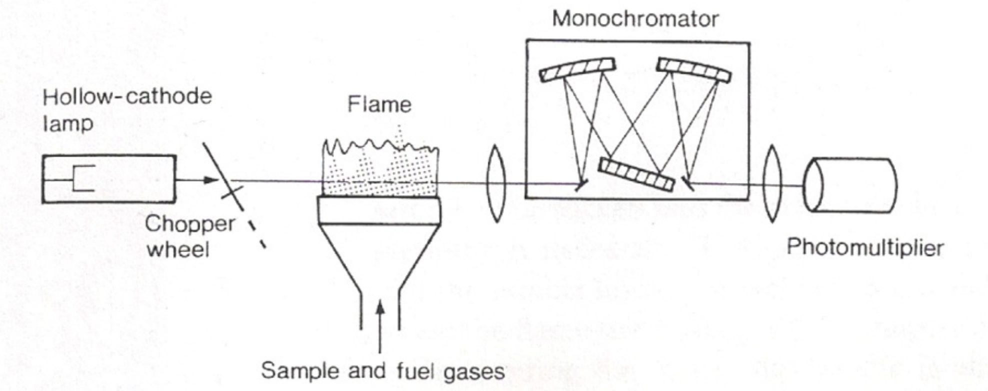

Fig. A.1 - Scheme of FAAS [68]. Light of wavelength characteristic of the sample of interest is generated in the lamp and passes through the flame containing the atomized sample. The light is quantitatively absorbed in the flame and the wavelengths are separated in the monochromator. The intensity of the transmitted light is measured in a photomultiplier.

On entering the flame, the sample is almost immediately converted into atomic vapor. This is then in the ideal form to absorb characteristic radiation from the light source through the flame, and the amount of radiation absorbed at a particular wavelength is directly proportional to the concentration of that particular element in the flame, according to the Beer-Lambert Law, Eq(A.1).

For certain elements it is necessary to increase the temperature of the flame in order to ensure the complete atomization. This is done by changing the mixture of gases used, from the normal compressed air / acetylene mixture, which burns at about 2200°C, to nitrous oxide / acetylene, giving a temperature of up to 3000°C. The latter gases require a slightly different design of burner, so the change-over cannot be made at will [68].

The light from the hollow-cathode lamp shines directly through the flame into a slit and monochromator device, which disperses the light into its constituent wavelengths and selects a particular wavelength for transmission onto the detector, which is a photomultiplier tube capable of quantitatively converting the light into an electric current which is easily measured. Usually, the light intensity passing through the flame is first of all measured without any sample being aspirated (blank), and then with the sample introduced. The difference between the two is the absorption due to the atoms in the sample, and this absorption is calibrated by measuring the absorption due to the aspiration of a solution containing a known concentration of that element (standard solution).

Instead of a flame, a graphite furnace (GF-AAS) may be used for the atomization and sample analysis. This furnace is a cylindrical tube open in both extremes and with a small hole in the center for the introduction of the sample. The length of the tube is approximately 5 cm and its diameter ≈1 cm. The main advantages of this kind of atomization are the higher sensibility respect to the flame and the minor quantity of sample required to perform the analysis [30]. An image of the GF-AAS technique can be seen in Fig. A.2.

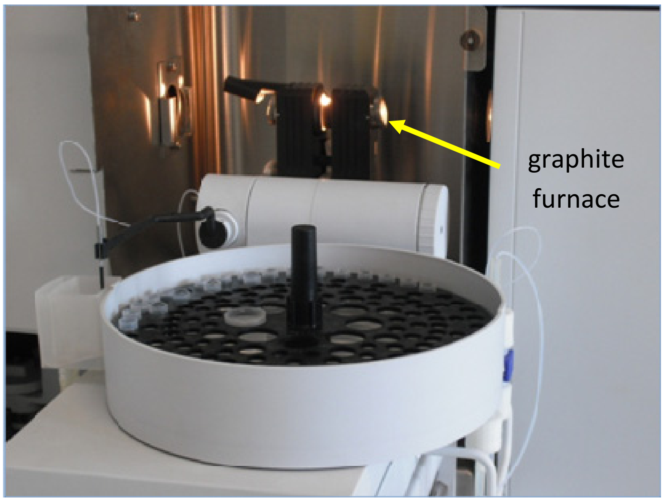

Fig. A.2 - Graphite furnace in the GF-AAS technique

- Relationship between light absorption and concentration

The amount of light absorbed in the atom cell will depend on the concentration of atoms in the atom cell [69]. If the incident light falling on the atom cell has intensity I_0, and the transmitted light reaching the detector is I_t, as shown in Fig A.3:

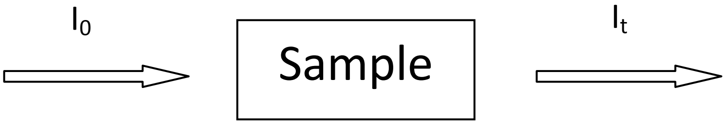

Fig. A.3 - Light passing through a sample

Then the concentration "c" is given by:

$$\log (I_0/I_t) = \varepsilon \, c \, l$$

Where:

I_0 = incident light (J s^{-1} cm^{-1})

I_t = transmitted light (J s^{-1} cm^{-1})

c = concentration (mol L^{-1})

ε = molar absorptivity coefficient (L mol^{-1} cm^{-1}), a measure of the intensity with which the atoms absorb the light, and it depends on both the nature of the atom and the wavelength.

l = path length through the atom cell (cm)

In a particular determination of a given element at a fixed wavelength "ε" is a constant and the path length is also a constant, as this is determined by the width of the flame. The concentration then is related directly to the logarithm of the ratio I_0/I_t. A more convenient equation can be obtained by defining the absorbance "A" as:

$$A = \log (I_0/I_t)$$

Therefore:

$$A = \varepsilon \, c \, l \qquad \text{(Eq. A.1)}$$

As I_t decreases (meaning more light is absorbed) to zero then "A" increases to infinity. However, the useful practical range is $0 < A < 1$, corresponding to $100\% > I_t > 10\%$. The absorbance is far more useful than I_t since it is linearly related to the concentration (Fig. A.4), allowing the use of a plot "A" vs "c" as a calibration graph.

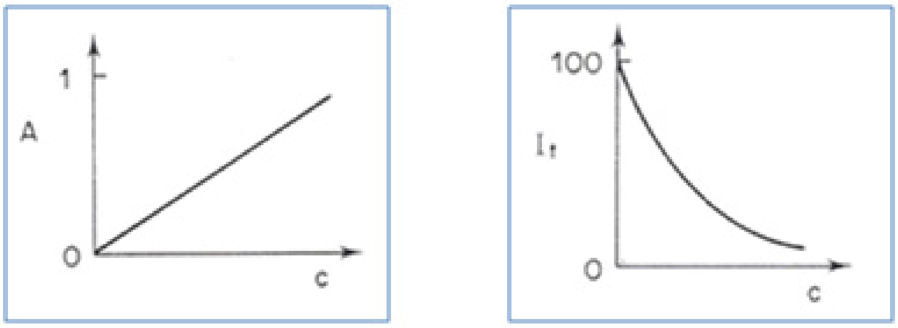

Fig. A.4 - Relationship between concentration-absorbance (left) and concentration-transmitted light (right) [69]

X-ray fluorescence (XRF)

XRF is a spectroscopic technique based on the fluorescence of atoms in the X-ray domain, to provide qualitative and quantitative information on the elemental composition of a sample. The versatility, the speed with which the measurements can be carried out and the potential to examine most materials without preparation in a wide range of elemental concentration, all contribute to the success of this analytical method, which in most cases does not destroy the sample.

When the sample is irradiated by an X-ray source, it emits X-ray photoluminescence which is characteristic of the elements present in the sample. The signal can be used for identification of the elements (i.e. qualitative analysis) and, after suitable calibration, quantitative analysis.

X-ray fluorescence is a two-step process (shown in Fig. A.5):

1. The interaction of a photon of sufficient energy with an isolated atom can lead to the stripping off of a lower shell electron, a so-called photoelectron. Each photoelectron has an energy determined by the difference between the energy of the incident X-ray photon and that of the electronic level initially occupied by the ejected electron.

2. The energy gap caused by step 1 is immediately followed by an electron reorganisation that takes the atom back to its ground state, emitting an X-radiation with an energy equal to the difference between that of the initial electron and that of the electron that takes its place.

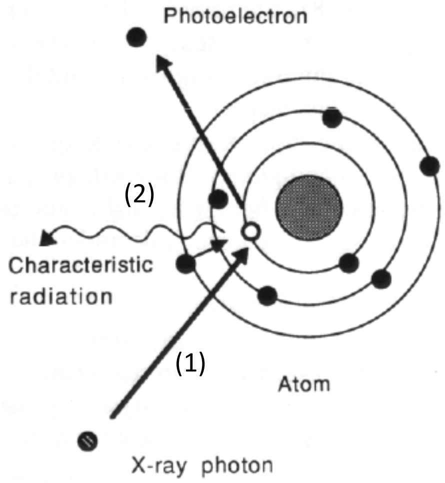

Fig. A.5 - X-ray fluorescence process: (1) The X-ray photon interacts with a lower shell electron, ejecting a photoelectron and (2) Electron reorganisation which emits a characteristic radiation (X-ray) [70].

The emitted fluorescence can be detected according to two modes:

(1) Simultaneously, by a cooled diode that detects all the photons at different energies (known as energy dispersive X-ray fluorescence, EDXRF instruments) or

(2) Sequentially, using a monochromator system and a goniometer assembly that select and detect the emitted wavelengths (known as wavelength dispersive X-ray fluorescence, WDXRF instruments).

XRF can be used to determine all the elements starting from boron (Z = 5) in solid (bulk or powder) or liquid samples without particular preparation.

As fluorescence transition can be usually associated to the correspondent elements, the qualitative analysis does not present any major difficulty. On the other hand, quantitative analysis is much more difficult: Serious problems can be encountered to avoid some undesirable phenomena, such as inter-element interactions, preferential excitation, self-absorption and, as a consequence, reference standards have to be analysed in matrices as similar as possible to those of the real samples.

Scanning electron microscopy + Energy dispersive spectroscopy (X-ray microanalysis)

Scanning electron microscope (SEM) is an electrical-optical instrument which permits, after the emission of an electron beam, to analyse several signals produced by the interaction of electrons in the beam with the analysed sample [30].

Conventional SEM is formed by the following elements [30]:

- An electronic column where the electron beam is created usually by a filament made of tungsten
- A vacuum chamber where the electron beam interacts with the sample
- Different kinds of detectors which acquire the signals of the beam-sample interaction
- A screen where the image of the signal is rebuilt

The area to be examined or the volume to be analysed is irradiated with a finely focused electron beam, which may be swept in a raster across the surface of the specimen to form images or may be static to obtain an analysis at one position. The types of signals produced from the interaction of the electron beam with the sample include secondary electrons, backscattered electrons, characteristic X-rays, and other photons of various energies (Fig. A.6). These signals are obtained from specific emission volumes within the samples and can be used to examine many characteristics of the sample (surface topography, crystallography, composition, etc.) [71].

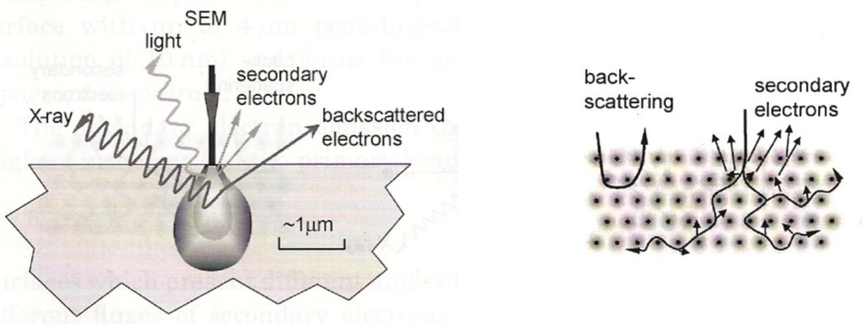

Fig. A.6 - Interaction of electrons with a solid showing effects of interaction volume (left) and difference between how back-scattered and secondary electrons are produced (right) [72]

Secondary electrons are emitted from the atoms occupying the top surface and produce a readily interpretable image of the surface. The contrast in the image is determined by the sample morphology, namely the emission efficiency of secondary electrons depends on the angle between the surface and the primary electron beam. A high resolution image can be obtained because of the small diameter of this beam [73].

Backscattered electrons are primary beam electrons which are “reflected” from atoms in the solid. The contrast in the image produced is determined by the atomic number of the elements in the sample. The image will therefore show the distribution of different chemical phases in the sample. Because these electrons are emitted from a higher depth in the sample (Fig. A.6 left) than secondary electrons, the resolution in the image is not as good as for secondary electrons [73]. The resulting image of the area of interest is in black and white, with different tonalities in gray, depending of the diversity in chemical composition of that area in the sample. In general, light gray areas are result of the presence of high atomic number elements, and dark gray areas are due to the presence of low atomic number elements [30].

Interaction of the primary electron beam with atoms in the sample may cause shell transitions which result in the emission of an X-ray. The emitted X-rays have an energy characteristic of the emitting element. Detection and measurement of the energy permits elemental analysis (Energy Dispersive X-ray Spectroscopy or EDS). EDS can provide rapid qualitative or, with adequate standards, quantitative analysis of elemental composition with a sampling depth of 1-2 μm. X-rays may also be used to form maps or line profiles, showing the elemental distribution in a sample surface. EDS can be considered one of the variants of XRF.

With some structural modifications to the conventional SEM, it is possible to observe non-conductive samples (extremely corroded metals, ceramics, polymers) without preliminary sample preparation (i.e. covering with conductive materials such as gold). Keeping low vacuum in the chamber and high vacuum in the electronic column (to avoid damage in the filament of tungsten), the production of positive ions is induced, followed by collisions between the residual molecules in the atmosphere of the chamber and the electrons in the electron beam, which are in condition to neutralize the accumulation of negative charge in the non-conductive sample [30].

Raman spectroscopy

The Raman effect arises when a beam of intense monochromatic radiation passes through a sample that contains molecules that undergo a change in molecular polarisability as they vibrate. Polarisability is the value of the induced dipole moment divided by the strength of the field that causes the induced dipole moment; in other words, the electron cloud of the molecule must be more readily deformed in one extreme of the vibration than in the other extreme [74].

Most collisions of the incident photons in the beam with the sample molecules are elastic, which is called Rayleigh scattering. As shown in Figure A.7, the incident radiation does not raise the molecule to any particular quantized level; rather, the molecule is considered to be in a virtual excited state. As the electromagnetic wave passes, the polarised molecule ceases to oscillate and returns to its original ground level in a very short time (ranging 10^{-12} s).

However, a small proportion of the excited molecule (one in a million) may undergo changes in polarisability during one or more of the normal vibrational modes, and this is the basis for the Raman effect. Usually incident radiation is absorbed by a molecule in the lowest vibrational state. If the molecule reemits by returning not to the original vibrational state, but to an excited vibrational level of the ground electronic state, the emitted radiation is of lower energy than the incident radiation. The difference is equal to a natural vibration frequency of the molecule's ground electronic state. Such shifted lines, known as Stokes lines, are normally observed in the Raman spectrum, corresponding to different vibrations in the molecule [74].

A few of the molecules initially absorb radiation while they are in an excited vibrational state and decay to a lower energy level, so that the Raman frequency is higher than the incident radiation. These are the anti-Stokes lines.

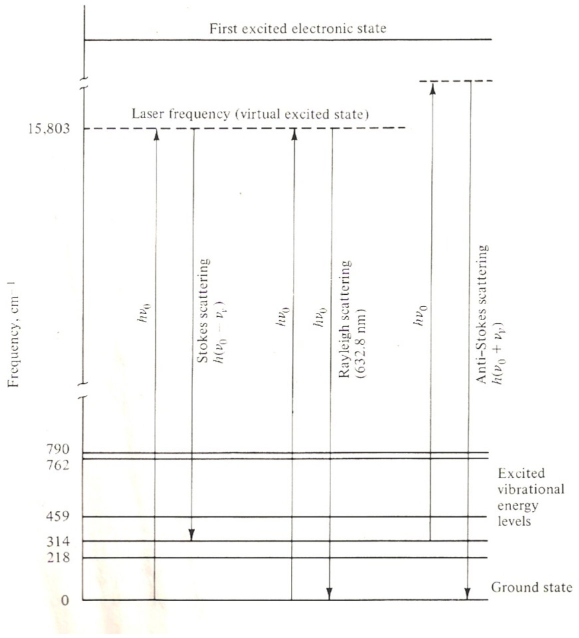

Fig. A.7 - Energy interchange involved in Rayleigh and Raman (Stokes and anti-Stokes) scattering [74]
]

The final spectrum of the scattered radiation consists of a relatively strong component with unshifted frequency (Rayleigh scattering) corresponding to photons scattered without energy exchange, and the two components of the Raman spectrum: The Stokes lines and the anti-Stokes lines, perfectly symmetric respect to the Rayleigh line (Fig. A.8). Normally only the Stokes lines are considered in chemical analysis because they are more intense given that, on the basis of the Boltzmann distribution law, at near room temperature the ground vibrational level is the most populated.

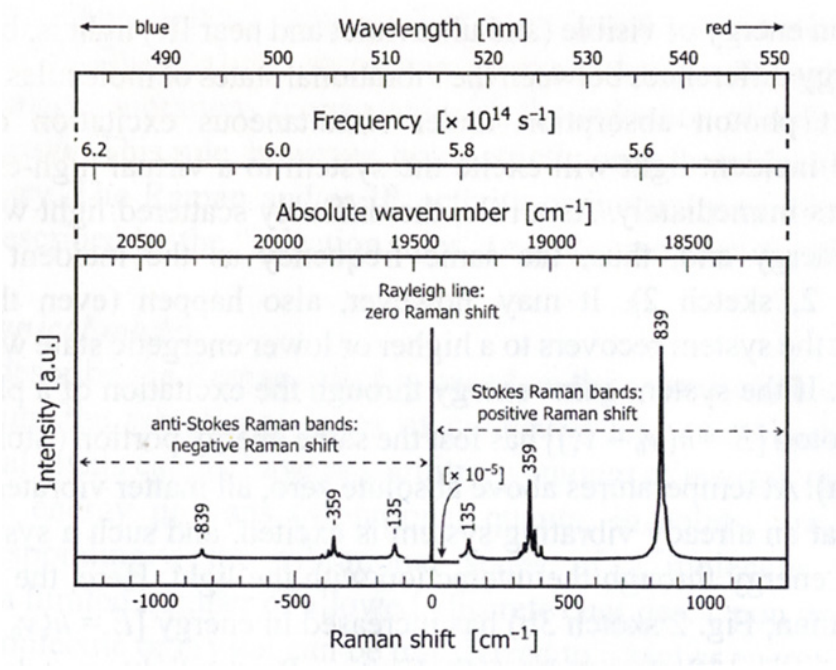

Fig. A.8 - Raman spectrum: Rayleigh, Stokes and anti-Stokes lines [75]

A Raman spectrum, as the one shown in Fig. A.8, plots the intensity of the scattered radiation as a function of the Raman shift expressed in wavenumber (cm^{-1}). The Raman shift is the difference between the wavenumber of the incident radiation and the wavenumber of the emitted radiation.

The wavenumber is defined as:

$$\tilde{v} = 1/\lambda = v/c \tag{Eq. A.2}$$

Where:

$\tilde{v}$ = wavenumber (cm^{-1})

λ = wavelength (cm)

v = frequency (s^{-1})

c = speed of light ($3x10^{10}$ $cm.s^{-1}$)

Attenuated total reflectance infrared spectroscopy (ATR-IR)

Infrared spectroscopy involves examination of the stretching, bending, twisting and rotating vibrational motions of atoms in a molecule when it interacts with infrared radiation and some portions of the incident radiation are absorbed at specific wavelengths.

At temperatures above absolute zero, all the atoms in molecules are in continuous vibration with respect to each other. The different vibrational motions of a molecule are called normal modes. The term values of these vibrational modes of molecules fall in the infrared (IR) region of the electromagnetic spectrum, which extends from the red end of the visible spectrum to the microwave region, including radiation from 0.7 to 500 μm or, in wavenumbers, between 14000 and 20 cm^{-1}, but usually the region known as mid-infrared (4000 to 200 cm^{-1}) is the most usual for this technique [74].

When infrared radiation reaches a sample, if the frequency of this radiation equals the vibrational frequency of the molecule, the photon is absorbed and a transition occurs [76]. The multiplicity of vibrations occurring simultaneously produces a highly complex absorption spectrum that is uniquely characteristic of the functional groups that make up the molecule and of the overall configuration of the molecule as well. The absorption or the lack of absorption in specific frequency regions can be correlated with vibrational motions of specific functional groups and, in some cases, with the relationship of these groups to the rest of the molecule.

However, not all the possible vibrations within a molecule result in an IR absorption band because, to be IR active, a vibration must result in a change of dipole moment during motion. Thus, diatomic homonuclear molecules (i.e. O_2) do not have IR active bands and are not visible in IR spectroscopy [76].

When interpreting the spectrum, it is possible to state that certain functional groups are present in the sample and others are absent. Taking this into account, the possibilities for unknown compounds can be sharply narrowed and compared with a library of spectra of pure compounds for identification [74].

Infrared spectroscopy may be performed by dispersive devices or by Fourier Transform ones. In the later ones, the radiation coming from the infrared source is divided into two beams and then these recombine in a beamsplitter, and the resulting signal, known as interferogram, contains all the information required to reconstruct the spectrum via the mathematical process known as Fourier transformation. The main advantage of these devices over the dispersive ones is that all wavelengths are simultaneously detected throughout the scan, achieving the same spectral signal-to-noise ratio as a dispersive spectrometer in a fraction of time. This is known as the Felgett's advantage.

Attenuated total reflectance (ATR) is a technique which uses infrared radiation in a special way. When a beam of radiation enters a prism with a high refractive index n_1 (known as internal reflection element, IRE) which is surrounded by or immersed in a sample with a refractive index $n_2 < n_1$, it is reflected internally if the angle of incidence at the interface between sample and prism is greater than the critical angle (θ_c, a function of the refractive indexes of the sample and the prism) (Fig. A.9).

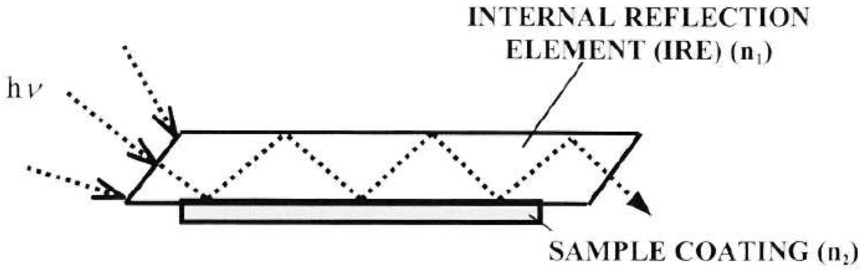

Fig. A.9 - Scheme of the ATR technique, n_1 is the refractive index of the prism and n_2 the one of the sample, with $n_1 > n_2$ [20]

In this technique all the energy is reflected, however, the beam slightly penetrates beyond the reflecting surface and then returns. When a material is placed in contact with the reflecting surface, the beam loses energy at those wavelengths where the material absorbs due to an interaction with the penetrating beam. This attenuated radiation, when measured and plotted as a function of wavelength, is an absorption spectrum characteristic of the material and is similar to an infrared spectrum obtained in the normal transmission mode.

ATR simplifies infrared sampling. Qualitative infrared absorption spectra are easily obtained from most solid materials without the need for grinding or dissolving.

IRE is a crystal with particular characteristics such as transmission of IR radiation, chemically inert, high refractive index and high hardness. It is usually made of Si, Ge, zinc selenite (ZnS) or diamond. An image of an ATR-IR device with diamond crystal is shown in Fig. A.10.

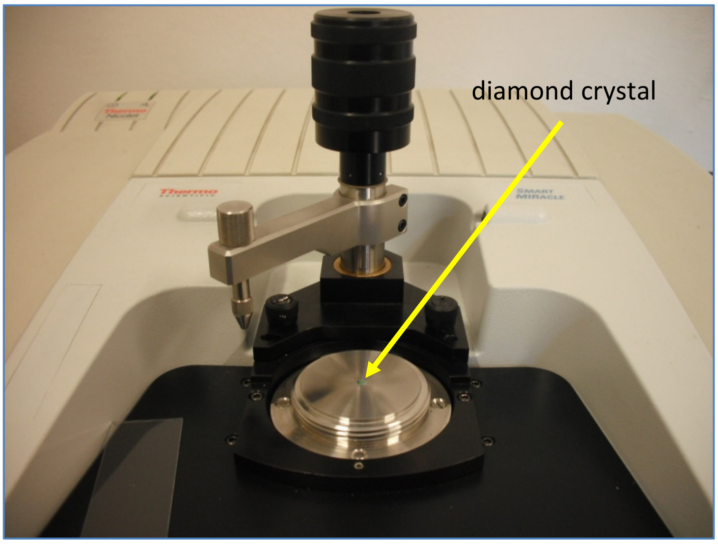

Fig. A.10 - ATR-IR device

Pyrolysis – Gas chromatography – Mass spectrometry (Py-GC-MS)

Chromatography is a method of separation where two mutually immiscible phases are brought into contact. One phase is stationary and the other is mobile. A sample is introduced into the mobile phase and carried along through a column which contains a distributed stationary phase. Species in the sample undergo repeated interactions or partitions between the mobile phase and the stationary phase. When both phases are properly chosen, the sample components are gradually separated into bands in the mobile phase and, at the end of the process, separated components emerge in order of increasing interaction with the stationary phase. The least retarded component emerges first and the most strongly retained component elutes last [74].

Partitions between the phases exploit differences in the physical and/or chemical properties of the components in the sample. Adjacent components (peaks) are separated when the later-emerging peak is retarded sufficiently to prevent overlap with the peak that emerges ahead of it. It is possible to obtain qualitative and quantitative information through chromatography.

The separation column is the most important part of the chromatograph, because it provides versatility in the types of analyses that can be performed.

The mobile phase can be a gas or a liquid, whereas the stationary phase can be only a liquid or a solid. When the mobile phase is a gas, the method may be called gas-liquid chromatography (GLC, if the stationary phase is liquid) or gas-solid chromatography (GSC, if the stationary phase is a solid).

A gas chromatograph consists of several modules with specific purposes [74]:

(1) Provide a constant flow of carrier (mobile phase) gas
(2) Permit the introduction of sample vapors into the flowing gas stream
(3) Contain the appropriate length of stationary phase
(4) Maintain the column at the appropriate temperature
(5) Detect the sample components as they elute from the column, and
(6) Provide a readable signal proportion in magnitude to the amount of each component

On the other hand, mass spectrometry (MS) is an analytical tool which provides qualitative and quantitative information about the atomic and molecular composition of inorganic and organic materials. The main advantages of MS are its increased sensitivity over most other analytical techniques and its specificity in identifying unknowns or confirming the presence of suspected compounds. The enhanced sensitivity results primarily from the action of the analyser as a mass/charge filter to reduce background interference and from the sensitive electron multipliers used for detection. Sample size requirements for solids and liquids range from a few milligrams to femtograms or even attograms in the most advanced MS devices, as long as the material can exist in the gaseous state at the temperature and pressure in the ion source. The excellent specificity results from characteristic fragmentation patterns which can give information about molecular weight and molecular structure [74].

A mass spectrometer is an essential adjunct to the use of stable isotopes in investigating reaction mechanisms and in tracer work, and has contributed greatly to a more detailed understanding of kinetics and mechanisms of unimolecular decomposition of molecules.

The components of a mass spectrometer can be seen in Fig. A.11.

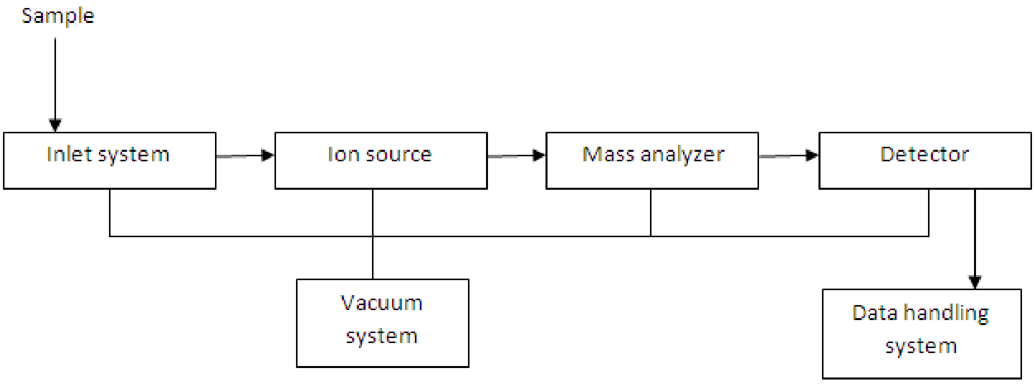

Fig. A.11 - Components of a mass spectrometer

GC and MS can be coupled together. The mass spectrometer is a universal detector for gas chromatographs since any compound that can pass through a gas chromatograph is converted into ions in the mass spectrometer. At the same time, the highly specific nature of a mass spectrum makes the mass spectrometer a very specific gas chromatographic detector. GC is an ideal separator, whereas MS is excellent for identification.

The aim of an interface arrangement between these two techniques is to operate both without degrading the performance of either instrument.

Pyrolysis (Py) is a thermal degradation technique in an inert environment. It decomposes molecules with high molecular weight into lighter volatile fragments, so that these can be characterised and identified through any analytical method, including GC-MS.

In the Py-GC-MS system, the sample is heated enough to break the bonds, and fragments are separated and taken to an analyser which provides the characteristic pyrolysis profile (pyrogram) which, under controlled experimental conditions, can be considered as a fingerprint of the substrate. Fragments are separated base on their affinity to the stationary phase in the chromatograph and detected by the mass spectrometer thanks to the ionization and separation according to their mass to charge ratios (m/z).

The main advantages of using Py-GC-MS are [65]:

1. No sample pretreatment is required
2. Very small quantity of sample is enough to perform the analysis
3. Permits to analyse very complex chemical matrices, usually not able to analyse with other techniques
4. Good reproducibility

The main drawback is that pyrolysis is a destructive technique, but this is attenuated by the fact that very small quantity of sample is needed.

The use of a derivatizing reagent is necessary in presence of polar compounds that cannot be analyzed with this chromatographic technique.

The derivatizing agent is usually a chemical compound able to transform polar groups such as the carboxylic and hydroxylic into non-polar groups, esters and ethers [65].

The most used derivatizing agents in Py-GC-MS are TMAH (tetramethylammonium hydroxide) [77] and HMDS (hexamethyldysilazane) [78].

The addition of the agent is performed directly on the sample, after it is introduced into a quartz tube and the derivatization reaction takes place simultaneously with the pyrolysis.

CIELAB color scale and gloss measurement

The CIELAB scale is an approximately uniform colour scale which is organized in a cube form with three axes [79]:

L* - A value of 100 represents a perfect reflecting diffuser, while 0 (zero) means black.

a* - The more positive indicates more tendency to red; the more negative, to green.

b* - The more positive indicates tendency to yellow; the more negative, to blue.

The color space of the CIELAB scale is illustrated in Fig. A.12.

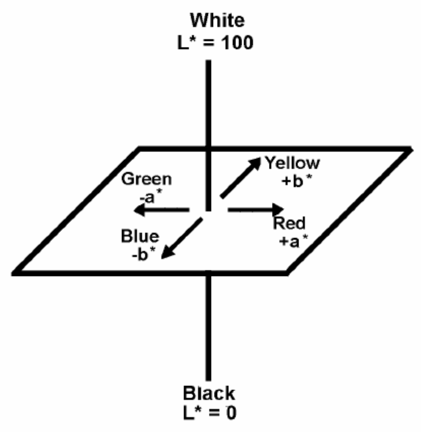

Fig. A.12 - CIELAB color space [79]

The total colour difference (ΔE*) is a metric created by the International Commission of Illumination (CIE) to express the colour change quantitatively and not only qualitatively, given that in certain fields colour change is the main variable. Additionally, human eye is more sensitive to certain colours than others, which makes more critical the need for a metric to measure colour change. “E” stands for *Empfindung*, German for “sensation” [80]. ΔE* is calculated as:

$$\Delta E* = \sqrt{(\Delta L*)^2 + (\Delta a*)^2 + (\Delta b*)^2}$$

A value of ΔE* = 3 is considered as the “just noticeable difference” in the cultural heritage field [67], meaning that a value equal or over 3 represents a noticeable colour change of the analysed sample.

Gloss measurement consists in determining the percentage of specularly reflected light after illuminating the surface with visible light at different angles (e.g. 20°, 60° and 85°). The percentage of reflected light depends on the refractive index of the material, the angle of incident light and the surface topography. Materials with smooth surfaces appear glossy, while very rough surfaces reflect no specular light and therefore appear matt [81].

Appendix B

SEM-EDS analyses

SEM-EDS analysis – Bottego alloy

<table>
<tr><th>Sample</th><th>SEM image</th><th>EDS analysis</th></tr>
<tr><td>B1
Site 1
Spec 1</td><td>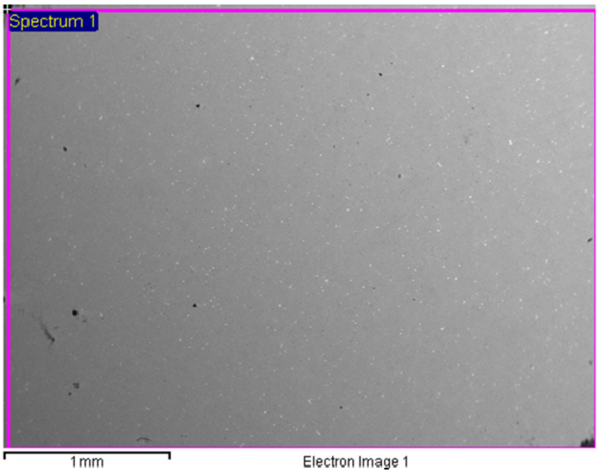
</td><td>
<table>
<tr><th>Element</th><th>% wt</th></tr>
<tr><td>Cu</td><td>88.91</td></tr>
<tr><td>Sn</td><td>7.15</td></tr>
<tr><td>Zn</td><td>3.35</td></tr>
<tr><td>Pb</td><td>0.58</td></tr>
<tr><td>O</td><td>---</td></tr>
<tr><td>Al</td><td>---</td></tr>
<tr><td>Sb</td><td>---</td></tr>
<tr><td>S</td><td>---</td></tr>
<tr><td>Cl</td><td>---</td></tr>
</table>
</td></tr>
<tr><td>B1
Site 2
Spec 1</td><td>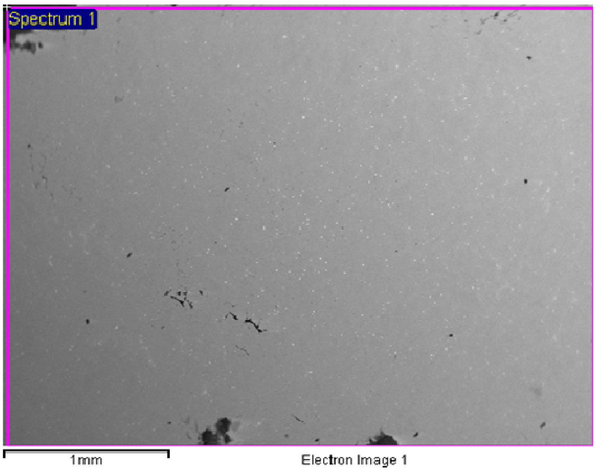
</td><td>
<table>
<tr><th>Element</th><th>% wt</th></tr>
<tr><td>Cu</td><td>89.11</td></tr>
<tr><td>Sn</td><td>7.09</td></tr>
<tr><td>Zn</td><td>3.62</td></tr>
<tr><td>Pb</td><td>0.18</td></tr>
<tr><td>O</td><td>---</td></tr>
<tr><td>Al</td><td>---</td></tr>
<tr><td>Sb</td><td>---</td></tr>
<tr><td>S</td><td>---</td></tr>
<tr><td>Cl</td><td>---</td></tr>
</table>
</td></tr>
</table>

<table>
<tr>
<td>B1
Site 3
Spec 1</td>
<td>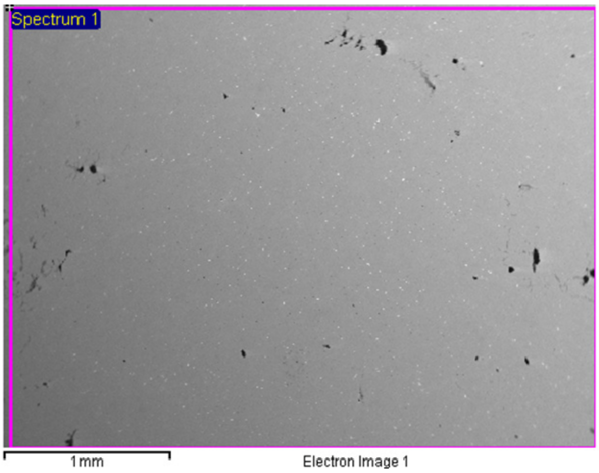
</td>
<td><table>
<tr><th>Element</th><th>% wt</th></tr>
<tr><td>Cu</td><td>88.91</td></tr>
<tr><td>Sn</td><td>6.99</td></tr>
<tr><td>Zn</td><td>3.73</td></tr>
<tr><td>Pb</td><td>0.38</td></tr>
<tr><td>O</td><td>---</td></tr>
<tr><td>Al</td><td>---</td></tr>
<tr><td>Sb</td><td>---</td></tr>
<tr><td>S</td><td>---</td></tr>
<tr><td>Cl</td><td>---</td></tr>
</table></td>
</tr>
<tr>
<td>B1
Site 4
Spec 1</td>
<td>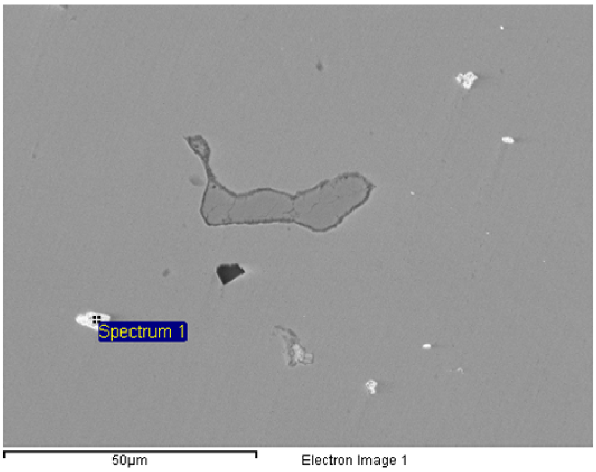
</td>
<td><table>
<tr><th>Element</th><th>% wt</th></tr>
<tr><td>Cu</td><td>11.09</td></tr>
<tr><td>Sn</td><td>---</td></tr>
<tr><td>Zn</td><td>---</td></tr>
<tr><td>Pb</td><td>81.81</td></tr>
<tr><td>O</td><td>7.09</td></tr>
<tr><td>Al</td><td>---</td></tr>
<tr><td>Sb</td><td>---</td></tr>
<tr><td>S</td><td>---</td></tr>
<tr><td>Cl</td><td>---</td></tr>
</table></td>
</tr>
<tr>
<td>B1
Site 4
Spec 2</td>
<td>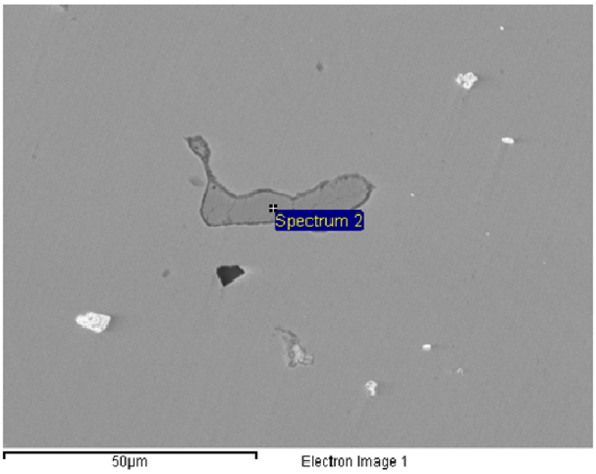
</td>
<td><table>
<tr><th>Element</th><th>% wt</th></tr>
<tr><td>Cu</td><td>86.57</td></tr>
<tr><td>Sn</td><td>---</td></tr>
<tr><td>Zn</td><td>---</td></tr>
<tr><td>Pb</td><td>---</td></tr>
<tr><td>O</td><td>13.43</td></tr>
<tr><td>Al</td><td>---</td></tr>
<tr><td>Sb</td><td>---</td></tr>
<tr><td>S</td><td>---</td></tr>
<tr><td>Cl</td><td>---</td></tr>
</table></td>
</tr>
</table>

B1
Site 4
Spec 3

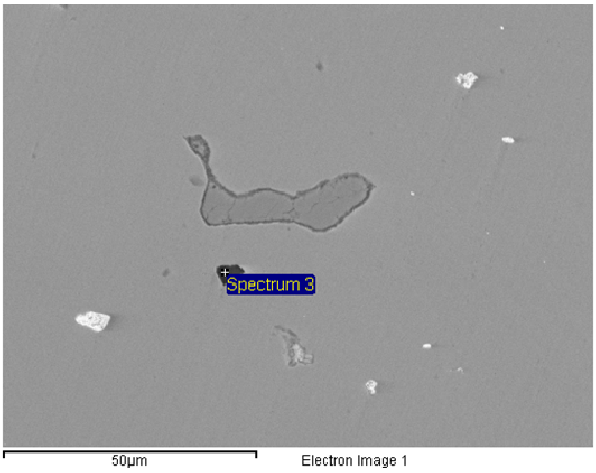

Element	% wt
Cu	32.08
Sn	3.38
Zn	1.31
Pb	---
O	31.63
Al	30.92
Sb	0.69
S	---
Cl	---

B1
Site 5
Spec 1

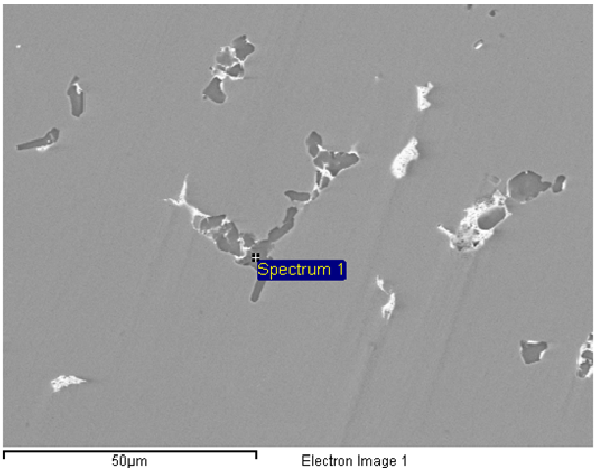

Element	% wt
Cu	4.10
Sn	---
Zn	63.29
Pb	---
O	---
Al	---
Sb	---
S	32.61
Cl	---

B1
Site 5
Spec 1

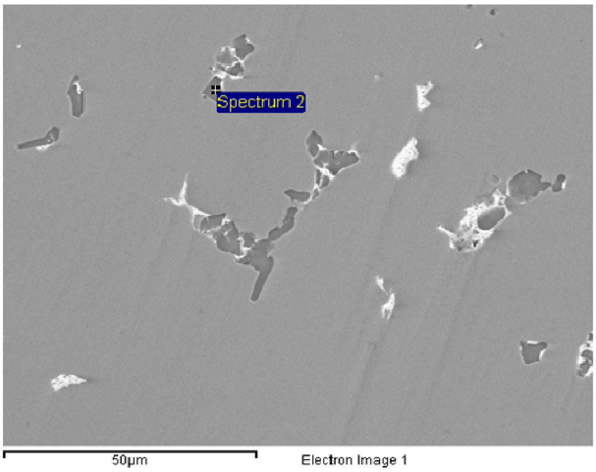

Element	% wt
Cu	8.49
Sn	---
Zn	60.00
Pb	---
O	---
Al	---
Sb	---
S	31.51
Cl	---

B1
Site 6
Spec 1

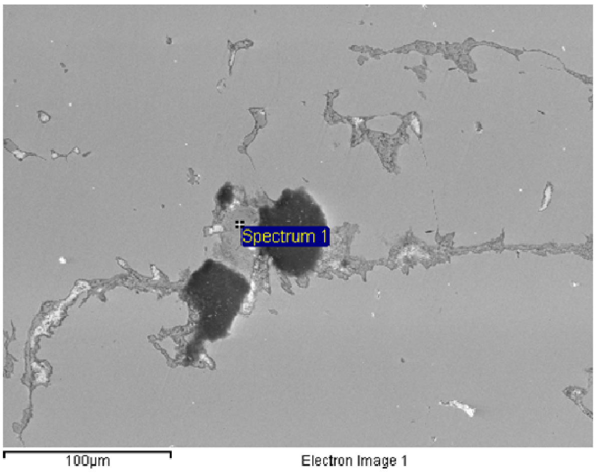

Element	% wt
Cu	79.70
Sn	---
Zn	2.80
Pb	---
O	17.50
Al	---
Sb	---
S	---
Cl	---

B1
Site 6
Spec 2

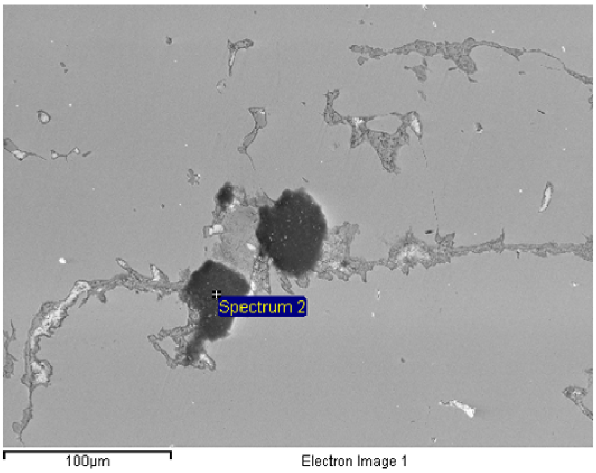

Element	% wt
Cu	6.66
Sn	0.77
Zn	---
Pb	---
O	10.33
Al	---
Sb	---
S	0.21
Cl	0.97
C	81.06

SEM-EDS analysis – Omo alloy

<table>
<tr><th>Sample</th><th>SEM image</th><th>EDS analysis</th></tr>
<tr><td>O1
Site 2
Spec 1</td><td>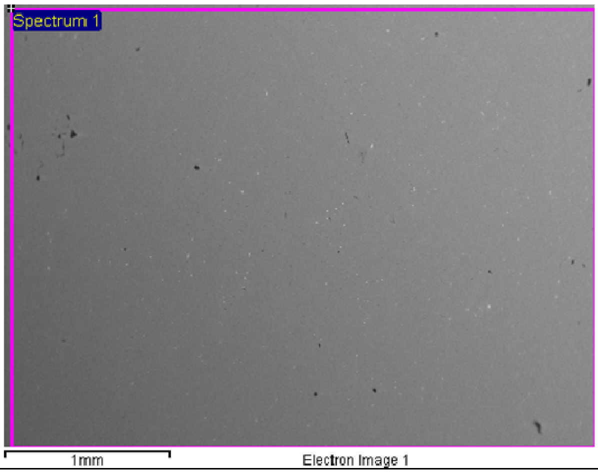
</td><td>
<table>
<tr><th>Element</th><th>% wt</th></tr>
<tr><td>Cu</td><td>91.38</td></tr>
<tr><td>Sn</td><td>6.77</td></tr>
<tr><td>Zn</td><td>1.53</td></tr>
<tr><td>Pb</td><td>0.32</td></tr>
<tr><td>O</td><td>---</td></tr>
<tr><td>Al</td><td>---</td></tr>
<tr><td>Si</td><td>---</td></tr>
<tr><td>S</td><td>---</td></tr>
<tr><td>Cl</td><td>---</td></tr>
</table></td></tr>
<tr><td>O1
Site 3
Spec 1</td><td>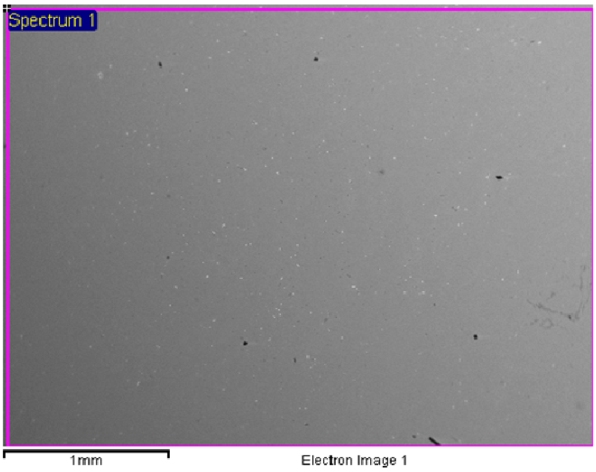
</td><td>
<table>
<tr><th>Element</th><th>% wt</th></tr>
<tr><td>Cu</td><td>91.65</td></tr>
<tr><td>Sn</td><td>6.23</td></tr>
<tr><td>Zn</td><td>1.09</td></tr>
<tr><td>Pb</td><td>1.04</td></tr>
<tr><td>O</td><td>---</td></tr>
<tr><td>Al</td><td>---</td></tr>
<tr><td>Si</td><td>---</td></tr>
<tr><td>S</td><td>---</td></tr>
<tr><td>Cl</td><td>---</td></tr>
</table></td></tr>
<tr><td>O1
Site 4
Spec 1</td><td>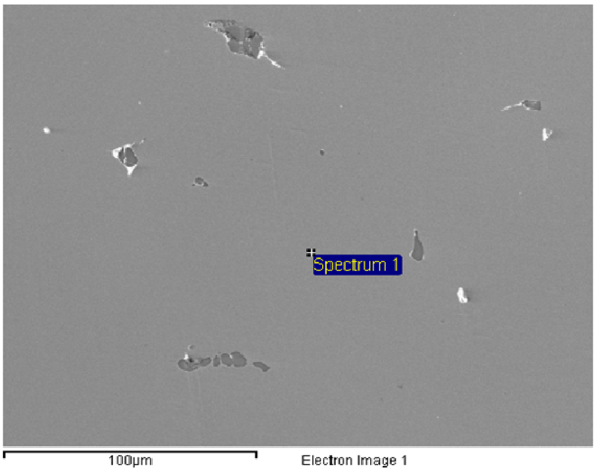
</td><td>
<table>
<tr><th>Element</th><th>% wt</th></tr>
<tr><td>Cu</td><td>37.89</td></tr>
<tr><td>Sn</td><td>---</td></tr>
<tr><td>Zn</td><td>---</td></tr>
<tr><td>Pb</td><td>51.24</td></tr>
<tr><td>O</td><td>10.87</td></tr>
<tr><td>Al</td><td>---</td></tr>
<tr><td>Si</td><td>---</td></tr>
<tr><td>S</td><td>---</td></tr>
<tr><td>Cl</td><td>---</td></tr>
</table></td></tr>
</table>

O1
Site 4
Spec 2

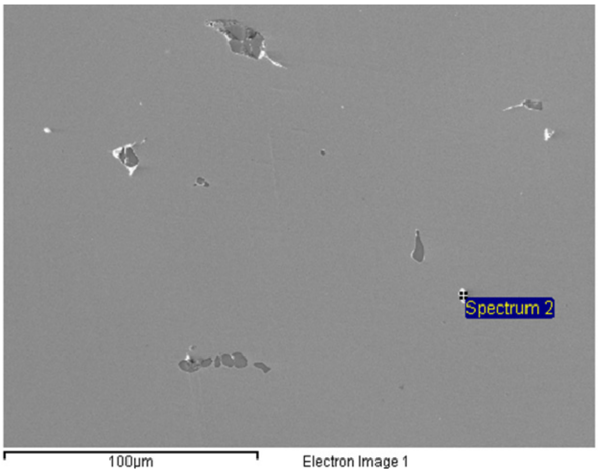

Element	% wt
Cu	14.78
Sn	---
Zn	---
Pb	76.81
O	6.78
Al	---
Si	---
S	---
Cl	1.63

O1
Site 4
Spec 3

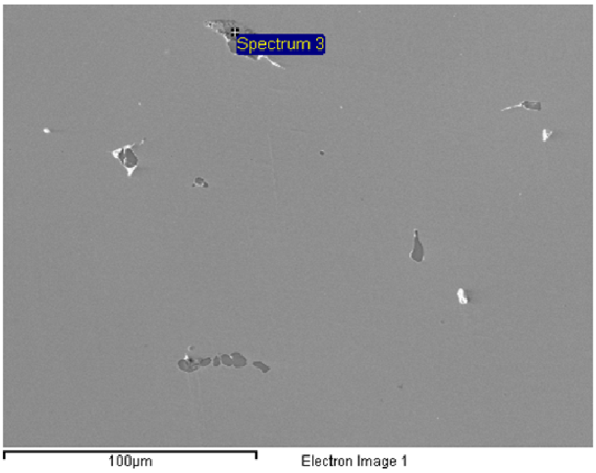

Element	% wt
Cu	4.49
Sn	---
Zn	59.86
Pb	---
O	13.43
Al	---
Si	---
S	35.13
Fe	0.52
Cl	---

O1
Site 4
Spec 4

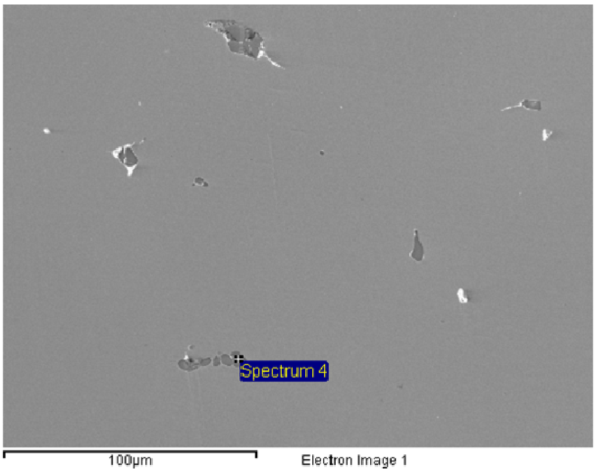

Element	% wt
Cu	6.13
Sn	---
Zn	59.18
Pb	---
O	---
Al	0.77
Si	---
S	33.92
Cl	---

O1
Site 4
Spec 5

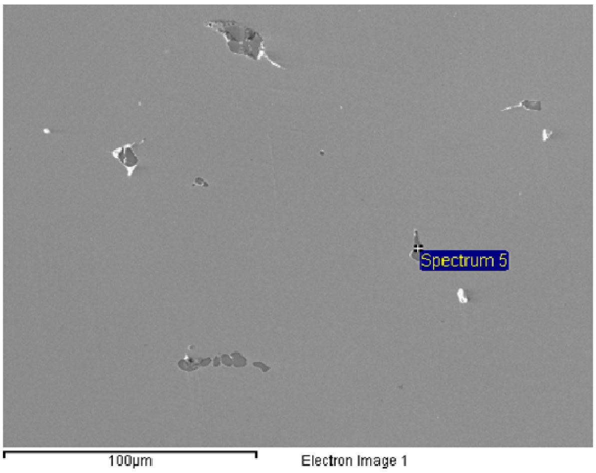

Element	% wt
Cu	64.12
Sn	5.69
Zn	19.53
Pb	---
O	---
Al	---
Si	---
S	10.67
Cl	---

O1
Site 5
Spec 1

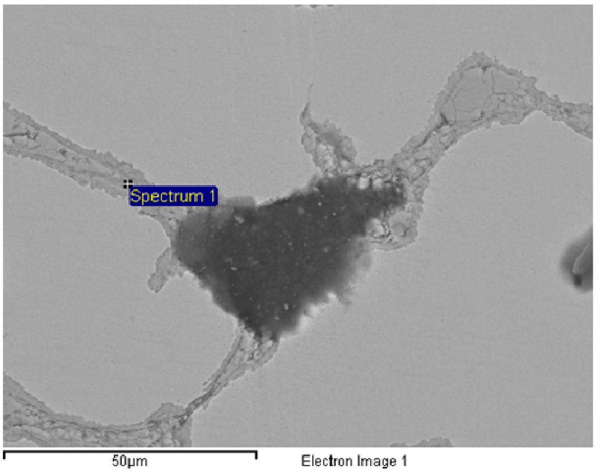

Element	% wt
Cu	74.12
Sn	5.61
Zn	---
Pb	---
O	19.21
Al	1.06
Si	---
S	---
Cl	---

O1
Site 5
Spec 2

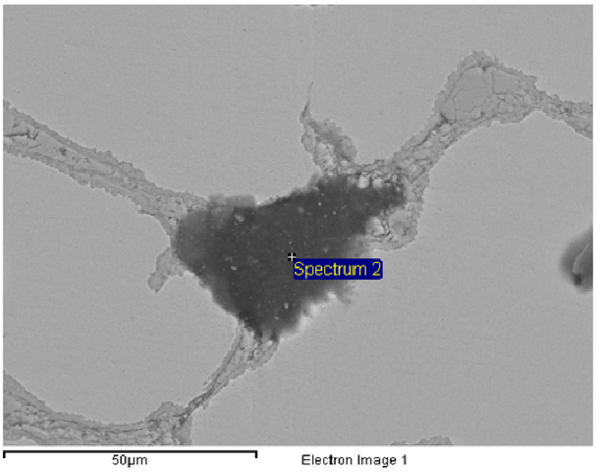

Element	% wt
Cu	6.80
Sn	0.99
Zn	---
Pb	---
O	6.82
Al	---
Si	---
S	---
Cl	1.09
C	84.30

O1
Site 5
Spec 3

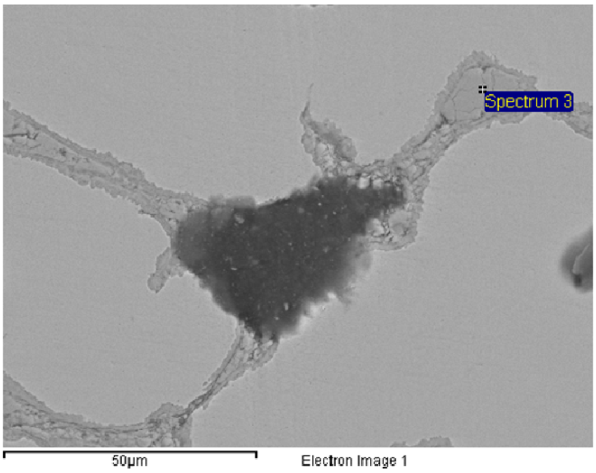

Element	% wt
Cu	87.04
Sn	---
Zn	---
Pb	---
O	12.96
Al	---
Si	---
S	---
Cl	---

O1
Site 6
Spec 1

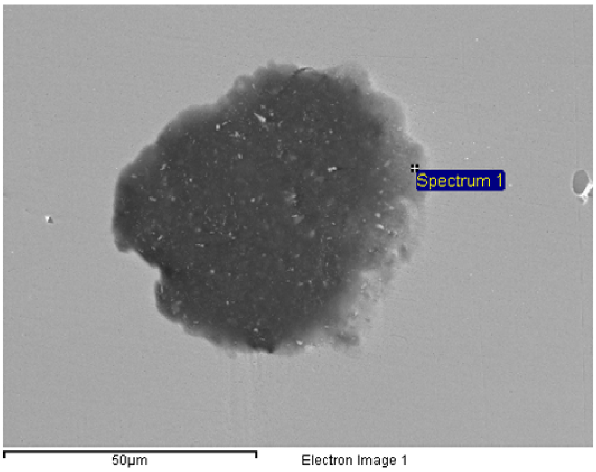

Element	% wt
Cu	31.63
Sn	3.36
Zn	---
Pb	---
O	---
Al	---
Si	---
S	---
Cl	1.41
C	63.59

O1
Site 6
Spec 2

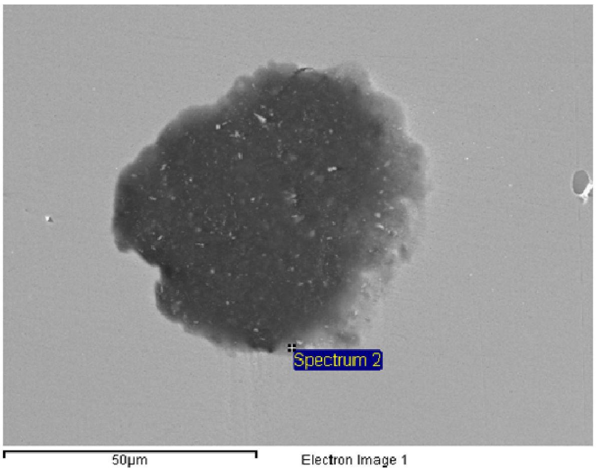

Element	% wt
Cu	39.08
Sn	4.34
Zn	---
Pb	---
O	6.18
Al	---
Si	0.21
S	---
Cl	0.81
C	49.38

SEM-EDS analysis – Giuba alloy

<table>
<tr><th>Sample</th><th>SEM image</th><th>EDS analysis</th></tr>
<tr><td>G1
Site 1
Spec 1</td><td>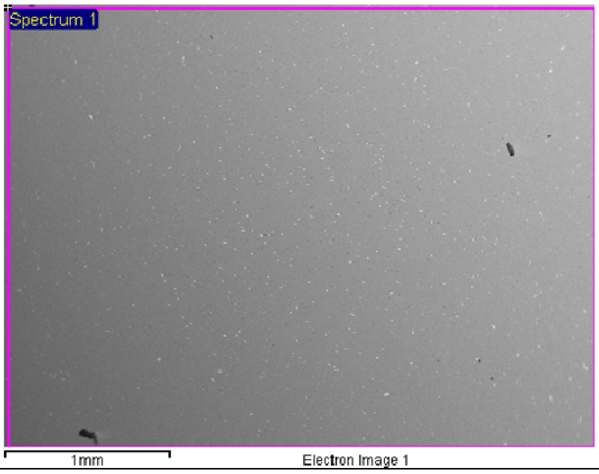
</td><td>
<table>
<tr><th>Element</th><th>% wt</th></tr>
<tr><td>Cu</td><td>90.57</td></tr>
<tr><td>Sn</td><td>6.46</td></tr>
<tr><td>Zn</td><td>2.22</td></tr>
<tr><td>Pb</td><td>0.74</td></tr>
<tr><td>O</td><td>---</td></tr>
<tr><td>Al</td><td>---</td></tr>
<tr><td>Fe</td><td>---</td></tr>
<tr><td>S</td><td>---</td></tr>
<tr><td>Cl</td><td>---</td></tr>
</table></td></tr>
<tr><td>G1
Site 2
Spec 1</td><td>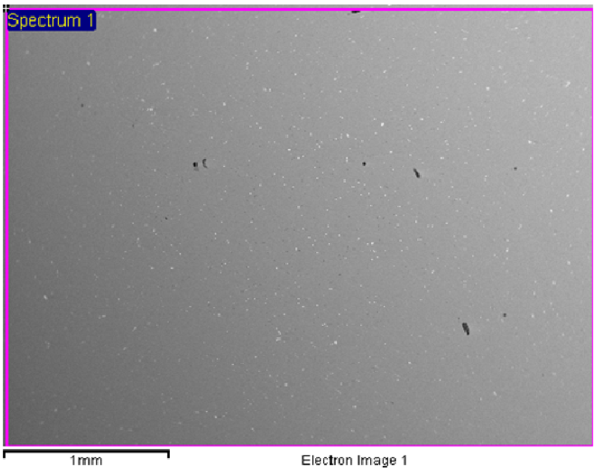
</td><td>
<table>
<tr><th>Element</th><th>% wt</th></tr>
<tr><td>Cu</td><td>89.78</td></tr>
<tr><td>Sn</td><td>6.91</td></tr>
<tr><td>Zn</td><td>2.67</td></tr>
<tr><td>Pb</td><td>0.65</td></tr>
<tr><td>O</td><td>---</td></tr>
<tr><td>Al</td><td>---</td></tr>
<tr><td>Fe</td><td>---</td></tr>
<tr><td>S</td><td>---</td></tr>
<tr><td>Cl</td><td>---</td></tr>
</table></td></tr>
<tr><td>G1
Site 3
Spec 1</td><td>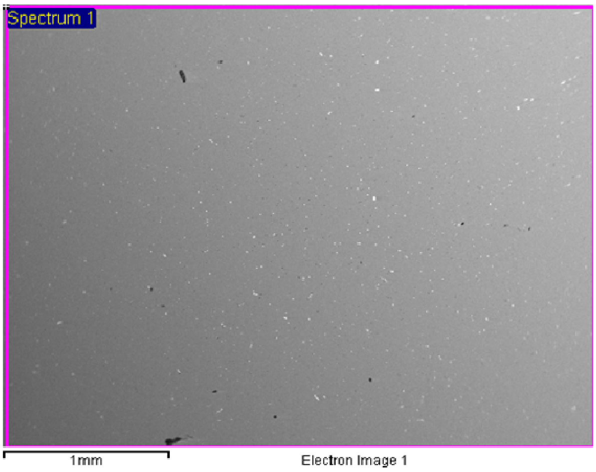
</td><td>
<table>
<tr><th>Element</th><th>% wt</th></tr>
<tr><td>Cu</td><td>89.68</td></tr>
<tr><td>Sn</td><td>6.66</td></tr>
<tr><td>Zn</td><td>2.77</td></tr>
<tr><td>Pb</td><td>0.88</td></tr>
<tr><td>O</td><td>---</td></tr>
<tr><td>Al</td><td>---</td></tr>
<tr><td>Fe</td><td>---</td></tr>
<tr><td>S</td><td>---</td></tr>
<tr><td>Cl</td><td>---</td></tr>
</table></td></tr>
</table>

G1
Site 4
Spec 1

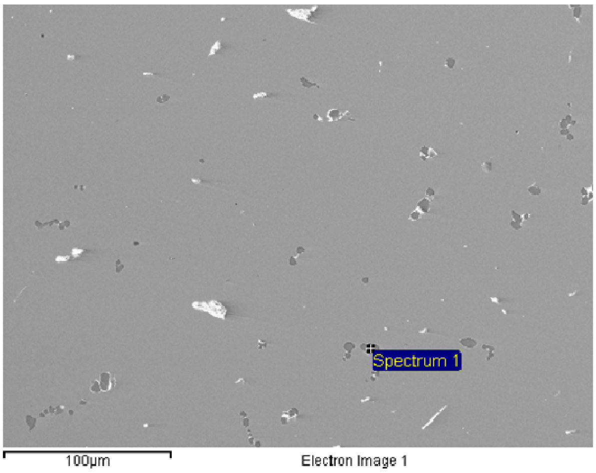

Element	% wt
Cu	3.59
Sn	---
Zn	62.19
Pb	---
O	---
Al	---
Fe	0.93
S	33.30
Cl	---

G1
Site 4
Spec 2

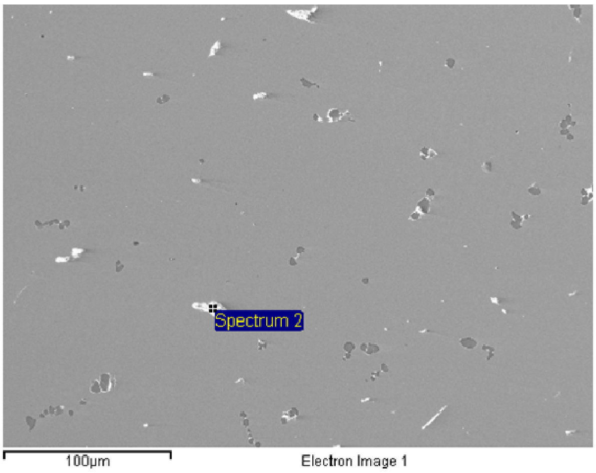

Element	% wt
Cu	6.50
Sn	---
Zn	---
Pb	88.85
O	4.64
Al	---
Fe	---
S	---
Fe	---
Cl	---

G1
Site 5
Spec 1

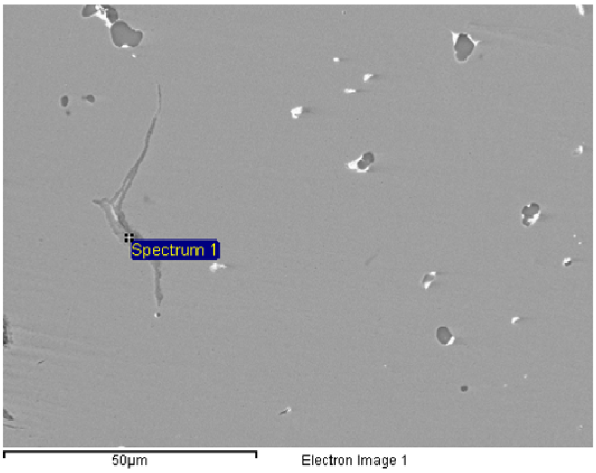

Element	% wt
Cu	75.98
Sn	8.57
Zn	---
Pb	---
O	14.20
Al	---
Fe	---
S	0.56
Cl	0.70

G1
Site 5
Spec 2

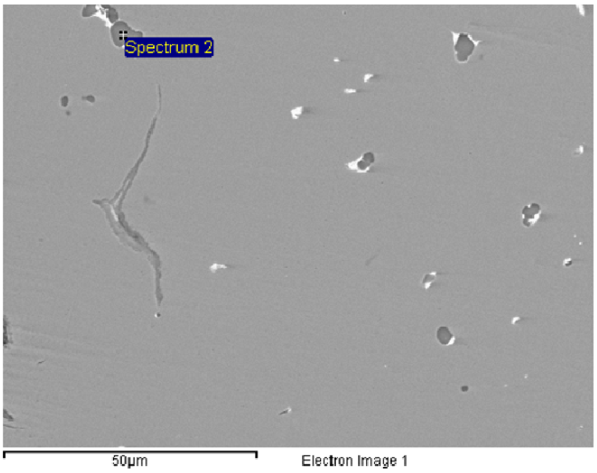

Element	% wt
Cu	14.02
Sn	---
Zn	56.24
Pb	---
O	---
Al	---
Fe	---
S	29.75
Cl	---

SEM-EDS analysis – Bottego corrosion products

Sheltered samples			
Sample	**SEM image**	**EDS analysis**	
		Element	**% wt**
B2 Site 2	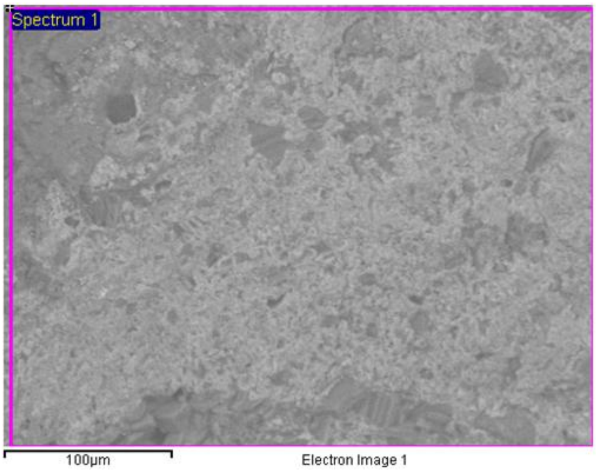	**C**	14.08
		O	45.12
		Mg	---
		Al	1.27
		Si	2.02
		P	---
		S	7.71
		Cl	---
		K	0.20
		Ca	3.86
		Fe	0.49
		Cu	25.26
		Zn	---
		As	---
		Sn	---
		Pb	---
		Element	**% wt**
B2 Site 3	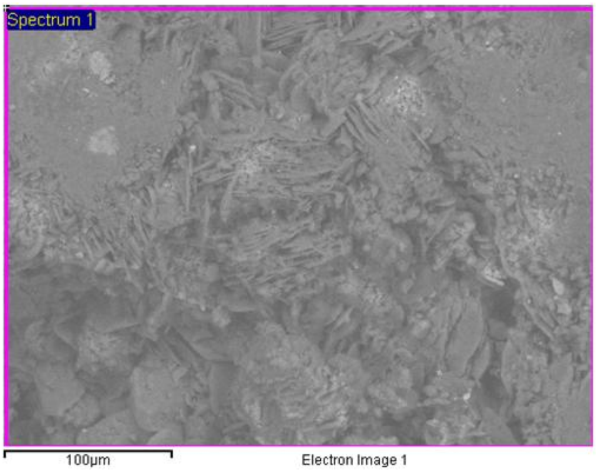	**C**	---
		O	53.30
		Mg	0.47
		Al	1.08
		Si	3.12
		P	---
		S	13.57
		Cl	0.66
		K	0.50
		Ca	16.19
		Fe	1.29
		Cu	9.82
		Zn	---
		As	---
		Sn	---
		Pb	---

B2
Site 4

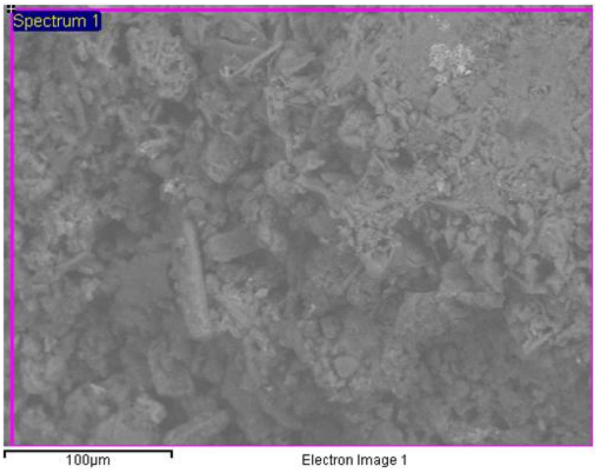

Element	% wt
C	---
O	49.30
Mg	1.00
Al	1.64
Si	7.66
P	---
S	9.23
Cl	0.36
K	0.73
Ca	11.40
Fe	3.28
Cu	15.40
Zn	---
As	---
Sn	---
Pb	---

B3
Site 1

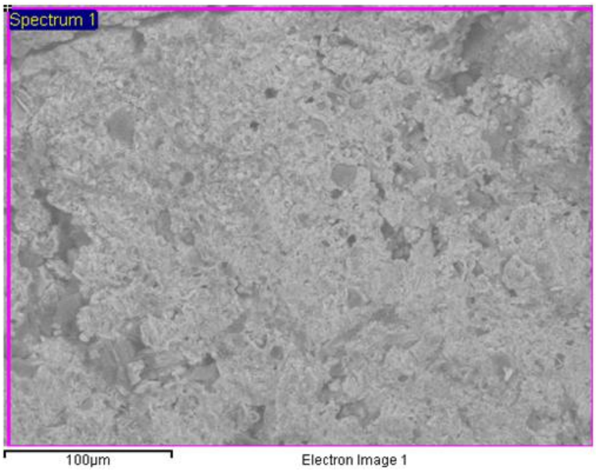

Element	% wt
C	9.93
O	39.90
Mg	---
Al	0.78
Si	3.17
P	---
S	6.60
Cl	---
K	0.18
Ca	1.47
Fe	0.62
Cu	37.35
Zn	---
As	---
Sn	---
Pb	---

B3
Site 2

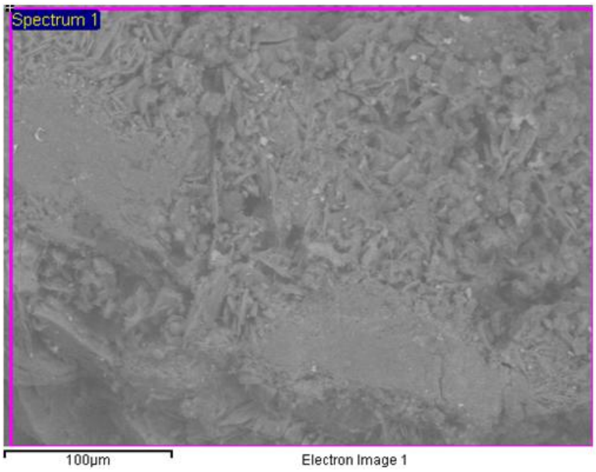

Element	% wt
C	17.49
O	50.59
Mg	0.44
Al	1.29
Si	3.52
P	---
S	9.42
Cl	0.22
K	0.39
Ca	11.04
Fe	1.05
Cu	4.56
Zn	---
As	---
Sn	---
Pb	---

B3
Site 3

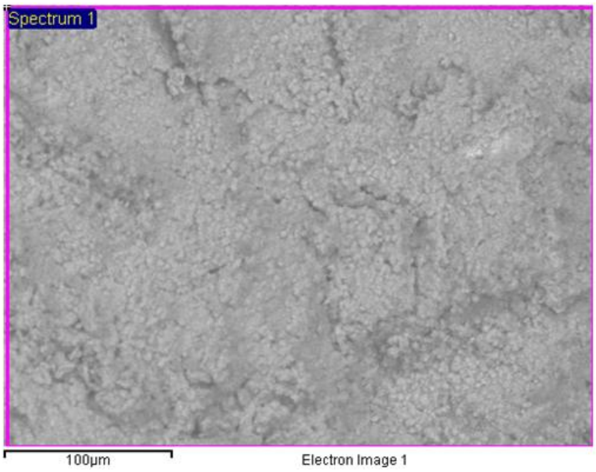

Element	% wt
C	17.18
O	42.70
Mg	---
Al	0.27
Si	0.71
P	---
S	5.38
Cl	0.18
K	---
Ca	0.37
Fe	0.25
Cu	31.28
Zn	0.32
As	---
Sn	1.36
Pb	---

B4
Site 1

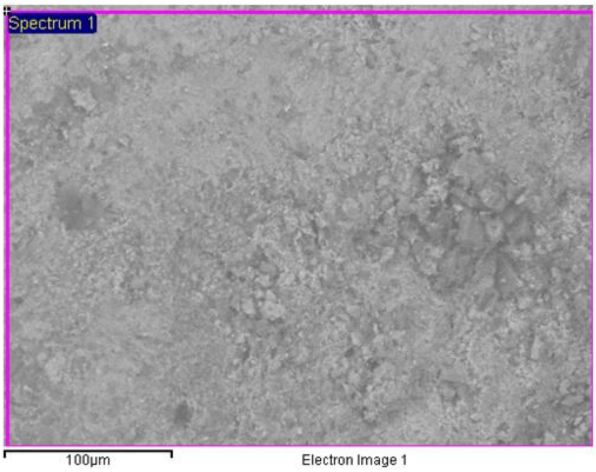

Element	% wt
C	16.69
O	45.53
Mg	0.21
Al	0.63
Si	2.40
P	---
S	6.71
Cl	---
K	0.24
Ca	3.70
Fe	0.45
Cu	23.40
Zn	0.06
As	---
Sn	---
Pb	---

B4
Site 2

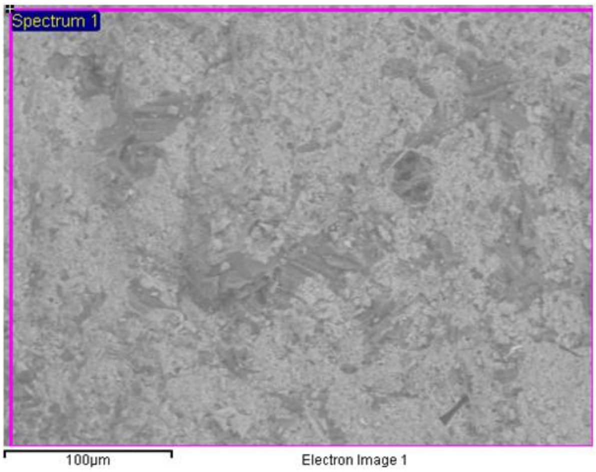

Element	% wt
C	17.89
O	36.36
Mg	---
Al	0.74
Si	2.01
P	---
S	6.54
Cl	---
K	0.14
Ca	2.93
Fe	0.44
Cu	32.96
Zn	---
As	---
Sn	---
Pb	---

<table>
<tr>
<td>B4
Site 3</td>
<td>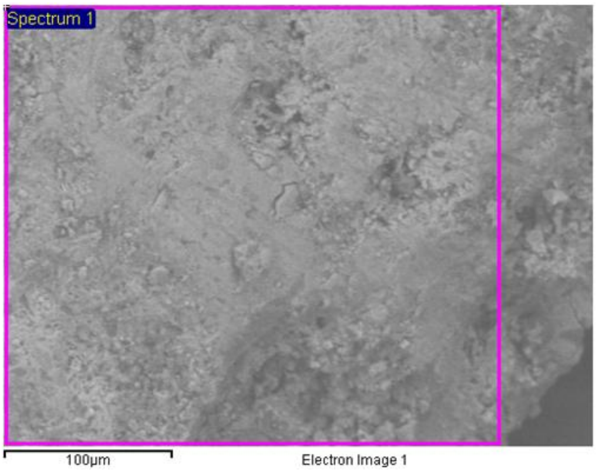
</td>
<td>
<table>
<tr><th>Element</th><th>% wt</th></tr>
<tr><td>C</td><td>22.62</td></tr>
<tr><td>O</td><td>41.17</td></tr>
<tr><td>Mg</td><td>---</td></tr>
<tr><td>Al</td><td>0.58</td></tr>
<tr><td>Si</td><td>1.66</td></tr>
<tr><td>P</td><td>---</td></tr>
<tr><td>S</td><td>5.28</td></tr>
<tr><td>Cl</td><td>---</td></tr>
<tr><td>K</td><td>0.31</td></tr>
<tr><td>Ca</td><td>1.10</td></tr>
<tr><td>Fe</td><td>0.47</td></tr>
<tr><td>Cu</td><td>26.57</td></tr>
<tr><td>Zn</td><td>0.25</td></tr>
<tr><td>As</td><td>---</td></tr>
<tr><td>Sn</td><td>---</td></tr>
<tr><td>Pb</td><td>---</td></tr>
</table>
</td>
</tr>
</table>

<table>
<tr><th colspan="3">Unsheltered samples</th></tr>
<tr><th>Sample</th><th>SEM image</th><th>EDS analysis</th></tr>
<tr>
<td>B5
Site 1</td>
<td>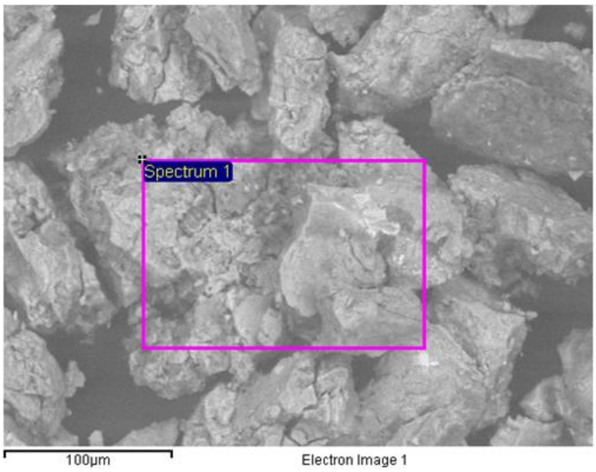
</td>
<td>
<table>
<tr><th>Element</th><th>% wt</th></tr>
<tr><td>C</td><td>13.44</td></tr>
<tr><td>O</td><td>40.60</td></tr>
<tr><td>Mg</td><td>---</td></tr>
<tr><td>Al</td><td>0.45</td></tr>
<tr><td>Si</td><td>0.87</td></tr>
<tr><td>P</td><td>3.80</td></tr>
<tr><td>S</td><td>0.51</td></tr>
<tr><td>Cl</td><td>0.49</td></tr>
<tr><td>K</td><td>---</td></tr>
<tr><td>Ca</td><td>1.14</td></tr>
<tr><td>Fe</td><td>0.38</td></tr>
<tr><td>Cu</td><td>19.61</td></tr>
<tr><td>Zn</td><td>1.58</td></tr>
<tr><td>As</td><td>0.65</td></tr>
<tr><td>Sn</td><td>16.48</td></tr>
<tr><td>Pb</td><td>---</td></tr>
</table>
</td>
</tr>
<tr>
<td>B5
Site 2</td>
<td>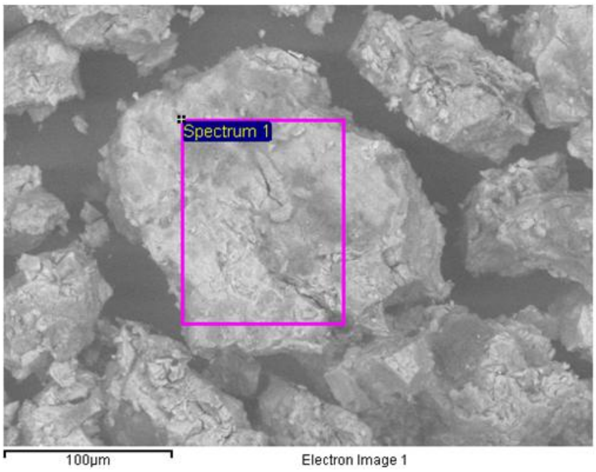
</td>
<td>
<table>
<tr><th>Element</th><th>% wt</th></tr>
<tr><td>C</td><td>12.34</td></tr>
<tr><td>O</td><td>38.52</td></tr>
<tr><td>Mg</td><td>0.31</td></tr>
<tr><td>Al</td><td>0.75</td></tr>
<tr><td>Si</td><td>1.57</td></tr>
<tr><td>P</td><td>3.83</td></tr>
<tr><td>S</td><td>0.34</td></tr>
<tr><td>Cl</td><td>0.49</td></tr>
<tr><td>K</td><td>---</td></tr>
<tr><td>Ca</td><td>1.30</td></tr>
<tr><td>Fe</td><td>0.66</td></tr>
<tr><td>Cu</td><td>17.53</td></tr>
<tr><td>Zn</td><td>2.49</td></tr>
<tr><td>As</td><td>---</td></tr>
<tr><td>Sn</td><td>19.87</td></tr>
<tr><td>Pb</td><td>---</td></tr>
</table>
</td>
</tr>
</table>

B5
Site 3

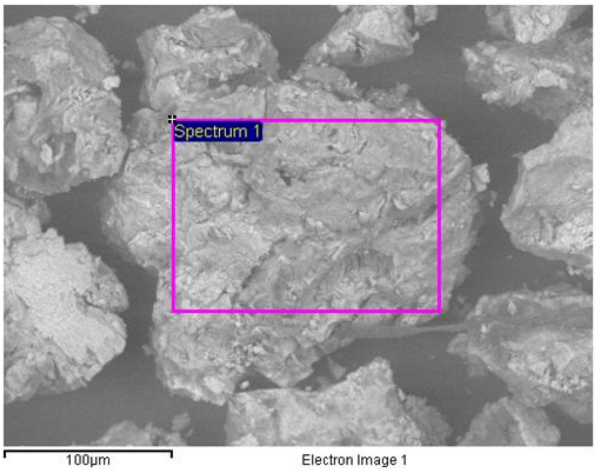

Element	% wt
C	15.00
O	37.01
Mg	---
Al	0.30
Si	0.41
P	2.19
S	1.41
Cl	0.46
K	---
Ca	0.55
Fe	0.28
Cu	27.41
Zn	1.26
As	---
Sn	13.73
Pb	---

B6
Site 1

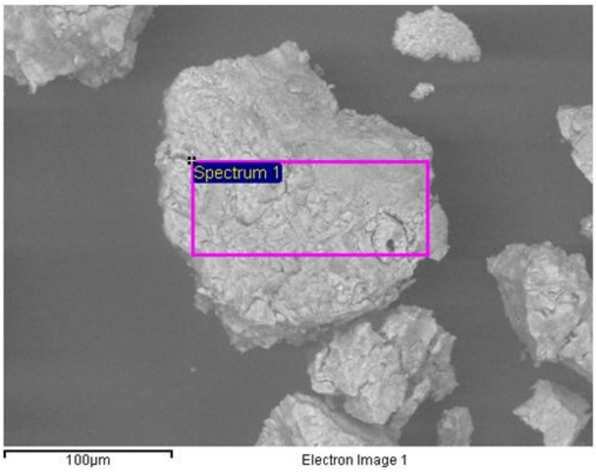

Element	% wt
C	25.58
O	39.08
Mg	---
Al	---
Si	0.16
P	1.59
S	1.42
Cl	0.16
K	---
Ca	0.31
Fe	0.20
Cu	18.48
Zn	---
As	---
Sn	13.02
Pb	---

B6
Site 2

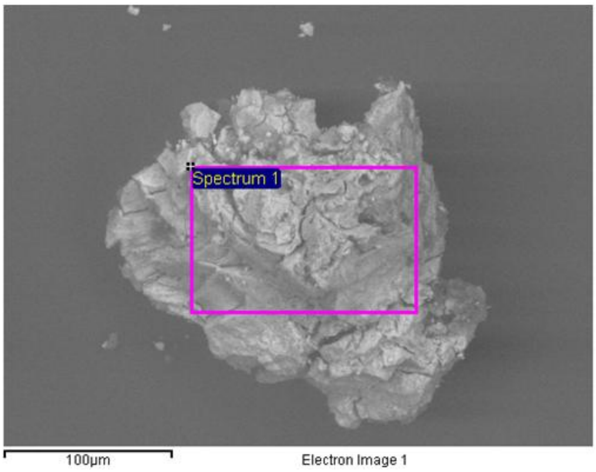

Element	% wt
C	43.68
O	30.04
Mg	---
Al	0.18
Si	---
P	1.37
S	0.54
Cl	0.22
K	---
Ca	0.50
Fe	---
Cu	14.59
Zn	0.69
As	0.49
Sn	7.70
Pb	---

B6
Site 3

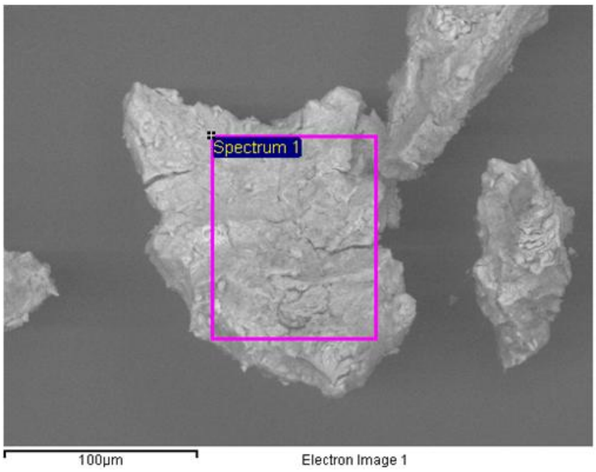

Element	% wt
C	36.68
O	29.79
Mg	---
Al	---
Si	---
P	1.70
S	0.85
Cl	0.48
K	---
Ca	0.54
Fe	---
Cu	21.55
Zn	0.76
As	---
Sn	7.64
Pb	---

B7
Site 2
Spec 1

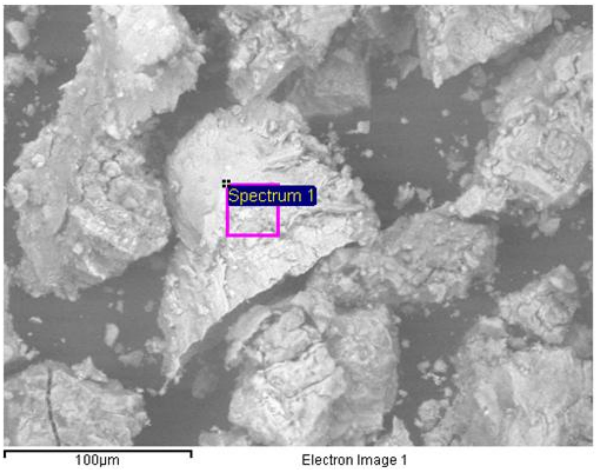

Element	% wt
C	15.68
O	17.03
Mg	---
Al	---
Si	---
P	0.61
S	0.50
Cl	4.35
K	---
Ca	---
Fe	---
Cu	45.98
Zn	1.25
As	---
Sn	11.36
Pb	3.23

B7
Site 2
Spec 2

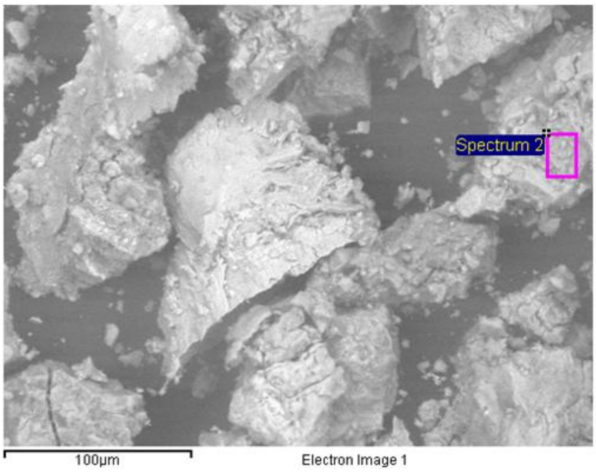

Element	% wt
C	15.06
O	33.07
Mg	---
Al	0.25
Si	0.28
P	3.21
S	0.74
Cl	0.47
K	---
Ca	0.99
Fe	0.26
Cu	25.04
Zn	1.49
As	0.57
Sn	18.58
Pb	---

B7
Site 3

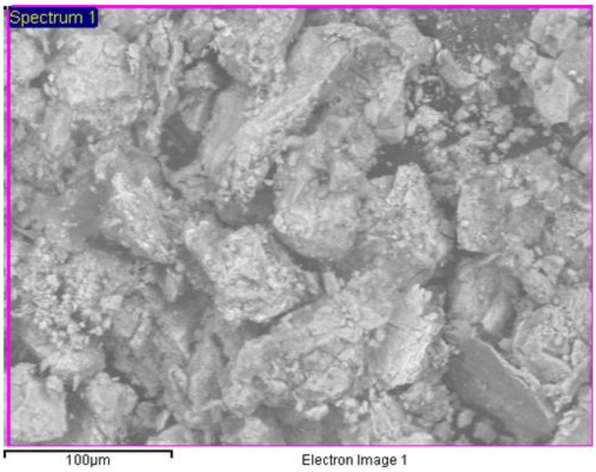

Element	% wt
C	17.56
O	34.87
Mg	---
Al	---
Si	0.45
P	3.08
S	0.55
Cl	0.55
K	---
Ca	0.96
Fe	0.35
Cu	24.98
Zn	1.50
As	0.56
Sn	14.58
Pb	---

B7
Site 4

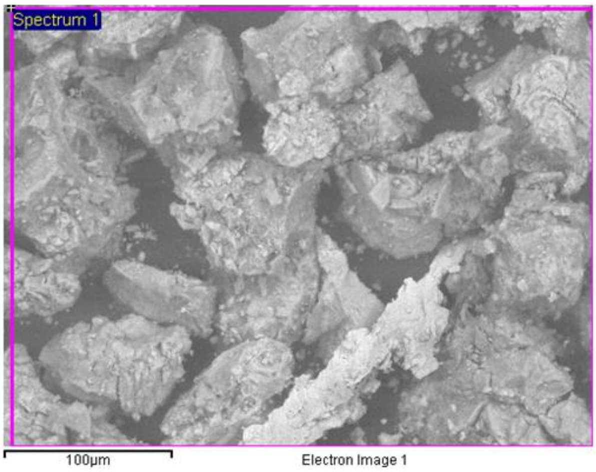

Element	% wt
C	21.21
O	33.63
Mg	---
Al	---
Si	0.35
P	2.59
S	0.69
Cl	0.47
K	---
Ca	0.62
Fe	---
Cu	24.60
Zn	1.40
As	0.66
Sn	13.76
Pb	---

SEM-EDS analysis – Omo corrosion products

<table>
<tr><th colspan="3">Sheltered samples</th></tr>
<tr><th>Sample</th><th>SEM image</th><th>EDS analysis</th></tr>
<tr><td>O6</td><td>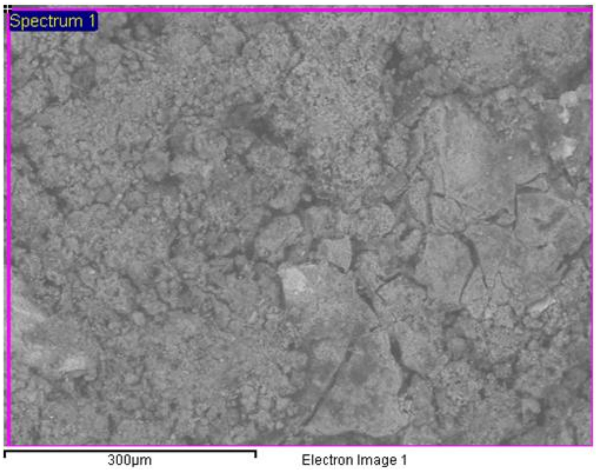
</td><td>
<table>
<tr><th>Element</th><th>% wt</th></tr>
<tr><td>C</td><td>21.91</td></tr>
<tr><td>O</td><td>35.85</td></tr>
<tr><td>Mg</td><td>0.63</td></tr>
<tr><td>Al</td><td>1.69</td></tr>
<tr><td>Si</td><td>5.03</td></tr>
<tr><td>P</td><td>1.61</td></tr>
<tr><td>S</td><td>1.79</td></tr>
<tr><td>Cl</td><td>0.67</td></tr>
<tr><td>K</td><td>0.25</td></tr>
<tr><td>Ca</td><td>1.27</td></tr>
<tr><td>Fe</td><td>2.99</td></tr>
<tr><td>Cu</td><td>26.32</td></tr>
<tr><td>Zn</td><td>---</td></tr>
<tr><td>As</td><td>---</td></tr>
<tr><td>Sn</td><td>---</td></tr>
<tr><td>Pb</td><td>---</td></tr>
</table></td></tr>
<tr><td>O7</td><td>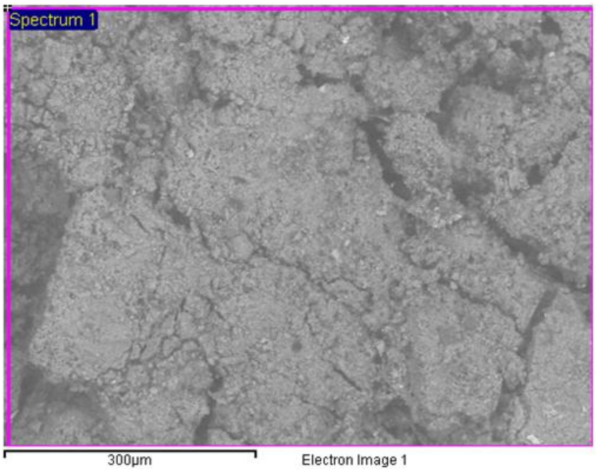
</td><td>
<table>
<tr><th>Element</th><th>% wt</th></tr>
<tr><td>C</td><td>19.11</td></tr>
<tr><td>O</td><td>36.24</td></tr>
<tr><td>Mg</td><td>0.72</td></tr>
<tr><td>Al</td><td>1.43</td></tr>
<tr><td>Si</td><td>5.24</td></tr>
<tr><td>P</td><td>1.58</td></tr>
<tr><td>S</td><td>1.79</td></tr>
<tr><td>Cl</td><td>0.81</td></tr>
<tr><td>K</td><td>0.37</td></tr>
<tr><td>Ca</td><td>1.05</td></tr>
<tr><td>Fe</td><td>3.09</td></tr>
<tr><td>Cu</td><td>28.57</td></tr>
<tr><td>Zn</td><td>---</td></tr>
<tr><td>As</td><td>---</td></tr>
<tr><td>Sn</td><td>---</td></tr>
<tr><td>Pb</td><td>---</td></tr>
</table></td></tr>
</table>

Unsheltered samples

Sample	SEM image	EDS analysis	
		Element	**% wt**
O3 Site 1	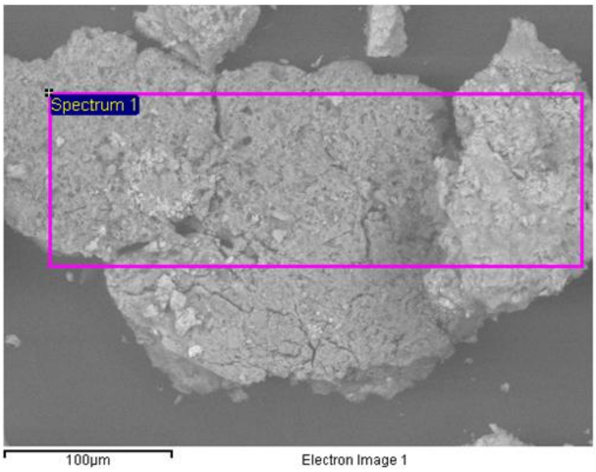	**C**	29.56
		O	35.61
		Mg	---
		Al	0.51
		Si	1.27
		P	0.53
		S	1.89
		Cl	---
		K	---
		Ca	---
		Fe	1.07
		Cu	25.01
		Zn	---
		As	---
		Sn	4.56
		Pb	---
		Element	**% wt**
O3 Site 2	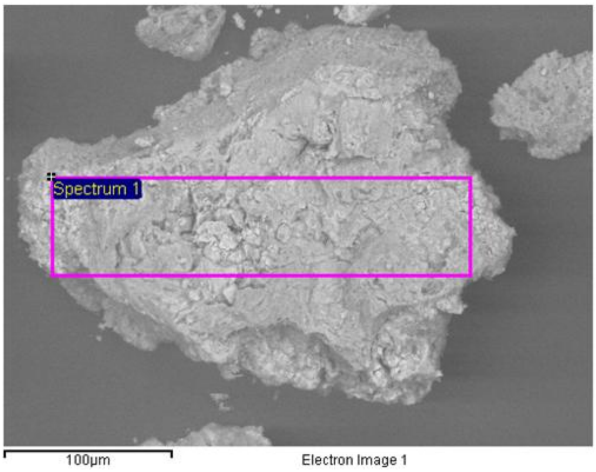	**C**	34.30
		O	30.47
		Mg	---
		Al	0.18
		Si	0.20
		P	0.43
		S	1.32
		Cl	---
		K	---
		Ca	---
		Fe	0.21
		Cu	20.84
		Zn	---
		As	0.65
		Sn	11.40
		Pb	---

O3
Site 3

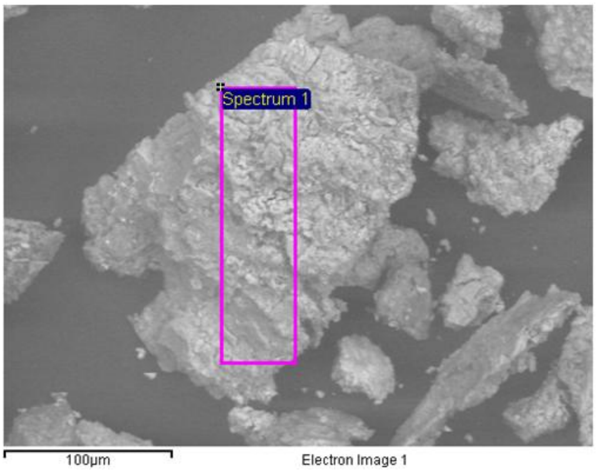

Element	% wt
C	26.02
O	30.50
Mg	---
Al	0.23
Si	0.43
P	0.87
S	1.07
Cl	---
K	---
Ca	---
Fe	0.33
Cu	25.00
Zn	---
As	1.07
Sn	14.48
Pb	---

O4
Site 1

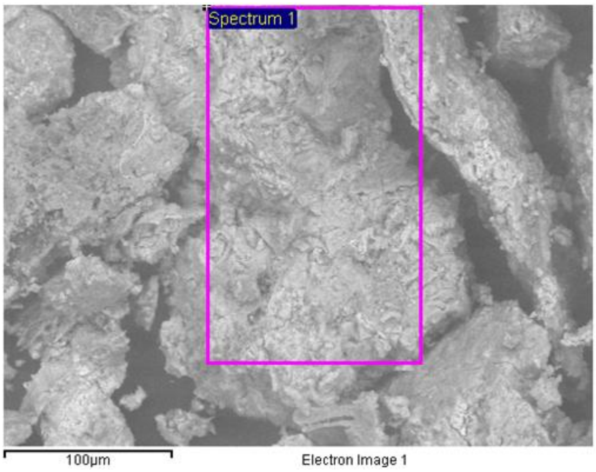

Element	% wt
C	13.29
O	30.76
Mg	---
Al	2.43
Si	0.57
P	0.81
S	1.97
Cl	---
K	---
Ca	---
Fe	0.58
Cu	38.46
Zn	---
As	---
Sn	11.11
Pb	---

O4
Site 3

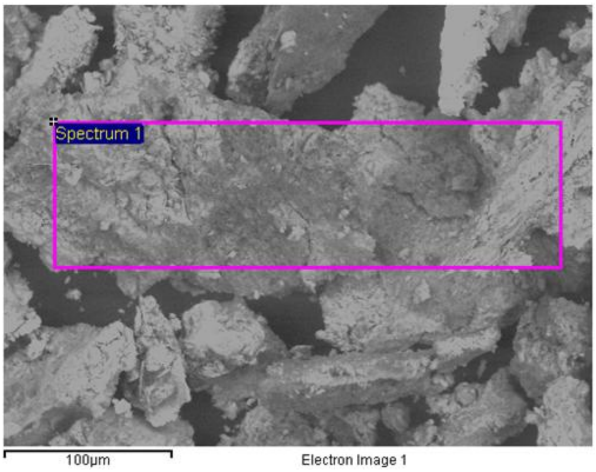

Element	% wt
C	14.02
O	32.14
Mg	---
Al	2.10
Si	1.18
P	0.78
S	1.90
Cl	0.19
K	---
Ca	---
Fe	1.12
Cu	37.62
Zn	---
As	0.70
Sn	8.25
Pb	---

O4
Site 4

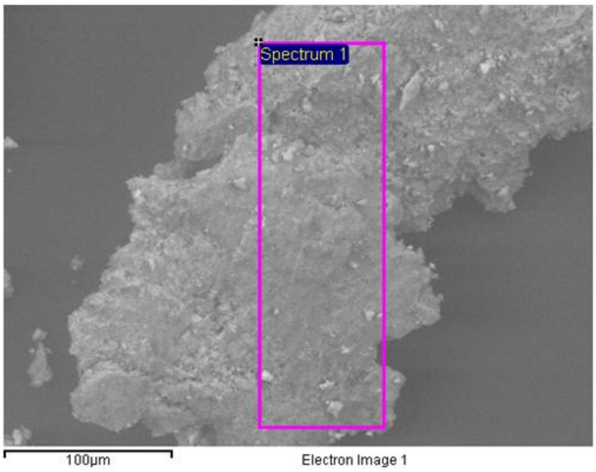

Element	% wt
C	28.59
O	39.94
Mg	0.28
Al	1.02
Si	2.03
P	0.81
S	2.21
Cl	---
K	---
Ca	0.17
Fe	1.86
Cu	22.03
Zn	---
As	---
Sn	1.05
Pb	---

O5
Site 1

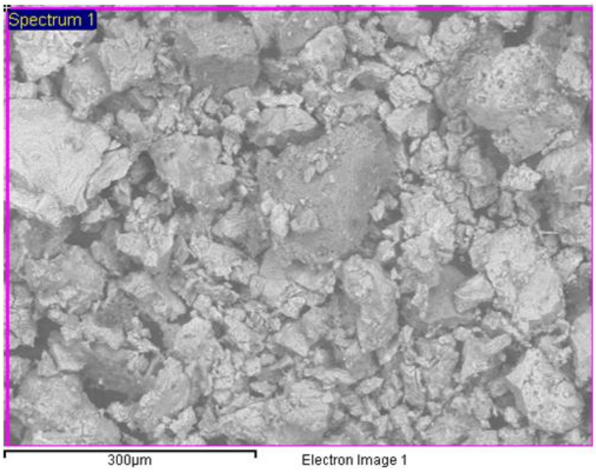

Element	% wt
C	8.44
O	36.89
Mg	---
Al	1.17
Si	0.78
P	2.21
S	1.20
Cl	0.59
K	---
Ca	---
Fe	0.70
Cu	32.85
Zn	---
As	0.72
Sn	14.44
Pb	---

O8
Soldering
material
Site 1

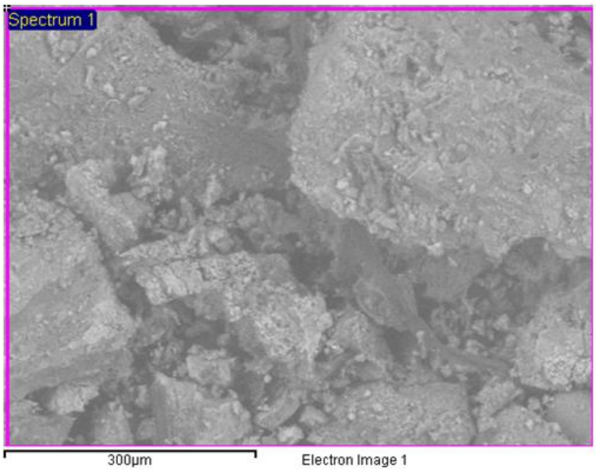

Element	% wt
C	11.40
O	52.25
Mg	0.95
Al	1.88
Si	7.75
P	---
S	0.65
Cl	---
K	0.15
Ca	18.45
Fe	1.97
Cu	4.74
Zn	---
As	---
Sn	---
Pb	---

SEM-EDS analysis – Shield handle corrosion products

<table>
<tr><th>Sample</th><th>SEM image</th><th>EDS analysis</th></tr>
<tr>
<td>Alloy
Site 1
Spec 1</td>
<td>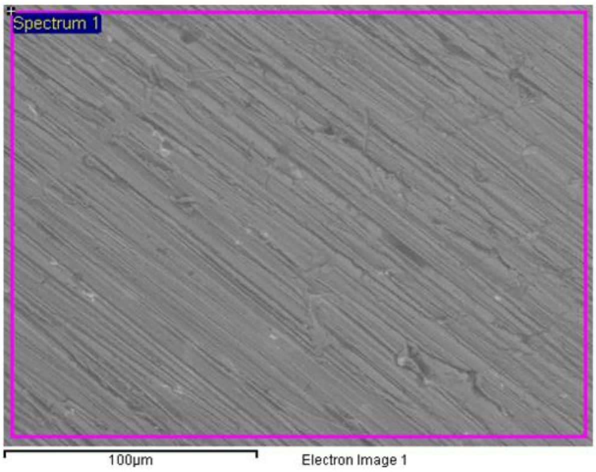
</td>
<td>
<table>
<tr><th>Element</th><th>% wt</th></tr>
<tr><td>C</td><td>---</td></tr>
<tr><td>O</td><td>32.30</td></tr>
<tr><td>Mg</td><td>---</td></tr>
<tr><td>Al</td><td>0.51</td></tr>
<tr><td>Si</td><td>0.85</td></tr>
<tr><td>P</td><td>---</td></tr>
<tr><td>S</td><td>3.04</td></tr>
<tr><td>Cl</td><td>0.68</td></tr>
<tr><td>K</td><td>---</td></tr>
<tr><td>Ca</td><td>---</td></tr>
<tr><td>Fe</td><td>0.51</td></tr>
<tr><td>Ni</td><td>---</td></tr>
<tr><td>Cu</td><td>48.11</td></tr>
<tr><td>Zn</td><td>2.84</td></tr>
<tr><td>As</td><td>---</td></tr>
<tr><td>Sn</td><td>7.29</td></tr>
<tr><td>Sb</td><td>---</td></tr>
<tr><td>Pb</td><td>3.87</td></tr>
</table>
</td>
</tr>
<tr>
<td>Alloy
Site 1
Spec 2</td>
<td>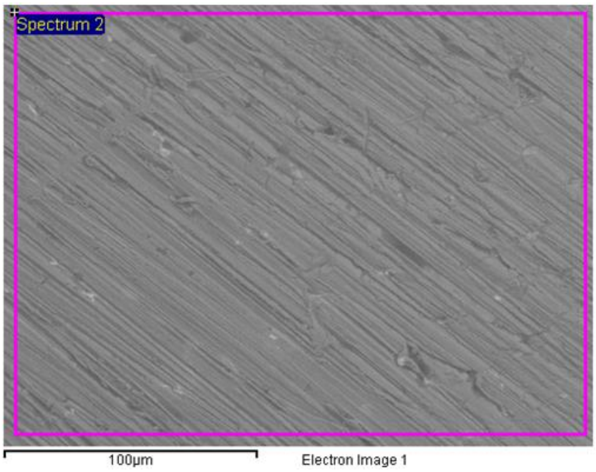
</td>
<td>
<table>
<tr><th>Element</th><th>% wt</th></tr>
<tr><td>C</td><td>---</td></tr>
<tr><td>O</td><td>5.44</td></tr>
<tr><td>Mg</td><td>---</td></tr>
<tr><td>Al</td><td>0.50</td></tr>
<tr><td>Si</td><td>---</td></tr>
<tr><td>P</td><td>---</td></tr>
<tr><td>S</td><td>0.35</td></tr>
<tr><td>Cl</td><td>---</td></tr>
<tr><td>K</td><td>---</td></tr>
<tr><td>Ca</td><td>---</td></tr>
<tr><td>Fe</td><td>0.46</td></tr>
<tr><td>Ni</td><td>0.28</td></tr>
<tr><td>Cu</td><td>77.47</td></tr>
<tr><td>Zn</td><td>9.73</td></tr>
<tr><td>Sn</td><td>4.02</td></tr>
<tr><td>Sb</td><td>0.29</td></tr>
<tr><td>Pb</td><td>1.47</td></tr>
</table>
</td>
</tr>
</table>

Corrosion product right side (rivet side) Site 1

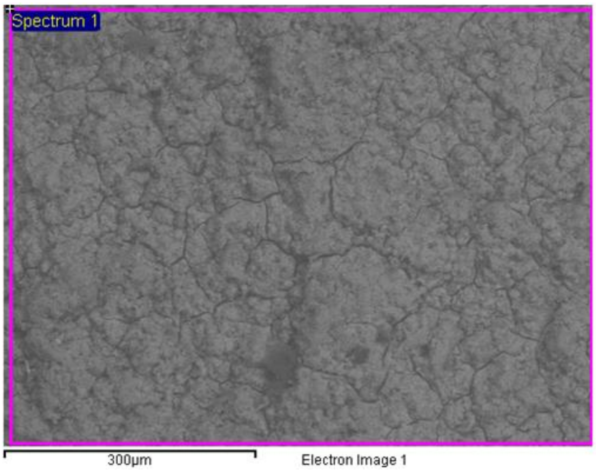

Element	% wt
C	---
O	38.37
Mg	0.95
Al	2.25
Si	6.21
P	3.33
S	2.57
Cl	0.56
K	0.61
Ca	1.15
Fe	3.04
Ni	---
Cu	36.91
Zn	4.05
As	---
Sn	---
Sb	---
Pb	---

Corrosion product right side (rivet side) Site 3 Spec 2

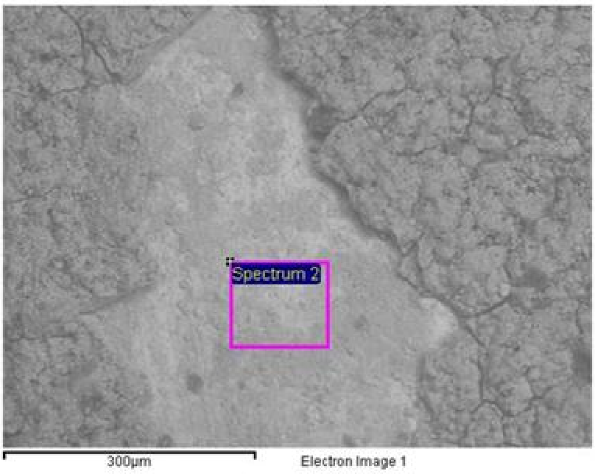

Element	% wt
C	---
O	31.98
Mg	---
Al	1.14
Si	2.63
P	1.10
S	3.39
Cl	0.43
K	---
Ca	0.35
Fe	1.83
Ni	---
Cu	45.33
Zn	11.82
As	---
Sn	---
Sb	---
Pb	---

Corrosion product right side (rivet side) Site 3 Spec 3

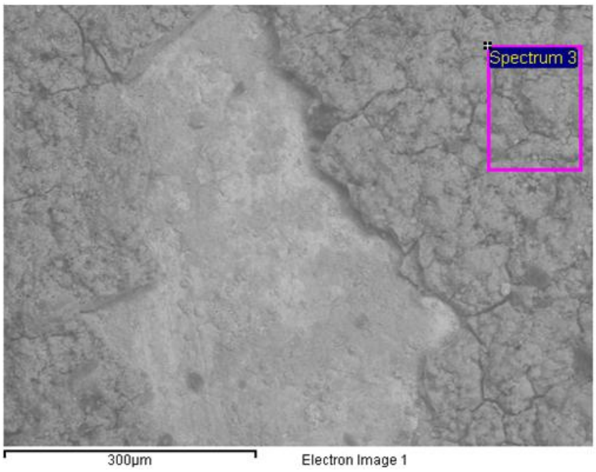

Element	% wt
C	---
O	37.84
Mg	0.55
Al	2.19
Si	6.59
P	3.30
S	1.94
Cl	0.54
K	0.57
Ca	0.87
Fe	3.25
Ni	---
Cu	39.23
Zn	3.12
As	---
Sn	---
Sb	---
Pb	---

Corrosion product left side (rivet side)

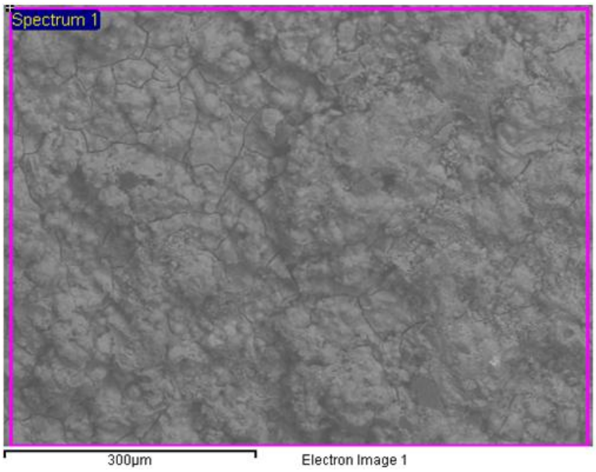

Element	% wt
C	---
O	35.52
Mg	---
Al	1.39
Si	3.20
P	1.79
S	4.41
Cl	0.70
K	0.30
Ca	0.51
Fe	1.27
Ni	---
Cu	47.29
Zn	3.62
As	---
Sn	---
Sb	---
Pb	---

Rivet fracture Site 1

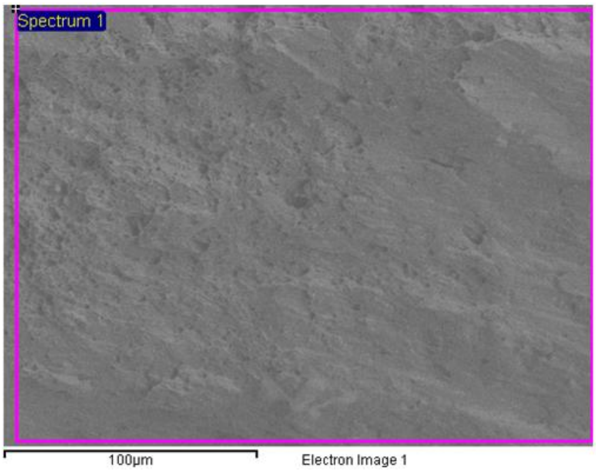

Element	% wt
C	---
O	2.97
Mg	---
Al	---
Si	---
P	---
S	---
Cl	---
K	---
Ca	---
Fe	---
Ni	---
Cu	51.76
Zn	34.93
As	---
Sn	---
Sb	---
Pb	10.33

Rivet fracture Site 2

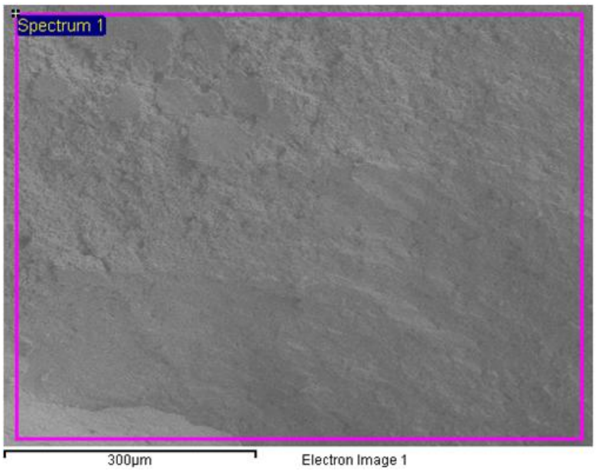

Element	% wt
C	---
O	2.65
Mg	---
Al	---
Si	---
P	---
S	---
Cl	---
K	---
Ca	---
Fe	---
Ni	---
Cu	52.87
Zn	36.09
As	---
Sn	---
Sb	---
Pb	8.39

Rivet fracture Site 3 Spec 1

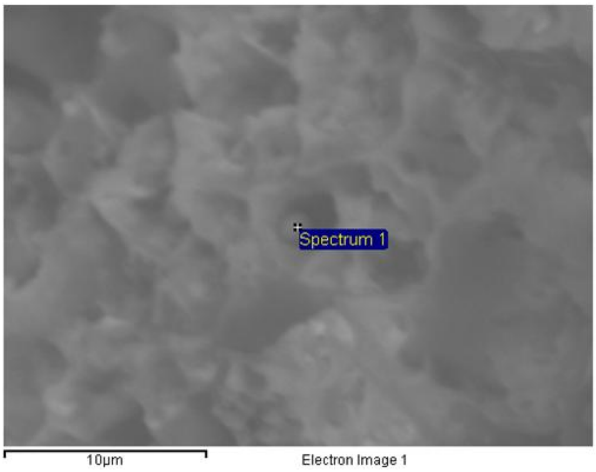

Element	% wt
C	---
O	7.47
Mg	---
Al	---
Si	2.21
P	---
S	---
Cl	---
K	---
Ca	1.38
Fe	0.75
Ni	---
Cu	43.34
Zn	42.78
As	---
Sn	---
Sb	---
Pb	2.07

Rivet fracture Site 3 Spec 2

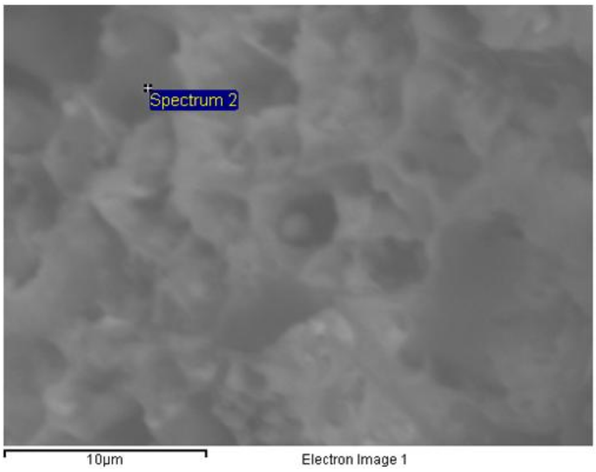

Element	% wt
C	---
O	9.00
Mg	---
Al	0.87
Si	2.32
P	---
S	0.34
Cl	---
K	0.37
Ca	1.44
Fe	0.76
Ni	---
Cu	51.01
Zn	31.77
As	---
Sn	---
Sb	---
Pb	2.12

SEM-EDS analyses – Wet & dry samples before exposure

<table>
<tr><th>Coupon</th><th>SEM image</th><th>EDS analysis</th></tr>
<tr>
<td>A-NI

Aged
Non
inhibited

Site 2
Spec 1</td>
<td>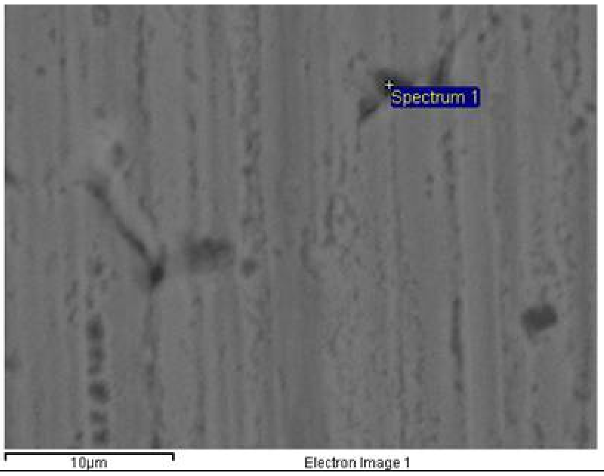
Sn-rich area</td>
<td><table>
<tr><th>Element</th><th>% wt</th></tr>
<tr><td>C</td><td>---</td></tr>
<tr><td>O</td><td>5.64</td></tr>
<tr><td>Al</td><td>---</td></tr>
<tr><td>Si</td><td>---</td></tr>
<tr><td>S</td><td>---</td></tr>
<tr><td>Cl</td><td>---</td></tr>
<tr><td>Cu</td><td>91.13</td></tr>
<tr><td>Zn</td><td>---</td></tr>
<tr><td>Sn</td><td>3.23</td></tr>
<tr><td>Pb</td><td>---</td></tr>
<tr><td>Sb</td><td>---</td></tr>
</table></td>
</tr>
<tr>
<td>A-NI

Aged
Non
inhibited

Site 2
Spec 2</td>
<td>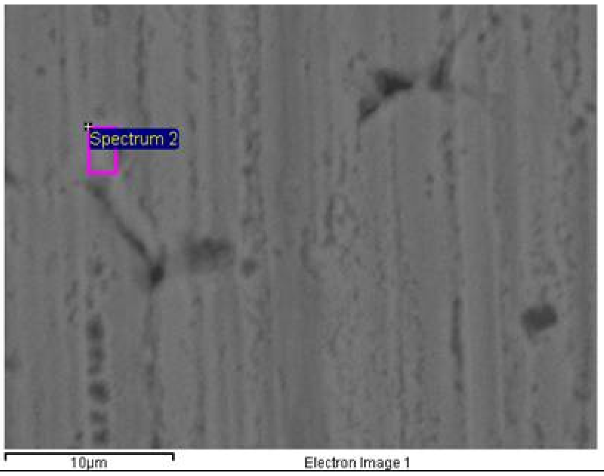
Pb-rich area</td>
<td><table>
<tr><th>Element</th><th>% wt</th></tr>
<tr><td>C</td><td>---</td></tr>
<tr><td>O</td><td>10.44</td></tr>
<tr><td>Al</td><td>---</td></tr>
<tr><td>Si</td><td>---</td></tr>
<tr><td>S</td><td>---</td></tr>
<tr><td>Cl</td><td>---</td></tr>
<tr><td>Cu</td><td>71.63</td></tr>
<tr><td>Zn</td><td>---</td></tr>
<tr><td>Sn</td><td>2.80</td></tr>
<tr><td>Pb</td><td>15.13</td></tr>
<tr><td>Sb</td><td>---</td></tr>
</table></td>
</tr>
</table>

A-NI

Aged
Non
inhibited

Site 2
Spec 3

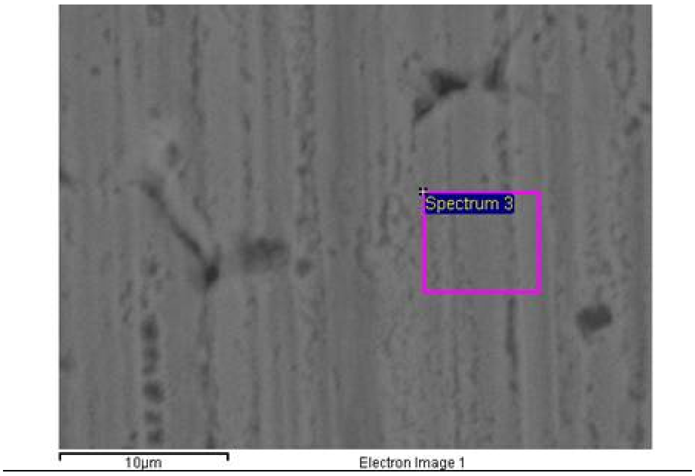

Cu-rich matrix

Element	% wt
C	---
O	8.52
Al	---
Si	---
S	---
Cl	---
Cu	87.35
Zn	1.62
Sn	2.51
Pb	---
Sb	---

A-NI

Aged
Non
inhibited

Site 2
Spec 4

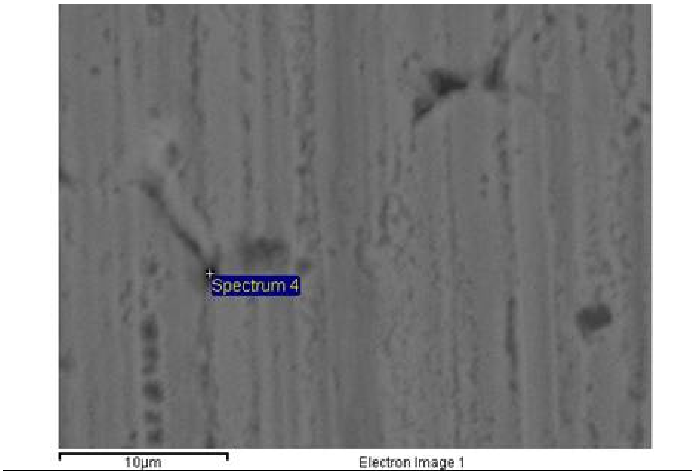

Presence of Sb

Element	% wt
C	---
O	5.56
Al	---
Si	---
S	---
Cl	---
Cu	90.48
Zn	---
Sn	2.81
Pb	---
Sb	1.16

A-NI

Aged
Non
inhibited

Site 2
Spec 5

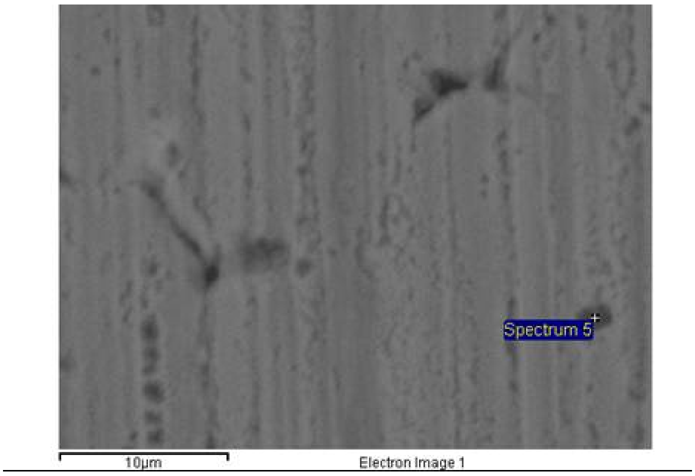

Presence of Al

Element	% wt
C	---
O	17.00
Al	15.24
Si	---
S	---
Cl	---
Cu	64.33
Zn	1.24
Sn	2.20
Pb	---
Sb	---

NA-P

Not aged
PropS-SH

Site 1
Spec 1

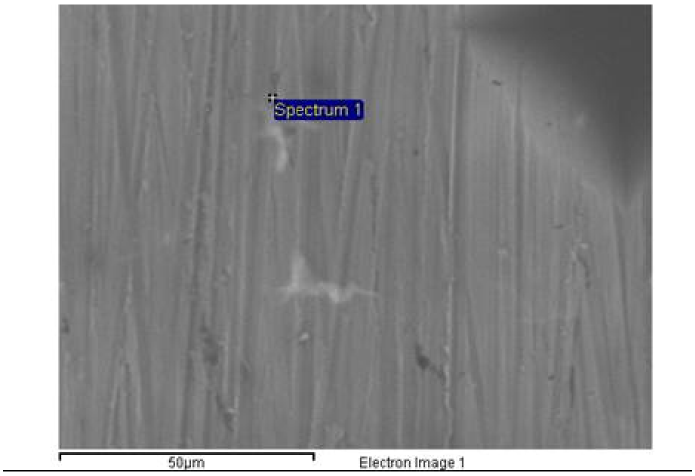

Pb-rich globule with inhibitor film

Element	% wt
C	17.76
O	15.49
Al	---
Si	8.58
S	7.59
Cl	---
Cu	33.21
Zn	---
Sn	1.15
Pb	16.22
Sb	---

NA-P

Not aged
PropS-SH

Site 1
Spec 2

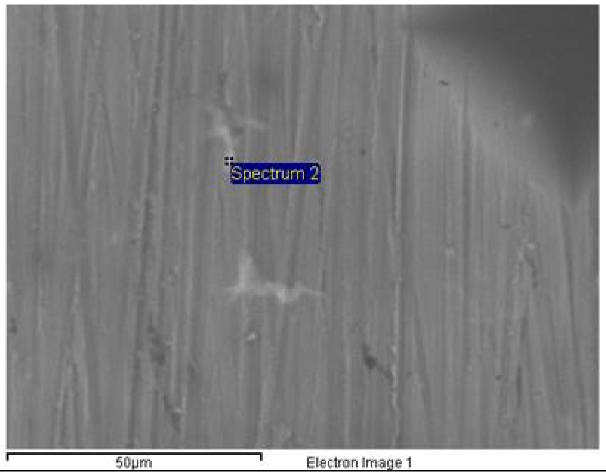

Pb-rich globule with inhibitor film

Element	% wt
C	15.91
O	15.25
Al	---
Si	6.66
S	6.02
Cl	---
Cu	35.00
Zn	---
Sn	1.22
Pb	19.94
Sb	---

NA-P

Not aged
PropS-SH

Site 1
Spec 3

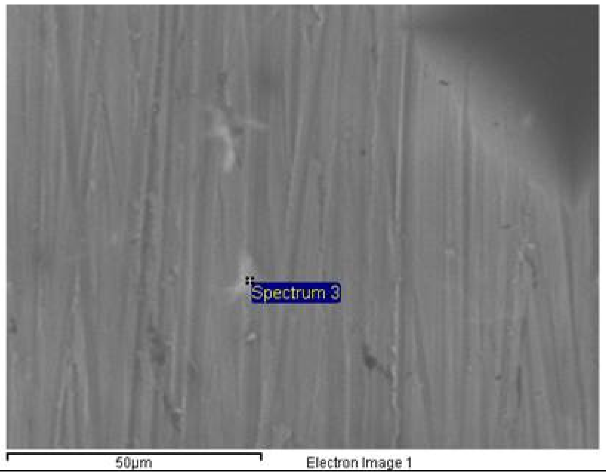

Pb-rich globule with inhibitor film

Element	% wt
C	16.82
O	14.41
Al	---
Si	6.56
S	5.94
Cl	0.48
Cu	30.99
Zn	1.09
Sn	---
Pb	23.70
Sb	---

NA-P

Not aged
PropS-SH

Site 1
Spec 4

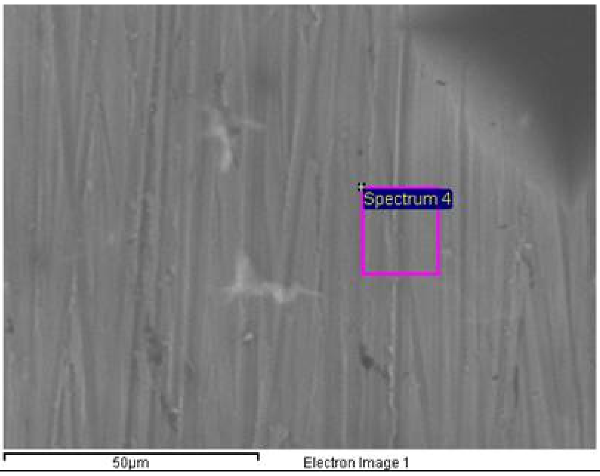

Cu-rich matrix with inhibitor film

Element	% wt
C	17.61
O	11.77
Al	---
Si	7.10
S	4.91
Cl	---
Cu	55.75
Zn	1.53
Sn	1.33
Pb	---
Sb	---

NA-P

Not aged
PropS-SH

Site 1
Spec 5

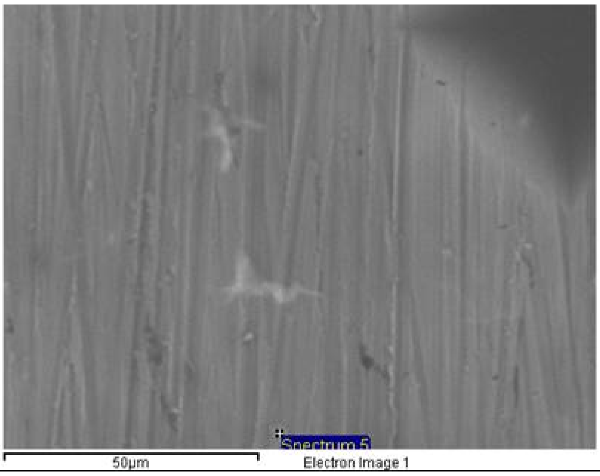

Cu-rich matrix with inhibitor film

Element	% wt
C	15.90
O	12.60
Al	---
Si	7.05
S	5.41
Cl	---
Cu	55.69
Zn	1.78
Sn	1.56
Pb	---
Sb	---

NA-P

Not aged
PropS-SH

Site 2
Spec 1

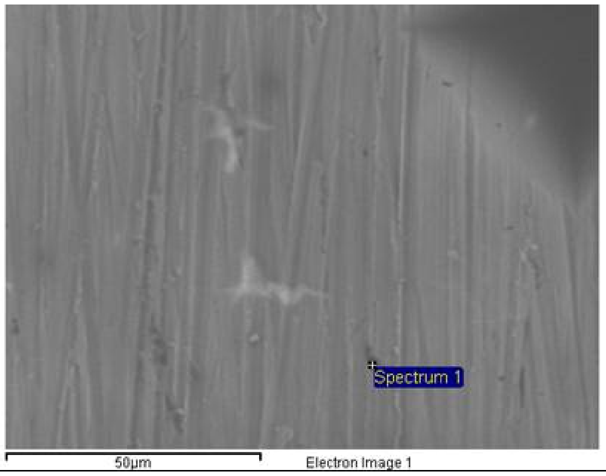

Presence of Al

Element	% wt
C	18.18
O	13.66
Al	10.76
Si	6.65
S	4.76
Cl	---
Cu	45.10
Zn	---
Sn	0.88
Pb	---
Sb	---

SEM-EDS analyses – Wet & dry samples after exposure

<table>
<tr><th>Coupon</th><th>SEM image</th><th>EDS analysis</th></tr>
<tr><td>A-NI

Aged
Non
inhibited

Site 2
Spec 1</td><td>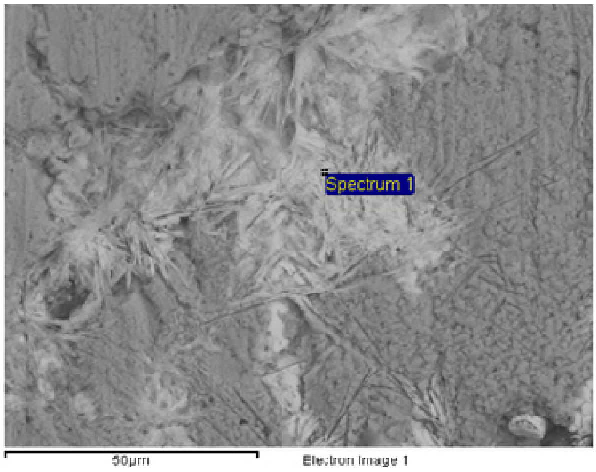
</td><td><table>
<tr><th>Element</th><th>% wt</th></tr>
<tr><td>C</td><td>---</td></tr>
<tr><td>O</td><td>15.99</td></tr>
<tr><td>Al</td><td>---</td></tr>
<tr><td>Si</td><td>---</td></tr>
<tr><td>S</td><td>---</td></tr>
<tr><td>Cl</td><td>---</td></tr>
<tr><td>Cu</td><td>34.25</td></tr>
<tr><td>Zn</td><td>---</td></tr>
<tr><td>Sn</td><td>---</td></tr>
<tr><td>Pb</td><td>49.75</td></tr>
<tr><td>Sb</td><td>---</td></tr>
</table></td></tr>
<tr><td>1
Aged
Not
inhibited
Site 2
Spec 2</td><td>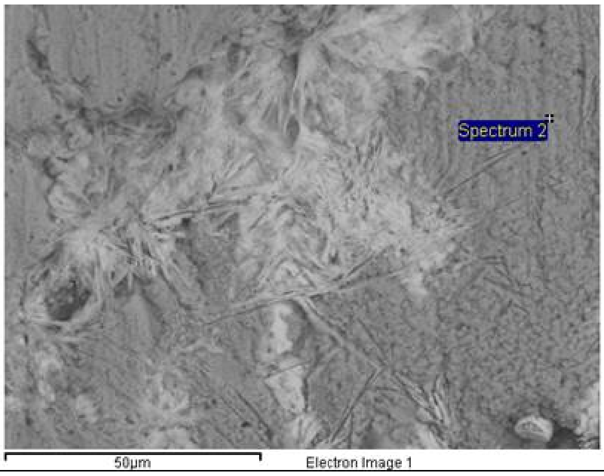
</td><td><table>
<tr><th>Element</th><th>% wt</th></tr>
<tr><td>C</td><td>---</td></tr>
<tr><td>O</td><td>11.73</td></tr>
<tr><td>Al</td><td>---</td></tr>
<tr><td>Si</td><td>---</td></tr>
<tr><td>S</td><td>---</td></tr>
<tr><td>Cl</td><td>---</td></tr>
<tr><td>Cu</td><td>84.49</td></tr>
<tr><td>Zn</td><td>---</td></tr>
<tr><td>Sn</td><td>1.43</td></tr>
<tr><td>Pb</td><td>2.35</td></tr>
<tr><td>Sb</td><td>---</td></tr>
</table></td></tr>
</table>

<table>
<tr>
<td>A-NI

Aged
Non
inhibited

Site 3
Spec 1</td>
<td>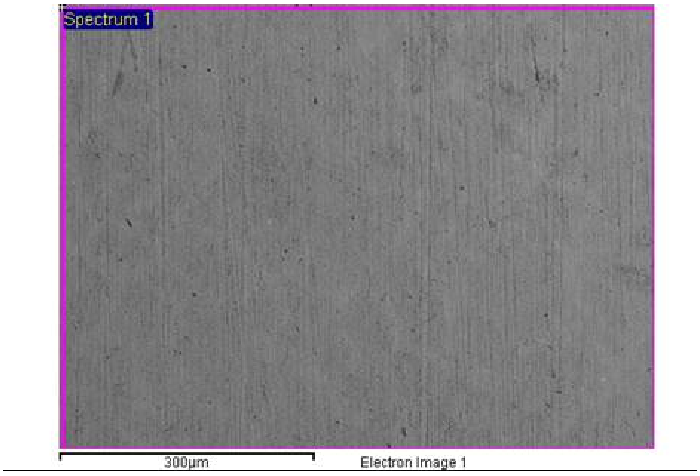
</td>
<td>
<table>
<tr><th>Element</th><th>% wt</th></tr>
<tr><td>C</td><td>---</td></tr>
<tr><td>O</td><td>9.64</td></tr>
<tr><td>Al</td><td>---</td></tr>
<tr><td>Si</td><td>---</td></tr>
<tr><td>S</td><td>---</td></tr>
<tr><td>Cl</td><td>---</td></tr>
<tr><td>Cu</td><td>87.57</td></tr>
<tr><td>Zn</td><td>---</td></tr>
<tr><td>Sn</td><td>2.14</td></tr>
<tr><td>Pb</td><td>0.66</td></tr>
<tr><td>Sb</td><td>---</td></tr>
</table>
</td>
</tr>
<tr>
<td>NA-P

Not aged
PropS-SH

Site 1
Spec 1</td>
<td>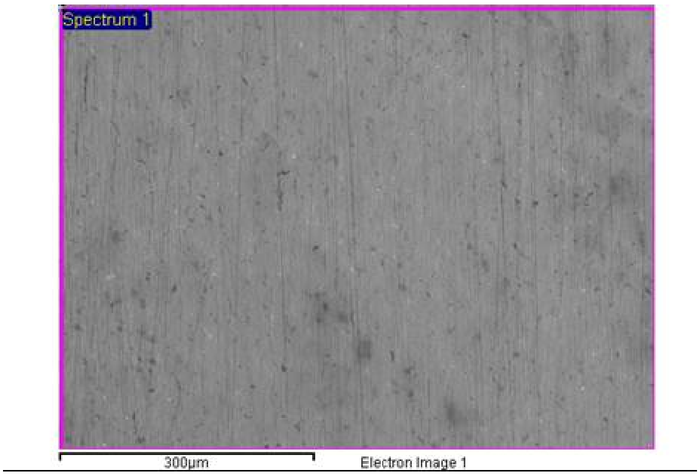
</td>
<td>
<table>
<tr><th>Element</th><th>% wt</th></tr>
<tr><td>C</td><td>19.57</td></tr>
<tr><td>O</td><td>10.97</td></tr>
<tr><td>Al</td><td>---</td></tr>
<tr><td>Si</td><td>4.29</td></tr>
<tr><td>S</td><td>3.07</td></tr>
<tr><td>Cl</td><td>---</td></tr>
<tr><td>Cu</td><td>58.52</td></tr>
<tr><td>Zn</td><td>1.16</td></tr>
<tr><td>Sn</td><td>1.62</td></tr>
<tr><td>Pb</td><td>---</td></tr>
<tr><td>Sb</td><td>0.80</td></tr>
</table>
</td>
</tr>
<tr>
<td>NA-P

Not aged
PropS-SH

Site 2
Spec 1</td>
<td>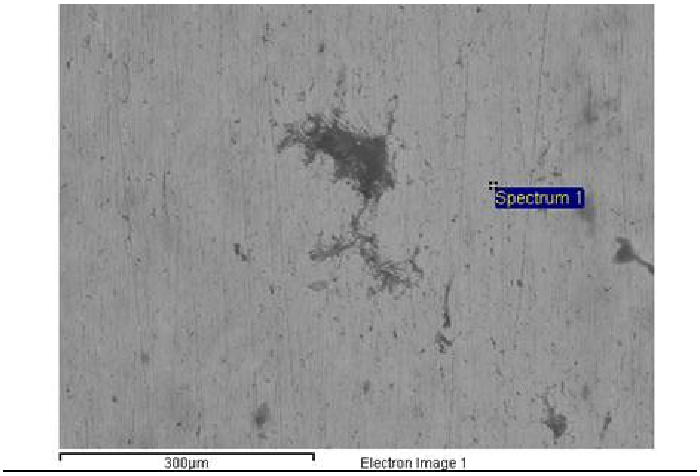
</td>
<td>
<table>
<tr><th>Element</th><th>% wt</th></tr>
<tr><td>C</td><td>18.15</td></tr>
<tr><td>O</td><td>9.17</td></tr>
<tr><td>Al</td><td>---</td></tr>
<tr><td>Si</td><td>2.92</td></tr>
<tr><td>S</td><td>2.13</td></tr>
<tr><td>Cl</td><td>---</td></tr>
<tr><td>Cu</td><td>63.37</td></tr>
<tr><td>Zn</td><td>---</td></tr>
<tr><td>Sn</td><td>2.72</td></tr>
<tr><td>Pb</td><td>---</td></tr>
<tr><td>Sb</td><td>1.55</td></tr>
</table>
</td>
</tr>
</table>

<table>
<tr>
<td>NA-P
Not aged
PropS-SH
Site 2
Spec 2</td>
<td>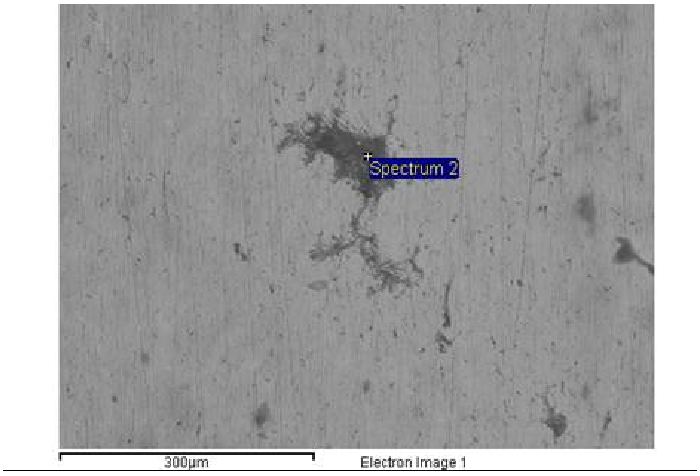
</td>
<td><table>
<tr><th>Element</th><th>% wt</th></tr>
<tr><td>C</td><td>21.59</td></tr>
<tr><td>O</td><td>10.66</td></tr>
<tr><td>Al</td><td>---</td></tr>
<tr><td>Si</td><td>4.18</td></tr>
<tr><td>S</td><td>2.99</td></tr>
<tr><td>Cl</td><td>---</td></tr>
<tr><td>Cu</td><td>59.20</td></tr>
<tr><td>Zn</td><td>---</td></tr>
<tr><td>Sn</td><td>1.38</td></tr>
<tr><td>Pb</td><td>---</td></tr>
<tr><td>Sb</td><td>---</td></tr>
</table></td>
</tr>
<tr>
<td>NA-P
Not aged
PropS-SH
Site 4
Spec 1</td>
<td>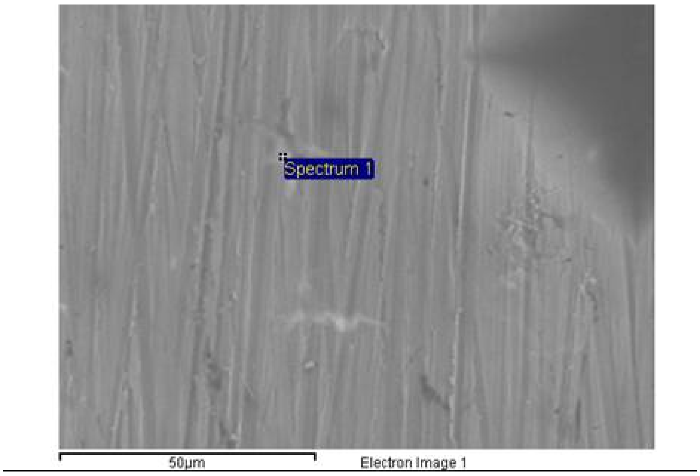
</td>
<td><table>
<tr><th>Element</th><th>% wt</th></tr>
<tr><td>C</td><td>19.45</td></tr>
<tr><td>O</td><td>18.50</td></tr>
<tr><td>Al</td><td>---</td></tr>
<tr><td>Si</td><td>6.91</td></tr>
<tr><td>S</td><td>6.67</td></tr>
<tr><td>Cl</td><td>---</td></tr>
<tr><td>Cu</td><td>26.83</td></tr>
<tr><td>Zn</td><td>---</td></tr>
<tr><td>Sn</td><td>0.64</td></tr>
<tr><td>Pb</td><td>21.01</td></tr>
<tr><td>Sb</td><td>---</td></tr>
</table></td>
</tr>
<tr>
<td>NA-P
Not aged
PropS-SH
Site 4
Spec 2</td>
<td>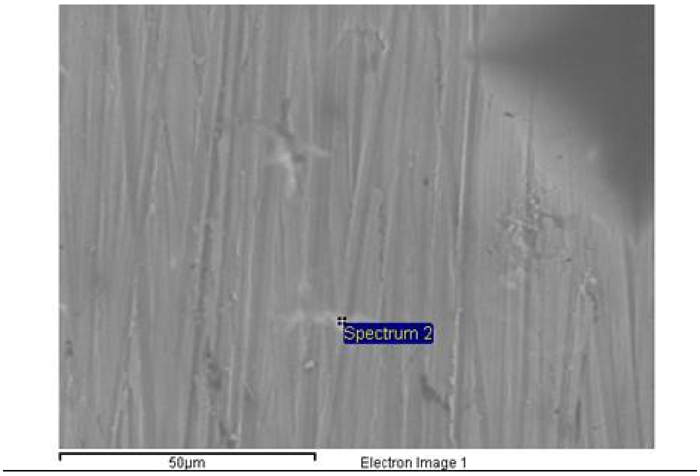
</td>
<td><table>
<tr><th>Element</th><th>% wt</th></tr>
<tr><td>C</td><td>19.35</td></tr>
<tr><td>O</td><td>16.83</td></tr>
<tr><td>Al</td><td>---</td></tr>
<tr><td>Si</td><td>5.79</td></tr>
<tr><td>S</td><td>5.54</td></tr>
<tr><td>Cl</td><td>1.24</td></tr>
<tr><td>Cu</td><td>26.76</td></tr>
<tr><td>Zn</td><td>0.20</td></tr>
<tr><td>Sn</td><td>0.94</td></tr>
<tr><td>Pb</td><td>23.36</td></tr>
<tr><td>Sb</td><td>---</td></tr>
</table></td>
</tr>
</table>

NA-P

Not aged
PropS-SH

Site 4
Spec 3

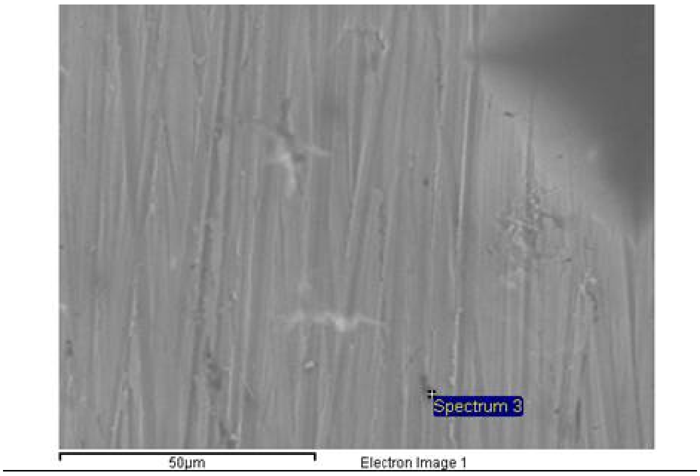

Element	% wt
C	21.14
O	18.00
Al	8.67
Si	6.59
S	4.96
Cl	1.24
Cu	39.67
Zn	---
Sn	0.97
Pb	---
Sb	---

NA-P

Not aged
PropS-SH

Site 4
Spec 4

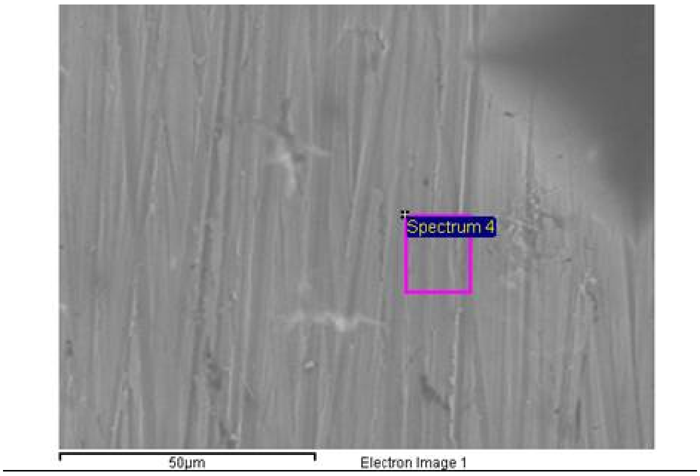

Element	% wt
C	15.93
O	13.59
Al	---
Si	7.37
S	5.36
Cl	---
Cu	55.76
Zn	1.14
Sn	0.85
Pb	---
Sb	---

NA-P

Not aged
PropS-SH

Site 4
Spec 5

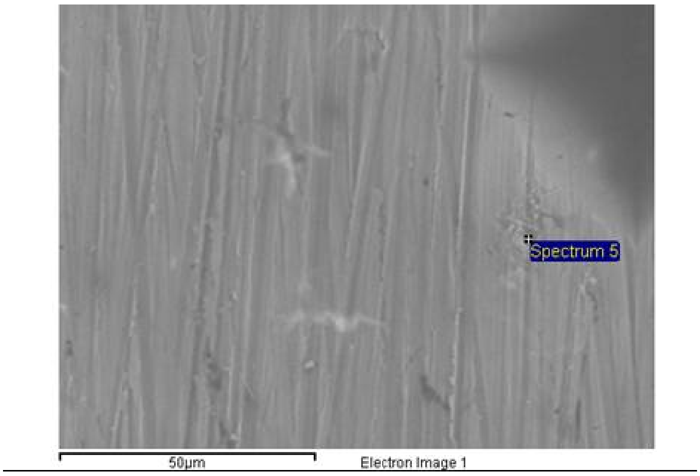

Element	% wt
C	20.83
O	12.38
Al	---
Si	6.51
S	4.95
Cl	---
Cu	52.75
Zn	1.12
Sn	1.45
Pb	---
Sb	---

NA-P

Not aged
PropS-SH

Site 4
Spec 6

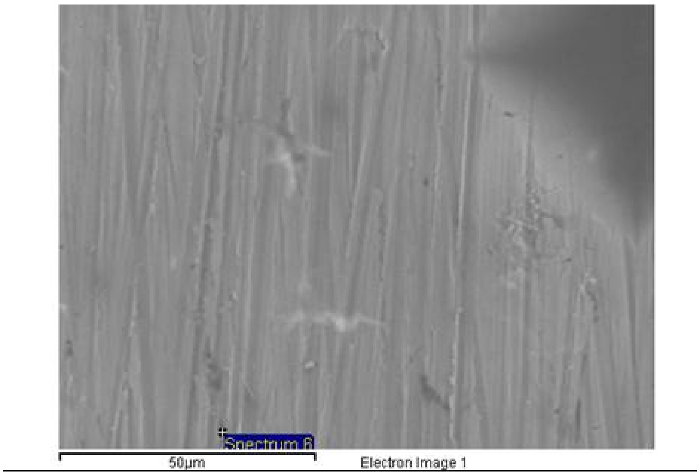

Element	% wt
C	20.63
O	12.07
Al	---
Si	7.26
S	5.22
Cl	---
Cu	52.72
Zn	0.80
Sn	1.29
Pb	---
Sb	---

A-P

Aged
PropS-SH

Site 1
Spec 1

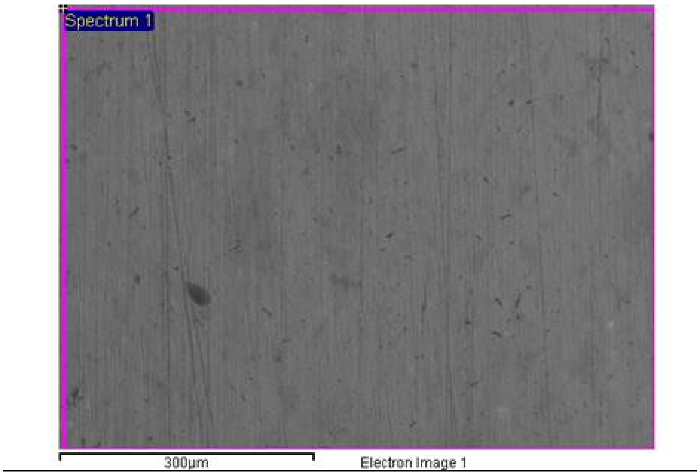

Element	% wt
C	17.50
O	13.99
Al	---
Si	4.53
S	3.44
Cl	---
Cu	58.96
Zn	---
Sn	1.58
Pb	---
Sb	---

A-PC

Aged
PropS-SH
+ CeO_2

Site 1
Spec 1

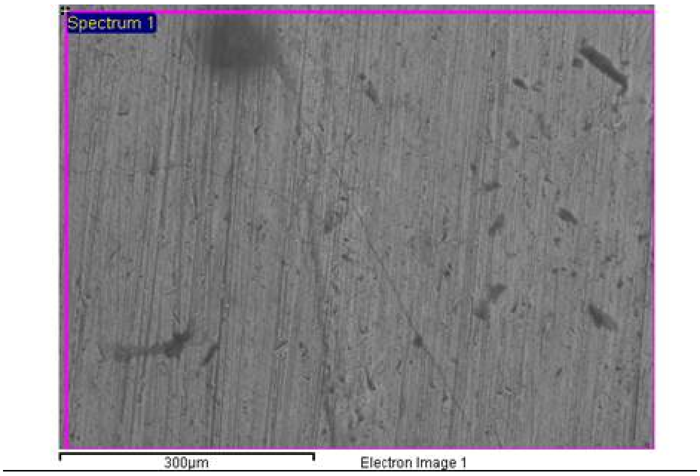

Element	% wt
C	20.11
O	14.52
Al	0.27
Si	5.65
S	4.60
Cl	---
Cu	51.57
Zn	0.85
Sn	1.41
Pb	---
Sb	0.80
Ce	0.21

A-PC

Aged PropS-SH + CeO_2

Site 2
Spec 1

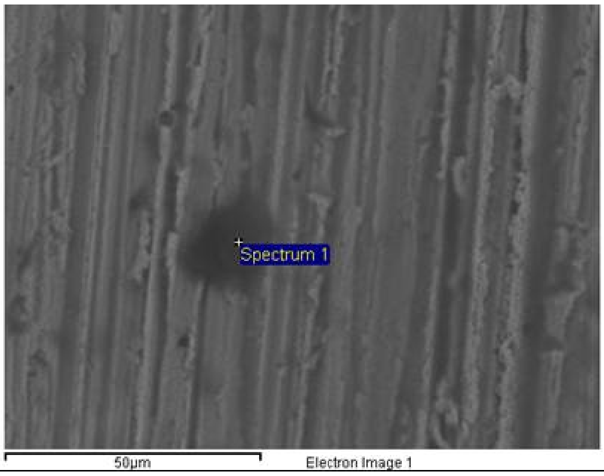

Element	% wt
C	56.26
O	16.71
Al	0.21
Si	4.18
S	3.29
Cl	0.23
Cu	19.10
Zn	---
Sn	---
Pb	---
Sb	---
Ce	0.02

A-PC

Aged PropS-SH + CeO_2

Site 3
Spec 1

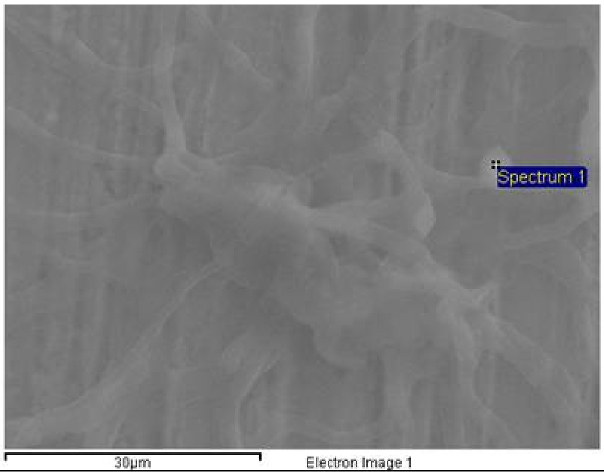

Element	% wt
C	59.98
O	17.41
Al	---
Si	2.38
S	2.20
Cl	---
Cu	17.37
Zn	0.30
Sn	0.31
Pb	---
Sb	---
Ce	0.06

A-PC

Aged
PropS-SH
+ CeO_2

Site 3
Spec 2

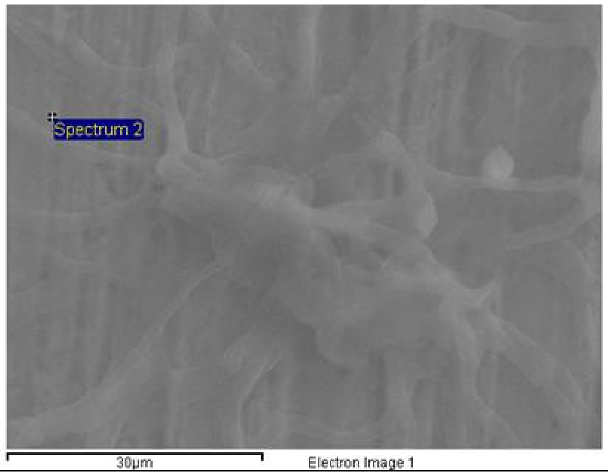

Element	% wt
C	23.25
O	16.85
Al	0.59
Si	4.44
S	3.56
Cl	0.23
Cu	48.00
Zn	0.68
Sn	1.60
Pb	---
Sb	0.72
Ce	0.10

A-PC

Aged
PropS-SH
+ CeO_2

Site 3
Spec 3

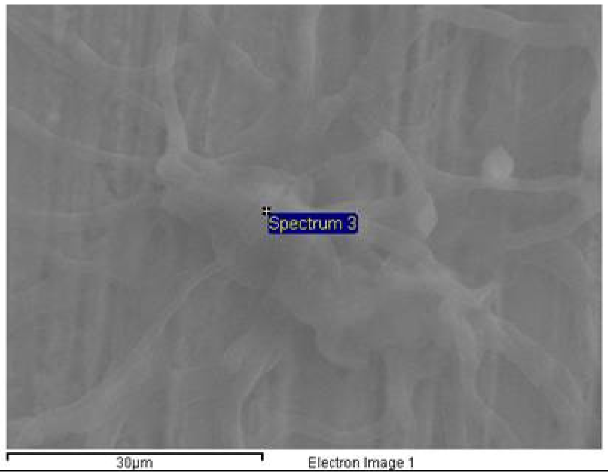

Element	% wt
C	58.62
O	12.62
Al	0.15
Si	2.59
S	2.39
Cl	---
Cu	22.54
Zn	0.35
Sn	0.62
Pb	---
Sb	---
Ce	0.12

A-PC

Aged
PropS-SH
+ CeO_2

Site 3
Spec 4

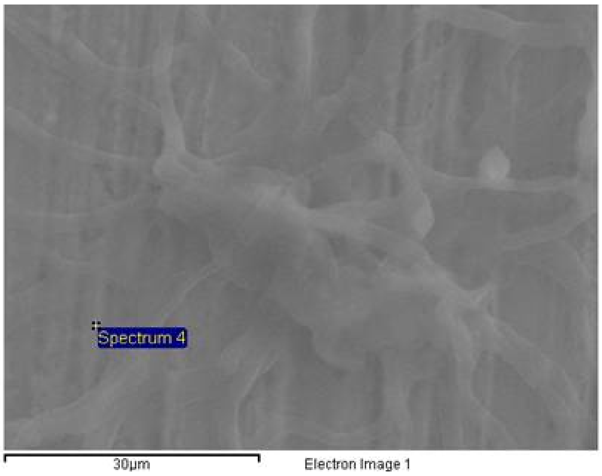

Element	% wt
C	27.15
O	13.76
Al	---
Si	4.90
S	3.45
Cl	---
Cu	49.21
Zn	0.74
Sn	0.73
Pb	---
Sb	---
Ce	0.06

SEM-EDS analyses – Total immersion samples after exposure

<table>
<tr><th>Coupon</th><th>SEM image</th><th>EDS analysis</th></tr>
<tr>
<td>P-NaCl

PropS-SH
NaCl 3.5%

Site 1
Spec 1</td>
<td>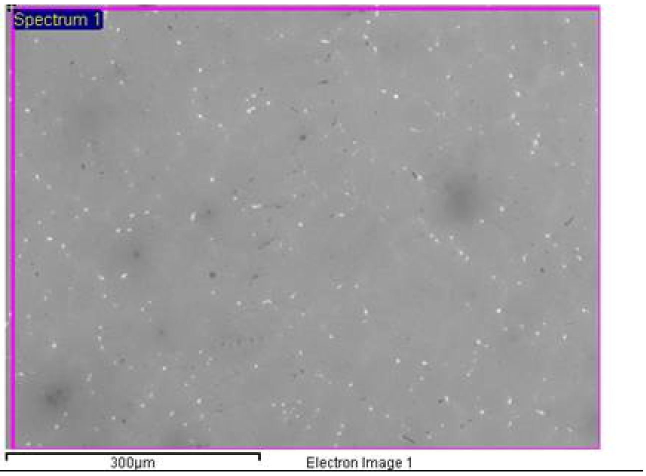
</td>
<td><table>
<tr><th>Element</th><th>% wt</th></tr>
<tr><td>C</td><td>16.28</td></tr>
<tr><td>O</td><td>12.52</td></tr>
<tr><td>Al</td><td>---</td></tr>
<tr><td>Si</td><td>6.97</td></tr>
<tr><td>S</td><td>5.23</td></tr>
<tr><td>Cl</td><td>---</td></tr>
<tr><td>Cu</td><td>55.60</td></tr>
<tr><td>Zn</td><td>1.36</td></tr>
<tr><td>Sn</td><td>1.44</td></tr>
<tr><td>Pb</td><td>---</td></tr>
<tr><td>Sb</td><td>0.62</td></tr>
</table></td>
</tr>
<tr>
<td>P-NaCl

PropS-SH
NaCl 3.5%

Site 2
Spec 1</td>
<td>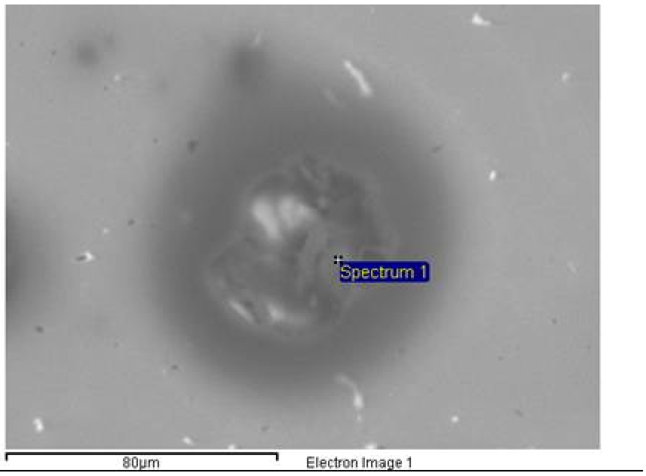
</td>
<td><table>
<tr><th>Element</th><th>% wt</th></tr>
<tr><td>C</td><td>23.69</td></tr>
<tr><td>O</td><td>18.92</td></tr>
<tr><td>Al</td><td>---</td></tr>
<tr><td>Si</td><td>13.52</td></tr>
<tr><td>S</td><td>12.13</td></tr>
<tr><td>Cl</td><td>---</td></tr>
<tr><td>Cu</td><td>30.03</td></tr>
<tr><td>Zn</td><td>0.66</td></tr>
<tr><td>Sn</td><td>1.06</td></tr>
<tr><td>Pb</td><td>---</td></tr>
<tr><td>Sb</td><td>---</td></tr>
</table></td>
</tr>
</table>

P-NaCl

PropS-SH
NaCl 3.5%

Site 2
Spec 2

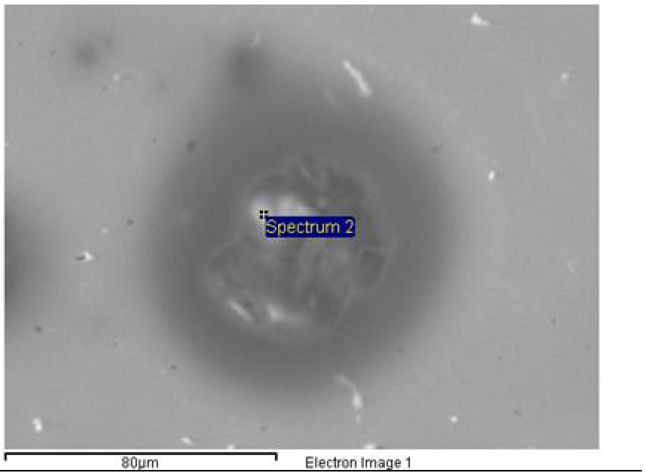

Element	% wt
C	17.12
O	10.55
Al	---
Si	6.28
S	4.58
Cl	---
Cu	59.08
Zn	1.37
Sn	1.03
Pb	---
Sb	---

P-NaCl

PropS-SH
NaCl 3.5%

Site 2
Spec 3

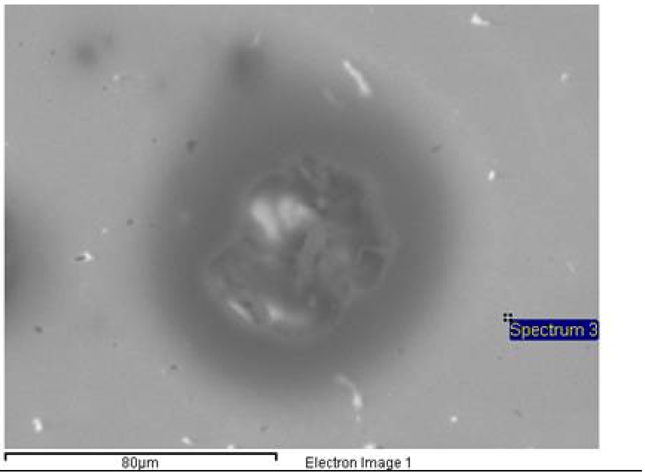

Element	% wt
C	16.25
O	11.10
Al	---
Si	5.50
S	3.87
Cl	---
Cu	59.63
Zn	1.69
Sn	1.41
Pb	---
Sb	0.54

P-AR

PropS-SH
Acid rain
10x

Site 1
Spec 1

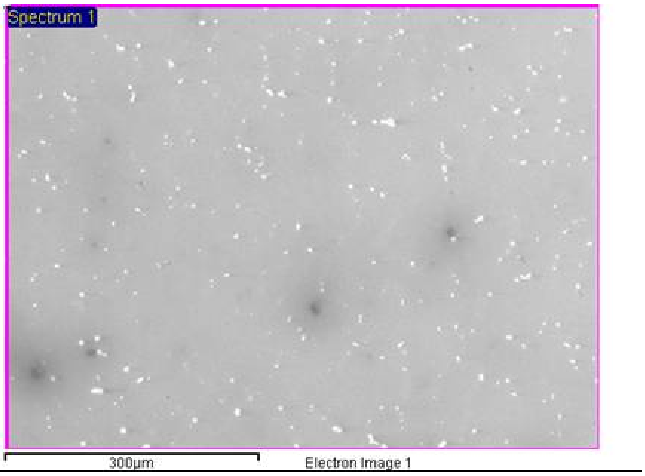

Element	% wt
C	15.91
O	11.95
Al	---
Si	6.03
S	4.34
Cl	---
Cu	58.22
Zn	1.40
Sn	1.53
Pb	---
Sb	0.61

<table>
<tr>
<td>P-AR

PropS-SH
Acid rain
10x

Site 2
Spec 1</td>
<td>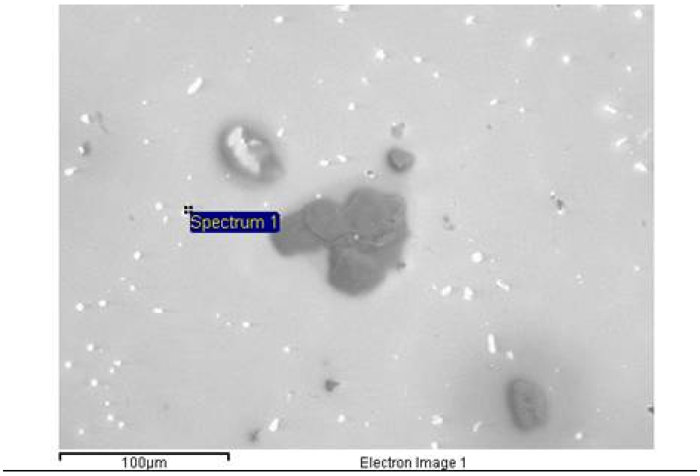
</td>
<td><table>
<tr><th>Element</th><th>% wt</th></tr>
<tr><td>C</td><td>18.10</td></tr>
<tr><td>O</td><td>12.06</td></tr>
<tr><td>Al</td><td>---</td></tr>
<tr><td>Si</td><td>2.77</td></tr>
<tr><td>S</td><td>2.48</td></tr>
<tr><td>Cl</td><td>---</td></tr>
<tr><td>Cu</td><td>28.41</td></tr>
<tr><td>Zn</td><td>---</td></tr>
<tr><td>Sn</td><td>0.93</td></tr>
<tr><td>Pb</td><td>35.26</td></tr>
<tr><td>Sb</td><td>---</td></tr>
</table></td>
</tr>
<tr>
<td>P-AR

PropS-SH
Acid rain
10x

Site 2
Spec 2</td>
<td>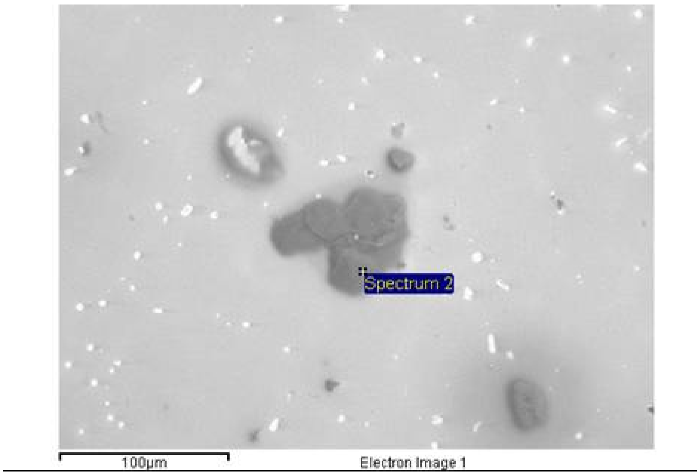
</td>
<td><table>
<tr><th>Element</th><th>% wt</th></tr>
<tr><td>C</td><td>27.50</td></tr>
<tr><td>O</td><td>18.81</td></tr>
<tr><td>Al</td><td>---</td></tr>
<tr><td>Si</td><td>13.69</td></tr>
<tr><td>S</td><td>12.76</td></tr>
<tr><td>Cl</td><td>---</td></tr>
<tr><td>Cu</td><td>25.96</td></tr>
<tr><td>Zn</td><td>0.75</td></tr>
<tr><td>Sn</td><td>0.52</td></tr>
<tr><td>Pb</td><td>---</td></tr>
<tr><td>Sb</td><td>---</td></tr>
</table></td>
</tr>
<tr>
<td>P-AR

PropS-SH
Acid rain
10x

Site 2
Spec 3</td>
<td>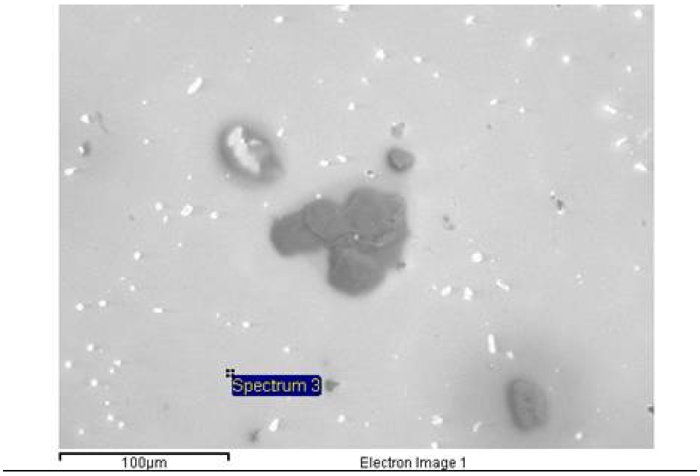
</td>
<td><table>
<tr><th>Element</th><th>% wt</th></tr>
<tr><td>C</td><td>15.94</td></tr>
<tr><td>O</td><td>9.49</td></tr>
<tr><td>Al</td><td>---</td></tr>
<tr><td>Si</td><td>4.52</td></tr>
<tr><td>S</td><td>3.20</td></tr>
<tr><td>Cl</td><td>---</td></tr>
<tr><td>Cu</td><td>64.15</td></tr>
<tr><td>Zn</td><td>1.60</td></tr>
<tr><td>Sn</td><td>1.10</td></tr>
<tr><td>Pb</td><td>---</td></tr>
<tr><td>Sb</td><td>---</td></tr>
</table></td>
</tr>
</table>

PC-AR

PropS-SH
+ CeO_2
Acid rain
10x

Site 2
Spec 1

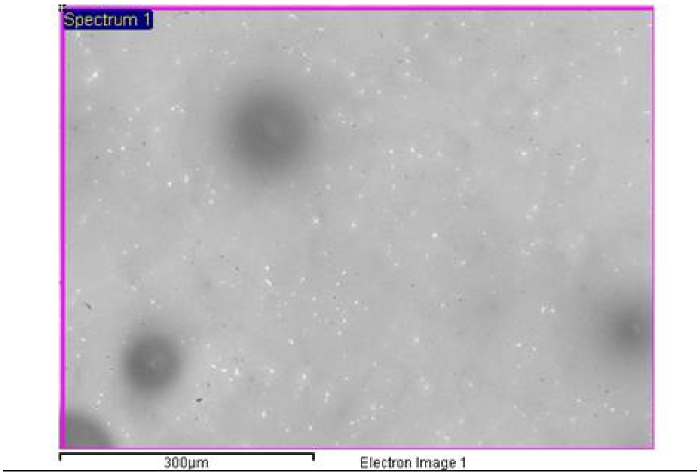

Element	% wt
C	18.47
O	11.27
Al	---
Si	6.73
S	5.00
Cl	---
Cu	55.86
Zn	1.43
Sn	1.24
Pb	---
Sb	---

PC-AR

PropS-SH
+ CeO_2
Acid rain
10x

Site 3
Spec 1

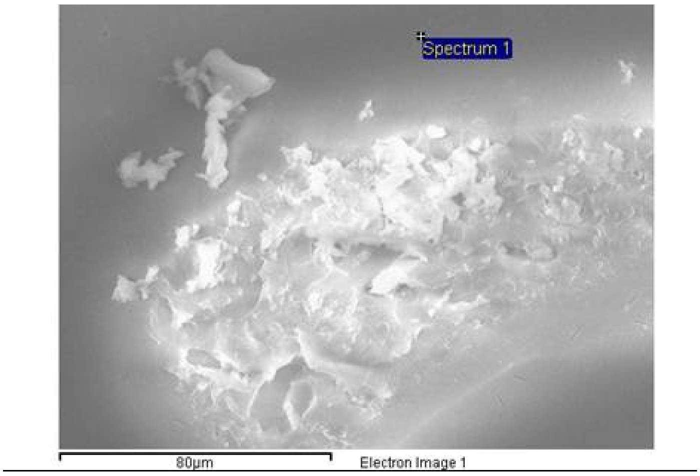

Element	**% wt**
C	22.93
O	16.75
Al	---
Si	17.77
S	16.56
Cl	---
Cu	24.67
Zn	0.75
Sn	0.57
Pb	---
Sb	---

PC-AR

PropS-SH
+ CeO_2
Acid rain
10x

Site 3
Spec 2

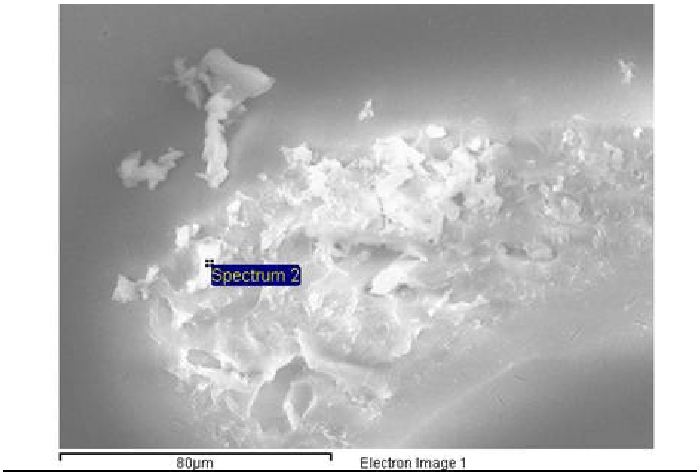

Element	**% wt**
C	30.90
O	28.64
Al	---
Si	14.05
S	12.90
Cl	---
Cu	13.51
Zn	---
Sn	---
Pb	---
Sb	---

PC-AR

PropS-SH
+ CeO_2
Acid rain
10x

Site 4
Spec 1

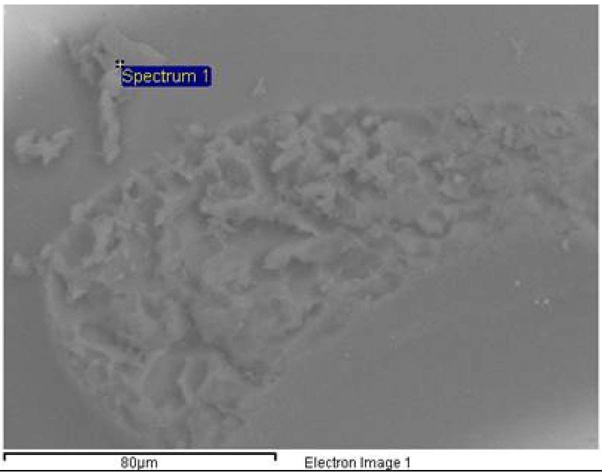

Element	% wt
C	24.37
O	25.22
Al	---
Si	13.54
S	11.41
Cl	---
Cu	17.56
Zn	---
Sn	0.44
Pb	---
Sb	---
Ce	8.34

PC-AR

PropS-SH
+ CeO_2
Acid rain
10x

Site 4
Spec 2

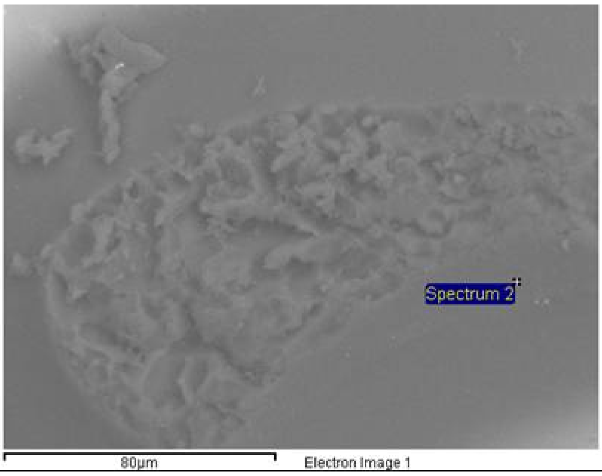

Element	% wt
C	25.80
O	20.47
Al	---
Si	16.72
S	15.87
Cl	---
Cu	17.45
Zn	0.54
Sn	---
Pb	---
Sb	---
Ce	3.16

PC-AR

PropS-SH
+ CeO_2
Acid rain
10x

Site 4
Spec 3

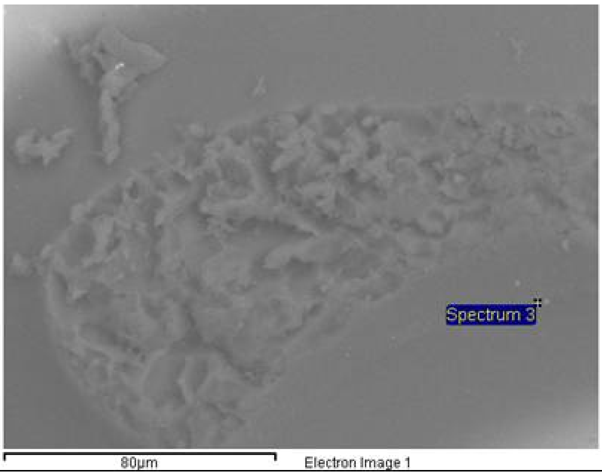

Element	% wt
C	27.70
O	22.61
Al	---
Si	15.83
S	15.10
Cl	---
Cu	16.43
Zn	---
Sn	0.52
Pb	---
Sb	---
Ce	1.82

PC-AR

PropS-SH
+ CeO_2
Acid rain
10x

Site 5
Spec 1

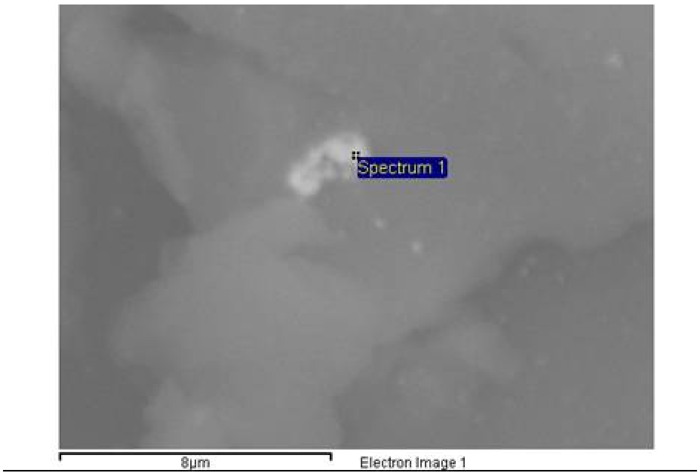

Element	% wt
C	22.55
O	26.08
Al	---
Si	13.41
S	11.08
Cl	---
Cu	17.27
Zn	---
Sn	---
Pb	---
Sb	---
Ce	9.60

PC-AR

PropS-SH
+ CeO_2
Acid rain
10x

Site 5
Spec 1

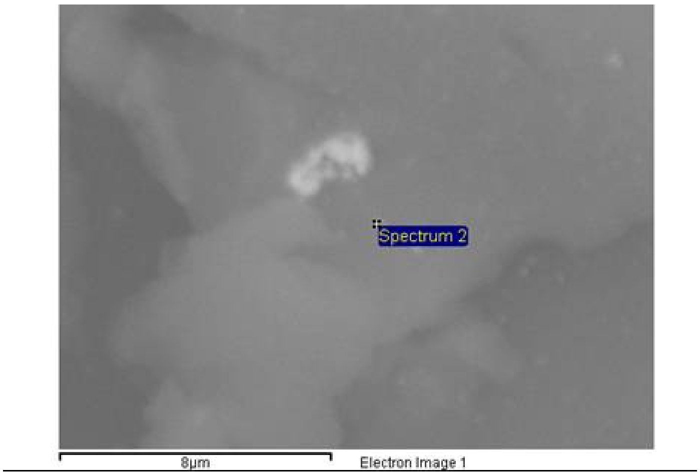

Element	% wt
C	26.56
O	22.33
Al	---
Si	16.66
S	15.48
Cl	---
Cu	17.89
Zn	---
Sn	---
Pb	---
Sb	---
Ce	1.07

PC-AR

PropS-SH
+ CeO_2
Acid rain
10x

Site 5
Spec 3

Element	% wt
C	27.12
O	23.77
Al	---
Si	15.42
S	14.05
Cl	---
Cu	17.85
Zn	---
Sn	---
Pb	---
Sb	---
Ce	1.80

NI-AR

Non
inhibited
Acid rain
10x

Site 1
Spec 1

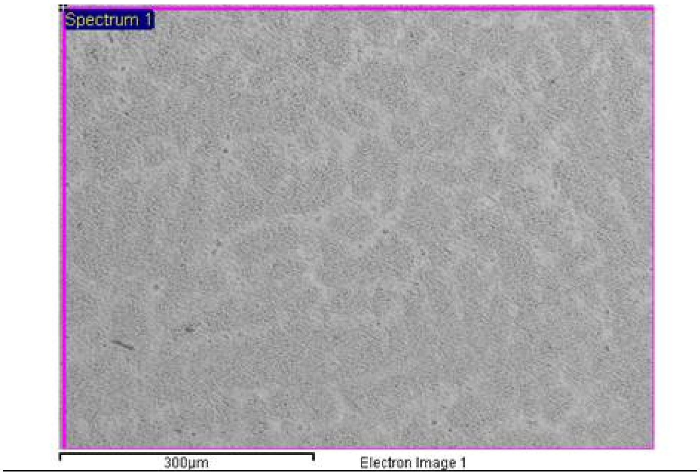

Element	% wt
C	---
O	12.97
Al	---
Si	---
S	---
Cl	---
Cu	83.64
Zn	---
Sn	2.60
Pb	---
Sb	0.80

NI-AR

Non
inhibited
Acid rain
10x

Site 2
Spec 2

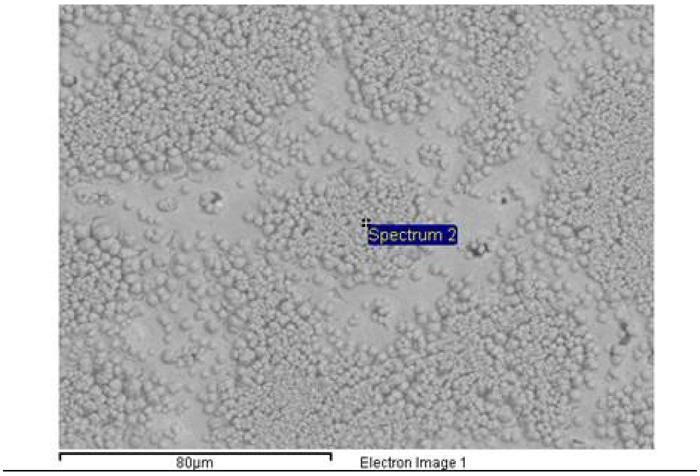

Element	% wt
C	---
O	11.23
Al	---
Si	---
S	---
Cl	---
Cu	87.60
Zn	---
Sn	1.17
Pb	---
Sb	---

NI-AR

Non
inhibited
Acid rain
10x

Site 2
Spec 3

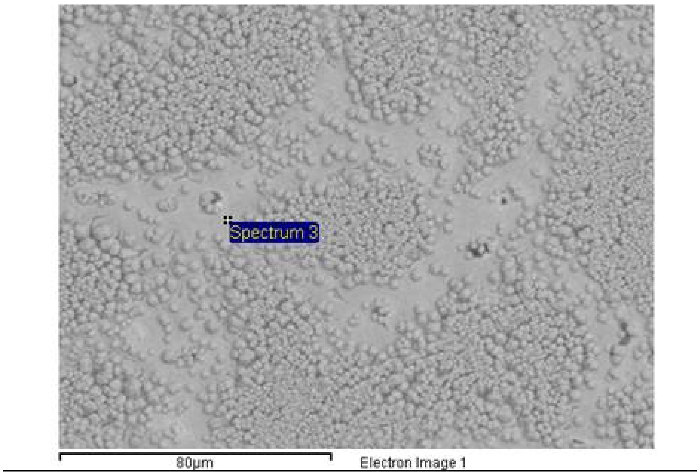

Element	% wt
C	---
O	14.00
Al	---
Si	---
S	---
Cl	0.31
Cu	75.83
Zn	---
Sn	6.02
Pb	1.71
Sb	2.13

<table>
<tr>
<td>NI-AR
Non
inhibited
Acid rain
10x
Site 2
Spec 4</td>
<td>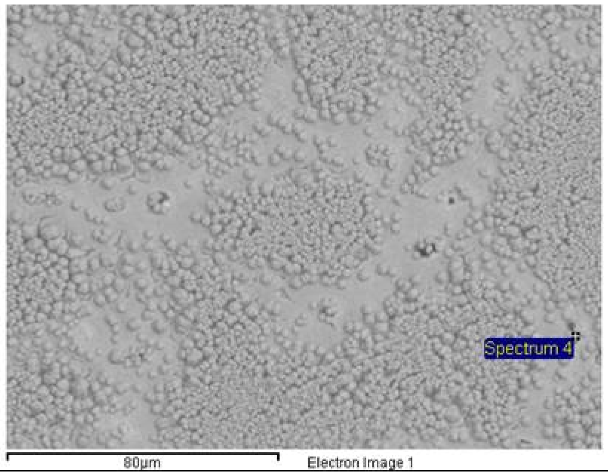
</td>
<td>
<table>
<tr><th>Element</th><th>% wt</th></tr>
<tr><td>C</td><td>---</td></tr>
<tr><td>O</td><td>8.30</td></tr>
<tr><td>Al</td><td>---</td></tr>
<tr><td>Si</td><td>---</td></tr>
<tr><td>S</td><td>---</td></tr>
<tr><td>Cl</td><td>---</td></tr>
<tr><td>Cu</td><td>88.08</td></tr>
<tr><td>Zn</td><td>---</td></tr>
<tr><td>Sn</td><td>2.13</td></tr>
<tr><td>Pb</td><td>1.53</td></tr>
<tr><td>Sb</td><td>---</td></tr>
</table>
</td>
</tr>
</table>

Appendix Ⓒ

micro-Raman analyses

(spectra interpretation based on [82])

micro-Raman analyses – Bottego corrosion products

Sheltered samples		
Sample	**Microscope image**	**Raman spectrum and detected products**
B2-1	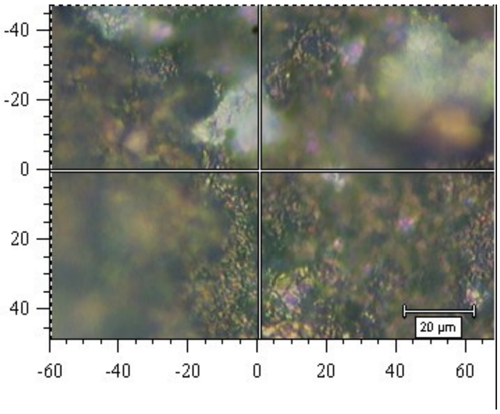	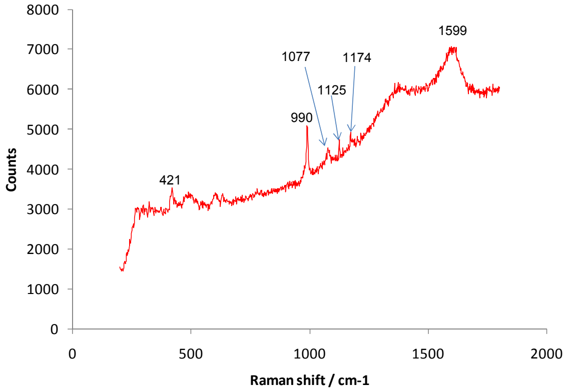 Brochantite, traces of antlerite
B2-2	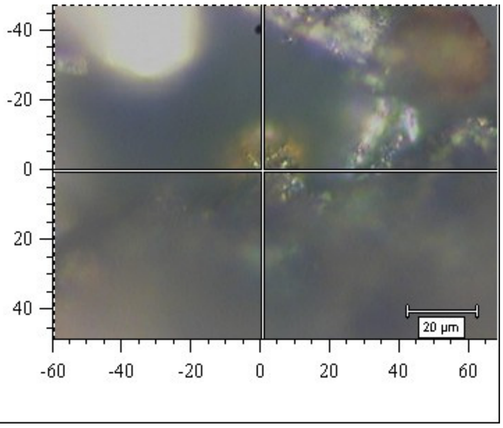	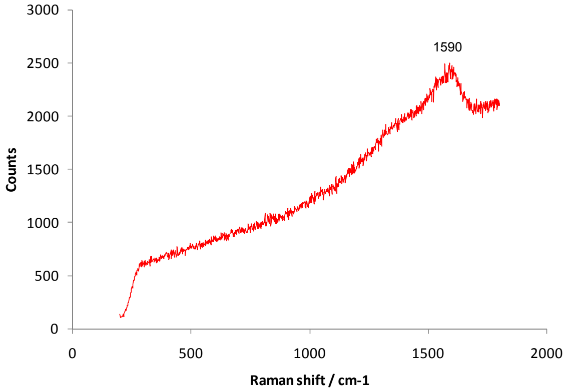

B2-3	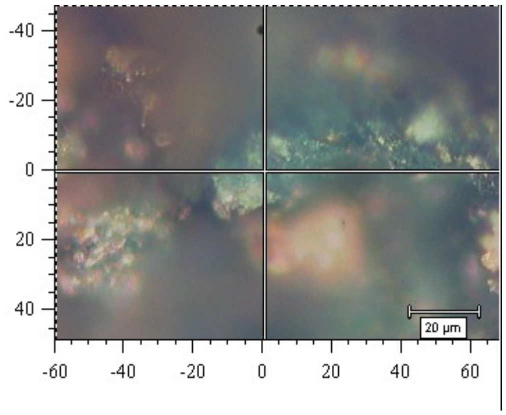	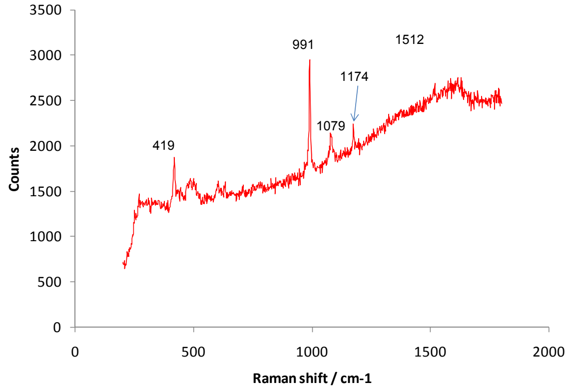 Brochantite, traces of antlerite and atacamite
B2-4	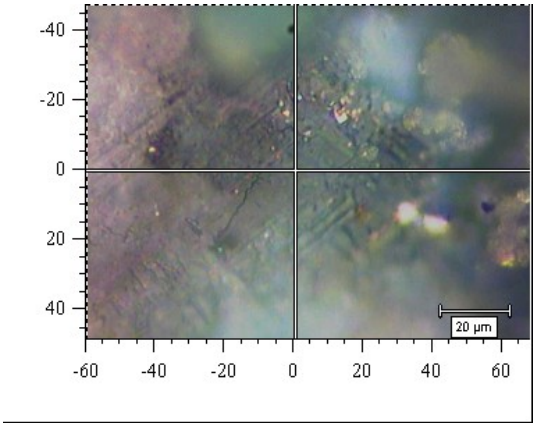	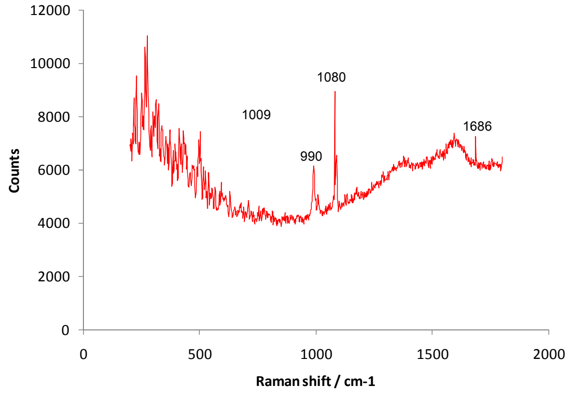 Copper sulphate
B3-1	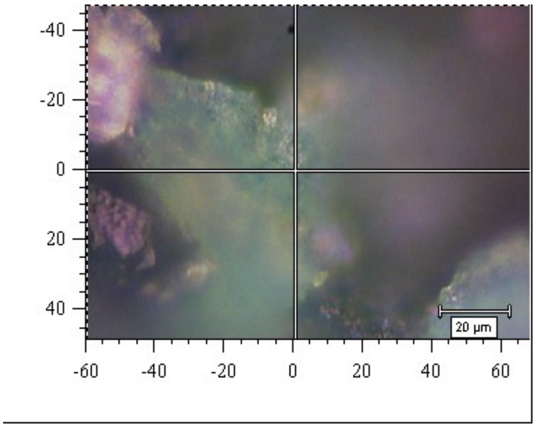	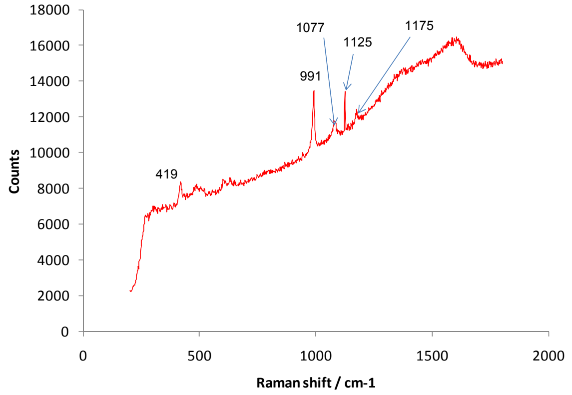 Brochantite, traces of antlerite

B3-2	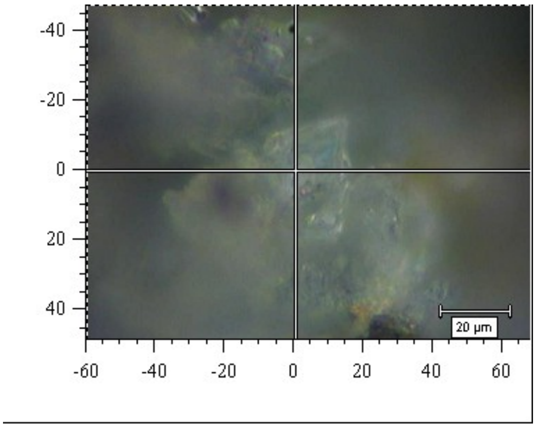	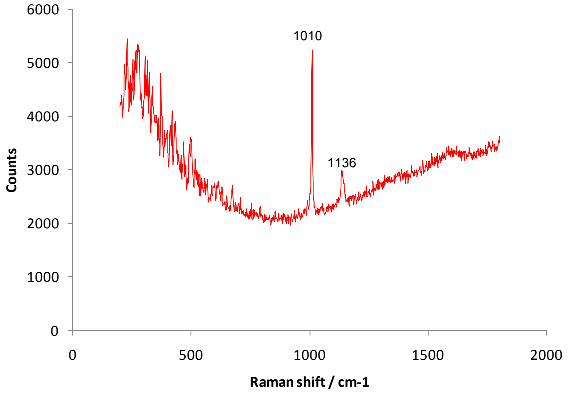 Gypsum
B3-3	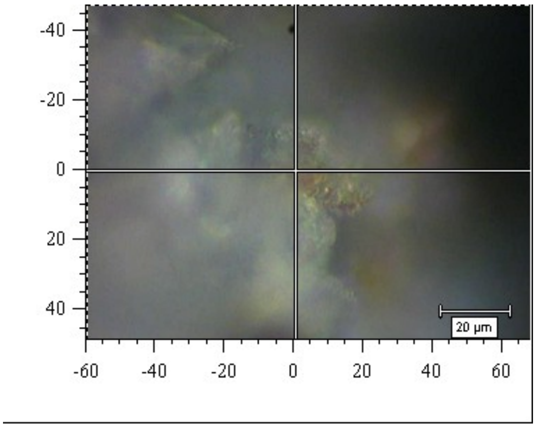	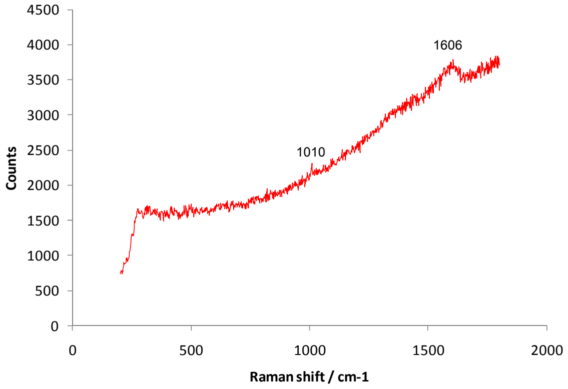
B4-1	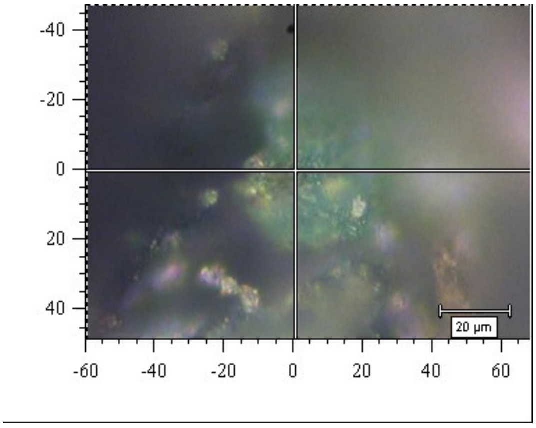	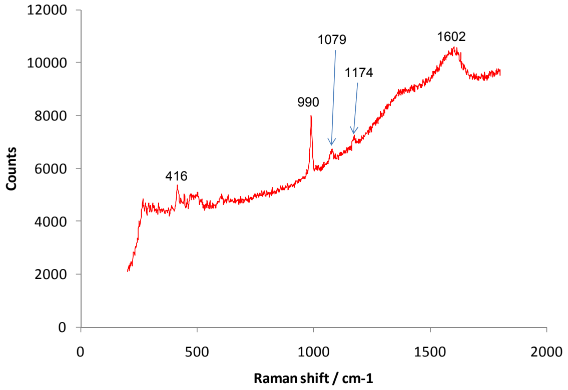 Brochantite

B4-2	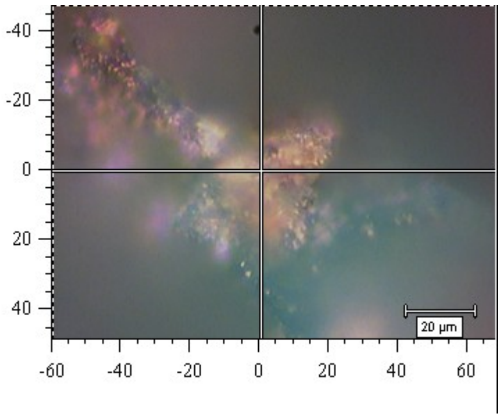	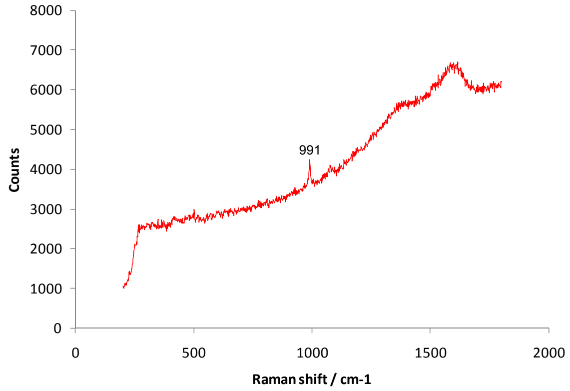 Brochantite
B4-3	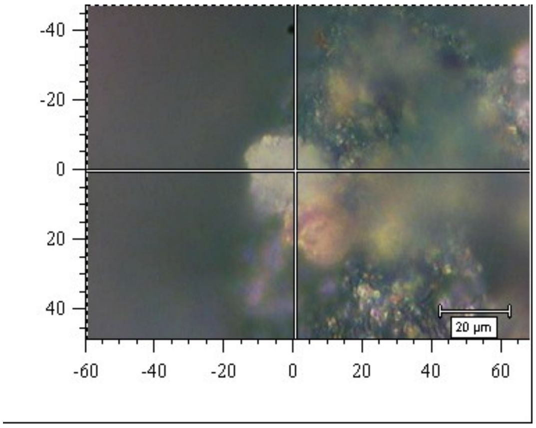	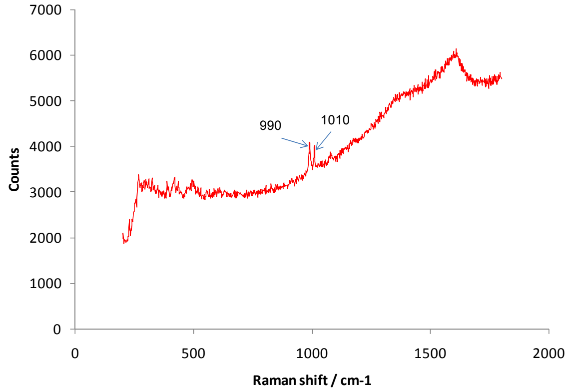 Copper sulphate, gypsum

<table>
<tr><th colspan="3">Unsheltered samples</th></tr>
<tr><th>Sample</th><th>Microscope image</th><th>Raman spectrum and detected products</th></tr>
<tr><td>B5-1</td><td>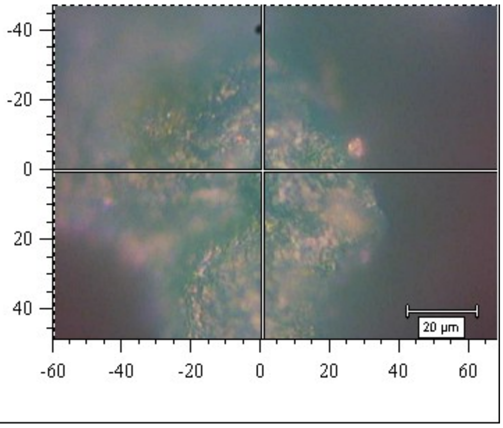
</td><td>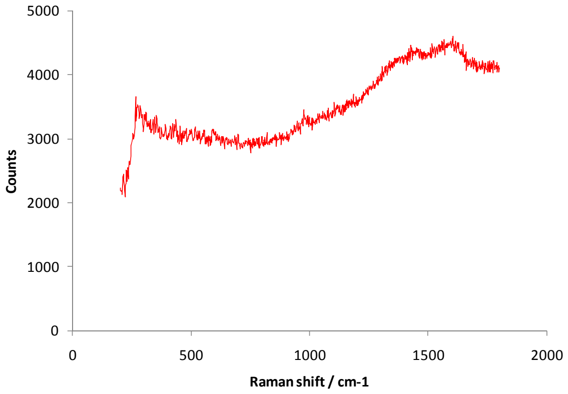

Traces of posnjakite</td></tr>
<tr><td>B5-2</td><td>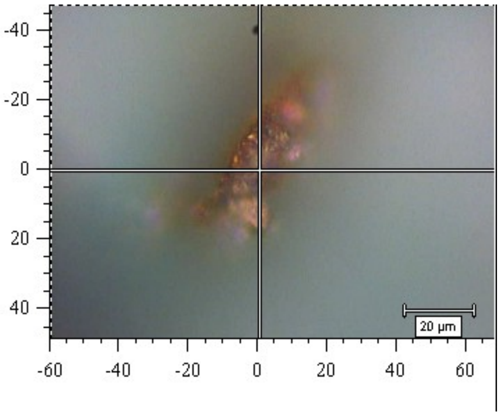
</td><td>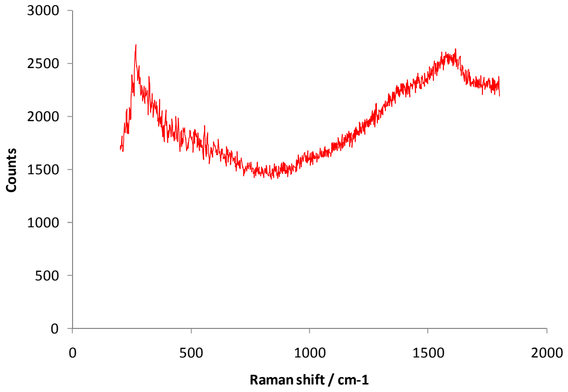
</td></tr>
<tr><td>B5-3</td><td>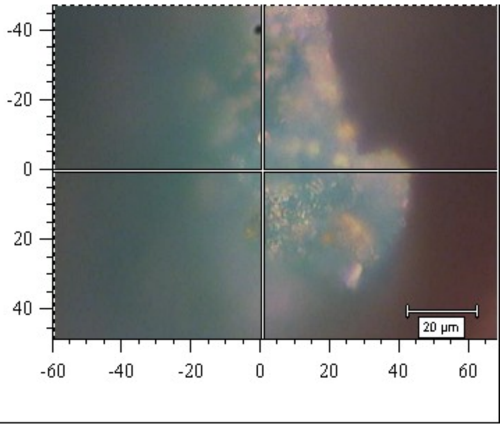
</td><td>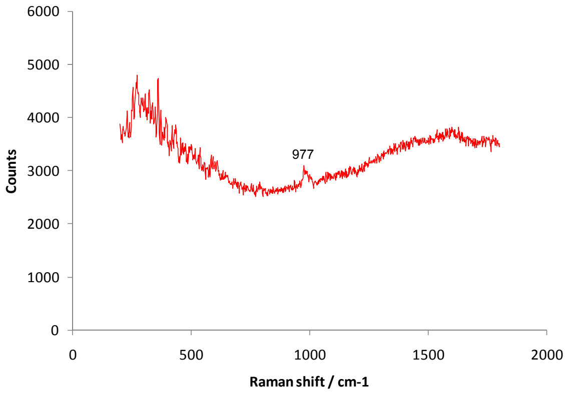

Traces of atacamite</td></tr>
</table>

B6-1	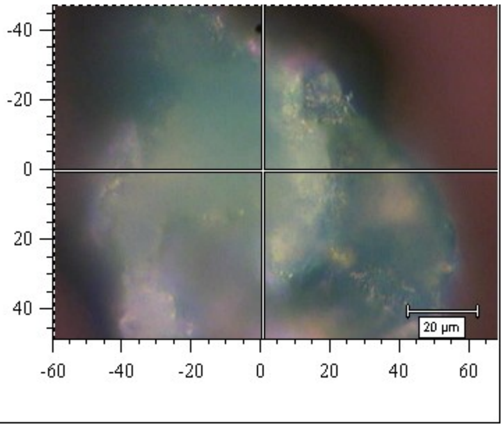	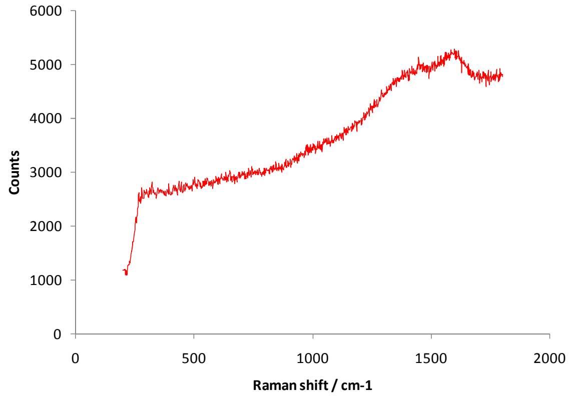
B6-2	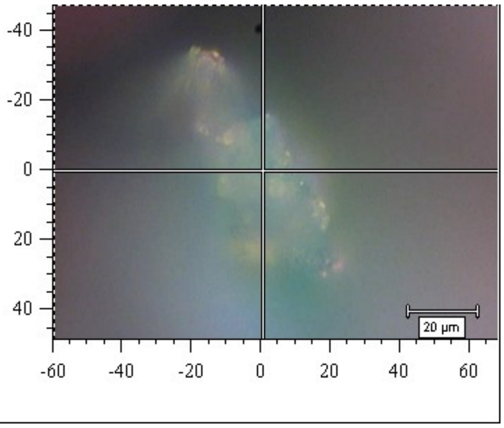	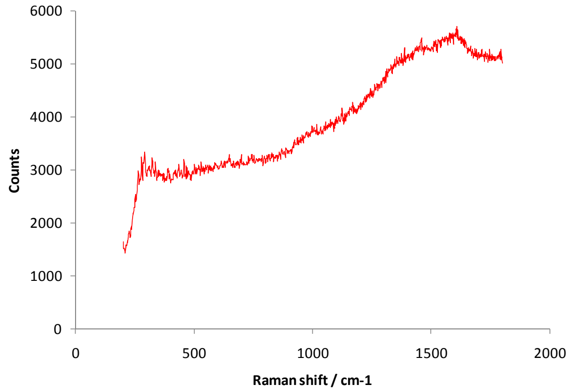
B6-3	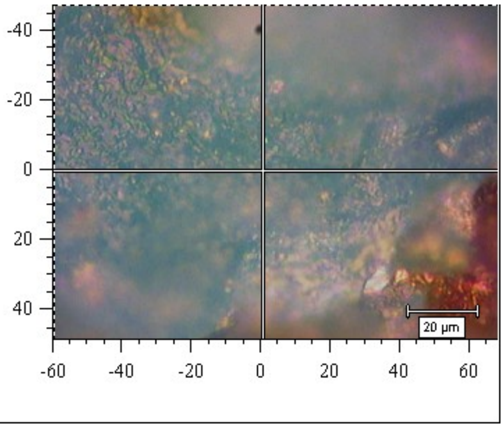	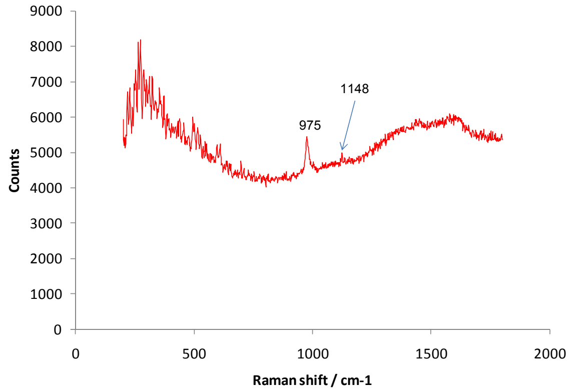 Copper sulphate, traces of gypsum

B7-1	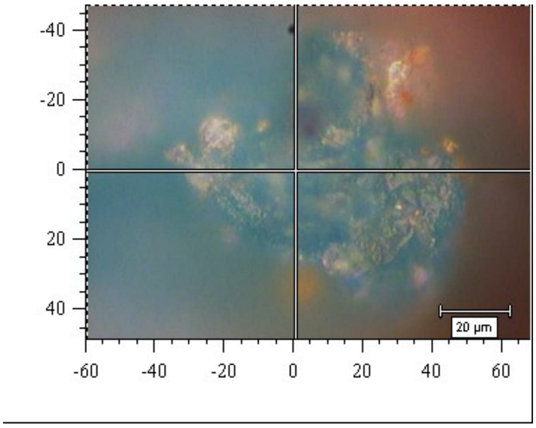-40 -20 0 20 40 -60 -40 -20 0 20 40 60 20 µm	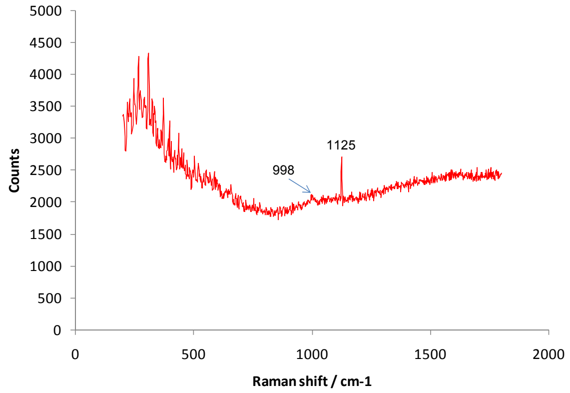5000 4500 4000 3500 3000 2500 2000 1500 1000 500 0 Counts 998 1125 0 500 1000 1500 2000 Raman shift / cm-1
B7-2	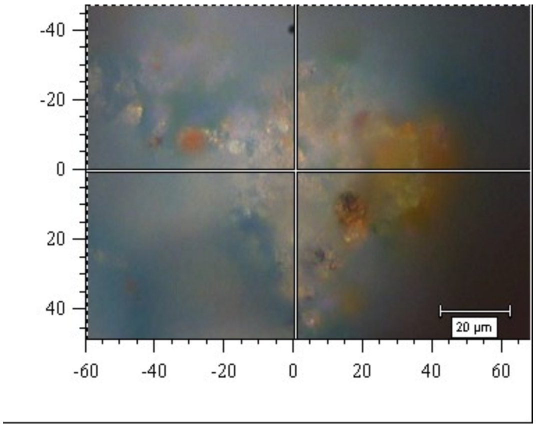-40 -20 0 20 40 -60 -40 -20 0 20 40 60 20 µm	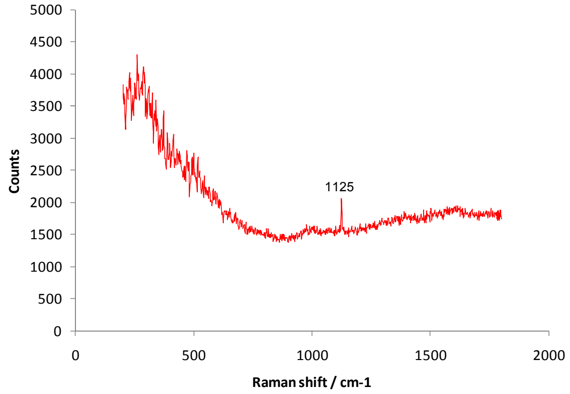5000 4500 4000 3500 3000 2500 2000 1500 1000 500 0 Counts 1125 0 500 1000 1500 2000 Raman shift / cm-1
B7-3	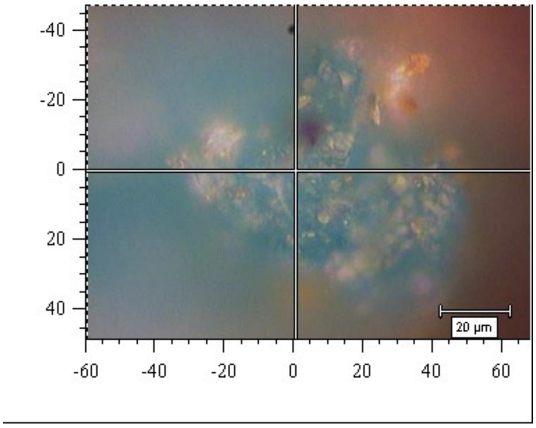-40 -20 0 20 40 -60 -40 -20 0 20 40 60 20 µm	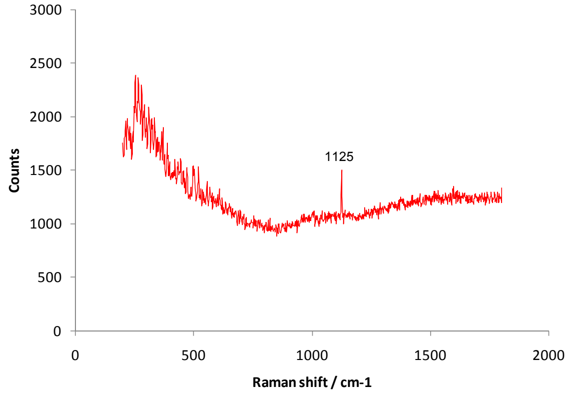3000 2500 2000 1500 1000 500 0 Counts 1125 0 500 1000 1500 2000 Raman shift / cm-1

micro-Raman analyses – Omo corrosion products

Sheltered samples		
Sample	**Microscope image**	**Raman spectrum and detected products**
O6-1	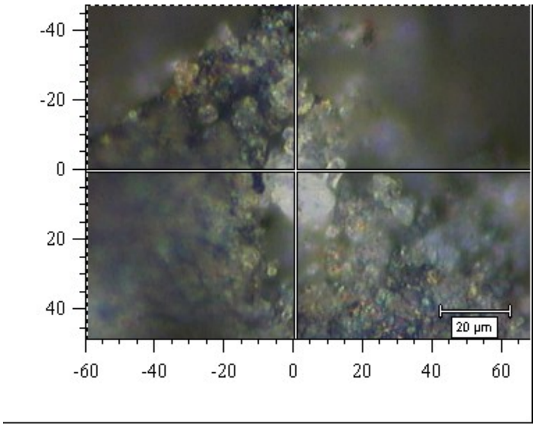	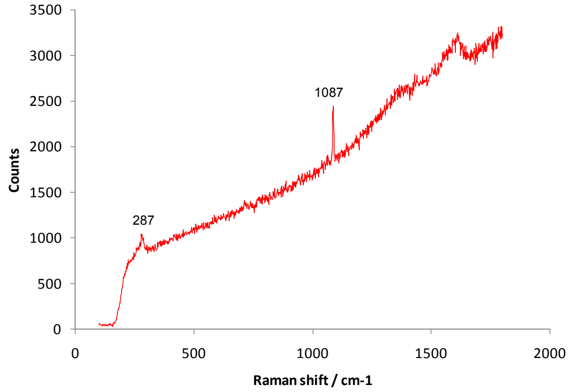 Calcite
O6-2	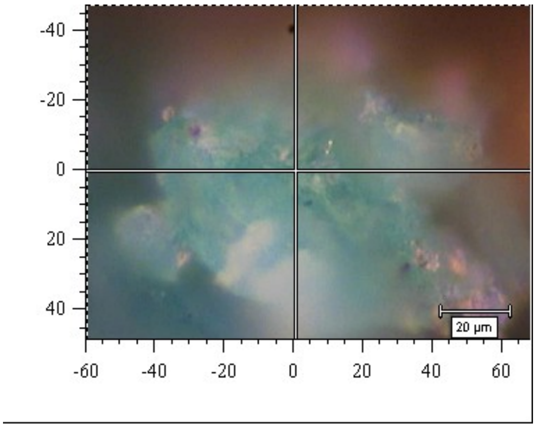	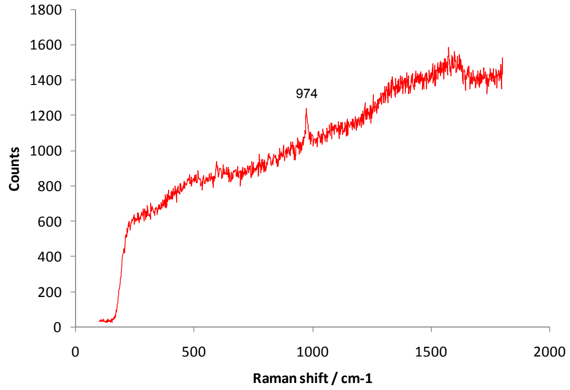 Posnjakite
O6-2 bis		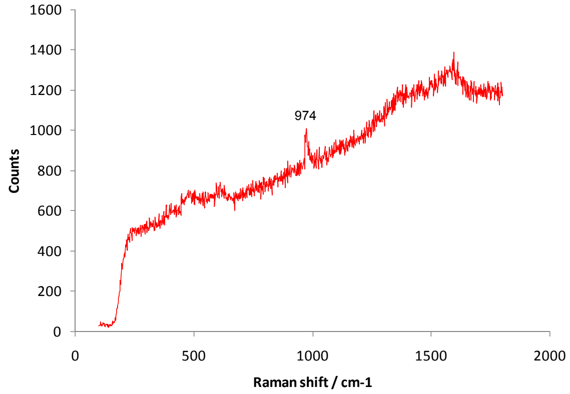 Posnjakite

O6-2 tris		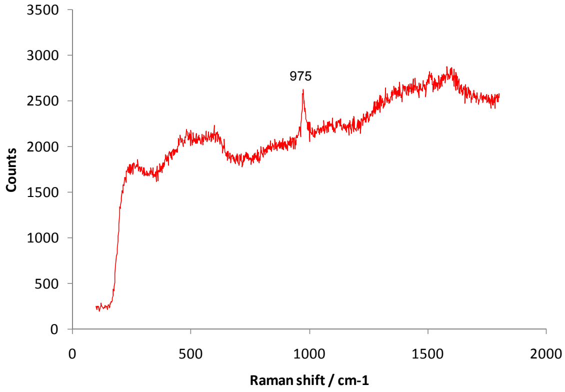 Posnjakite
O6-3	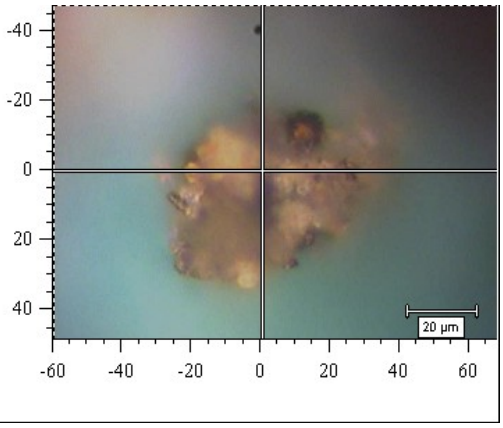	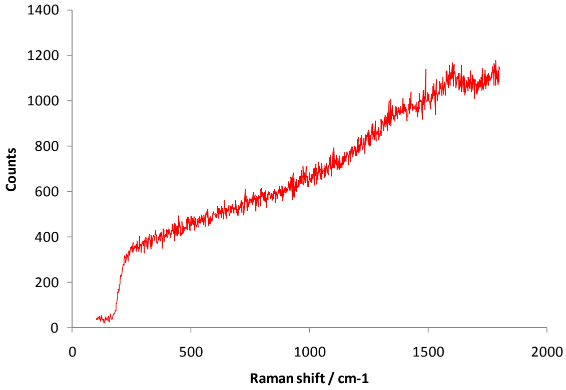
O6-4	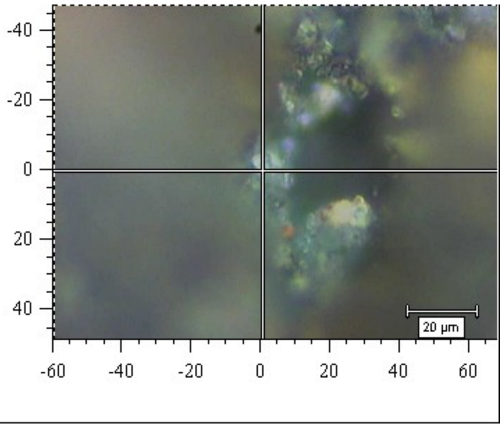	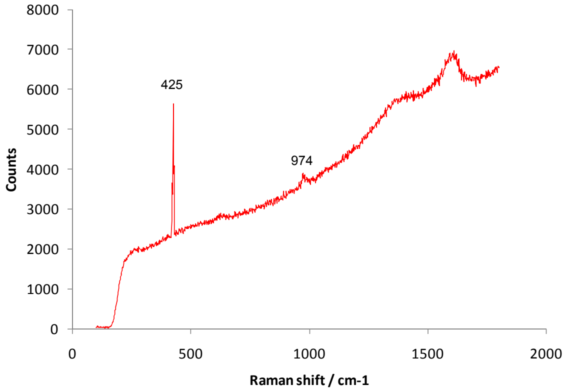

O7-1	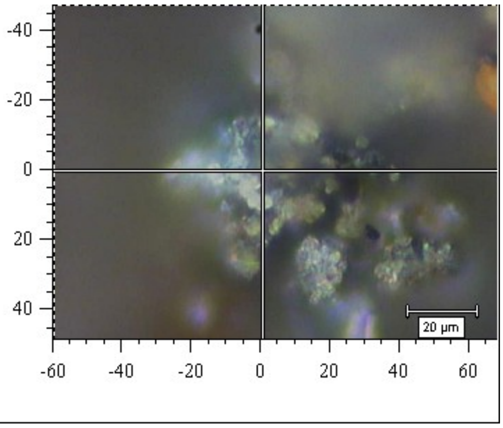	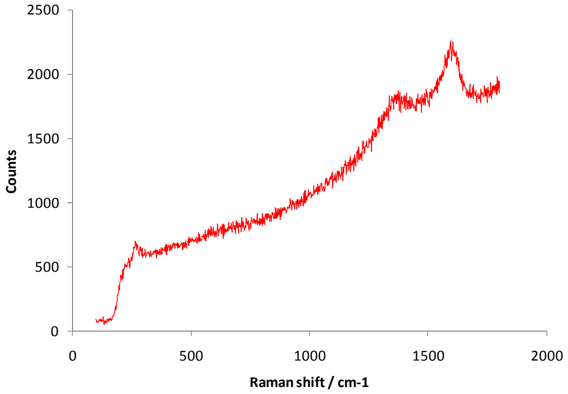
O7-2	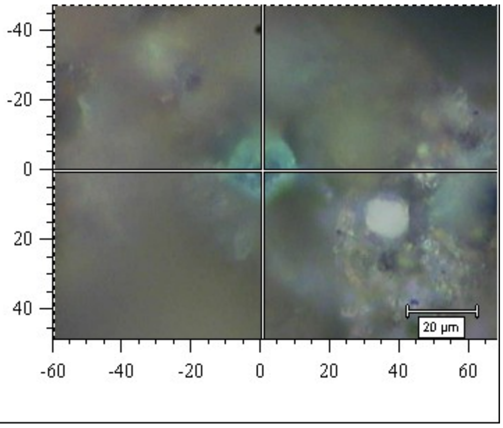	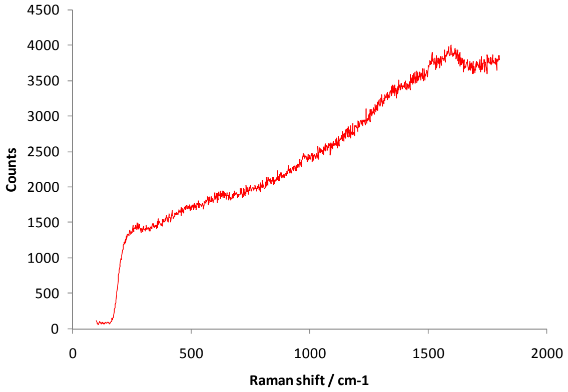
O7-3	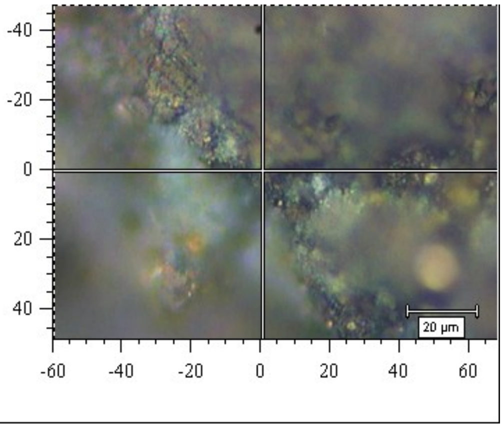	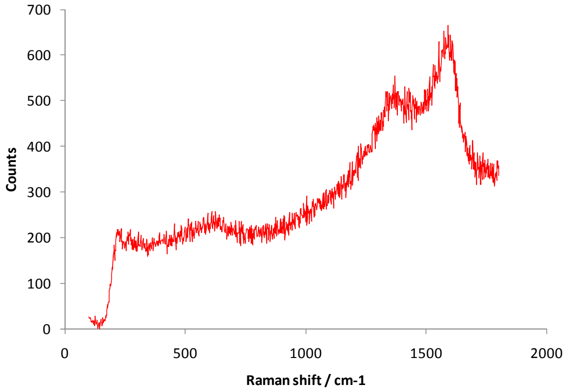 Amorphous carbon

Unsheltered samples		
Sample	**Microscope image**	**Raman spectrum and detected products**
O3-1	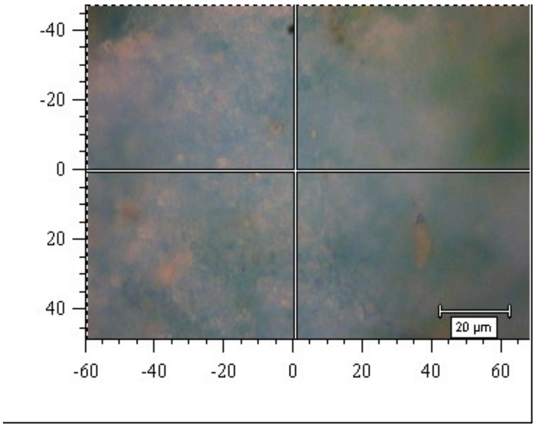	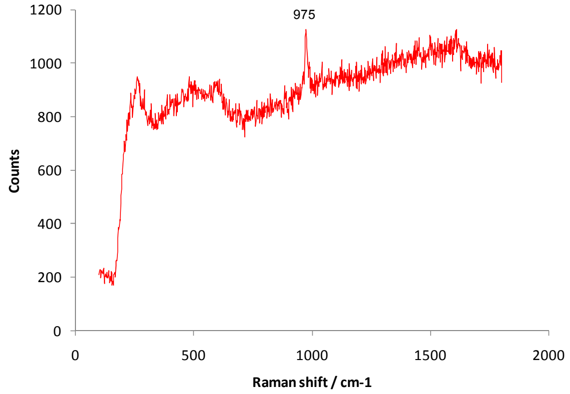 Traces of hydrated chlorides, probably atacamite
O3-2	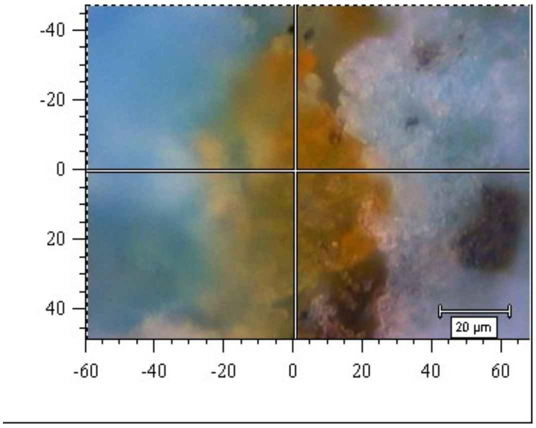	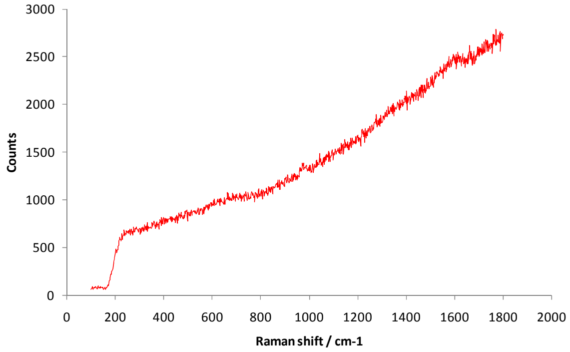
O3-3	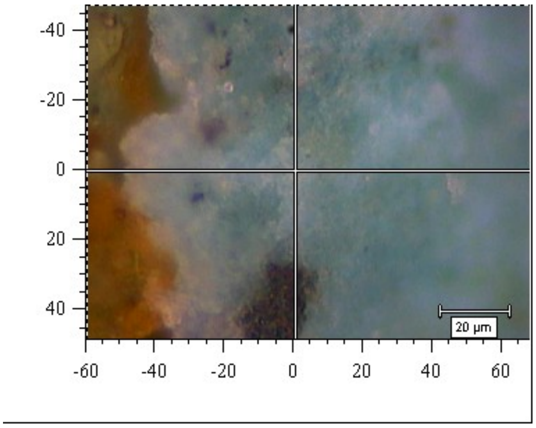	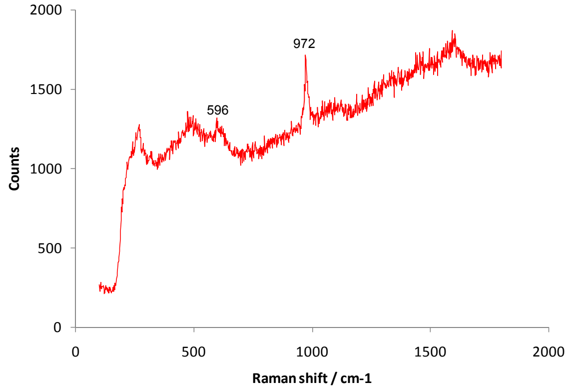 Langite, traces of antlerite

O4-1	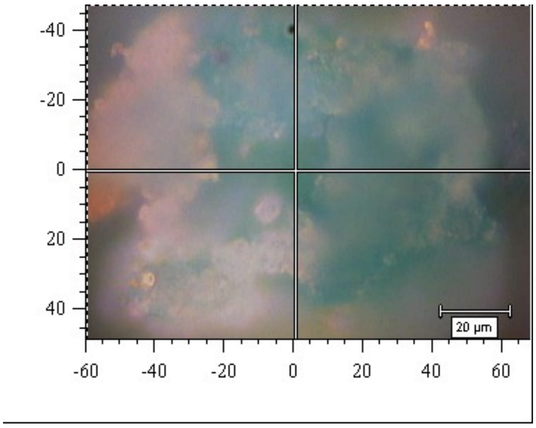	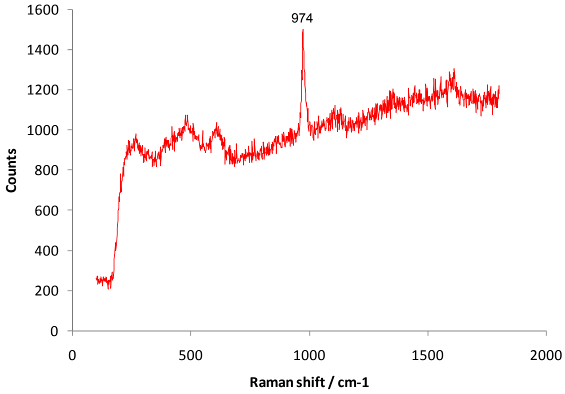 Cuprite
O4-2	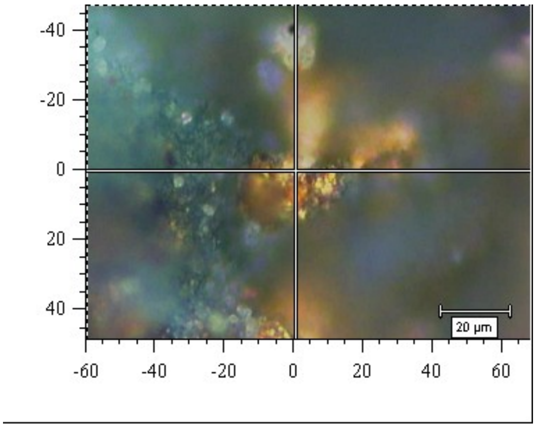	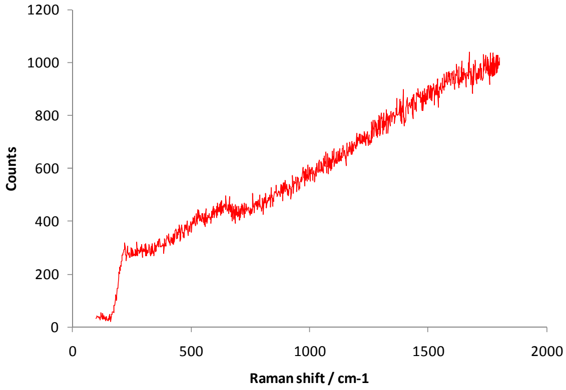 Traces of cassiterite
O4-3	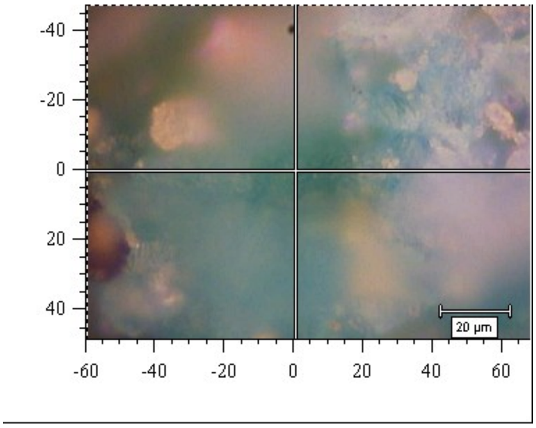	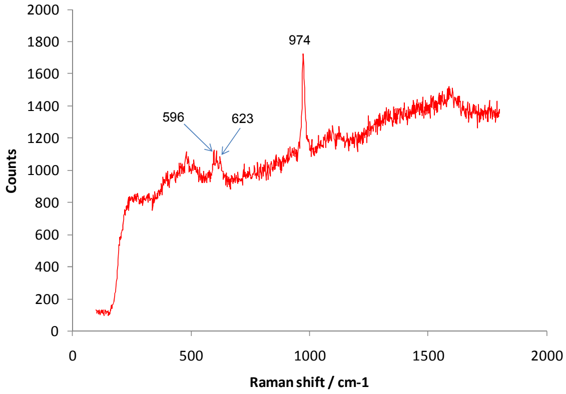 Brochantite

O5-1	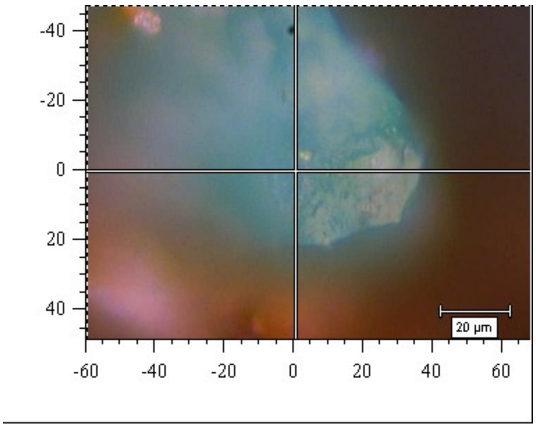	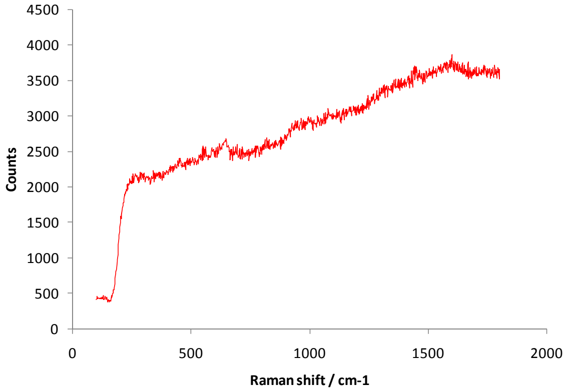
O5-2	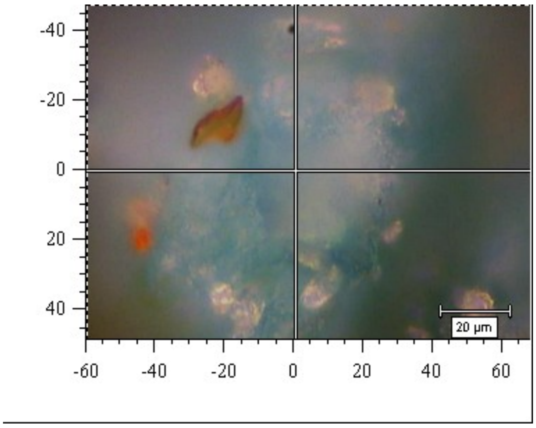	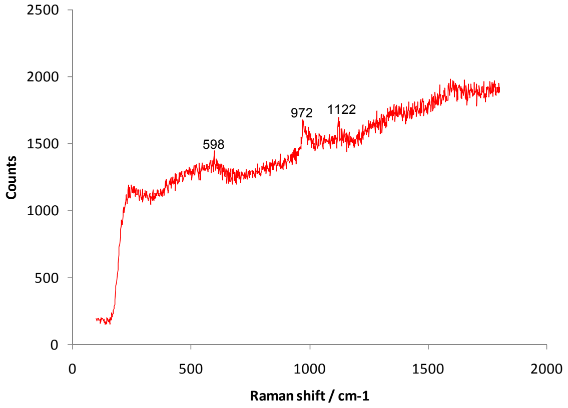 Langite
O5-3	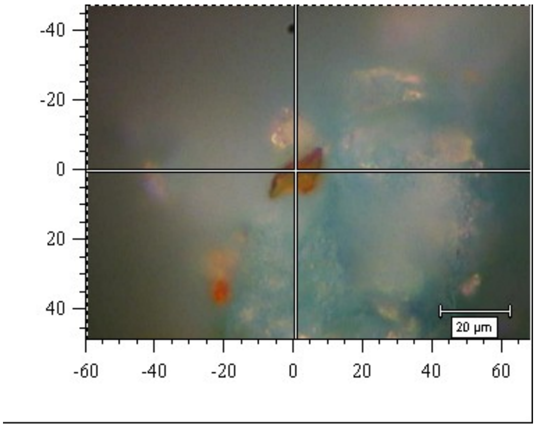	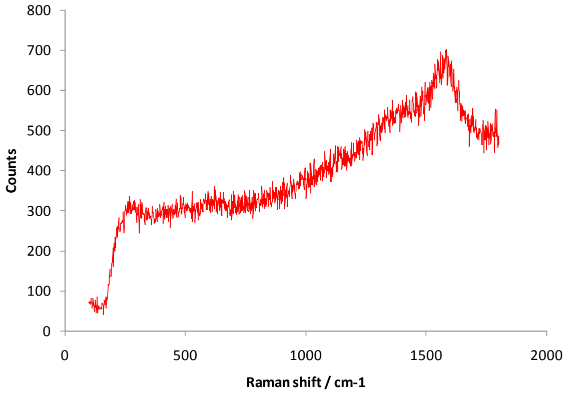

micro-Raman analyses – Wet & dry samples before exposure

Coupon	Microscope image	Raman spectrum and detected products
A-NI Aged Non inhibited (1-1)	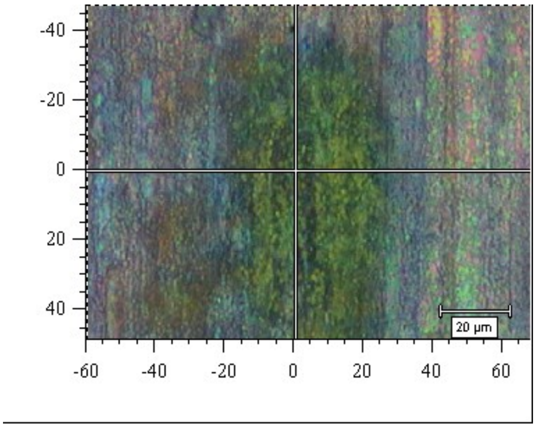	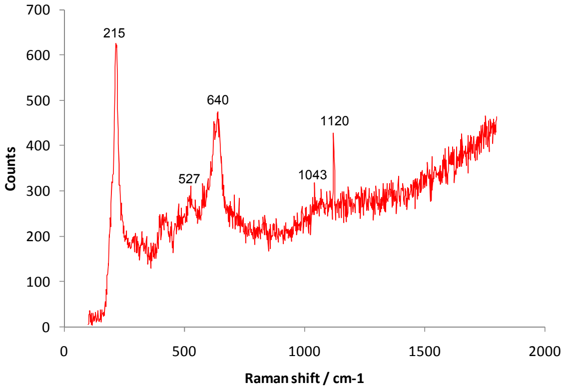 Cuprite
A-NI Aged Non inhibited (1-2)	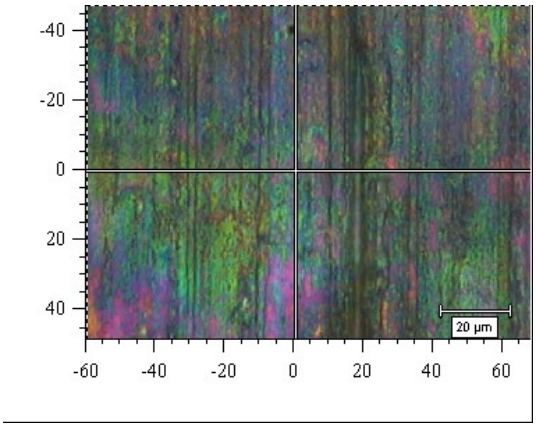	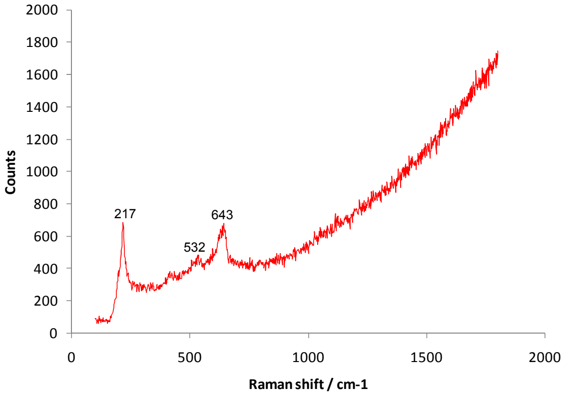 Cuprite, traces of cassiterite
A-NI Aged Non inhibited (1-3)	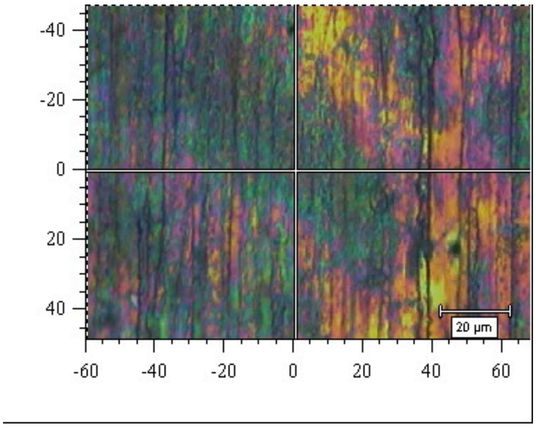	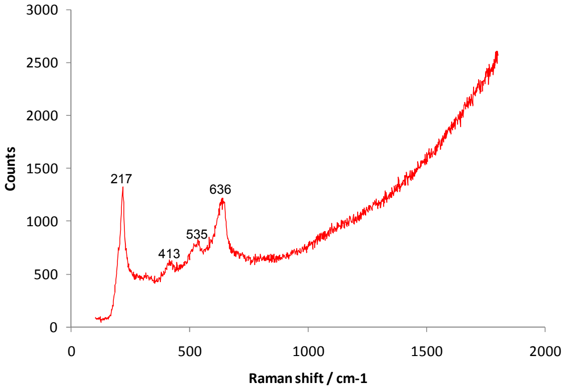 Cuprite

A-NI Aged Non inhibited (1-4)	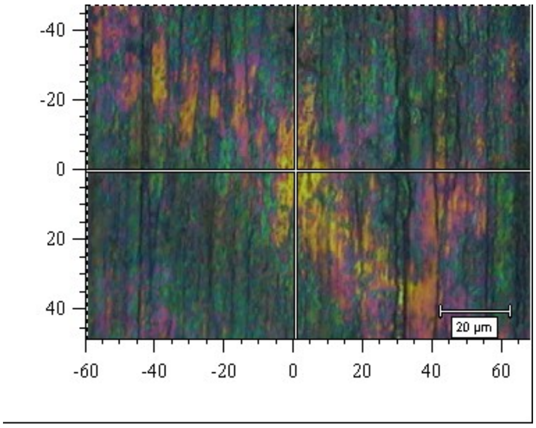	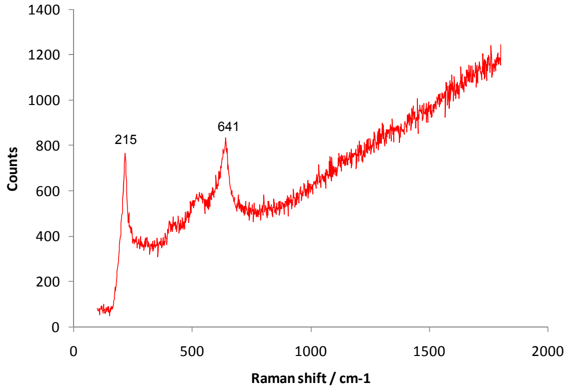 Cuprite, traces of nantokite
NA-P Non aged PropS-SH (2-1)	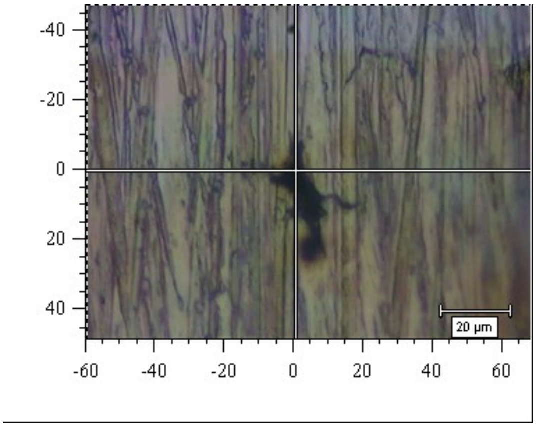	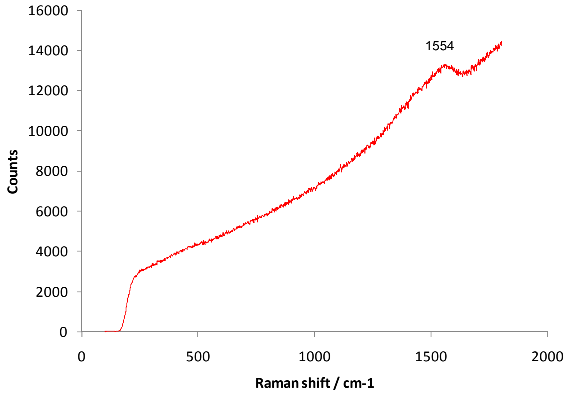 Fluorescence due to inhibitor
NA-P Non aged PropS-SH (2-1 bis)		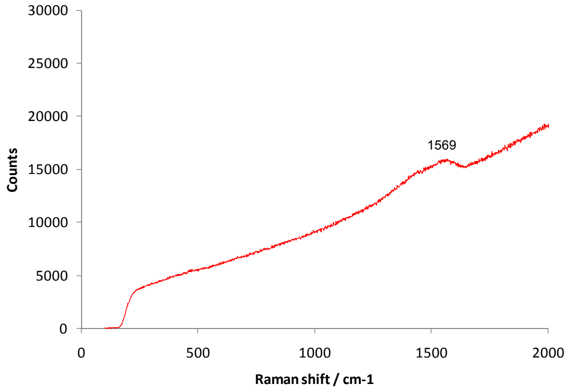 Fluorescence due to inhibitor

NA-P Non aged PropS-SH (2-2)	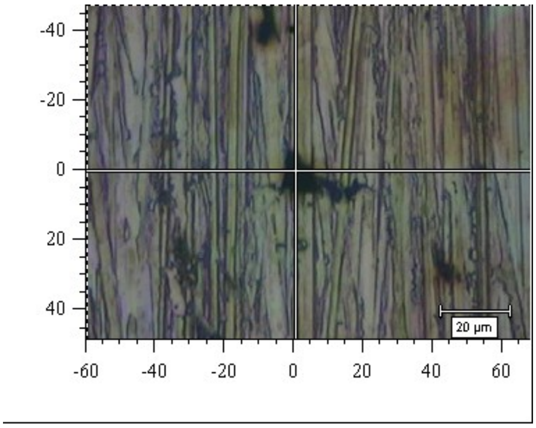	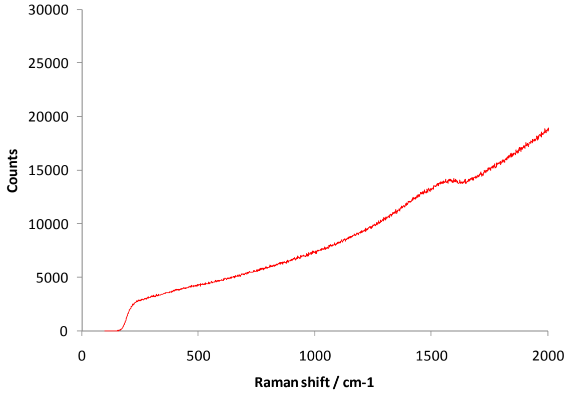 Fluorescence due to inhibitor

micro-Raman analyses – Wet & dry samples after exposure

Coupon	Microscope image	Raman spectrum and detected products
A-NI Aged Non inhibited (1-1)	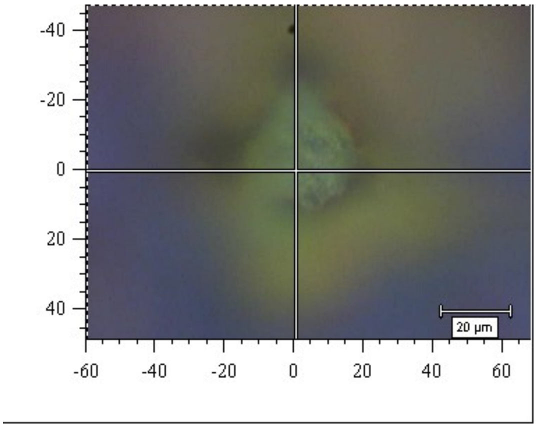	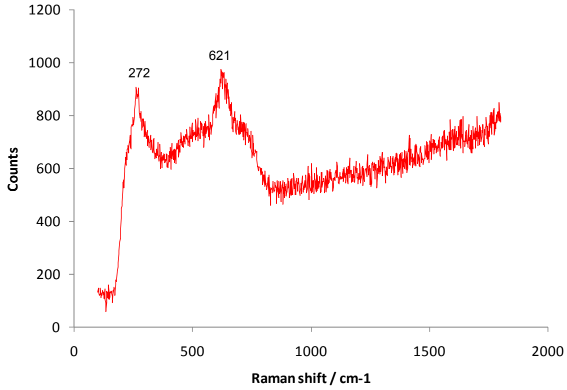 Posnjakite
A-NI Aged Non inhibited (1-2)	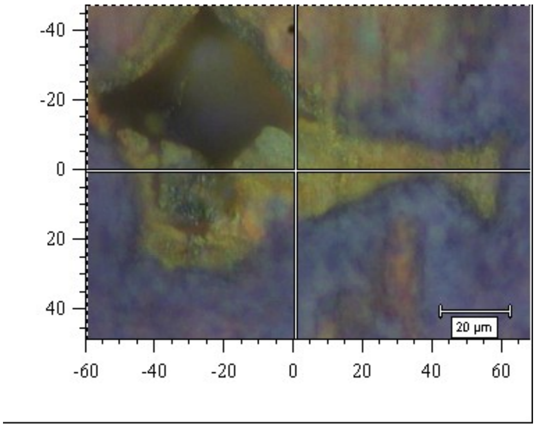	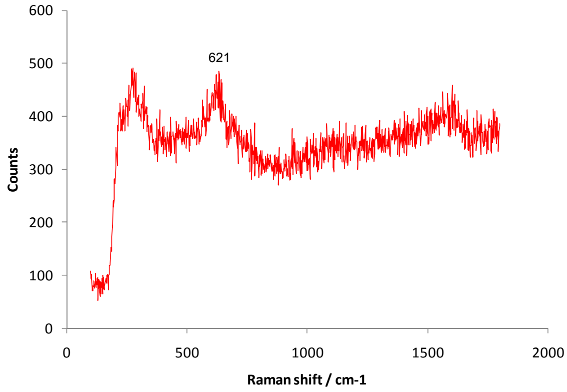
A-NI Aged Non inhibited (1-3)	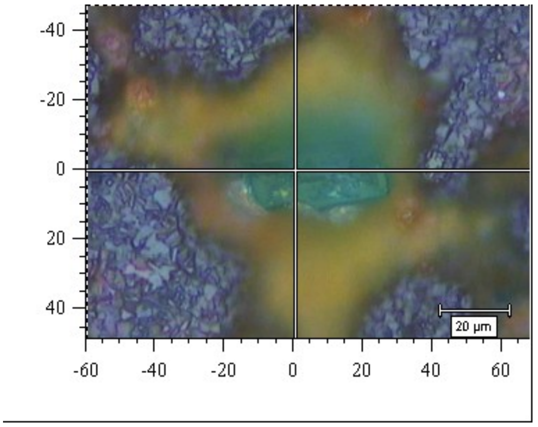	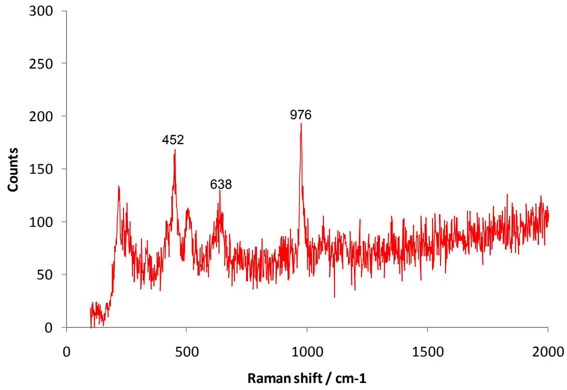 Cuprite, posnjakite

A-NI Aged Non inhibited (1-3 bis)		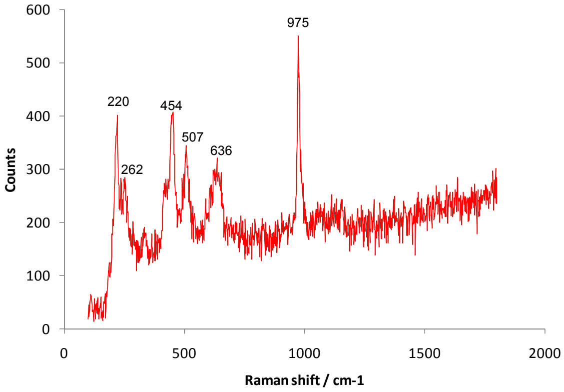 Cuprite, posnjakite
A-NI Aged Non inhibited (1-4)	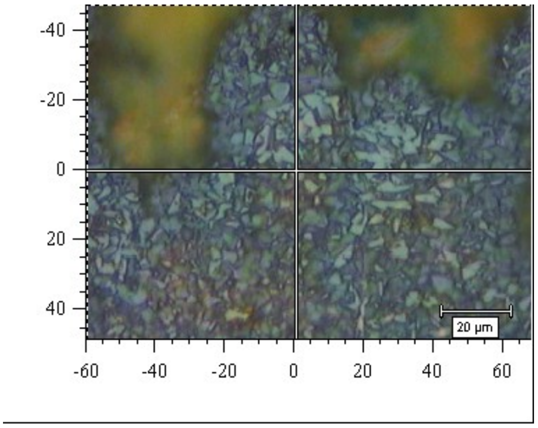	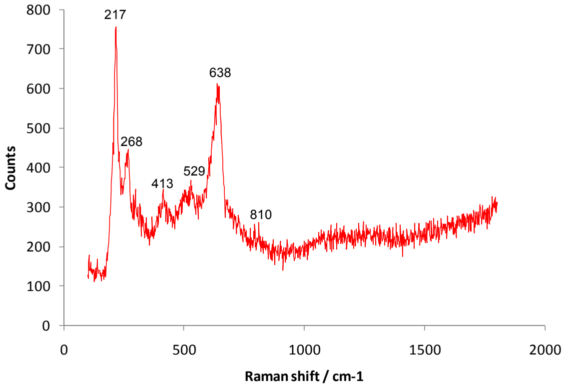 Cuprite, posnjakite
A-NI Aged Non inhibited (1-5)	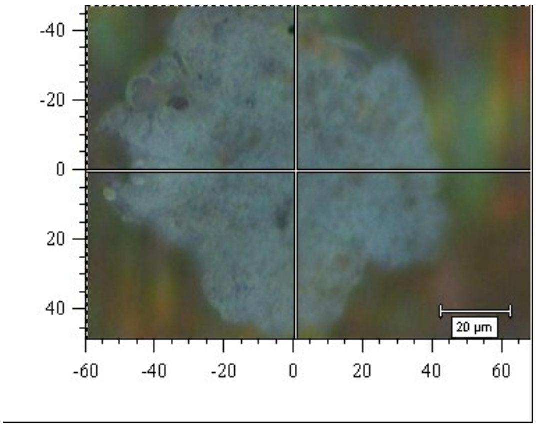	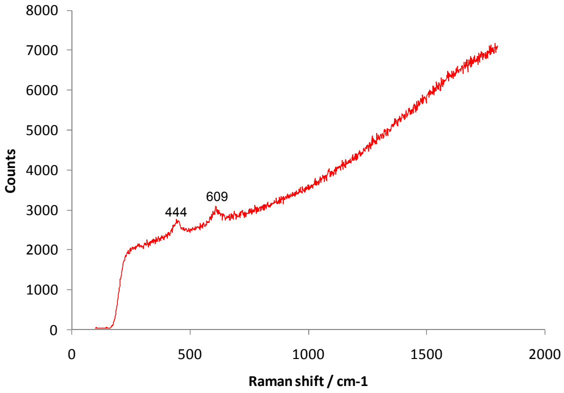

NA-P Non aged PropS-SH (2-1)	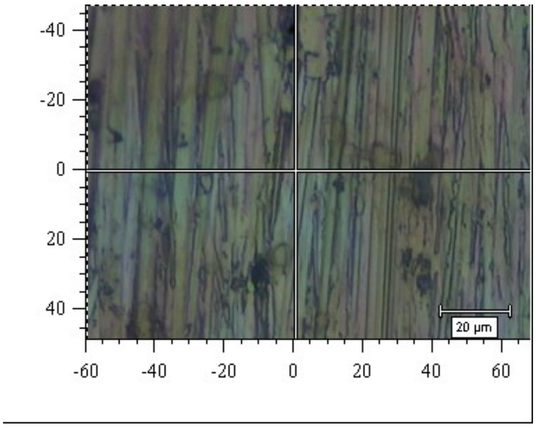	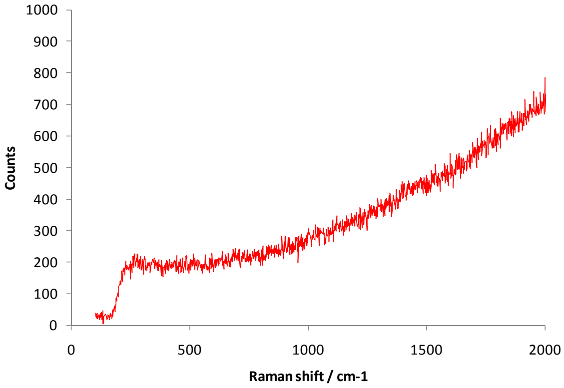 Fluorescence due to inhibitor
NA-P Non aged PropS-SH (2-2)	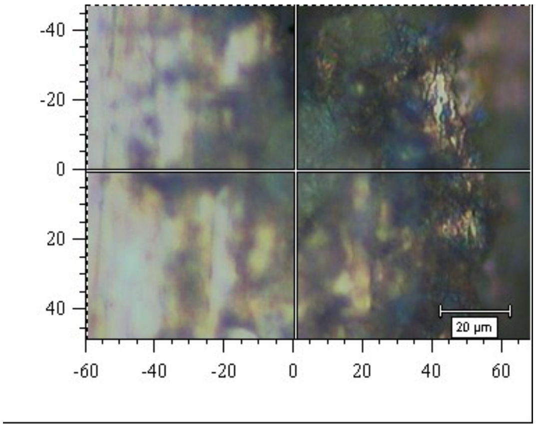	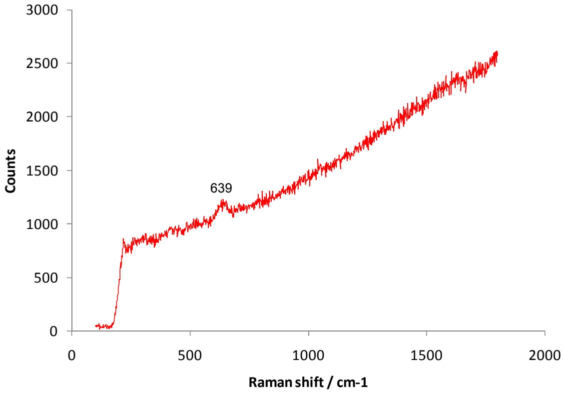 Traces of cuprite
A-P Aged PropS-SH (3-1)	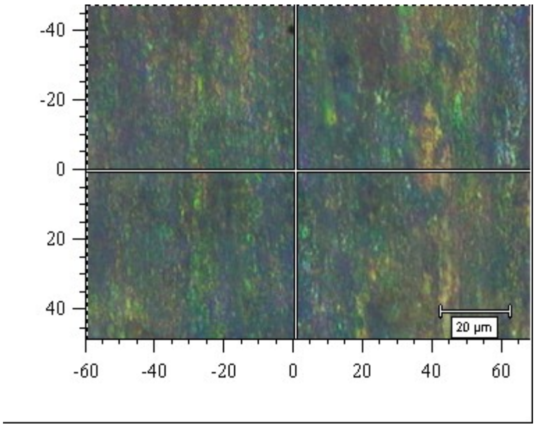	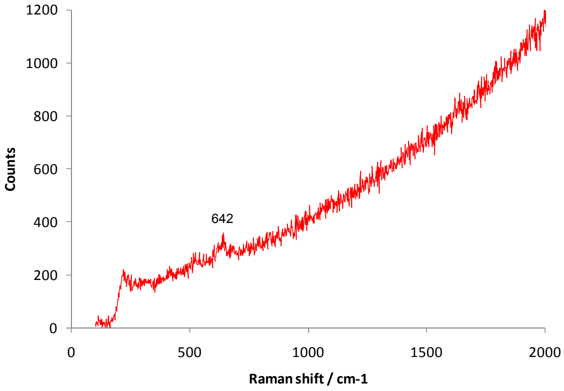 Traces of cuprite

A-P Aged PropS-SH (3-1 bis)		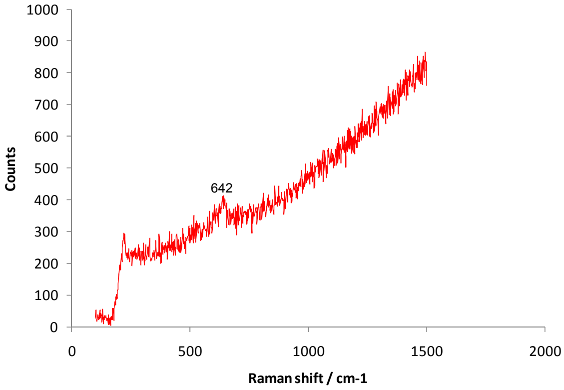 Cuprite
A-P Aged PropS-SH (3-2)	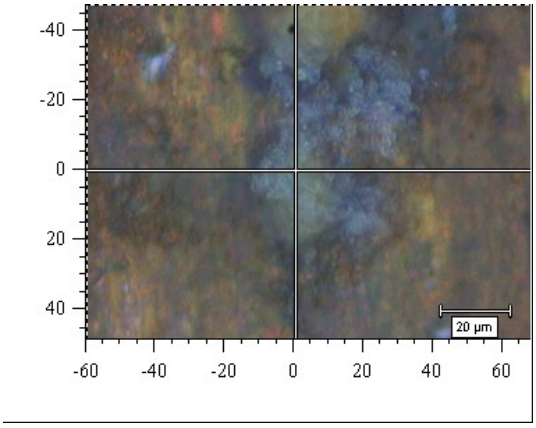	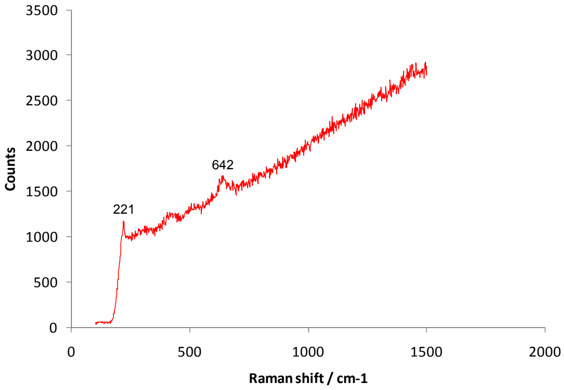 Cuprite
A-PC Aged PropS-SH + CeO_2 (4-1)	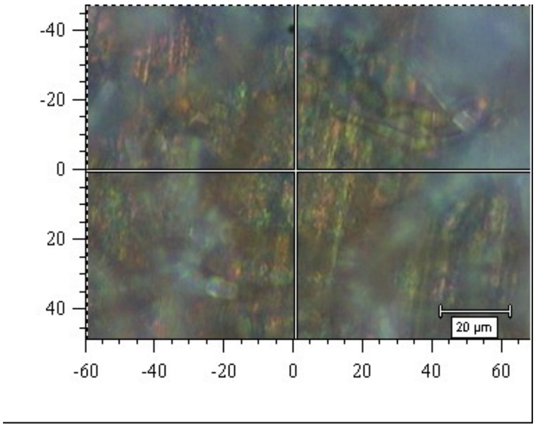	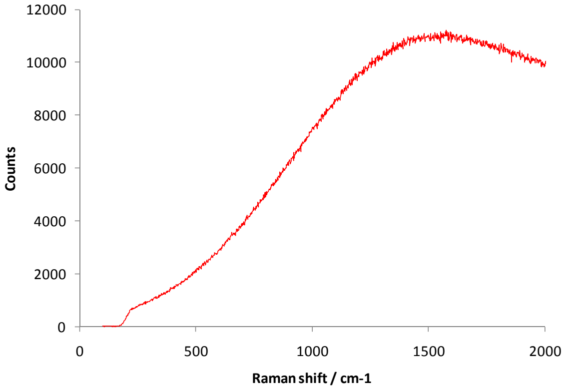 Fluorescence due to inhibitor

A-PC Aged PropS-SH + CeO$_2$ (4-1 net)	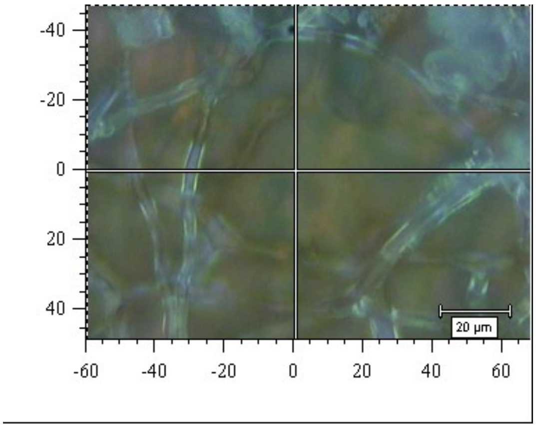	
A-PC Aged PropS-SH + CeO$_2$ (4-2)	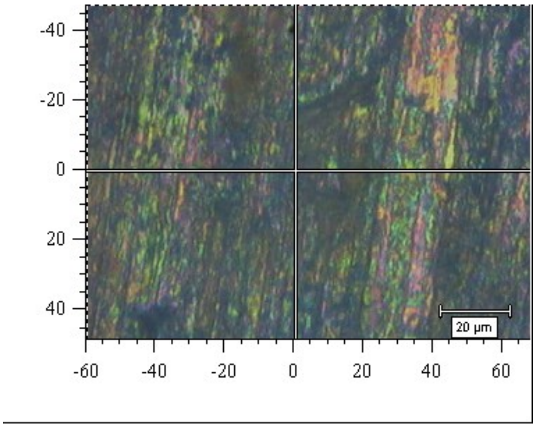	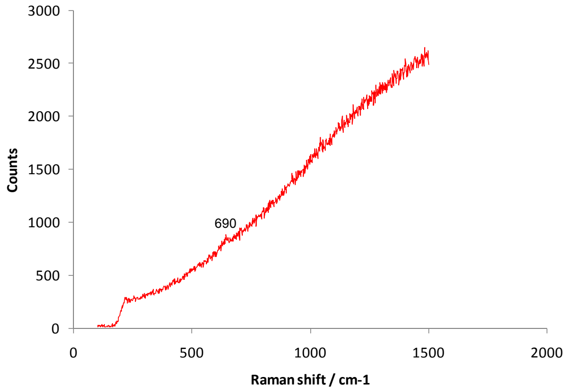

micro-Raman analyses – Total immersion samples after exposure

Coupon	Microscope image	Raman spectrum and detected products
P-NaCl PropS-SH NaCl 3.5% (1-1)	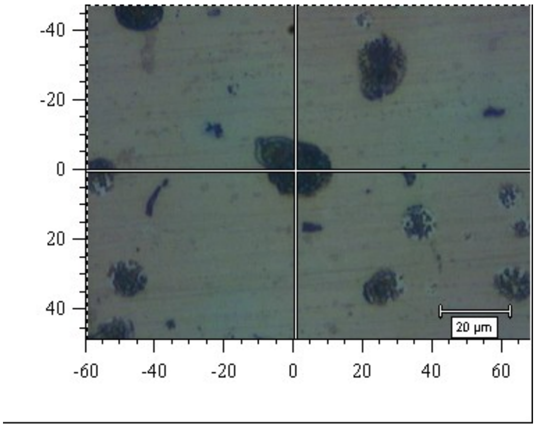	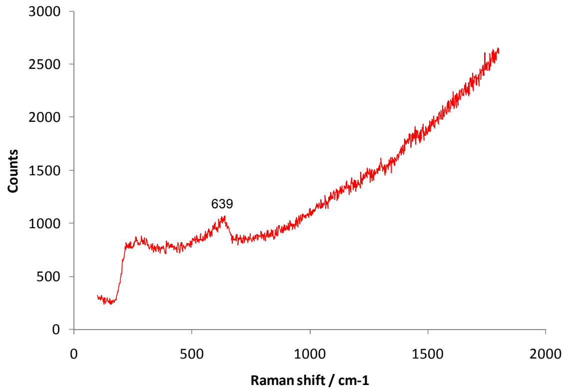 Traces of cuprite and cassiterite
P-NaCl PropS-SH NaCl 3.5% (1-2)	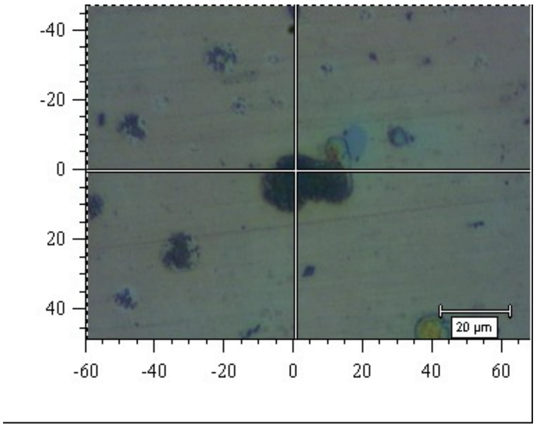	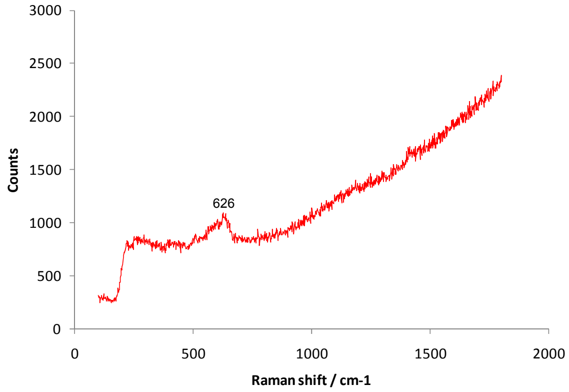 Traces of cuprite and cassiterite
P-NaCl PropS-SH NaCl 3.5% (1-3)	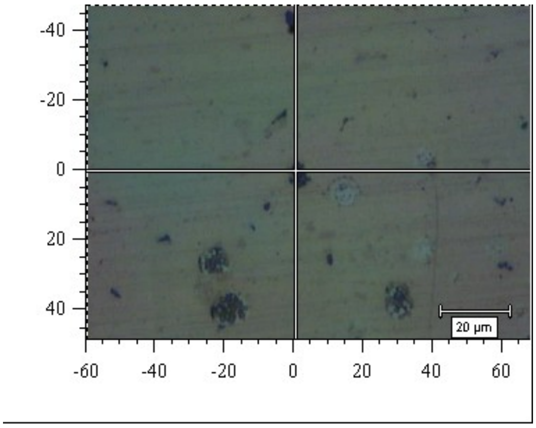	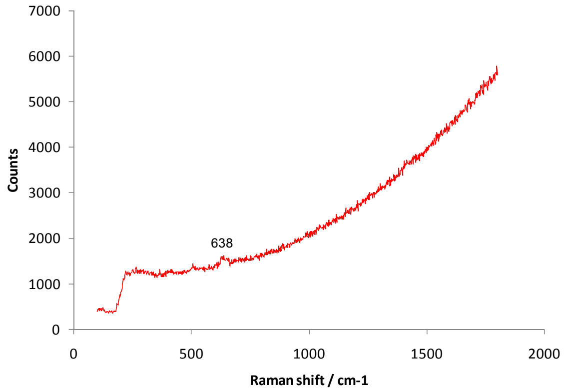 Traces of cuprite and cassiterite

<table>
<tr>
<td>
P-AR

PropS-SH
Acid rain
10x

(2-1)
</td>
<td>
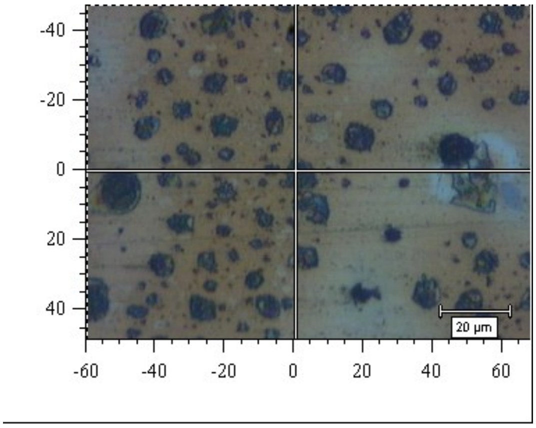

</td>
<td>
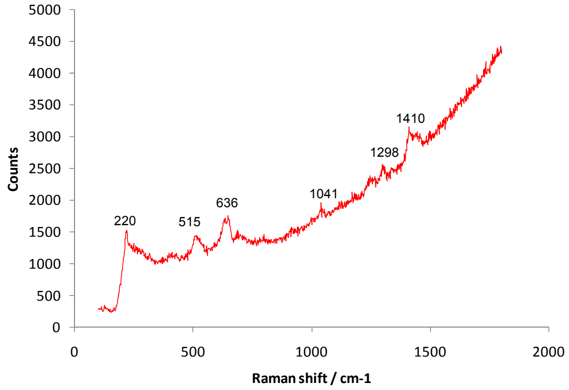

Traces of cuprite and inhibitor bands
</td>
</tr>
<tr>
<td>
P-AR

PropS-SH
Acid rain
10x

(2-2)
</td>
<td>
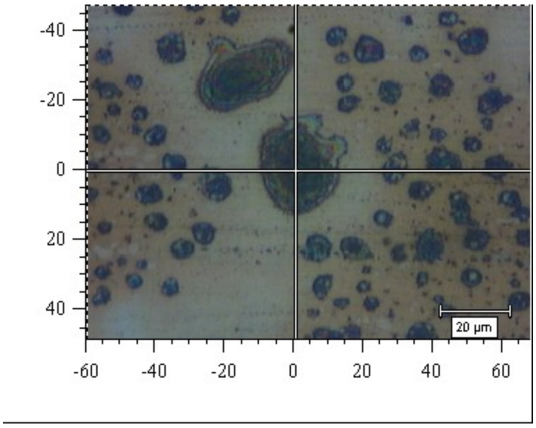

</td>
<td>
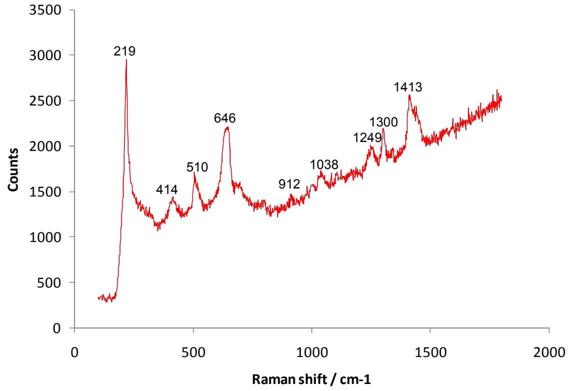

Cuprite, traces of copper sulphate
</td>
</tr>
<tr>
<td>
PC-AR

PropS-SH +
CeO_2
Acid rain
10x

(3-1)
</td>
<td>
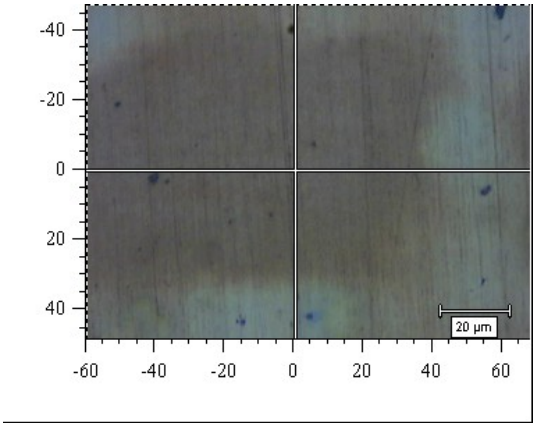

</td>
<td>
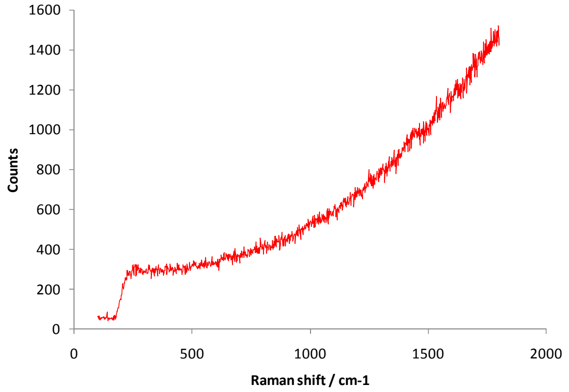

Fluorescence due to inhibitor
</td>
</tr>
</table>

PC-AR PropS-SH + CeO_2 Acid rain 10x (3-2)	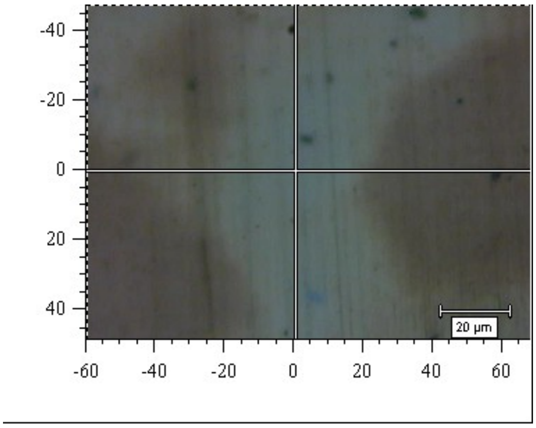	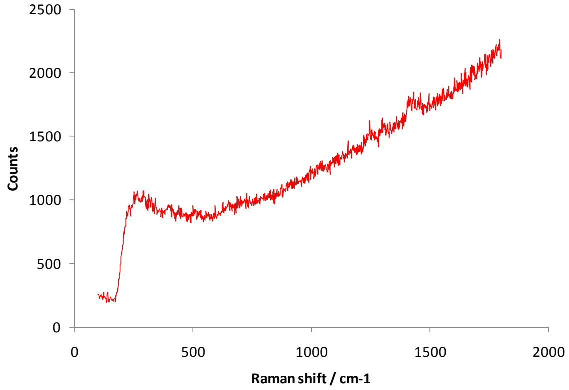 Fluorescence due to inhibitor
NI-AR Non inhibited Acid rain 10x (4-1)	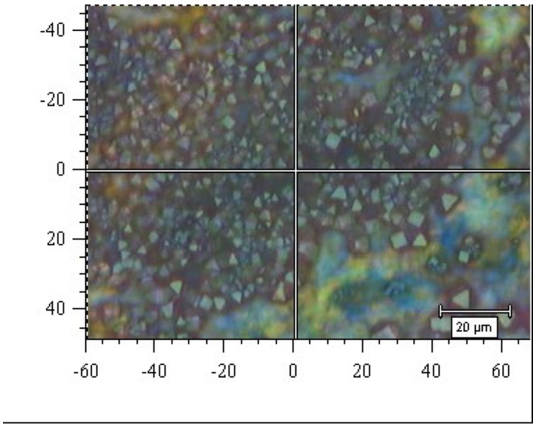	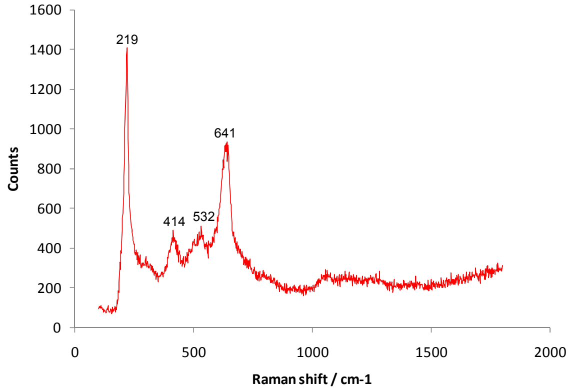 Cuprite, traces of copper sulphate
NI-AR Non inhibited Acid rain 10x (4-2)	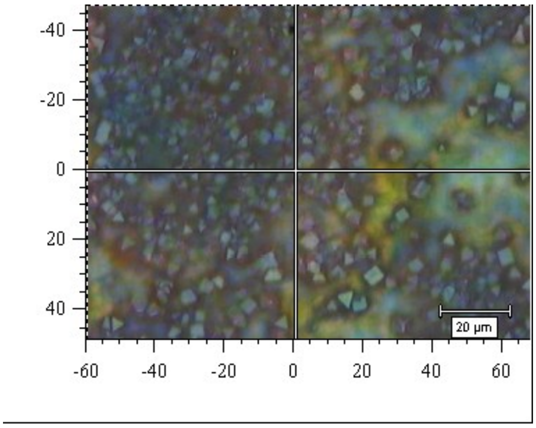	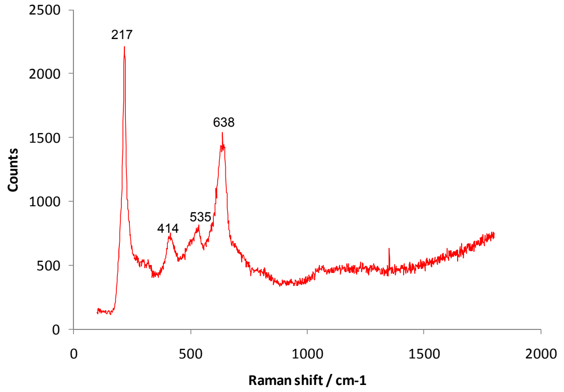 Cuprite

NI-AR Non inhibited Acid rain 10x (4-3)	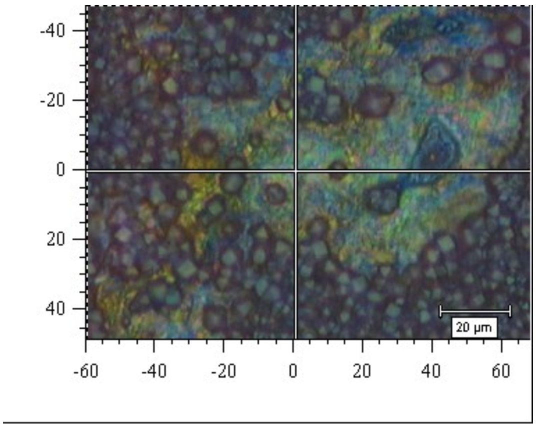	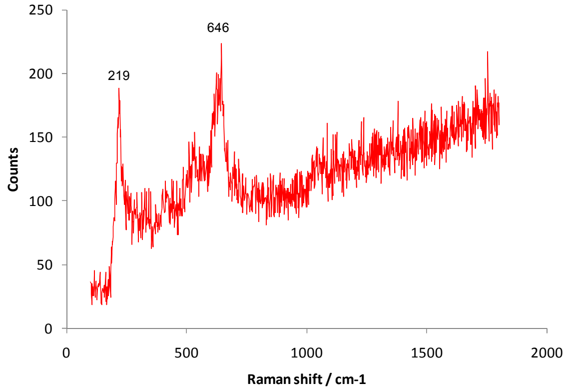 Cuprite
NI-AR Non inhibited Acid rain 10x (4-4)	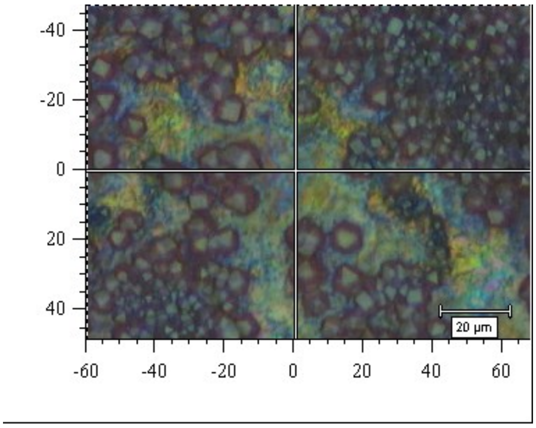	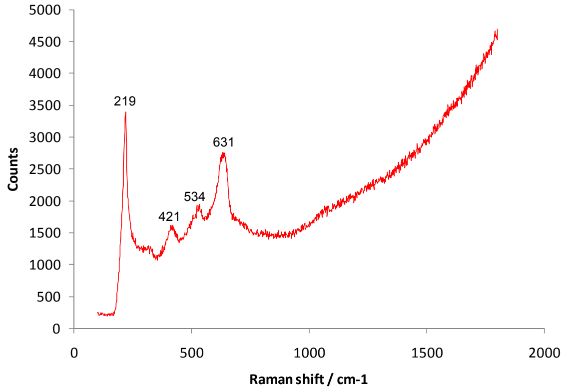 Cuprite
NI-AR Non inhibited Acid rain 10x (4-5)	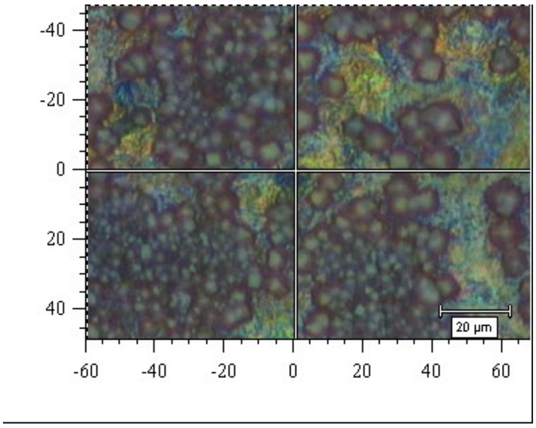	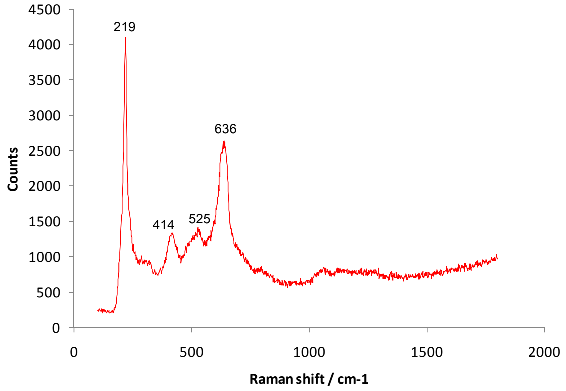 Cuprite

NI-AR Non inhibited Acid rain 10x (4-6)	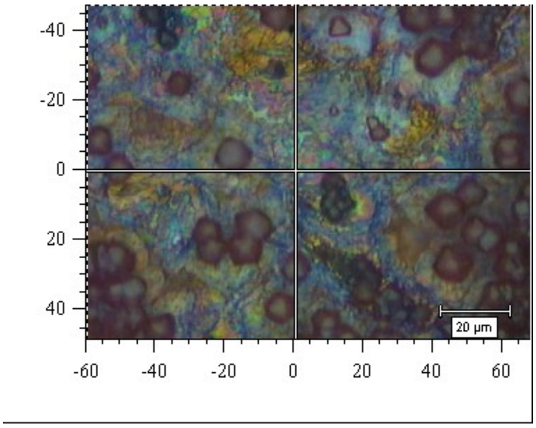	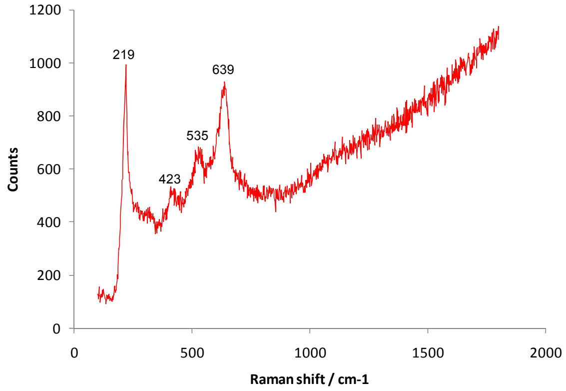 Cuprite

Appendix D

ATR-IR analyses

(spectra interpretation based on [83])

ATR-IR analyses - Bottego corrosion products

<table>
<tr><th colspan="2">Sheltered samples</th></tr>
<tr><th>Sample</th><th>ATR spectrum and detected products</th></tr>
<tr><td>B2</td><td>
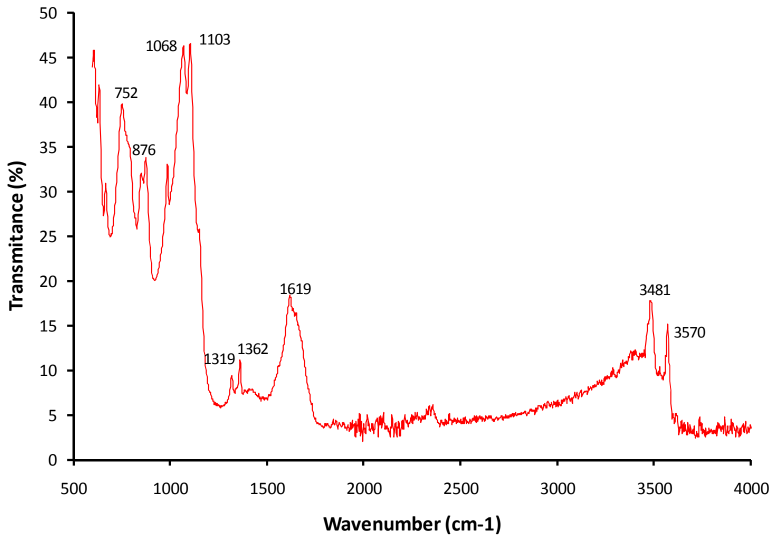

Langite, posnjakite</td></tr>
<tr><td>B3</td><td>
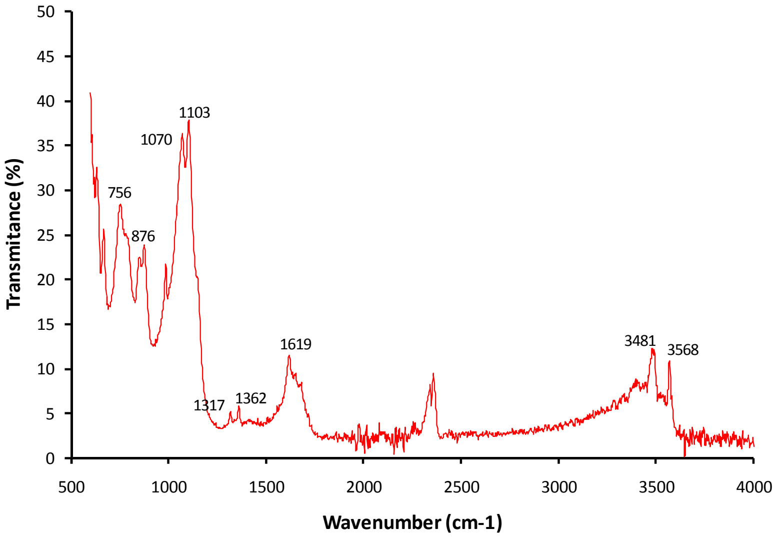

Langite, posnjakite</td></tr>
</table>

B4	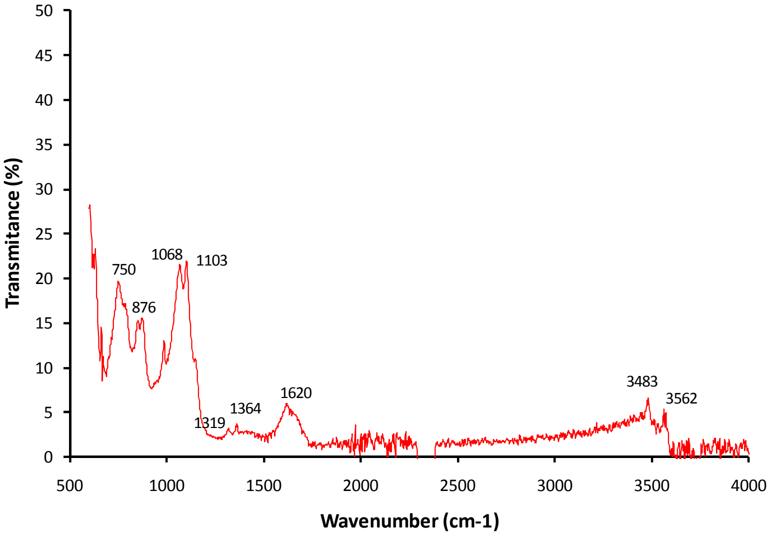 Langite, posnjakite

Unsheltered samples	
Sample	**ATR spectrum and detected products**
B5	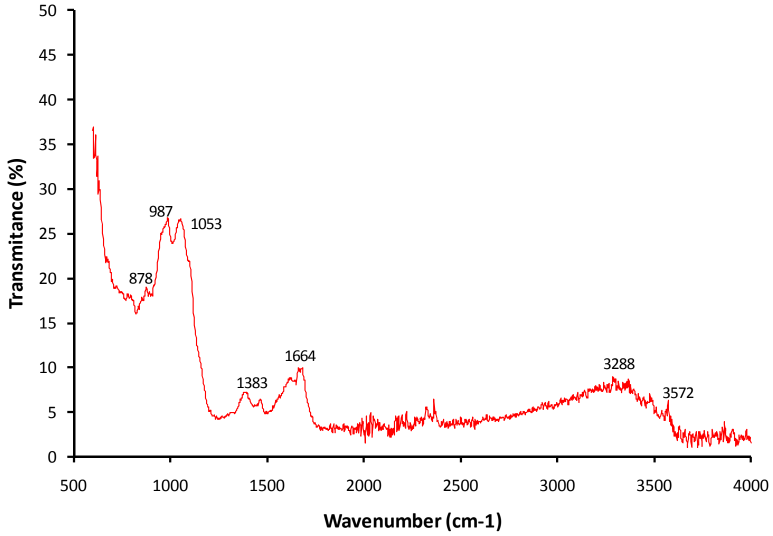 Posnjakite, copper phosphate
B6	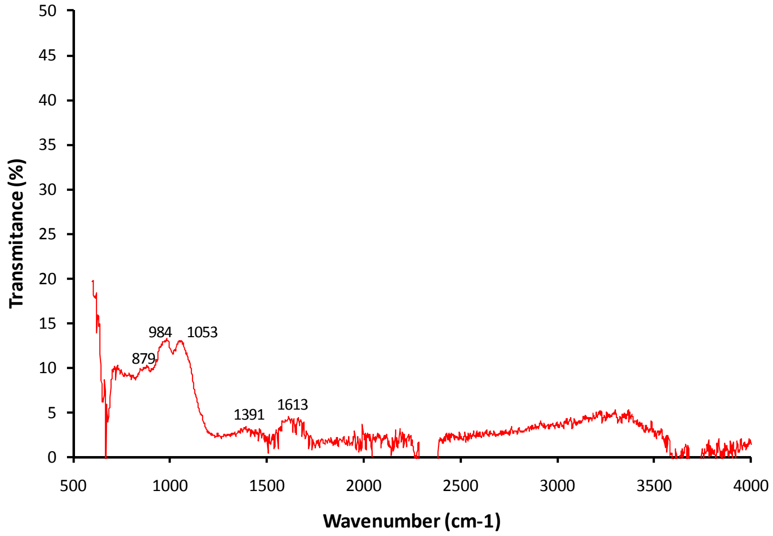 Posnjakite, copper phosphate

B7	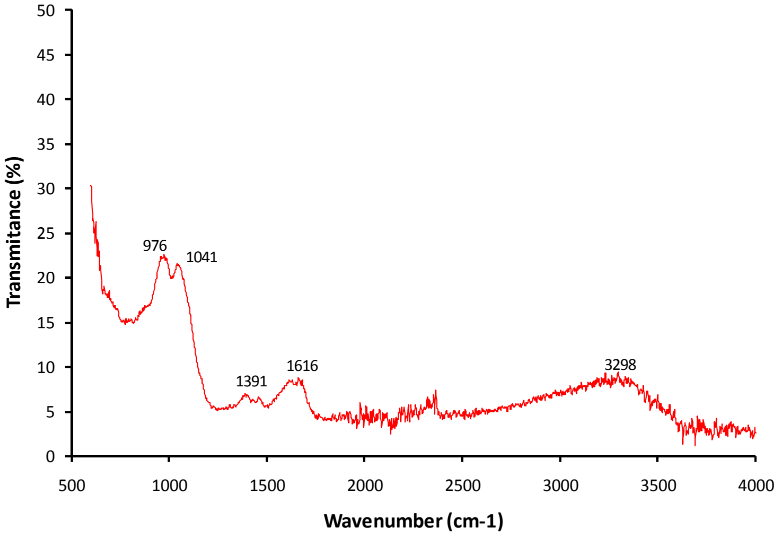 Posnjakite, copper phosphate

ATR-IR analyses - Omo corrosion products

Sheltered samples	
Sample	**ATR spectrum and detected products**
O6	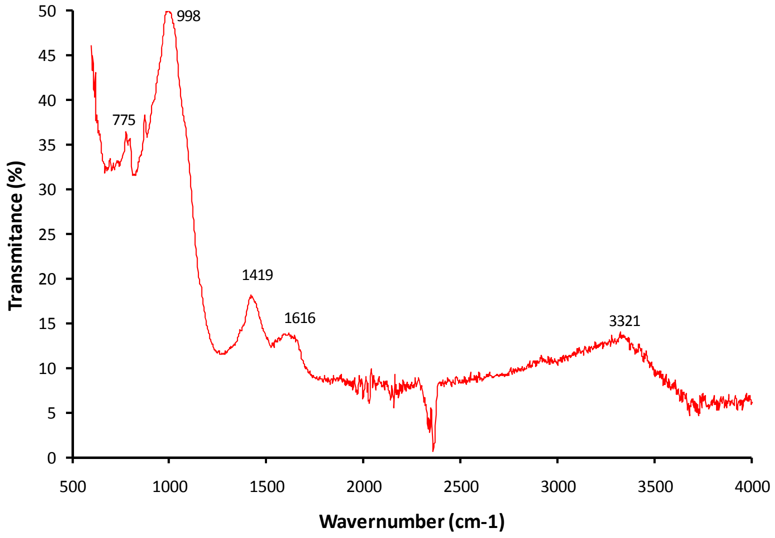 Silicate
O7	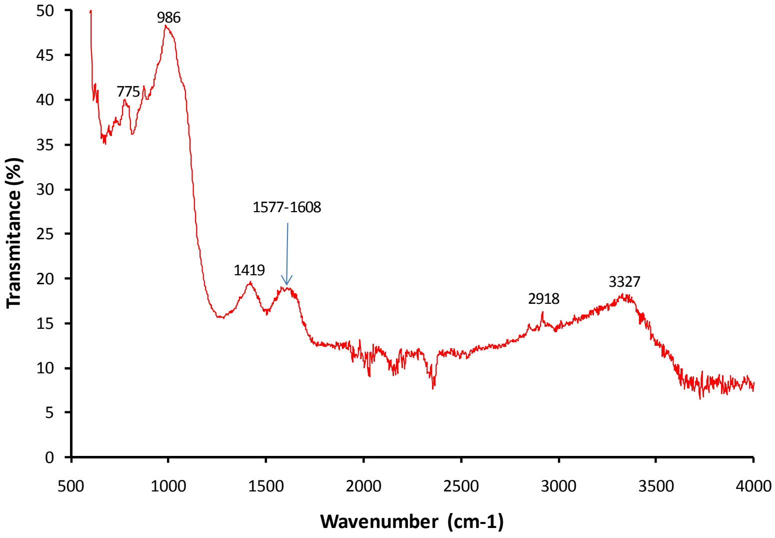 Silicate

<table>
<tr><th colspan="2">Unsheltered samples</th></tr>
<tr><th>Sample</th><th>ATR spectrum and detected products</th></tr>
<tr><td>O3</td><td>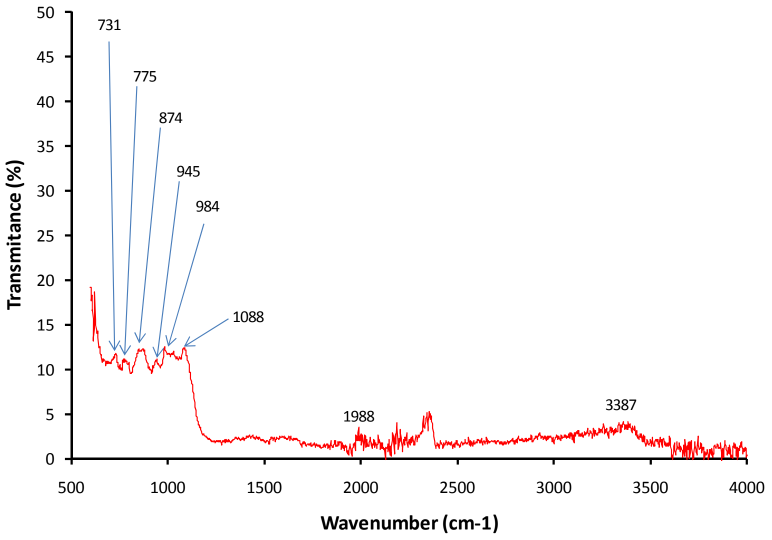

Brochantite</td></tr>
<tr><td>O4</td><td>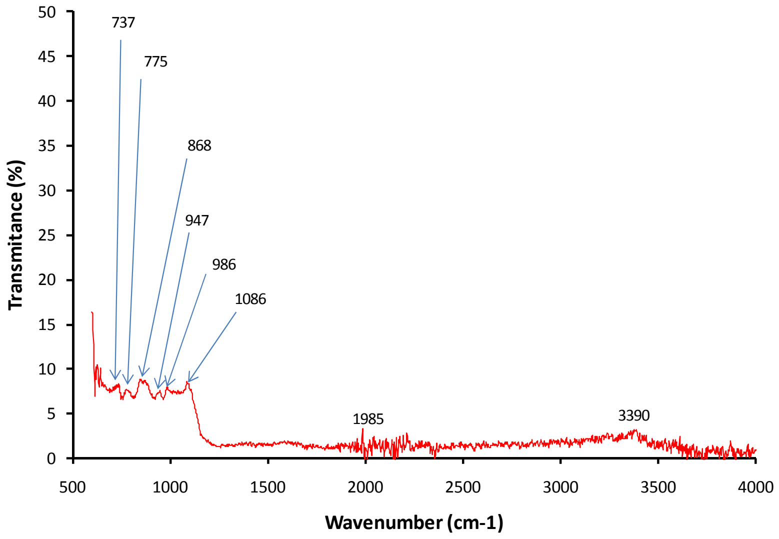

Brochantite</td></tr>
</table>

O5	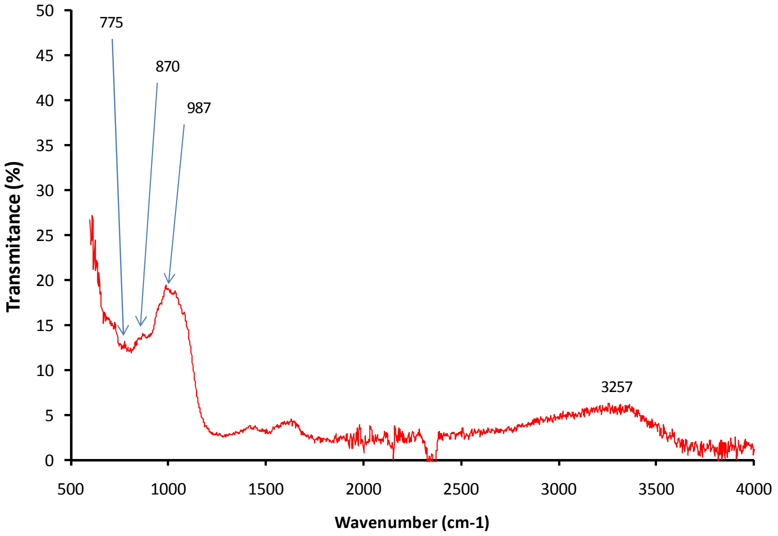775 870 987 3257 Transmitance (%) 50 45 40 35 30 25 20 15 10 5 0 500 1000 1500 2000 2500 3000 3500 4000 Wavenumber (cm-1) Silicate

Appendix E

Portable XRF analyses

Portable XRF analyses - Omo statue (*in situ)*

Geom. exposure	Unsheltered
Location	Shoulder

Before cleaning

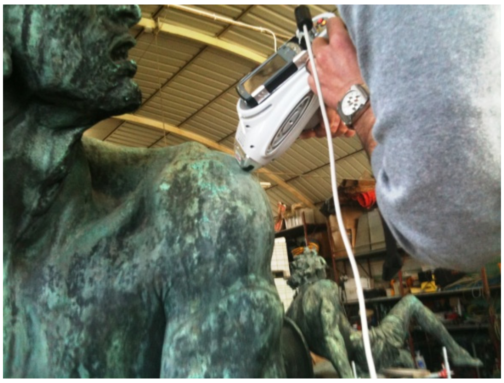

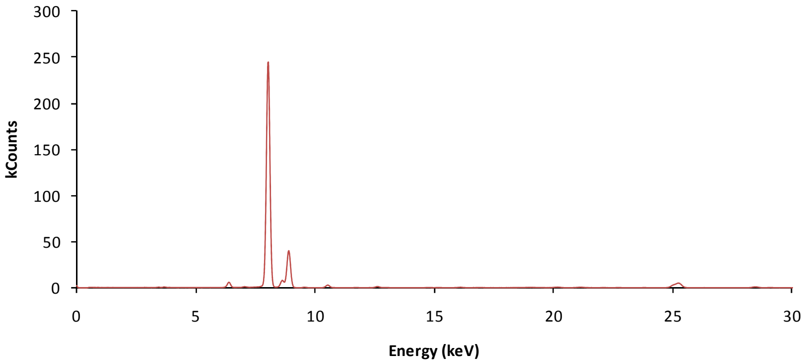

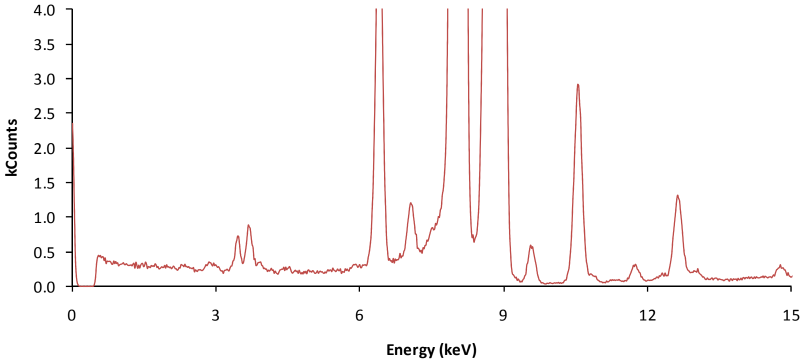

After cleaning

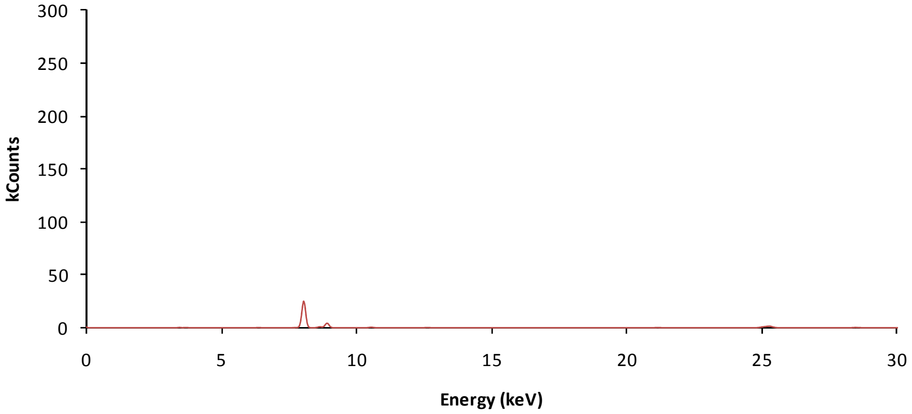

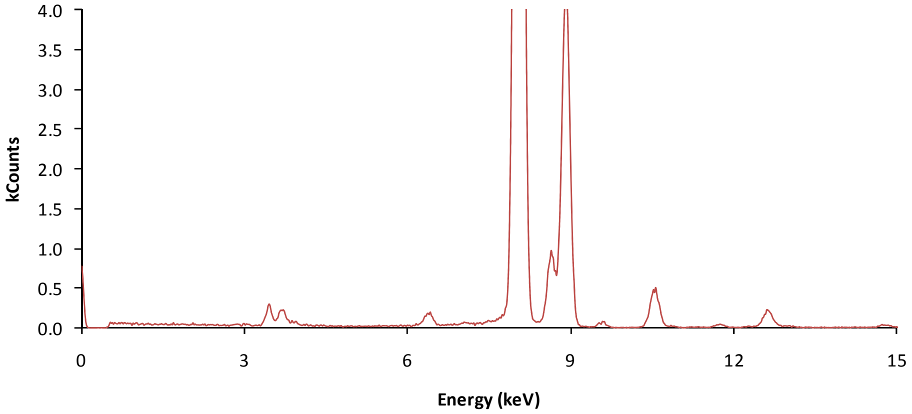

Geom. exposure	Unsheltered
Location	Calf

Before cleaning

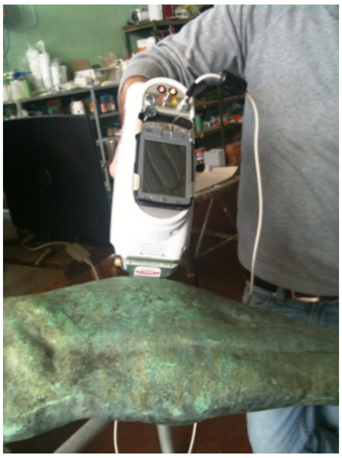

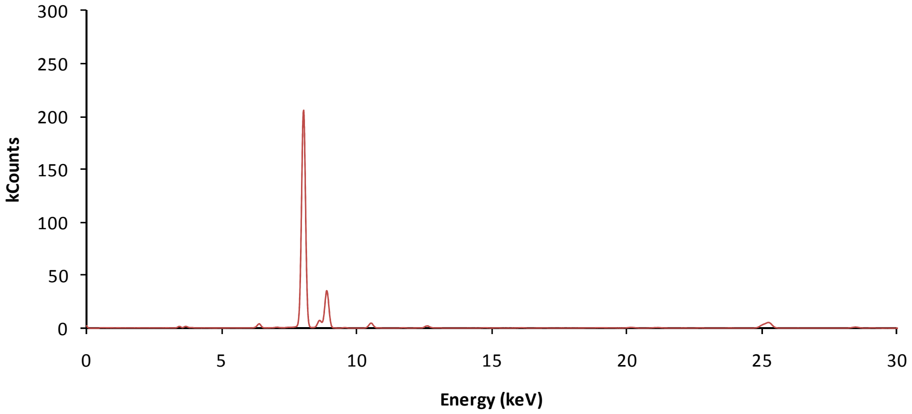

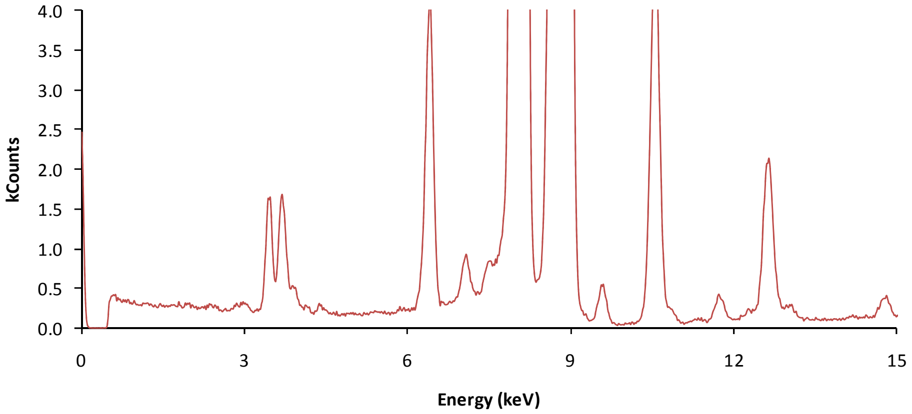

After cleaning

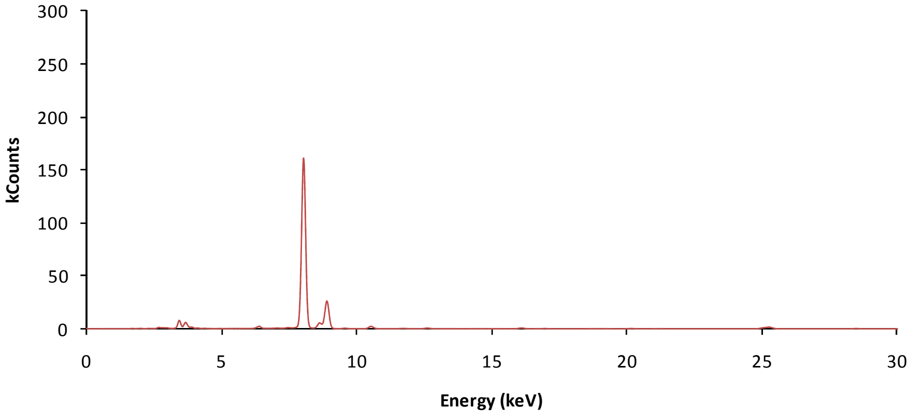

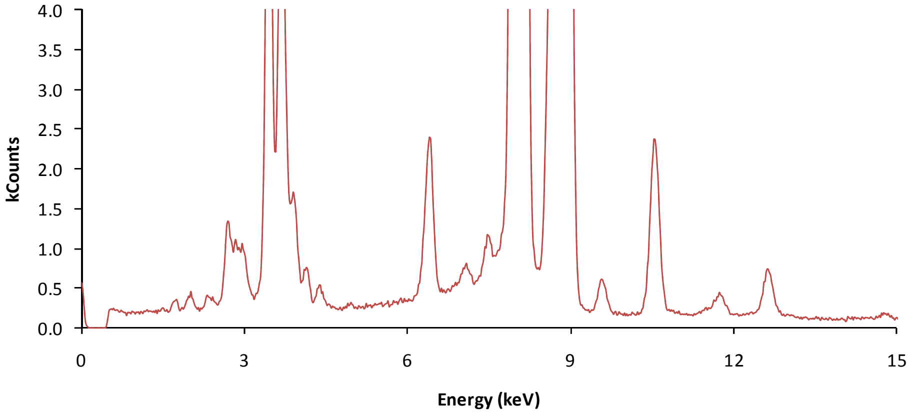

Geom. exposure	Sheltered
Location	Neck

Before cleaning

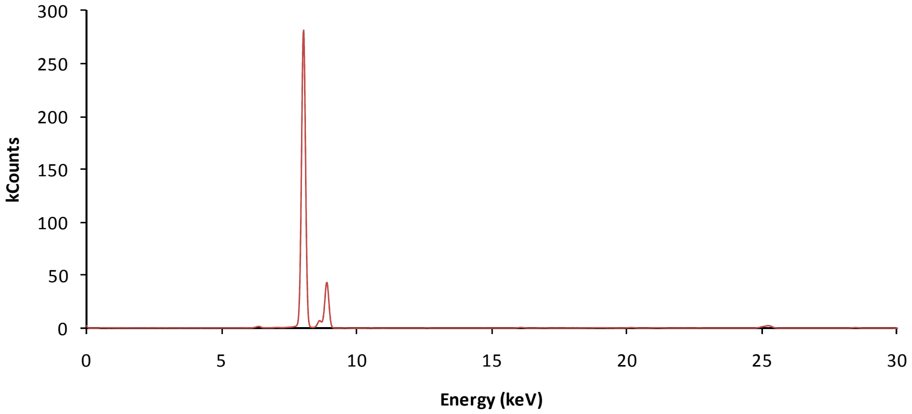

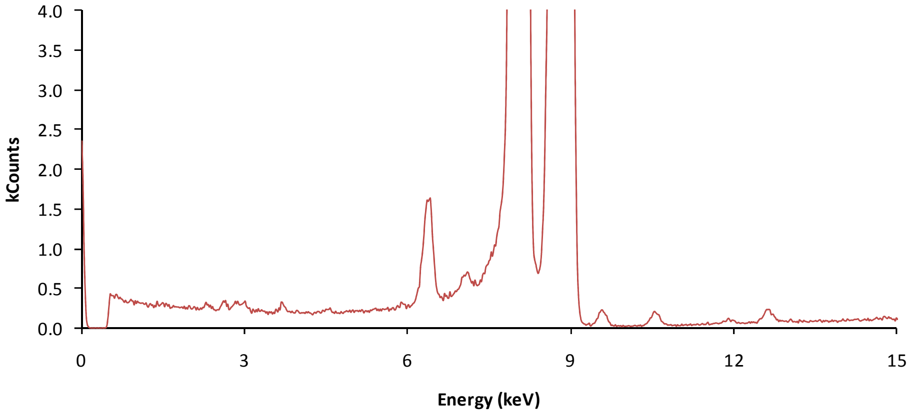

After cleaning

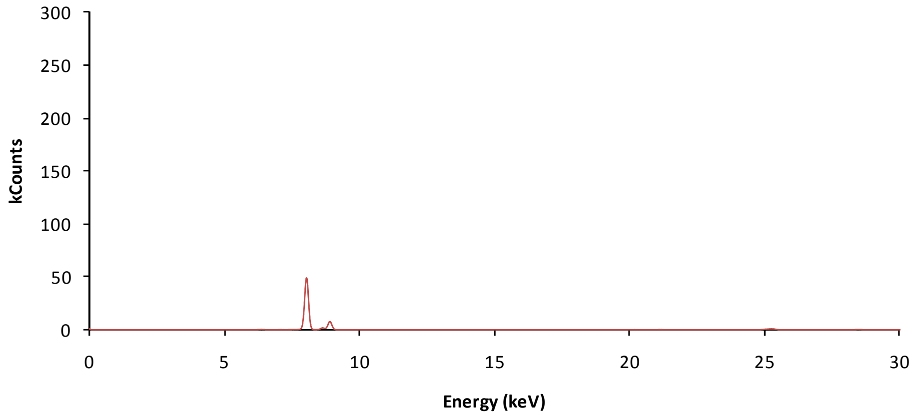

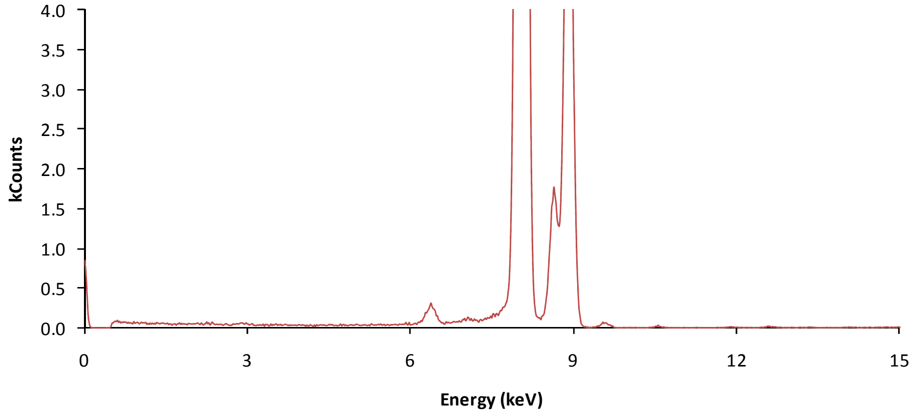

Geom. exposure	Sheltered
Location	Armpit

Before cleaning

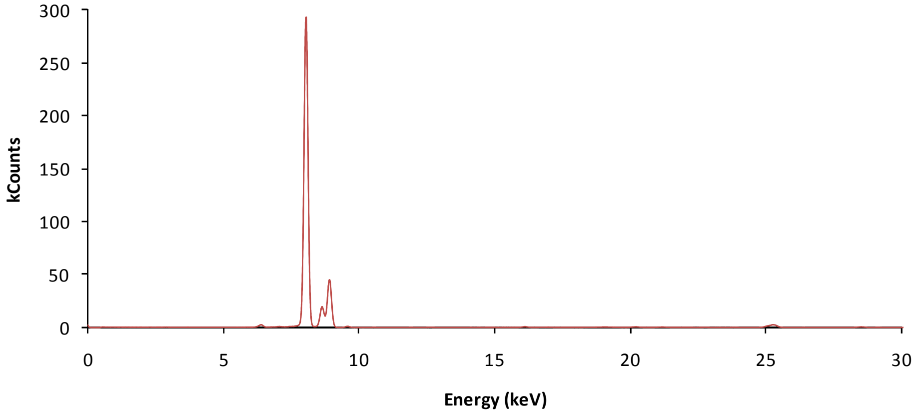

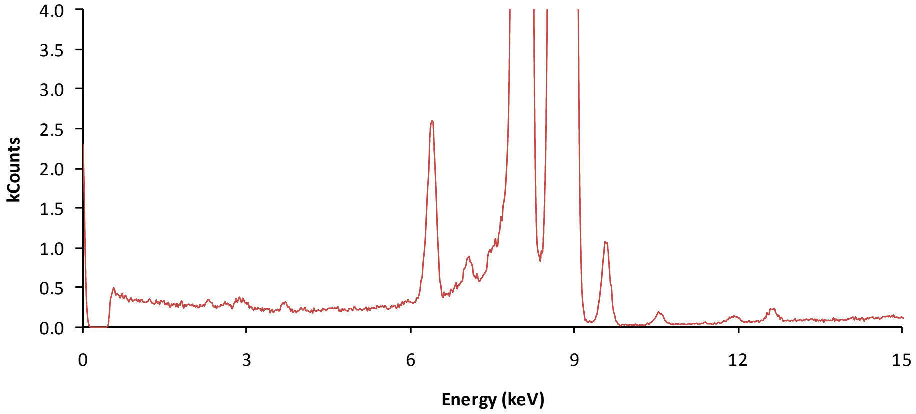

Appendix F

Mineral names and chemical formulas

Mineral name	**Formula**
Copper	Cu
Oxides and Hydroxides	
Tenorite	CuO
Cuprite	Cu_2O
Cu (II) hydroxide	$Cu(OH)_2$
Sulphides	
Covellite	CuS
Chalcocite	Cu_2S
Sulphates	
Chalcocyanite	$CuSO_4$
Chalcanthite	$CuSO_4 \cdot 5H_2O$
Antlerite	$Cu_3(SO_4)(OH)_4$
Brochantite	$Cu_4(SO_4)(OH)_6$
Posnjakite	$Cu_4(SO_4)(OH)_6 \cdot H_2O$
Langite	$Cu_4(SO_4)(OH)_6 \cdot 2H_2O$
Strandbergite	$Cu_{2.5}(SO_4)(OH)_3 \cdot 2H_2O$
Chlorides	
Nantokite	$CuCl$
Atacamite	$Cu_2\,Cl\,(OH)_3$
Paratacamite	$Cu_2\,Cl\,(OH)_3$
Clinoatacamite	$Cu_2\,Cl\,(OH)_3$
Botallakite	$Cu_2\,Cl\,(OH)_3$
Carbonates	
Malachite	$Cu_2(CO_3)(OH)_2$
Azurite	$Cu_3(CO_3)_2(OH)_2$
Chalconatronite	$Na_2Cu(CO_3)_2 \cdot 3H_2O$
Nitrates	
Gerhardtite	$Cu_2(NO_3)(OH)_3$
Phosphates	
Pseudomalachite	$Cu_5(PO_4)_2(OH)_4$
Libethenite	$Cu_2(PO_4)OH$
Cornetite	$Cu_3(PO_4)(OH)_3$
Organic compounds	
Cu (II) formate	$Cu(HCO_2)_2$
Cu (II) acetate	$Cu(CH_3CO_2)_2$
Cu (II) oxalate	$Cu(C_2O_4) \cdot xH_2O$

Tin	Sn
Oxide Cassiterite	SnO_2
Sulphide Herzenbergite	SnS
Lead	Pb
Oxide Litharge	PbO
Sulphate Anglesite	$PbSO_4$
Acetate Lead (II) acetate	$Pb(C_2H_3O_2)_2$
Carbonate Cerussite Hydrocerussite	$PbCO_3$ $Pb_3(CO_3)_2(OH)_2$